Fault ride-through of wind farms using series dynamic braking resistors

Thesis submitted for the degree of **Doctor of Philosophy**

NEWCASTLE UNIVERSITY LIBRARY
207 32504 2
Thesis L8880

Author: Andrew Causebrook

Newcastle University

School of Electrical, Electronic and Computer Engineering

Power Electronics, Drives and Machines Group

September 2008

Abstract

Wind power is one of the world's fastest growing industries. The resulting penetration of wind power has led to substantial changes in requirements for large wind farms. Fault Ride-Through (FRT) was an important new requirement for wind farms to remain connected and actively contribute to system stability during a wide range of network faults. The wind industry responded with several approaches to FRT compliance including dynamic Reactive Power Compensation (dRPC) and pitch control. New requirements, combined with the reduced cost and increased efficiency of power electronic converters has led to the increasing dominance of Variable Speed Wind Turbines (VSWTs). Recent research has therefore focused on VSWTs.

This Thesis presents a new technology, invented and developed during my PhD project, which provides a rearguard opportunity for Fixed Speed Wind Turbines (FSWTs) to comply with FRT requirements using a series Dynamic Braking Resistor (sDBR). sDBR contributes directly to the balance of active power during a fault by inserting a series resistor into the generation circuit, increasing generator terminal voltage. The aim of the analysis, simulation and experimental work in this Thesis is to demonstrate the potential and scope of sDBR to contribute to FRT compliance of FSWTs. sDBR is shown to be a simple and effective means of displacing expensive dRPC to achieve full compliance with Great Britain's FRT requirements. It is also shown to be capable of contributing to compliance with the more onerous FRT requirements in conjunction with other technologies. Detailed transient simulations of sDBR were confirmed by experimental results using a 7.5kW test-rig.

Although the FSWT market is severely weakened, opportunities remain in niche markets for new and existing wind farms. Continued research into high-speed switching, variable resistance and integrated control could further improve basic sDBR performance. Further research into new applications with distribution networks, small wind turbines and doubly-fed induction generators could also extend its application in new markets with longer horizons.

Table of Contents

Table of Figures

Appendices:

Definitions

Distribution system	Low, medium and high voltage networks distributing power to consumers and/or collecting power from distributed generators.
Dynamic model	Mathematical representation of an electrical and/or mechanical system that allows simulation of the system's response to disturbances
Dynamic stability	Ability of an electro-mechanical power system to return to a stable (steady-state) condition after a disturbance
Fault ride-through	Requirement for generators to remain transiently stable and connected to the power system during a defined set of system voltage disturbances.
Grid Code	Operating procedures and principles governing the transmission system operator's relationship with direct users and indirect users that impact on the transmission system (i.e. medium and large generators)
Grid Entry Point	Point at which the wind farm connects to the Transmission System.
Inertia	Property of a rotating body, proportional to mass, that resists change in speed. SI units are kg m^2.
Inertia constant	Conventional expression of rotating inertia in power system representing the inertial energy stored per unit machine power rating.
Large wind farm	For the purpose of this Thesis, a wind farm with an export power capacity in the range 30-150MW.
Large generators	Generators subject to the full requirements of Grid Codes.
Small generators	Generators not subject to the requirements of national Grid Codes.
Steady-state system	System with an unchanging or repetitively oscillating

	dynamic state
Stiffness	Ability of a coupling to resist twisting and is expressed as the ratio of torque to deflection. SI units are Nm/rad.
Supergrid voltage	Any voltage greater than 200kV
System operator	Entity with responsibility for operating a power system or part thereof
Transient stability	As dynamic stability but generally referring to the electrical system
Transmission system	High voltage network carrying bulk power across a power system

Abbreviations

AC	Alternating Current
DBR	Dynamic Braking Resistor
DFIG	Doubly Fed Induction Generator
dRPC	dynamic Reactive Power Compensation
DRR	Dynamic Rotor Resistance
IGBT	Insulated Gate Bipolar Transistor
FRT	Fault Ride-Through
FSWT	Fixed Speed Wind Turbine
HV	High Voltage (Voltages exceeding 35kV)
GB	Great Britain (England, Wales and Scotland)
LV	Low Voltage (Voltages not exceeding 1kV)
MV	Medium Voltage (Voltages between 1kV and 35kV)
PCB	Printed Circuit Board
pu	per unit (dimensionless unit system used through-out this Thesis)
PMSG	Permanent magnet synchronous generator
PWM	Pulse Width Modulation
QSS	Quasi-Steady-State (as defined in Appendix B)
rms	root-mean-square
RoI	Republic of Ireland
RPC	Reactive Power Compensation
sDBR	series Dynamic Braking Resistor (applied to *invention* in this Thesis)
SFIG	Singly Fed Induction Generator
STATCOM	STATic synchronous COMpensation
SVC	Static Var Compensation
TSC	Thyristor Switched Capacitors
VSWT	Variable Speed Wind Turbine
WRIG	Wound rotor induction generator
WTG	Wind Turbine Generator

Notation

General:

Capital letter symbols (i.e. V) refer to inherent, average or rms scalar values.

Non-capital letter symbols (i.e. v) refer to instantaneous scalar values.

Symbols with a top-bar (i.e. $\bar{v}$) are space vectors.

Symbols in vertical brackets (i.e. $|\bar{v}|$) are vector or phasor magnitudes.

Text quantities double underlining (i.e. <u>current</u>) are space vectors.

Subscripts describe the circuit and reference frame axis of a quantity.

English Symbols

a	turns ratio
B	friction coefficient (including windage and bearings)
C	Capacitance
E	Energy
f, F	frequency
H	inertia constant (units of seconds)
i, I	current
J	moment of inertia
K	Stiffness
L	Inductance
M	90^{o} rotation matrix
p, P	active power
pu	Per unit
q, Q	reactive power
R	Resistance
s	Slip
S	apparent power
t	Time
τ, T	Torque

u, U	Speed
v, V	voltage (line voltage in a 3-phase system unless otherwise qualified)

Greek Symbols

λ	Flux
ω, Ω	angular velocity or frequency

Subscript

b	Per-unit base value
c	Drive train coupling quantity
dc	direct current value or component
e	Electrical quantity
g	Generator quantity
l	leakage quantity (i.e. L_{sl} is stator leakage inductance)
m	magnetizing quantity
r	Generator rotor circuit quantity
s	Generator stator circuit quantity
t	Turbine quantity (w.r.t. drive train ref. to turbine rotor side of gearbox)

Acknowledgements

This PhD programme was supported by an EPSRC Postgraduate Research Studentship and an Industrial Scholarship from NaREC[1].

I would like to thank my academic supervisor, David Atkinson, and my industrial supervisor, Adrian Wilson, for their encouragement and direction. I would also like to thank my fellow PhD student, Graham Pannell, for sharing the *long road* with me and offering up "his" valuable test rig for my experimental work. My father has provided steadfast support including taking the time to read through this Thesis twice and giving helpful advice. However, I am most deeply indebted to my wife, Yolande, and son, Samuel, for the years of coping with my obsession with wind turbines and carbon footprints.

And finally, I thank *you* for reading this Thesis. I have tried my best to make it a great read but recognise my limitations!

[1] New and Renewable Energy Centre, Blyth, Northumberland, www.narec.co.uk

1. Introduction

1.1. Wind Penetration Growth and its Consequences

Wind power is one of the world's fastest growing industries. This growth, illustrated in Figure 1-1 (Hansen and Hansen 2007; Hansen and Hansen 2007), has been driven by international and national objectives on carbon emissions reductions and renewable energy penetration.

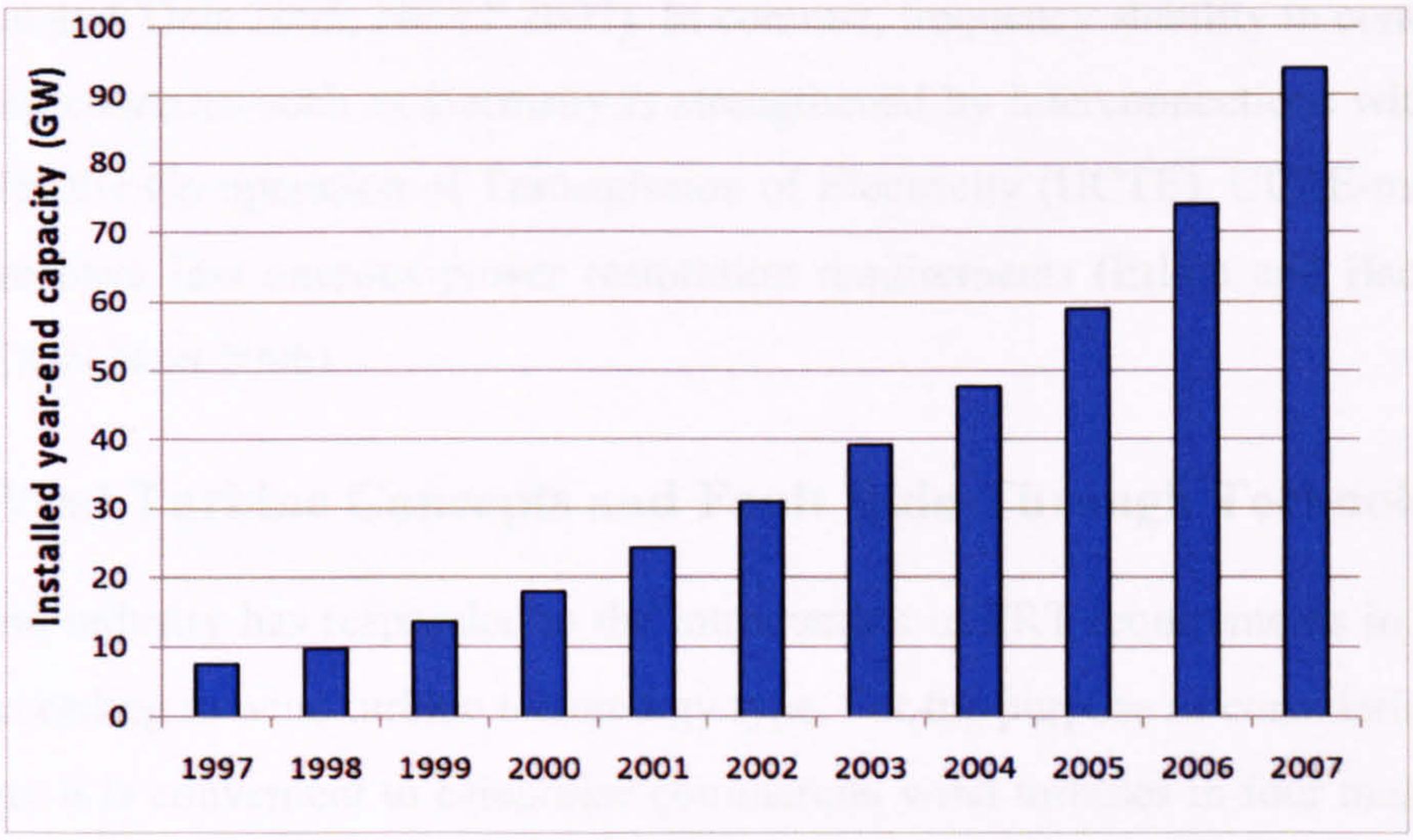

Figure 1-1: World-wide installed wind generation capacity (1997-2007)

Increasing penetration of wind power in power systems in the early years of this decade caused many Transmission System Operators (TSOs) to substantially revise existing codes (Grid Codes) that define the technical requirements for *large generators*. These changes were specifically designed to ensure that wind farms are able to support system stability and contribute to voltage and frequency control. A particular concern of the TSOs was that wind farms should remain connected and actively contribute to the system during a wide range of network faults. This requirement, known as fault ride-through (FRT), is now required for connection of large wind farms in most developed countries (Iov, Hansen et al. 2007). In Great Britain (GB), FRT is imposed on all wind farms classified as medium and large (≥10MW in northern Scotland and ≥50MW in England) and also on smaller embedded wind farms at the discretion of the Distribution Network Operators (DNOs).

FRT performance requirements differ according to the dynamic characteristics of the respective power system. Smaller power systems, with little or no interconnection, are more prone to frequency instability and hence their Grid Codes typically emphasise the provision of active power. Ireland (North and South), with a maximum system demand of 6GW, represents a small, near-isolated system with a challenging requirement to restore power within one second of fault clearance (ESB National Grid 2005; Fagan, Grimes et al. 2005). Great Britain, with a maximum demand of 60GW, represents a larger near-isolated system with similar requirements (Johnson and Tleis 2005; NGET 2007). In contrast, frequency stability in continental European countries such as Germany is strengthened by interconnections within the Union for the Co-operation of Transmission of Electricity (UCTE). UCTE-members therefore have less onerous power restoration requirements (Erlich and Bachmann 2005; E.ON Nezt 2006).

1.2. Wind Turbine Concepts and Fault Ride-Through Technologies

The wind industry has responded to the introduction of FRT requirements in several ways according to wind turbine technology type. For the purpose of considering FRT response, it is convenient to categorise commercial wind turbines in four main types (Hansen 2001; Hansen 2005), as shown in Figure 1-2.

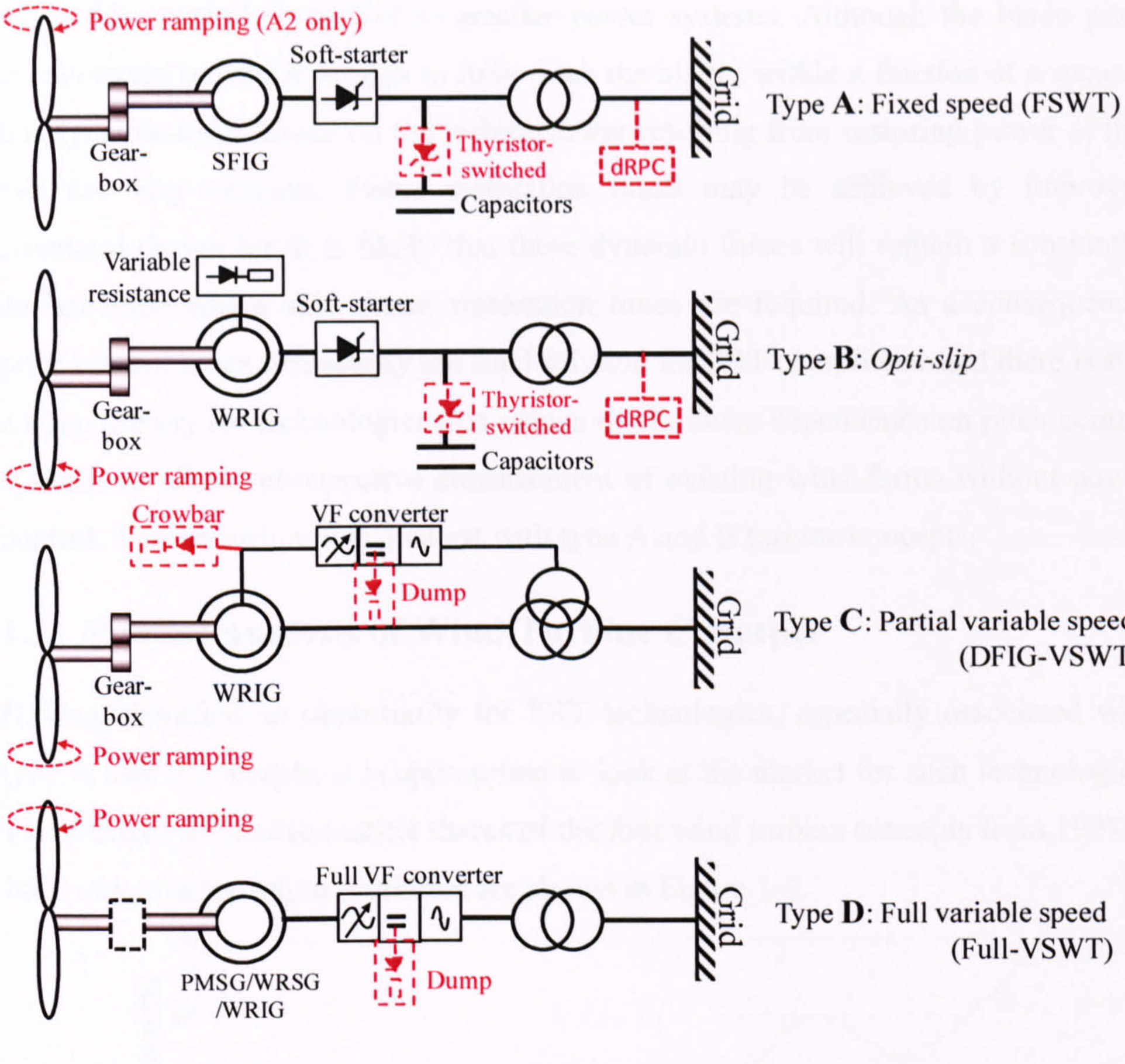

Figure 1-2: Classification of wind turbine concepts

The type A category can be further divided in two parts, A1 being fixed bladed (e.g. Nordex N60) and A2 being pitch controlled (e.g. Siemens 1.3MW *Combistall*). The red dotted "add-ons" to each concept in Figure 1-2 represent state-of-art technologies or enhancements used to contribute to meeting FRT requirements, as summarized in Table 1-1.

Type	FRT enhancement
A1.	Dynamic reactive power compensation (dRPC)
A2.	dRPC and pitch-control (power ramping)
B.	As A1.
C.	Rotor converter protection + pitch control (power ramping)
D.	Pitch control (power ramping) + braking resistors on dc link

Table 1-1: State-of-art technologies/enhancements to meet FRT requirements

Pitch control, where available, is therefore a central feature of most FRT strategies for modern wind turbines. However, there are still significant response limitations

when this method is applied to smaller power systems. Although the blade pitch actuators are powerful enough to fully pitch the blades within a fraction of a second, the dynamic axial forces on the turbine tower resulting from restoring power at this rate are very onerous. Faster restoration times may be achieved by improved structural design but it is likely that these dynamic forces will remain a substantial design issue where sub-second restoration times are required. As a consequence, pitch control is not necessarily the final solution for FRT compliance and there is still an opportunity for technologies that reduce or eliminate dependence on pitch control systems or allow retrospective enhancement of existing wind farms without power control. This opportunity is greatest with type A and B turbine concepts.

1.3. Market Analysis of Wind Turbine Concepts

Having identified an opportunity for FRT technologies, especially associated with type A and B concepts, it is appropriate to look at the market for such technologies. The changes in relative market shares of the four wind turbine concepts from 1997 to 2005 (latest information available) are shown in Figure 1-3.

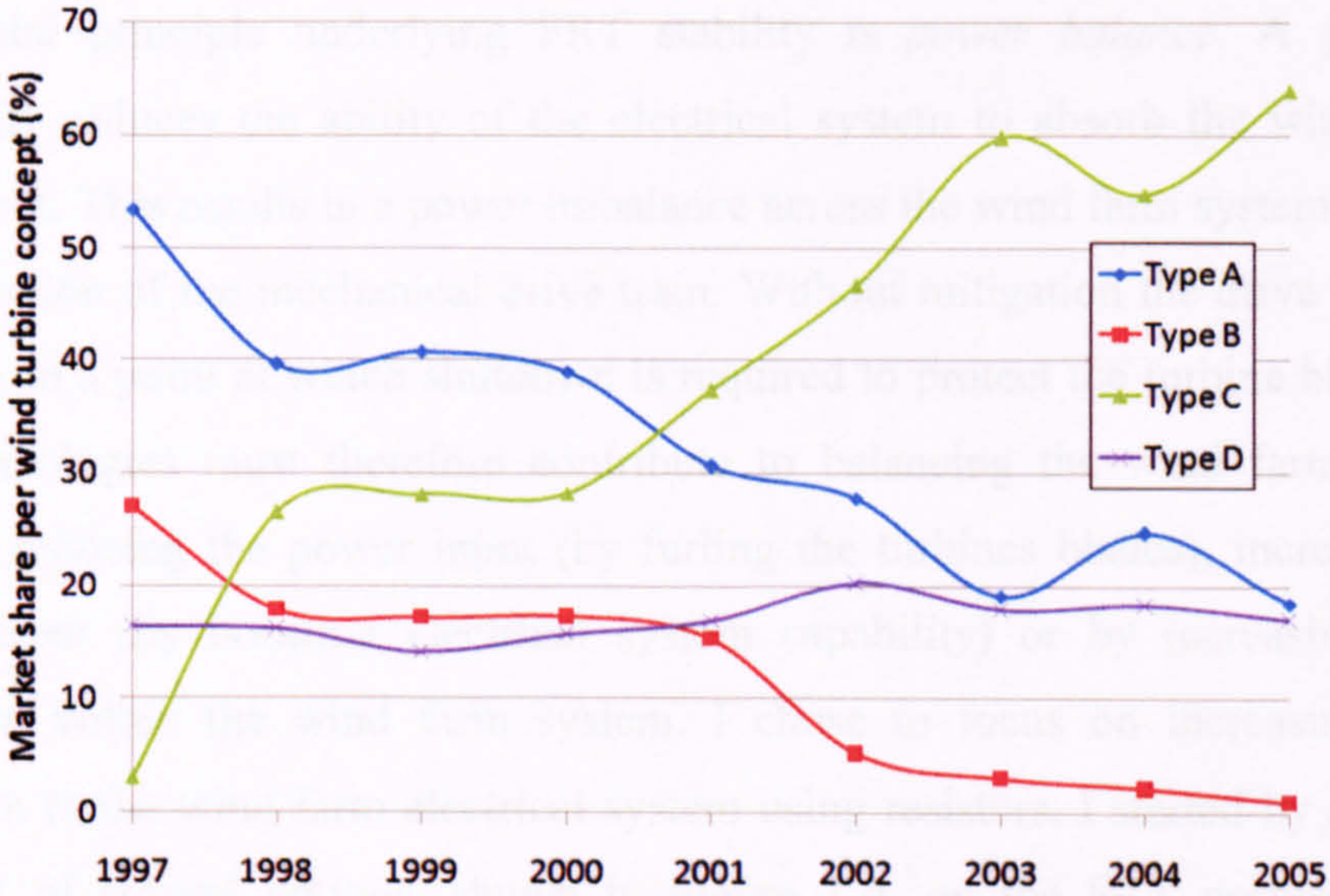

Figure 1-3: Relative market share of wind turbine concepts (Hansen and Hansen 2007)

Figure 1-3 shows the strong growth of the DFIG concept (type C) market share from 5% in 1997 to 64% in 2005. In contrast, the fixed speed (type A) and *Optislip* (type B) concepts have declined from a dominant combined share of 80% in 1997 to less than 20% in 2005. This decline has accelerated since the widespread introduction of FRT requirements in 2004/5 and the combined market share for types A and B is

now less than 10%. Notably, the two most common European multi-megawatt fixed speed turbines (Siemens 1.3MW and Nordex N60) are being withdrawn from the market. In contrast, there is a resurgence of smaller fixed speed machines in China because of the 300% growth in the Chinese wind industry in 2007.

There has therefore been a significant downturn in opportunities for enhancing the FRT performance of new wind farms projects with FSWTs in Europe. The greatest opportunity for FRT technologies specifically aimed at FSWTs is currently in the Asian market. The greatest opportunity associated with FSWTs in Europe could be the retrofitting of FRT technology to existing FSWT wind farms in countries such as Spain, Germany and Denmark, where there is high penetration of wind power pre-dating the requirements for FRT compliance.

1.4. PhD Methodology and Aim

My aim at the outset of this PhD programme in 2003/4 was to identify a novel concept that would address the fundamental principles of FRT, thereby avoiding excessive dependence on particular manufacturers' design or control. The most fundamental principle underlying FRT stability is *power balance*. A grid fault temporarily reduces the ability of the electrical system to absorb the wind farm's power input. This results in a power imbalance across the wind farm system resulting in acceleration of the mechanical drive train. Without mitigation the drive train will accelerate to a point at which shutdown is required to protect the turbine blades. All FRT technologies must therefore contribute to balancing the wind farm system, either by reducing the power input (by furling the turbines blades), increasing the power output (by boosting electrical system capability) or by increasing power dissipation within the wind farm system. I chose to focus on increasing power dissipation in the wind farm electrical system using resistors. I started by analysing the effect of several options, shown in Figure 1-4, on the FRT performance of FSWTs and DFIG-VSWTs.

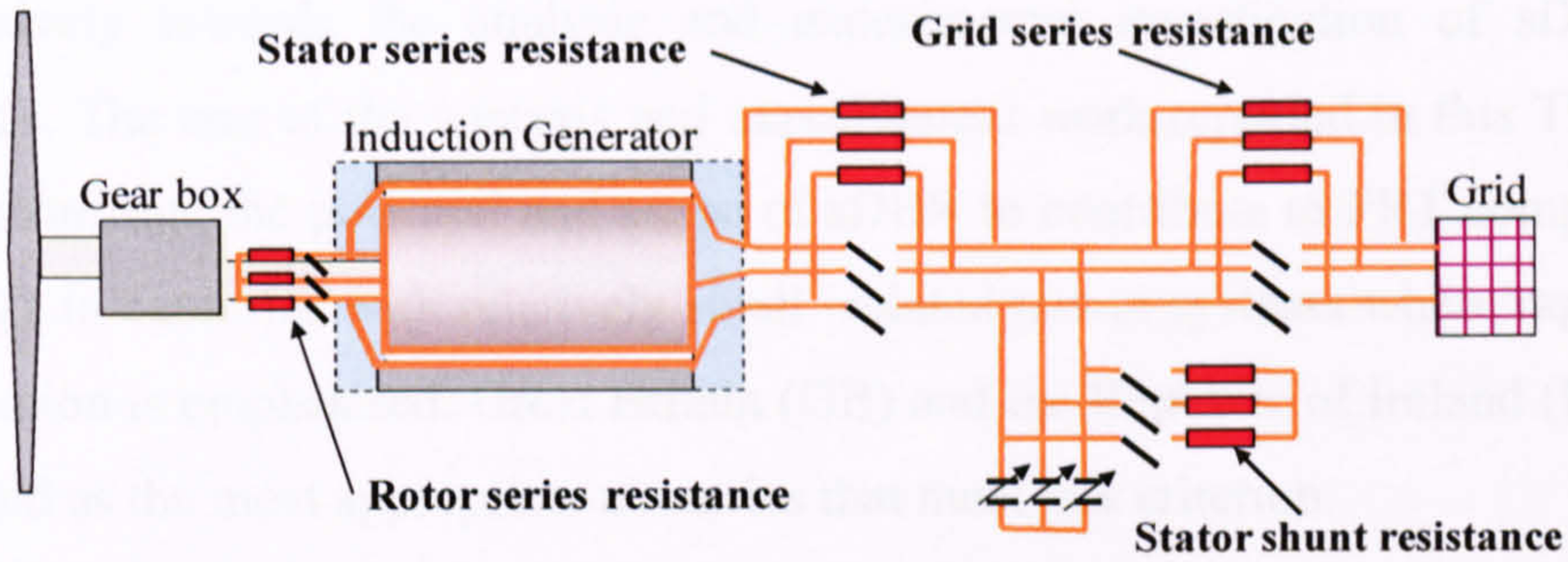

a. Switched resistor options with fixed speed wind turbines

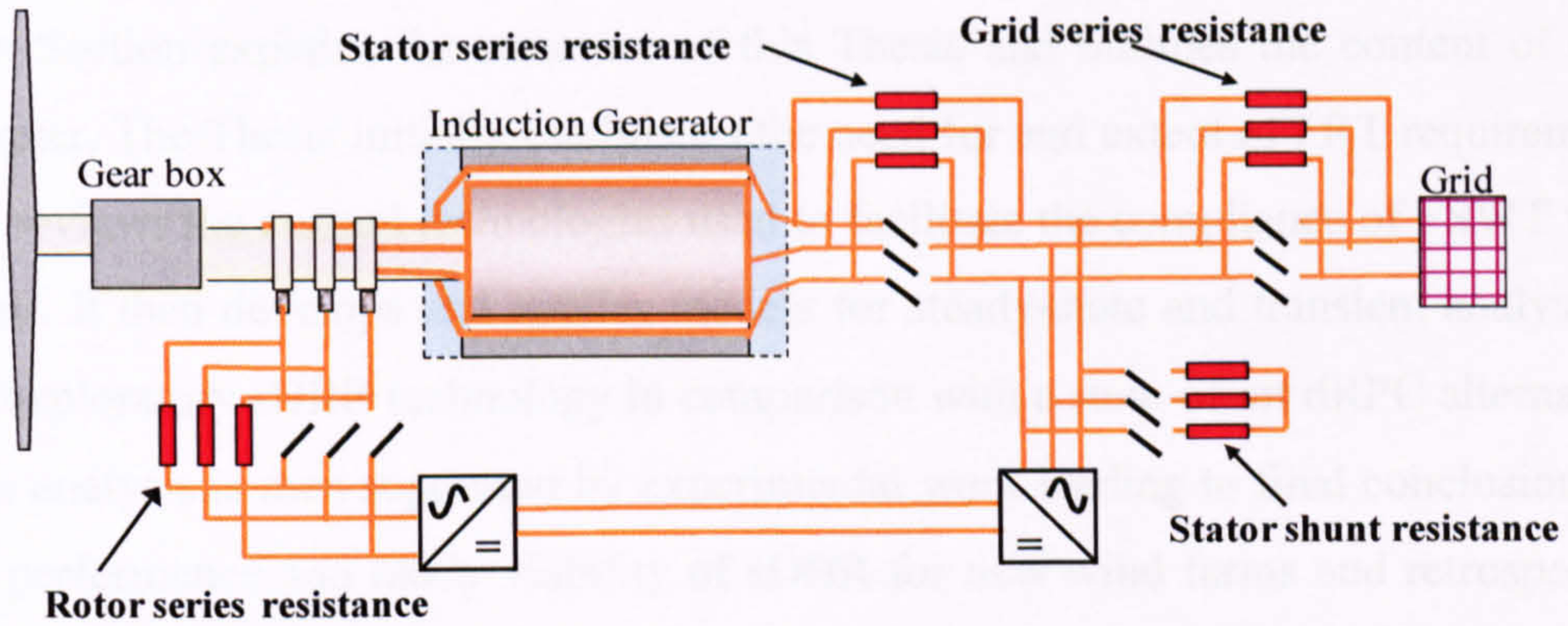

b. Switched resistor options with DFIG-variable speed wind turbines

Figure 1-4: Switched resistor options

Of these options, the switched grid series resistance was found to be the simplest and most effective at improving FRT performance. However, further analysis and discussion of rotor series resistance and stator shunt resistance is presented in Chapter 3.

Switched grid series resistance, subsequently termed *series dynamic braking resistance* (sDBR), therefore became the central focus of the PhD and is the central theme of this Thesis. I initially investigated the application of sDBR to both FSWT and DFIG-VSWTs wind turbines concepts and found that there were significant benefits in both cases. However, two factors persuaded me to focus on FSWTs. Firstly, *Vestas* had a prior patent (Fedderson 2006) on the use of a series resistor in association with DFIG-VSWT, albeit with a different objective. Secondly, the benefit of sDBR in conjunction with DFIG-VSWTs was significantly dependent on the interaction of the converter control system and the resistor. I considered that this dependency combined with the vast array of control strategies for this type of machine would make it difficult to produce persuasive and widely applicable results. I therefore decided to direct the remainder of the PhD and the whole of my Thesis

exclusively towards the analysis and experimental investigation of sDBR with FSWTs. The aim of the analysis and experimental work reported in this Thesis was to demonstrate the potential and scope of sDBR to contribute to FRT compliance of FSWTs in countries with relatively small isolated power systems where rapid power restoration is emphasised. Great Britain (GB) and the Republic of Ireland (RoI) were selected as the most appropriate countries that meet this criterion.

1.5. Structure of Thesis

This Section explains the structure of this Thesis and outlines the content of each Chapter. The Thesis initially establishes the need for and extent of FRT requirements and reviews the current technologies used to facilitate the compliance of FSWT wind farms. It then develops and applies models for steady-state and transient analysis of the exploratory sDBR technology in comparison with a state-of-art dRPC alternative. This analysis is then supported by experimental work leading to final conclusions on the performance and likely viability of sDBR for new wind farms and retrospective upgrades of existing wind farms.

Chapter 2 introduces the basis for FRT requirements and explains why fault-induced loss of generation is particularly significant for the stability of isolated power systems. GB and RoI Grid Code requirements are then used to derive benchmark fault scenarios and success criteria used to evaluate FRT technology performance.

Chapter 3 reviews the current technologies used to improve the FRT performance of FSWT wind farms, focusing on the means by which these technologies improve the dynamic stability and facilitate restoration of active power to the grid.

Chapter 4 derives reduced system models with sufficient accuracy for steady-state and transient FRT analysis of FSWT wind farms with sDBR and dRPC.

Chapter 5 uses the steady-state model derived in Chapter 4 to characterise the quasi-steady-state (QSS) behaviour of a representative wind farm and thereby infer the comparative FRT performance of dRPC and sDBR technologies. The application of QSS analysis is supported by background and theoretical underpinning in Appendix B.

Chapter 6 uses the transient model derived in Chapter 4 to analyse and compare the FRT performance of sDBR and dRPC technologies under the full range of benchmark fault scenarios defined in Chapter 2. The results are compared with QSS results of Chapter 5.

Chapter 7 demonstrates the sDBR concept experimentally using a very small-scale representation of a wind farm and grid system. An appropriate fault scenario was applied to the rig to test the beneficial effects of sDBR on wind farm stability.

Chapter 8 derives conclusions regarding the absolute and comparative FRT performance of sDBR from the results of theoretical analysis, numerical simulation and experimentation.

Appendix A clarifies the per unit system, used throughout this Thesis for equations that lay the foundation for all its analysis and simulation.

Appendix B defines and justifies the use of QSS analysis in this Thesis.

2. Fault Ride-Through Requirements

2.1. Introduction

Fault ride-through (FRT) is the ability of a generator to remain connected and actively contribute to system stability during a wide range of network fault scenarios. FRT is particularly important in securing stability in regions where wind is becoming a significant contributor to the power system's dynamic performance. The primary concern of a System Operator in this regard is that a transmission system fault that directly leads to the loss of its largest single power station, currently 1320MW in Great Britain (NGET 2004), does not lead to cascade tripping of other generators due to propagated voltage depression. A scenario of this type could lead to an unplanned system power imbalance with resulting frequency instability and under-frequency tripping of demand.

In contrast, Great Britain (GB) and Republic of Ireland (RoI) recommendations for embedded generation (ENA 1991; ENA 1995) have historically encouraged the disconnection of generators during grid faults as a means of preventing undesirable islanding of distribution networks. Furthermore, until 2003, GB and RoI Grid Codes excluded renewable generators from technical requirements, including fault ride-through (FRT), imposed on *large* generators. As a result, wind turbines would generally disconnect during a grid fault and reconnect after a few minutes delay. FRT requirements were only introduced in these countries in the period 2003-6.

This Chapter uses established principles (Kundur 1993; Machowski, Bialek et al. 1997) to explain why the loss of generation resulting from voltage disturbance is particularly significant for the stability of isolated power systems. The specific FRT requirements of Grid Codes in GB and RoI are then presented with reference to the characteristics of their respective power systems, based mainly on RoI studies. These Grid Code requirements are used to derive benchmark fault scenarios and criteria evaluate FRT technology performance in the remainder of this Thesis.

2.2. Power System Definition

For the purpose of this Thesis a power system is defined as an isolated, synchronous AC system that delivers power from rotary generators to consumer loads via an electrical network. The system may comprise a few generators and loads on a small island (e.g. Canaries or Eigg) or several thousand generators and loads distributed across a large geographic area (e.g. GB or Australia). A *power system* of this type is shown generically in Figure 2-1.

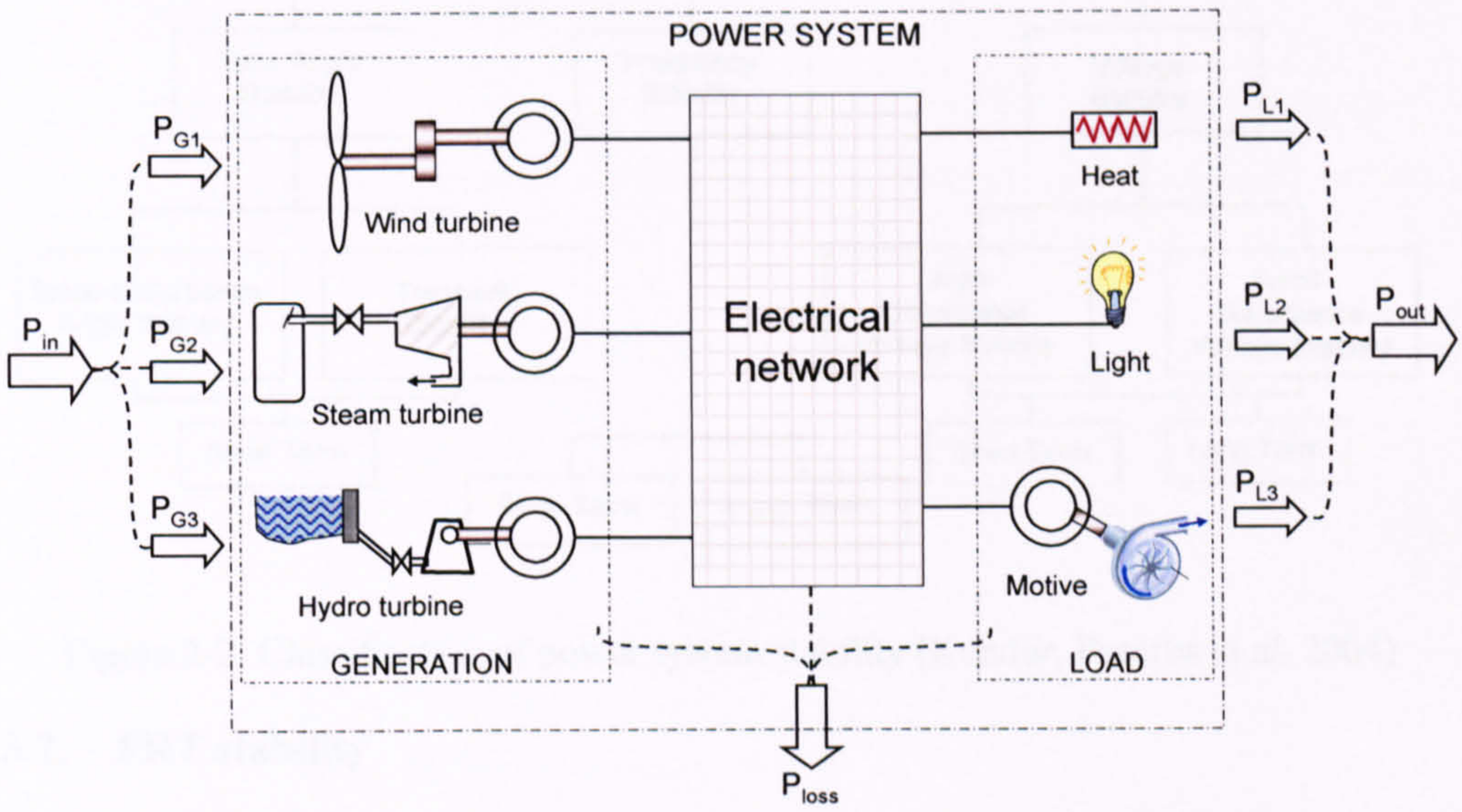

Figure 2-1: Isolated power system schematic

The common feature of isolated power systems, shown in Figure 2-1, is that energy is conserved and therefore total power supply and demand is instantaneously balanced in steady operation. This conservation principle is expressed by Eq. 2.1.

$$P_{in} = P_{loss} + P_{out} \qquad (2.1)$$

2.3. Power System Stability

2.3.1. Classification

Power system stability is defined as *"the ability of an electric power system, for a given initial operating condition, to regain a state of operating equilibrium after being subjected to a physical disturbance, with most system variables bounded so that practically the entire system remains intact."* (Kundur, Paserba et al. 2004). It is impractical and uneconomic for a power system to be stable for every possible disturbance. It is

therefore necessary to define the range of disturbances for which the power system should be designed and operated to remain stable. Grid Codes play an important role in this process by specifying minimum design and operating criteria for generators and their interface with the transmission system.

Due to its many dimensions and high complexity power system stability is generally classified in discrete categories as shown in Figure 2-2.

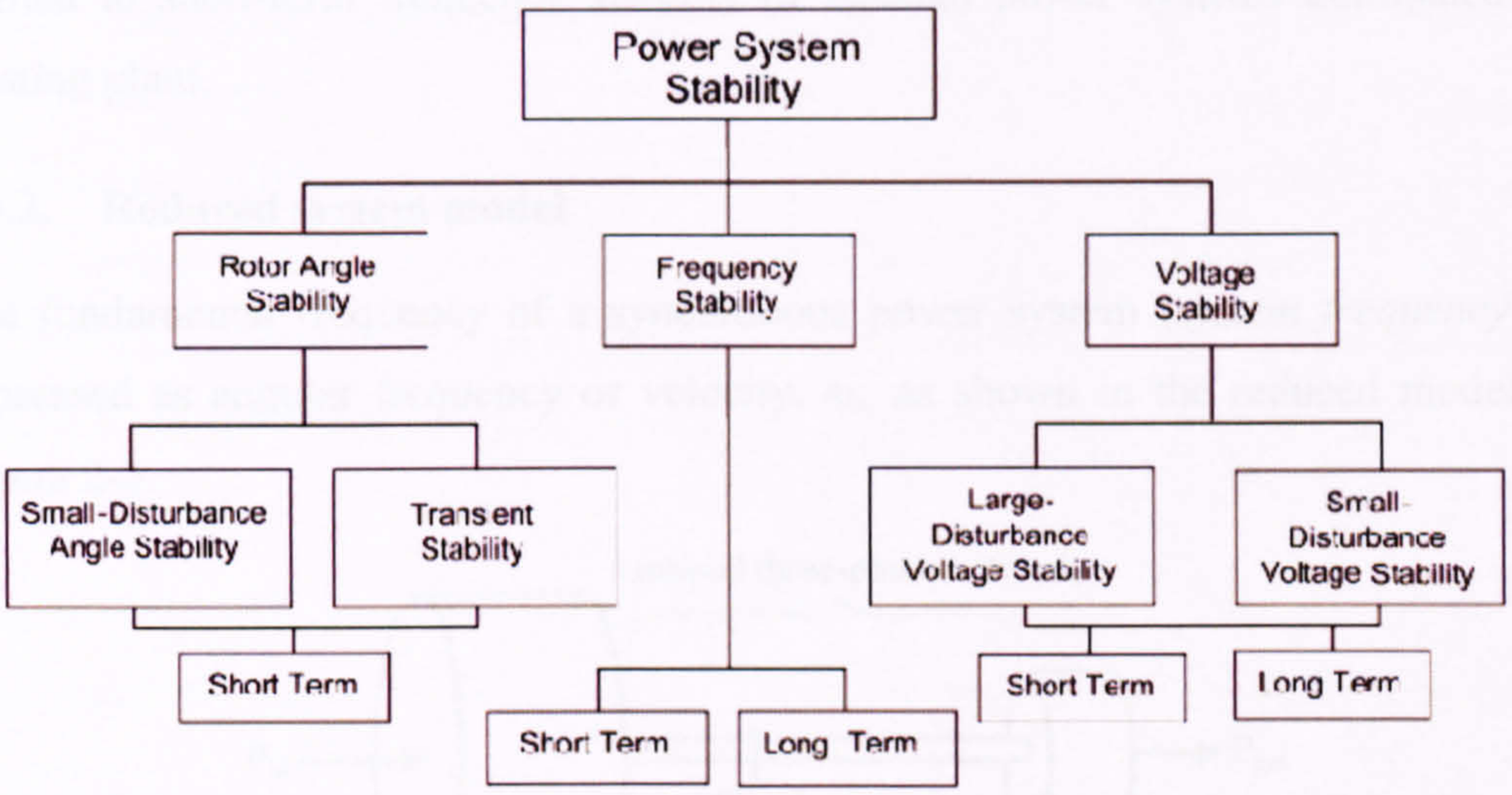

Figure 2-2: Classification of power system stability (Kundur, Paserba et al. 2004)

2.3.2. FRT stability

The undesirable tripping of a generator due to a transmission fault may affect ***rotor angle stability*** by causing excessive loading of an interconnecting transmission circuit, ***frequency stability*** by increasing system power imbalance and/or ***voltage stability*** by changing network voltage profiles. Voltage stability is a localized issue, typically associated with *weak* networks (Akhmatov 2003(a); Eirgrid 2004). Frequency stability is a system issue common to isolated systems with limited inertia and reserve (Horne, Flynn et al. 2004) but also impacting large interconnected systems following unplanned decoupling (UCTE 2006). This Thesis focuses on *short-term* frequency stability in isolation, in spite of the interaction of voltage and rotor angle stability, in order to address a central factor that drives the requirement for FRT and power restoration in isolated power systems. *Short-term* is defined in this context as being up to 10 seconds and relates to inertial and primary reserve response, as described in Section 2.4.

2.4. Frequency Stability

2.4.1. Purpose

The objective of this Section is to show how the loss of generation resulting from fault-induced disturbances can undermine the stability of a power system. The scope of this investigation, in accordance with the overall objectives of the Thesis, is limited to short-term frequency stability of isolated power systems dominated by rotating plant.

2.4.2. Reduced system model

The fundamental frequency of a synchronous power system (*system frequency*) is expressed as angular frequency or velocity, ω_s, as shown in the reduced model of Figure 2-3.

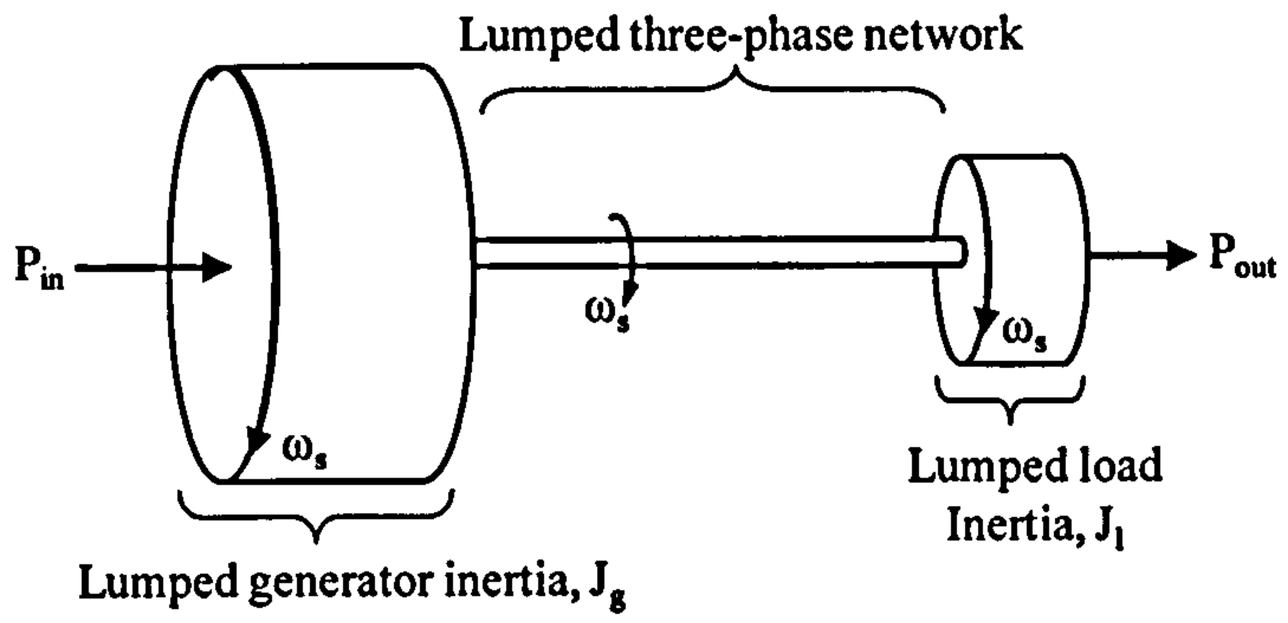

Figure 2-3: Reduced representation of a power system

The model of Figure 2-3 neglects secondary oscillations, caused by "flexible" mechanical and electrical couplings, in order to highlight the system's fundamental dynamic response. Given the stiff coupling of the two masses in Figure 2-3 and the dominance of generator inertia, the model can be further reduced to a single mass with inertia equal to the total inertia of generators connected to the system. A typical generation portfolio comprises high and low speed steam turbine generators with inertia [2] (J) in the range 5 to 20.0s on a per unit base of *connected rated capacity* (Kundur 1993,Table 3.2). However, the following analysis uses a *power demand* base, typically one-third less than the sum of connected rated capacities, and therefore a corrected lumped generation inertia of 15 is appropriate.

---

[2] Per unit inertia (J), as defined in the Definitions and Appendix A is used in place of inertia constant (H) through-out this Thesis.

2.4.3. System dynamics

The instantaneous loss of a large generation plant will lead to an initial power imbalance equal to the pre-loss output of the tripped plant, P_{gl}. This imbalance will result in acceleration given by Eq. 2.2 (Jenkins, Allan et al. 2000, Eq.3.45).

$$\frac{d\omega_s}{dt} = \frac{P_{in} - P_{out}}{J\omega_s} = \frac{P_{net}}{J\omega_s} \qquad (2.2)$$

Under steady-state conditions net power is, by definition, zero. Loss of generation power would therefore lead to a net power deficit, with the resulting deceleration counteracted by the response of primary spinning reserve plant and load shedding for more severe frequency depressions. In the following example, load shedding is neglected and the spinning reserve response is described by Eq. 2.3 as constant ramp rate, k_r (on reserve capacity base, P_r) starting at the instant of generation loss, t_0.

$$P_{net}(t) = k_r(t - t_0)P_r - P_{gl} \qquad (2.3)$$

Substituting Eq. 2.3 into Eq. 2.2, integrating and re-arranging gives Eq. 2.4, for the case where generation loss occurs at time zero and initial angular velocity is unity.

$$\omega_s = \sqrt{\frac{\left(k_r P_r t^2 - 2P_{gl} t + J\right)}{J}} \qquad (2.4)$$

Equation 2.4 is valid up for $k_r(t - t_0) < 1$ and can therefore be used to study the initial period of response including the sensitivity of the angular velocity nadir (lowest point).

2.4.4. All-Ireland case study

For this study the all-Ireland power system is defined by the parameters of Table 2-1.

Parameter description	Value	Value (pu)
System demand	4000MW	1.0
Generation loss, P_{gl}	400MW	0.1
Primary reserve, P_r	520MW	0.13
Reserve power ramp rate, k_r	68MW/s	0.13
Power system inertia, J_g	15 s	

Table 2-1: Dynamic parameters based on all-Ireland power system

The values in Table 2-1 are based on the all-Ireland power system with loss of a 400MW CCGT generation station (Horne, Flynn et al. 2004) during a period of moderate demand. Primary reserve has been selected at a level representative of

conservative system operation with the current level, 750MW, of wind power capacity (Doherty and O'Malley 2005, Fig 7).

Figure 2-4a compares the response of a simplified all-Ireland power system for three wind power loss scenarios by substituting parameters from Table 2-1 in Eq, 2.4.

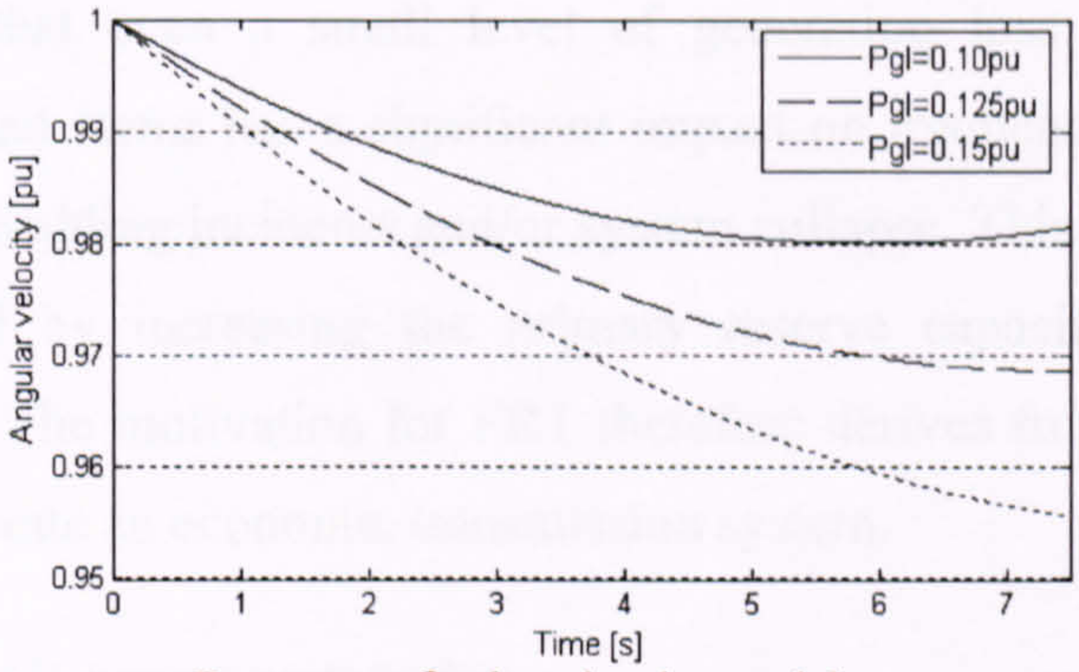

a. Response of reduced order model (from fault initiation to frequency nadir)

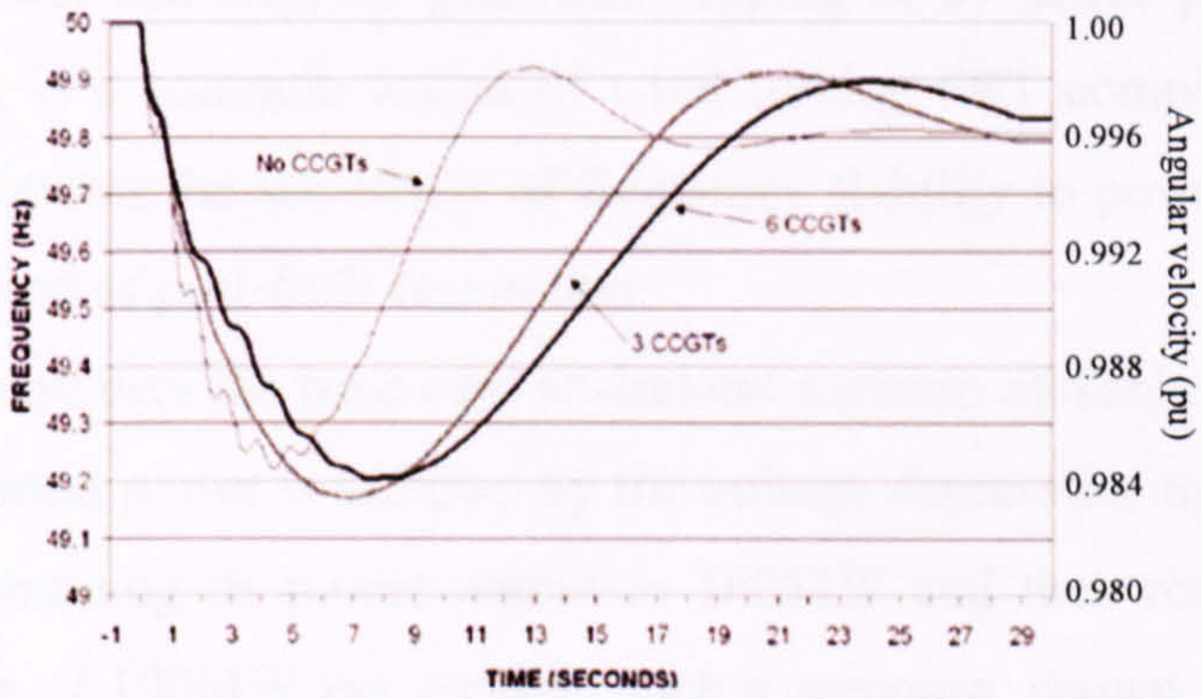

b. Full response of multiple order model (from Horne, Flynn et al. 2004)

Figure 2-4: Frequency response of all-Ireland system using simplified and full models

The solid line of Figure 2-4a shows the response of the base-case system of Table 2-1. The speed nadir of about 0.98pu occurs 6 seconds after the loss of generation. This nadir is more severe but comparable in form (noting the difference in timescale) to the response of Figure 2-4b resulting from a full transient model of the all-Ireland transmission system with the loss of 450MW from the HVDC link to Scotland (Horne, Flynn et al. 2004). The increased severity of this study may be due to a pessimistic choice of reserve, system demand and/or inertia, each unspecified in the referred study.

The dashed and dotted lines of Figure 2-4a show the effect of the consequential loss of 100MW and 200MW of wind power respectively. In the case of 100MW wind

power loss, load shedding is likely to be initiated[3] but the system still recovers without it from a speed nadir of 0.968pu. In the case of 200MW wind power loss, the system will collapse without the intervention of load shedding because there is insufficient primary reserve to compensate for the total generation loss.

It is apparent that even a small level of generation loss due to fault-induced instability of wind farms has a significant impact on frequency stability, leading to increased load shedding incidents and/or system collapse. This detrimental effect can be compensated by increasing the primary reserve capacity and hence system operating costs. The motivation for FRT therefore derives from the duty of System Operators to operate an economic transmission system.

2.4.5. Post- fault power restoration

Loss of wind power can arise by generator tripping or by active power constraint. Power constraint is a common aspect of wind turbine FRT compliance strategies. This Section illustrates the sensitivity of frequency stability to power constraint and the associated speed of post-fault restoration.

The following study uses the base-case all-Ireland scenario of Table 2-1 but assumes that 500MW of wind power is affected by the voltage depression and remains stable by initially constraining its power output to 100MW and then restoring its initial output at the rate of 100MW per second. Such a response, shown in Figure 2-5, is representative of a wind farm comprising wind turbines with active power control.

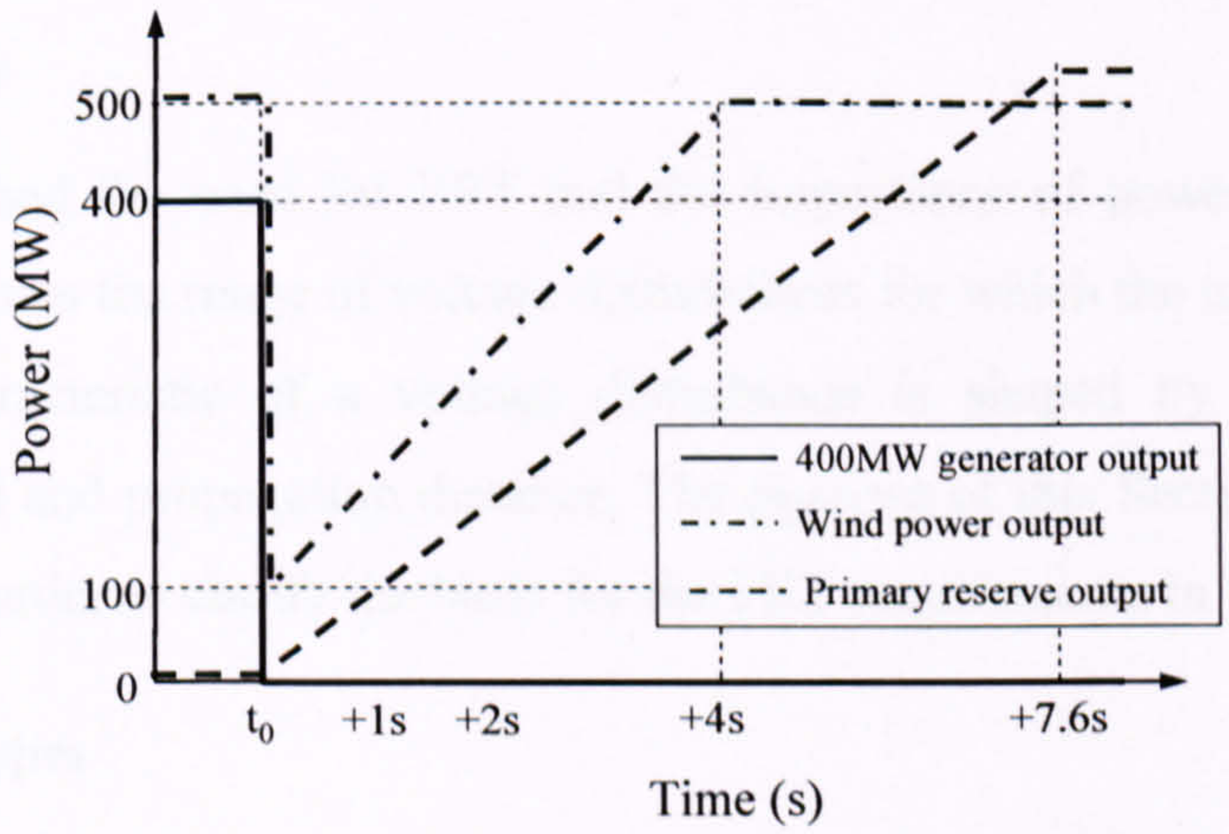

Figure 2-5: Power-time graph of power restoration scenario

[3] Under-frequency load shedding is applied to certain industrial customers in most power systems and is triggered below 0.98pu speed in Ireland. This feature is not modelled in this study.

A simple model was constructed in Matlab-Simulink to study the response of the scenario of Figure 2-5 and compare it with the base-case all-Ireland scenario of Section 2.4.4 and alternative constraint scenarios with faster restoration times. The results of these simulations are shown in Figure 2-6.

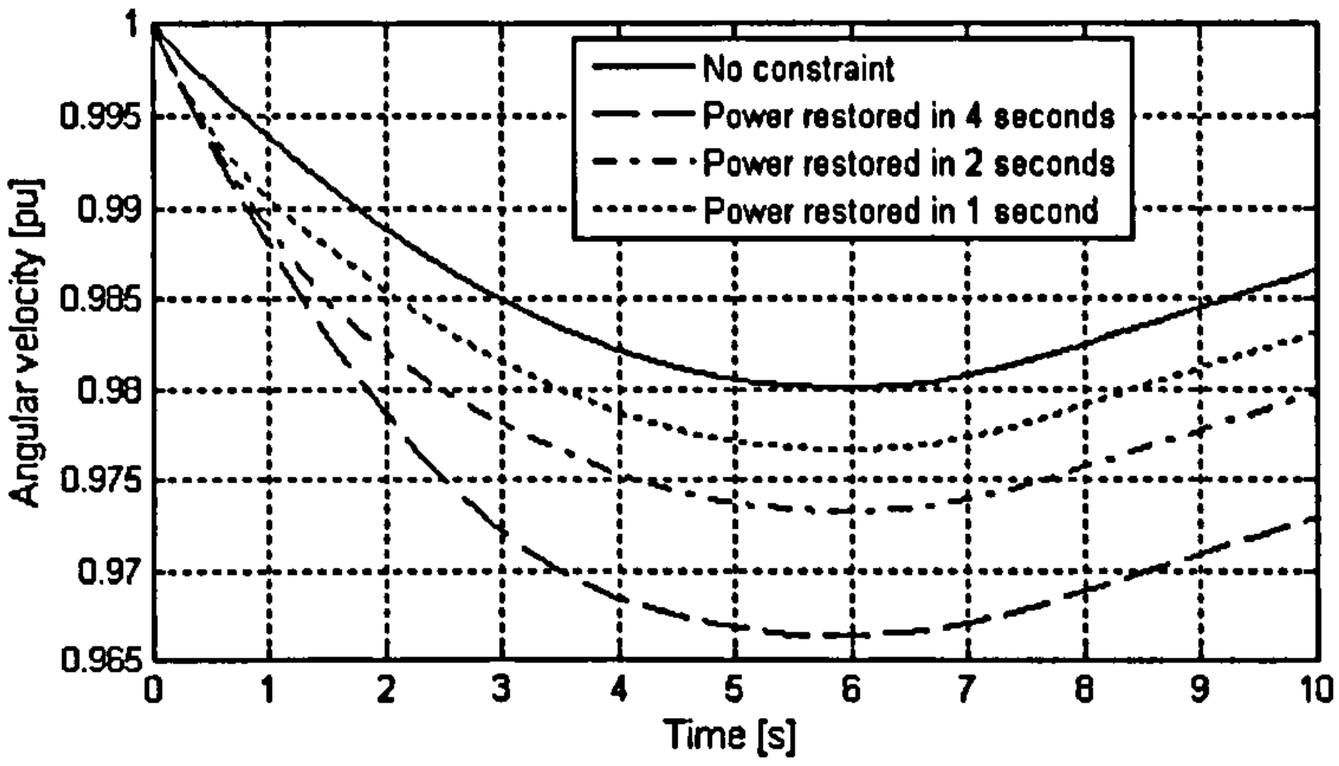

Figure 2-6: Comparison of frequency response for three power restoration rates

Figure 2-6 shows that the effect of wind power constraint with power restoration of 4 seconds is very severe. The frequency nadir is depressed from 0.98pu to 0.966pu which would result in substantial load shedding. The significant benefit shown for reducing the restoration time to 1 second explains why RoI and GB Grid Codes limit power restoration time to a maximum of 1 second, as described in Section 2.6.

2.5. Characteristics of Voltage Disturbance

2.5.1. Purpose

Having established the need for FRT and the importance of power recovery, this Section investigates the range of voltage disturbances for which the capability should apply. The characteristic of a voltage disturbance is shaped by the fault type, protection speed and propagation distance. The purpose of this Section is to explore these factors in order to clarify the basis for the FRT requirements in Section 2.6

2.5.2. Fault types

Severe voltage disturbances are caused by short-circuits between one phase and earth, two phases, two phases and earth or three phases of a transmission circuit, as shown by RoI statistical data of Figure 2-7.

Period	Voltage level	3-phase	2-phase	1-phase
15 years	400 kV	16·67	16·67	66·66
20 years	220 kV	14·29	8·96	76·75
20 years	110 kV	46·30	19·97	33·73

Figure 2-7: Fault type as a percentage of total faults (Eirgrid 2004, Table A4)

The most common fault types on higher voltage systems are shown in Figure 2-7 to be unbalanced phase-to-earth but the most severe stability scenarios are generally considered to be balanced three-phase (Akhmatov 2005(b), Table 4.3). A more extensive study of fault types and frequencies covering several European countries and the USA is given in a comprehensive Riso report (Iov, Hansen et al. 2007).

2.5.3. Protection speed

The objective of a protection system is to disconnect a fault from the rest of the transmission system in the shortest possible time. It achieves this using one or more main protection systems supported by one or more back-up protection systems. There are generally two categories of transmission protection, *unit* and *distance,* as shown in Figure 2-8.

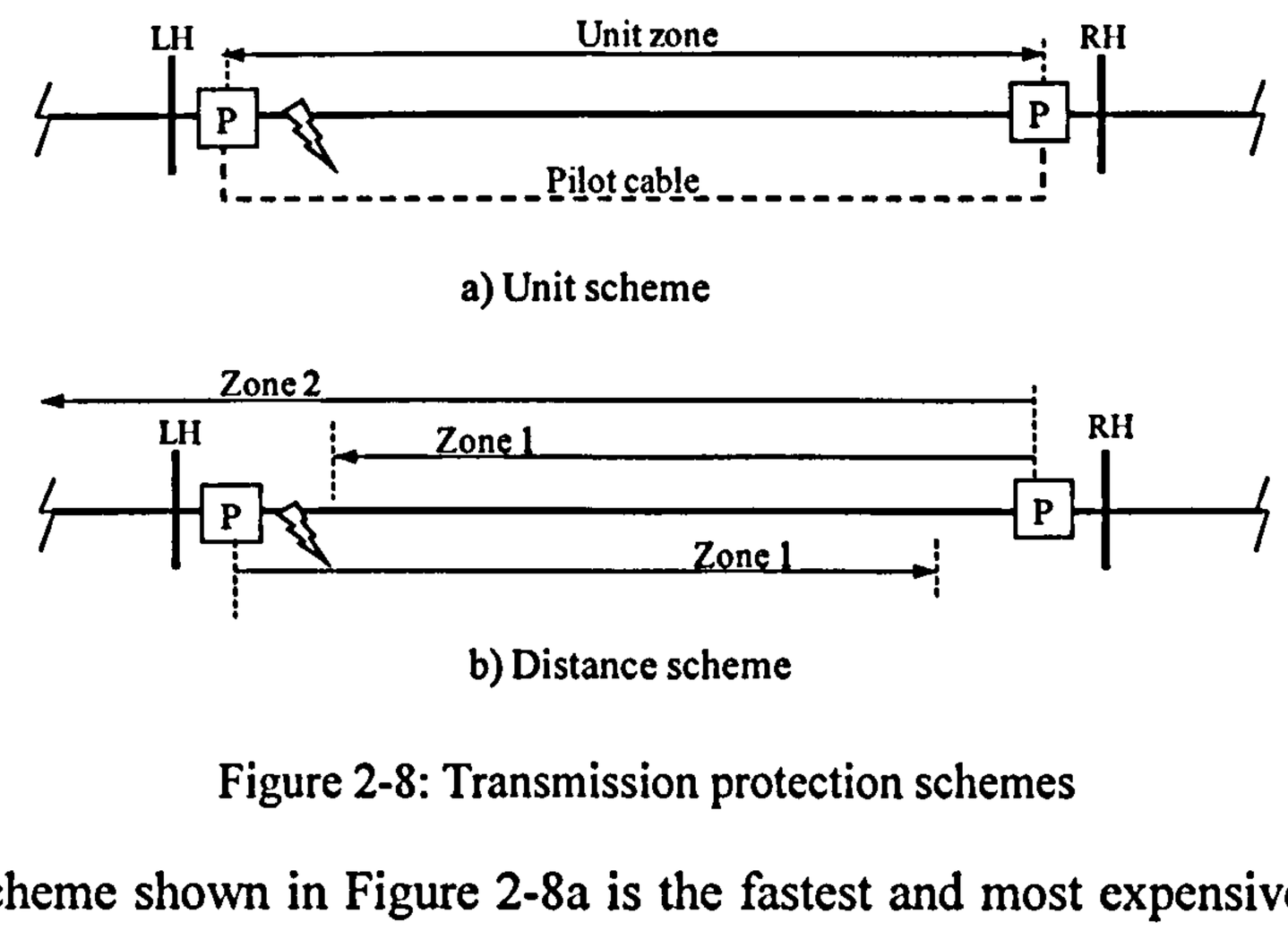

Figure 2-8: Transmission protection schemes

The *unit* scheme shown in Figure 2-8a is the fastest and most expensive protection method, used throughout the GB transmission system and on higher voltage circuits in the RoI system. They operate by measuring the difference between current flowing into and out of a single circuit or "zone". They are fast because they are inherently insensitive to faults outside their zone of detection and therefore have no reason to delay relay operation to discriminate with other devices. They are expensive because of the need for end-to-end communication by pilot cable but this expense is justified, especially on strategic circuits, by improving system stability. Typical worst case

clearance times of unit protection systems are 80ms at 400kV, 100ms at 275kV and 120ms at 132kV (National Grid Electricity Transmission (NGET) 2007, CC.6.2.2.2.2).

The ***distance*** scheme shown in Figure 2-8b is slower and cheaper than the unit protection scheme and is used widely on 110kV transmission circuits in RoI. They operate by independently measuring voltage and current at each end of a single circuit. They are slower because they are sensitive to faults outside their primary protection zone and must therefore discriminate between "internal" (zone 1) faults and "external" (zone 2) faults, as shown in Figure 2-8b. This discrimination is achieved by delaying relay operation by typically by 300-400ms for zone 2 faults.

The voltage disturbance characteristics of unit and distance protection schemes can be compared by the voltage-time trajectories of Figure 2-9.

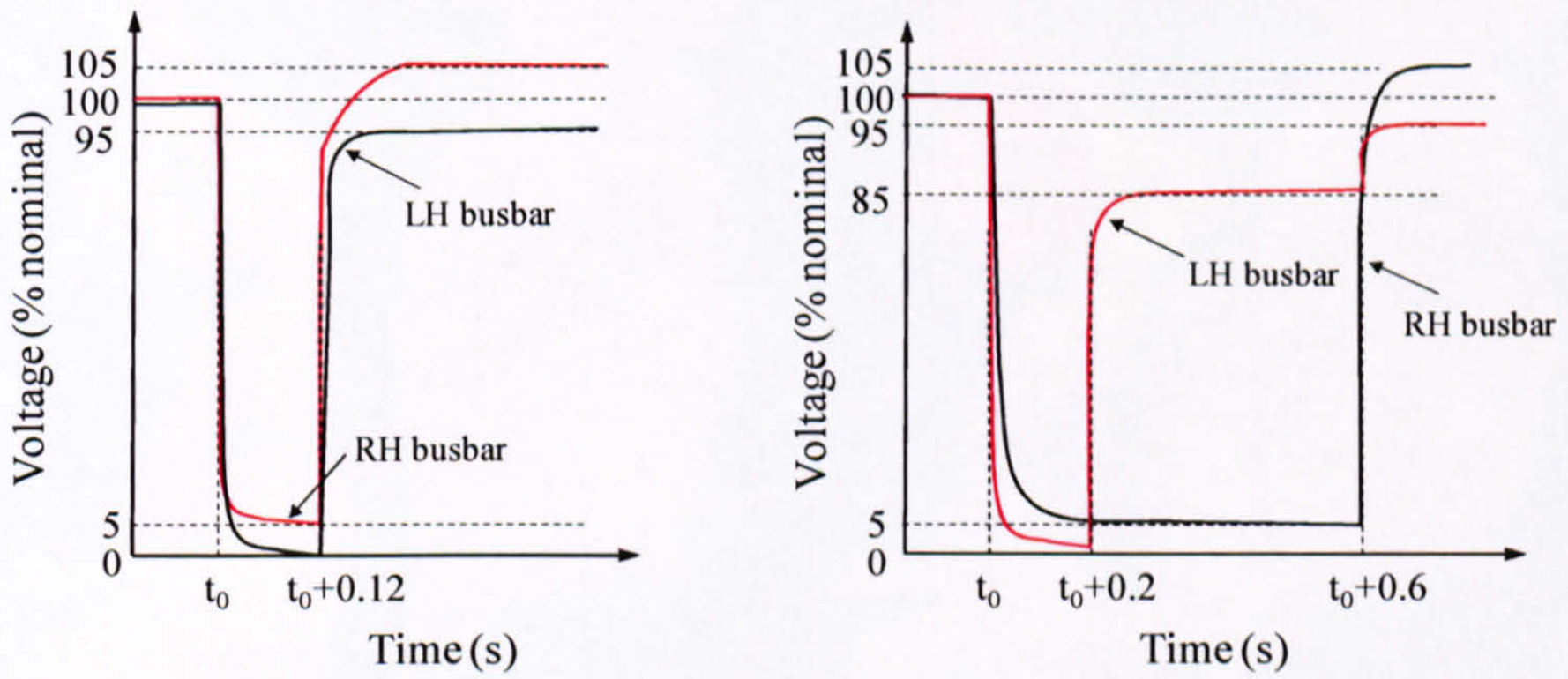

a. Unit protection scheme

b. Distance protection scheme

Figure 2-9: Voltage-time characteristics associated with 3-phase solid faults

The voltage-time characteristics of Figure 2-9 are the starting point for developing a range of FRT scenarios. Other scenarios may include cases where main protection systems fail and back-up protection systems are called upon with an operation times as long as one second. The statistical distribution of clearance times for the transmission system in RoI is shown in Table 2-2.

CLEARANCE TIME IN SECONDS	400 kV SYSTEM	220 kV SYSTEM	ESB 110 kV SYSTEM	Customers' 110 kV PLANT
0·0 - 0·1	2	25	19	-
0·1 - 0·2	-	5	45	1
0·2 - 0·6	-	-	5	1
0·6 - 1·0	-	-	2	-
1·0 - 1·2	-	-	-	-
OVER 1·2	-	-	1	-

Table 2-2: Statistical distribution of clearance times in RoI, 2000 (Eirgrid 2004, Table B2)

It can be noted from Table 2-2 that all 400kV and 220kV system faults and 90% of 110kV faults on the RoI system are cleared within 200ms and that only 3% of faults are not cleared within 600ms.

2.5.4. Propagation distance

Propagation distance depends on the electrical strength of the transmission system. The propagation of voltage depressions arising from two faults on the RoI transmission system (Eirgrid 2004) are shown in Figure 2-10.

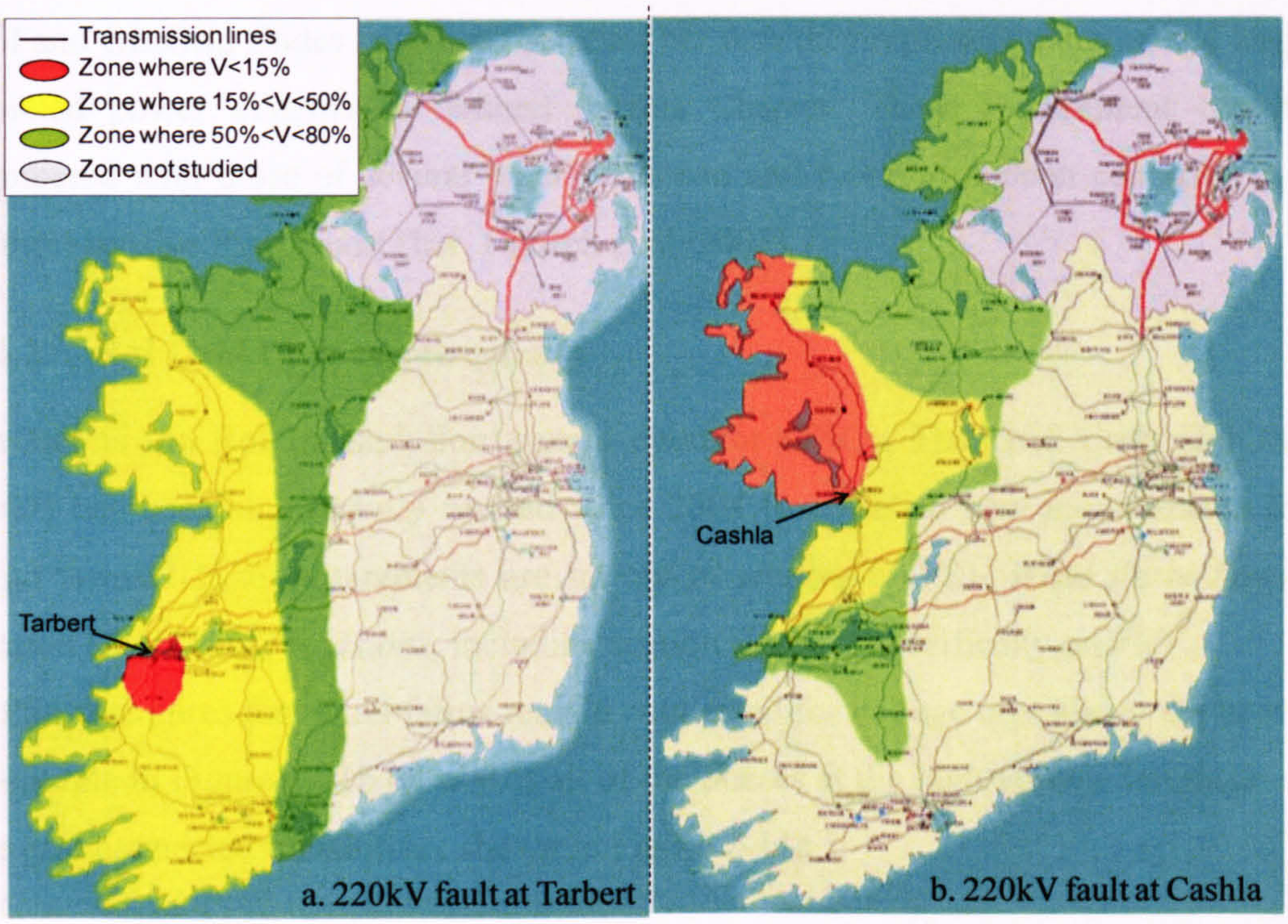

Figure 2-10: Fault-induced voltage depression in the Irish transmission system

Figure 2-10a shows the voltage profile across the whole of RoI during a short-circuit fault at the Tarbert 220kV substation in County Kerry. Figure 2-10b shows the voltage profile for a similar fault at Cashla in Galway. The figures illustrate that severe fault-induced voltage depression can extend over a wide geographical area and can therefore simultaneously impact on several generators. Similar studies carried out on the transmission system of GB (Wu, Holdsworth et al. 2003) show much smaller geographical distributions of voltage depression due to the greater electrical strength of the GB network.

2.6. National Grid Code Requirements

2.6.1. Code selection

Section 2.4 establishes the need for wind farm FRT and the desirability of rapid restoration of pre-fault output power. Section 2.5 provides the basis for a range of voltage depression scenarios that wind farms should ride-through in order to meet the need for stability. Each system operator must define its requirements according to the particular characteristics of its transmission system. The FRT requirements of the RoI and GB Grid Codes have been selected because they represent medium and large isolated power systems as defined in this Chapter. These requirement can be compared with those of several other European and North American countries in a comprehensive Riso report (Iov, Hansen et al. 2007)

2.6.2. RoI Grid Code requirements

EirGrid is the RoI transmission system operator (TSO). The Grid Code (EirGrid 2007) has been significantly revised since 2004 to establish new requirements for wind farms. These requirements are set out in section WFPS1, *Wind Farm Power Station Grid Code Provisions*, including section WPS1.4 specifically on FRT.

WPS1.4 requires that wind farms remain connected for voltage dips above the heavy black line in Figure 2-11b on any or all of the phases at the high voltage terminals of the grid connected transformer shown in Figure 2-11a,.

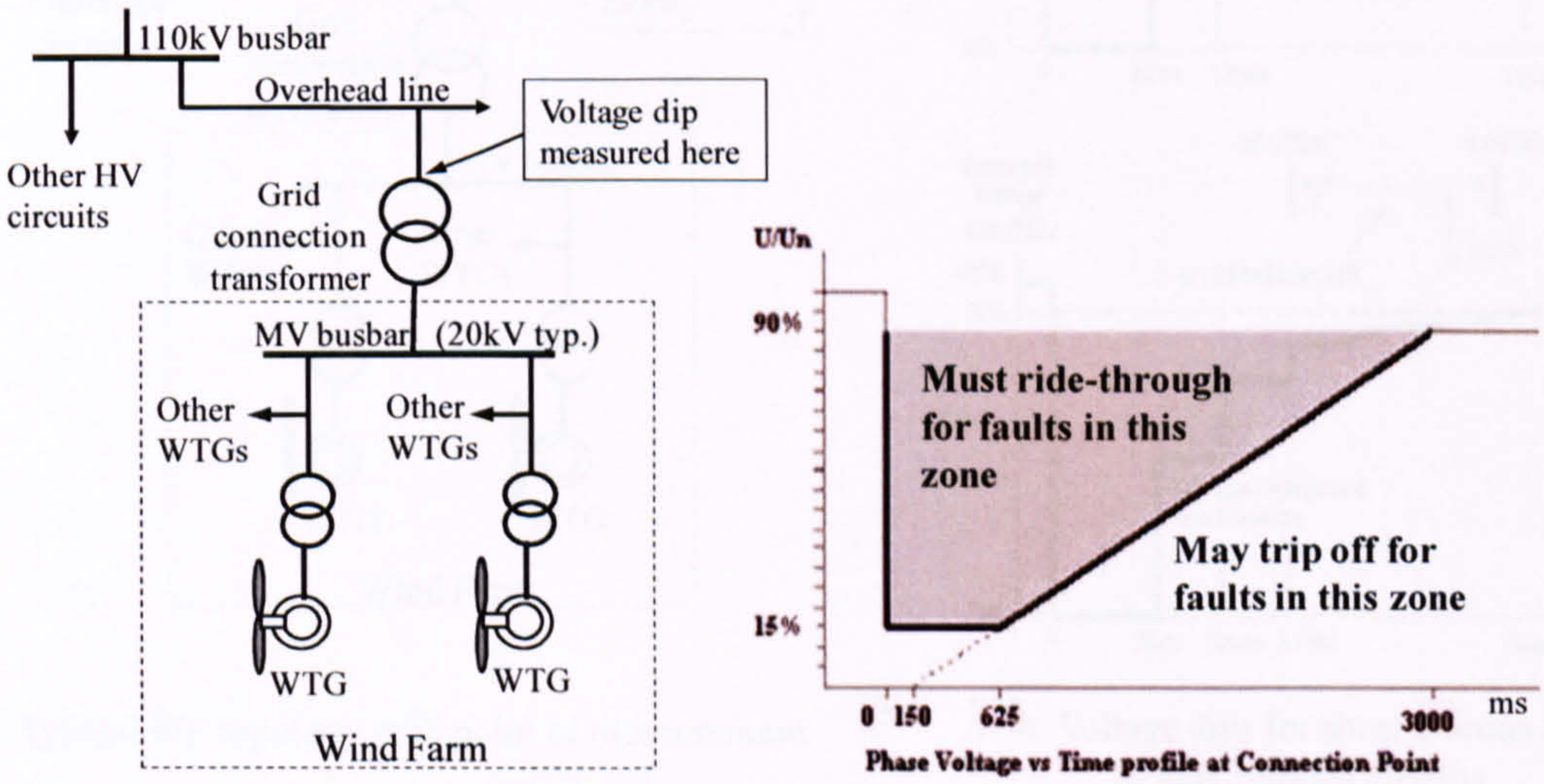

a. Typical WF topology with point of measurement b. FRT capability profile

Figure 2-11: FRT capability for wind farms

2.6. National Grid Code Requirements

2.6.1. Code selection

Section 2.4 establishes the need for wind farm FRT and the desirability of rapid restoration of pre-fault output power. Section 2.5 provides the basis for a range of voltage depression scenarios that wind farms should ride-through in order to meet the need for stability. Each system operator must define its requirements according to the particular characteristics of its transmission system. The FRT requirements of the RoI and GB Grid Codes have been selected because they represent medium and large isolated power systems as defined in this Chapter. These requirement can be compared with those of several other European and North American countries in a comprehensive Riso report (Iov, Hansen et al. 2007)

2.6.2. RoI Grid Code requirements

EirGrid is the RoI transmission system operator (TSO). The Grid Code (EirGrid 2007) has been significantly revised since 2004 to establish new requirements for wind farms. These requirements are set out in section WFPS1, *Wind Farm Power Station Grid Code Provisions*, including section WPS1.4 specifically on FRT.

WPS1.4 requires that wind farms remain connected for voltage dips above the heavy black line in Figure 2-11b on any or all of the phases at the high voltage terminals of the grid connected transformer shown in Figure 2-11a,.

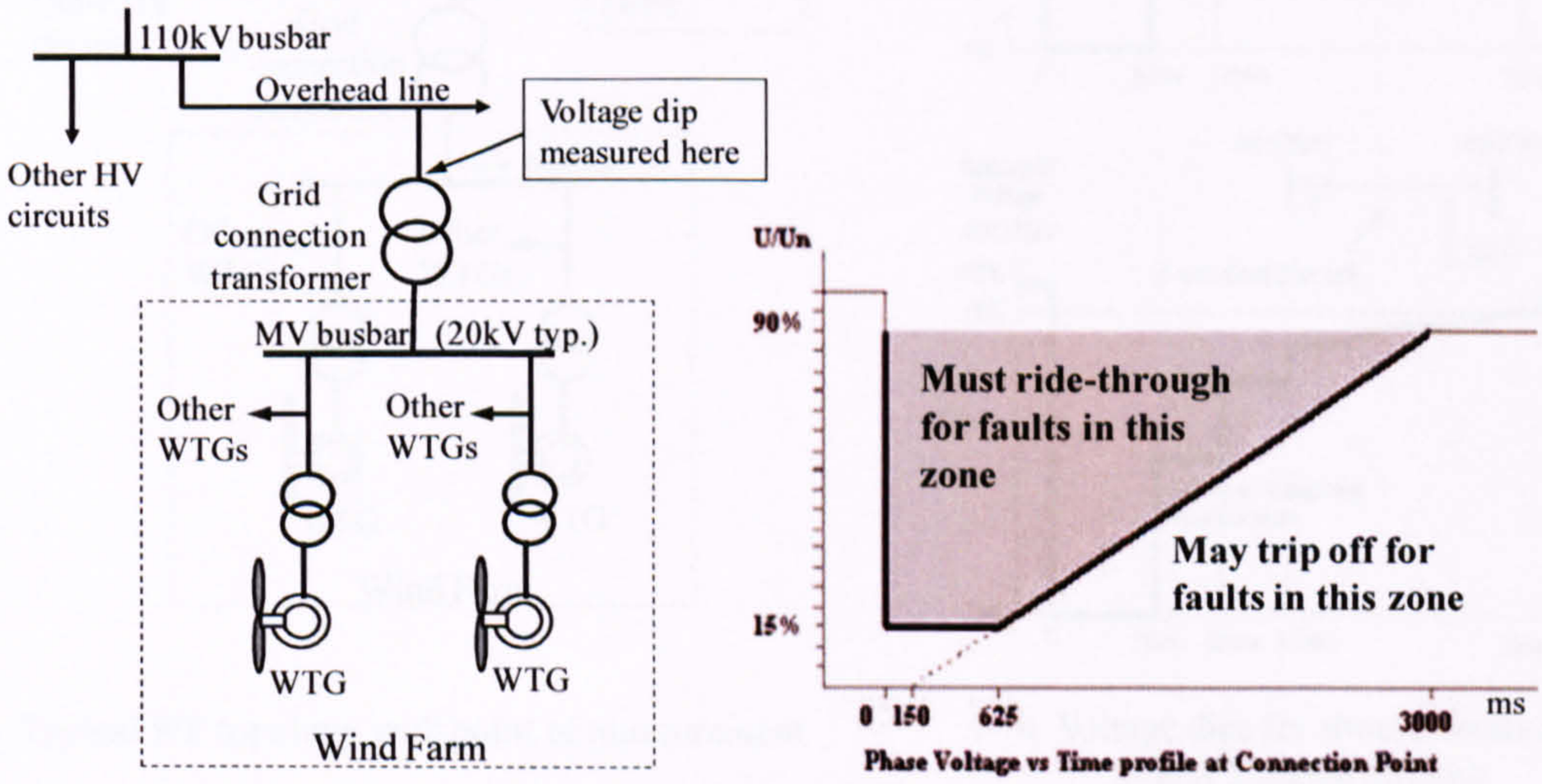

a. Typical WF topology with point of measurement b. FRT capability profile

Figure 2-11: FRT capability for wind farms

As well as remaining connected, WPS1.4 requires that the wind farm exports active power in proportion to the retained voltage during the voltage dip and restores at least 90% of available active power within one second of the recovery of transmission system voltage to the normal range (nominal ±10%).

2.6.3. GB Grid Code requirements

National Grid Electricity Transmission (NGET) is the GB TSO. The Grid Code (National Grid Electricity Transmission (NGET) 2007) has been significantly revised since 2003 to establish new requirements for all forms of generation including wind farms. The FRT requirements, contained in CC.6.3.15 and Appendix 4 of the Code, are classified as *short circuit* and *voltage dip*.

Short-circuit requirements of CC.6.3.15a state that a wind farm shall remain transiently stable and connected without tripping of any individual wind turbines for a solid short circuit three phase or unbalanced fault on the closest point of the Supergrid (275kV and above). The voltage-time profile of typical short circuit faults is shown in Figure 2-12b.

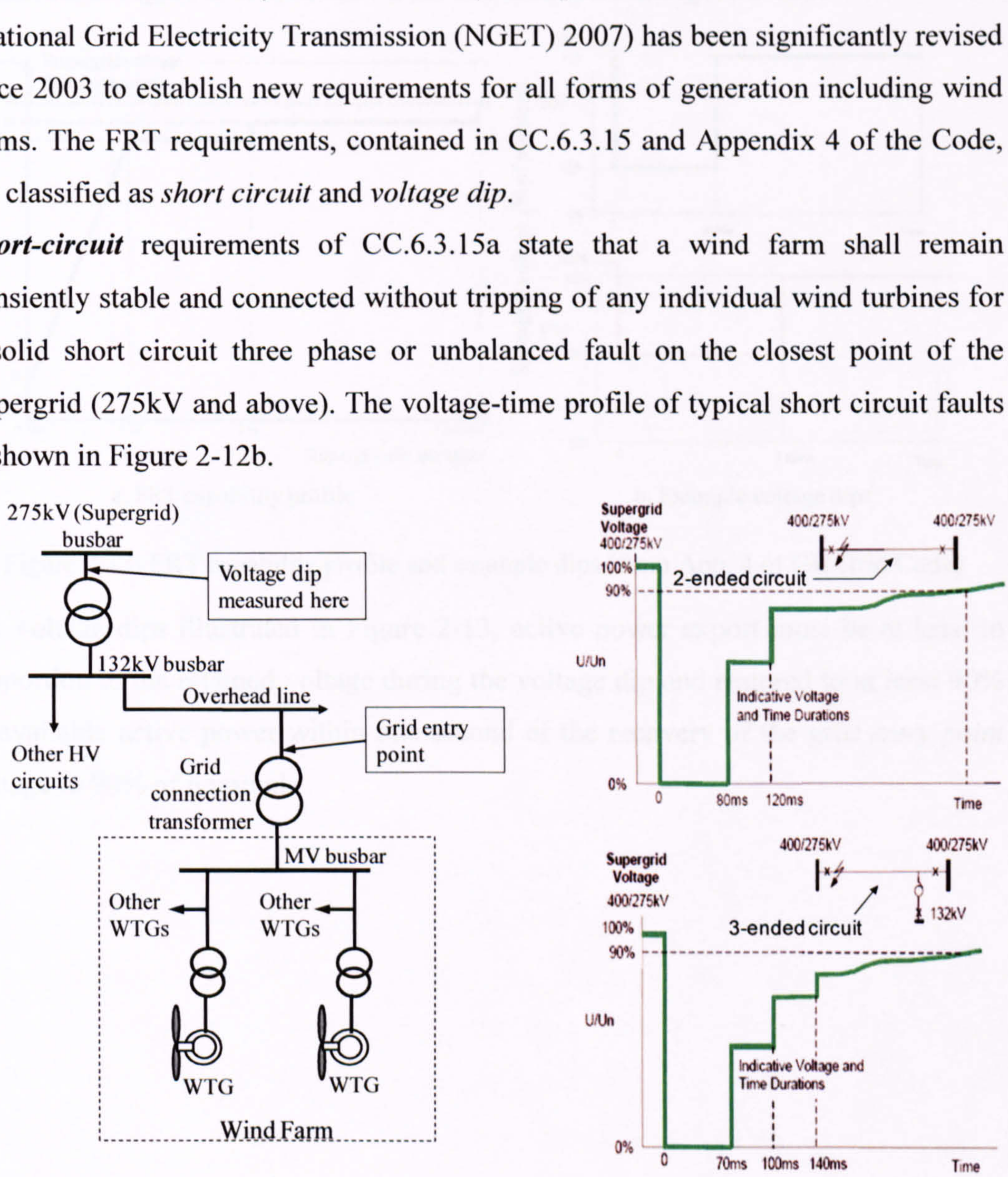

a. Typical WF topology with point of measurement

b. Voltage dips for short circuits on 2- and 3-ended circuits

Figure 2-12: Voltage-time profiles for Supergrid short circuits (App.4 of GB Grid Code)

For the short circuit faults illustrated in Figure 2-12, active power export must be restored to 90% of the available level within 0.5 seconds of the recovery of the *grid entry point* voltage, shown in Figure 2-12a, to 90% of nominal.

Voltage dip requirements of CC.6.3.15b state that a wind farm shall remain transiently stable and connected without tripping of any individual wind turbines for *balanced* Supergrid voltage dips and durations anywhere on or above the heavy black line in Figure 2-13a, as shown for two examples in Figure 2-13b.

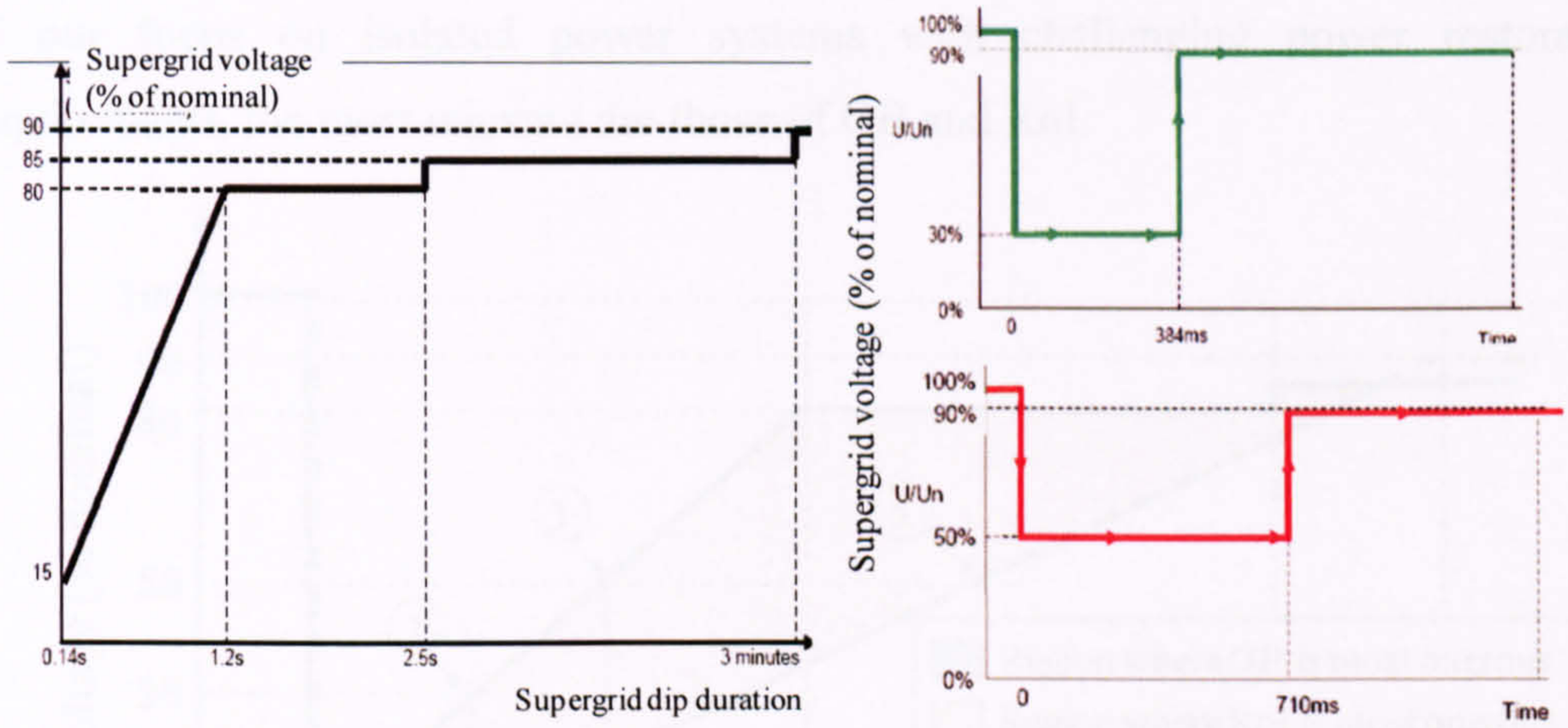

a. FRT capability profile

b. Example voltage dips

Figure 2-13: FRT capability profile and example dips (from App. 4 of GB Grid Code)

For voltage dips illustrated in Figure 2-13, active power export must be at least in proportion to the retained voltage during the voltage dip and restored to at least 90% of available active power within one second of the recovery of the *grid entry point* voltage to 90% of nominal.

2.7. FRT Test Scenarios

The purpose of this Section is to derive test scenarios and performance criteria for assessment of FRT techniques proposed in this Thesis. Since this Thesis proposes technologies with practical application in the near to medium term, it is reasonable to use scenarios that relate closely to current, relevant Grid Code requirements. In view of our focus on isolated power systems with challenging power restoration requirements, the most relevant are those of GB and RoI.

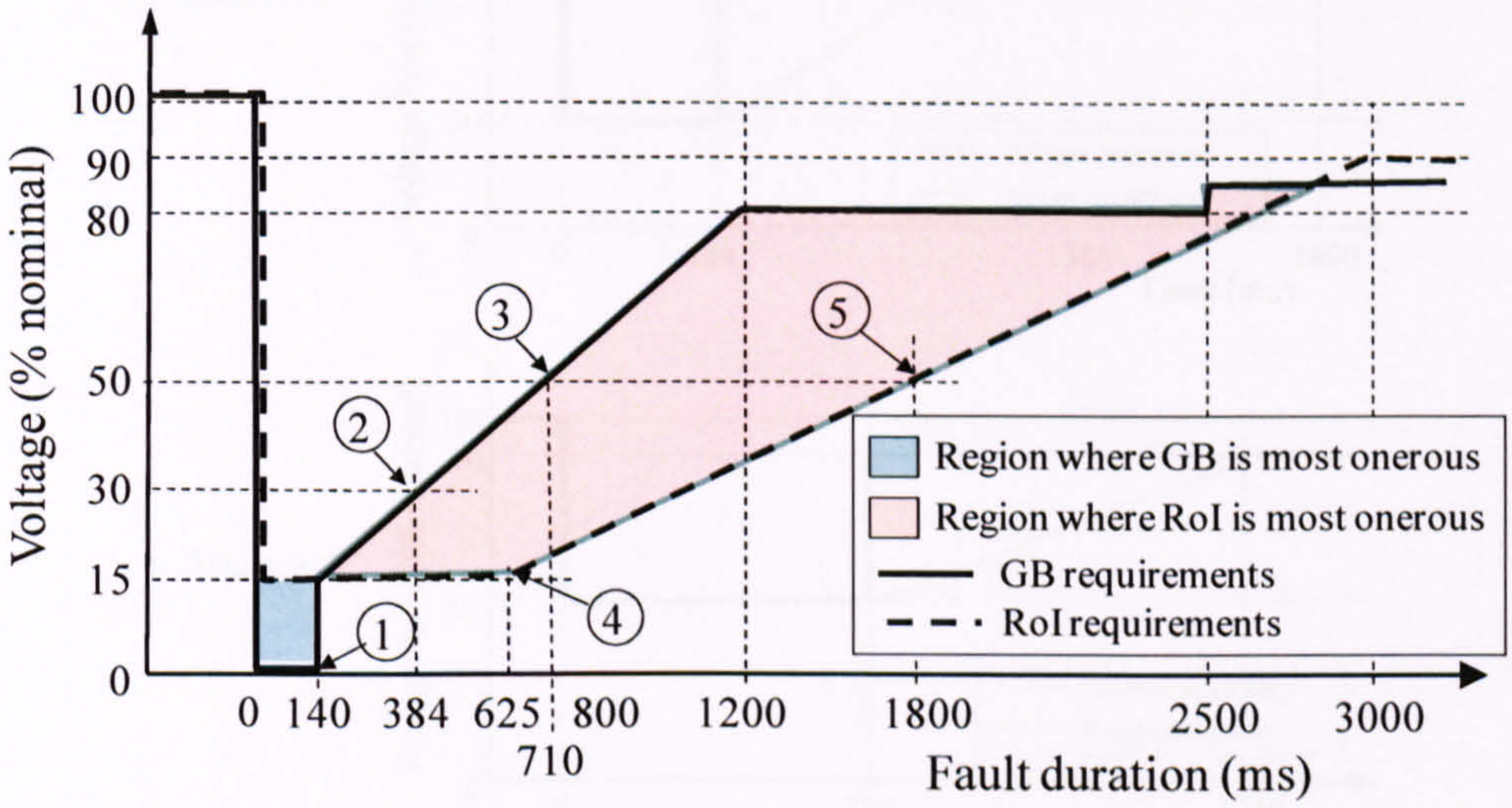

Figure 2-14: Comparison of Grid Code requirements of GB and RoI

Figure 2-14 overlays the FRT capability profiles for GB (from Figure 2-11b) and RoI (from Figure 2-13a). As expected, from considerations of the different protection systems in these regions, the RoI requirements are more onerous for longer fault durations (pink region of graph) whereas the GB requirements are more onerous for close-up short-circuits (blue region of graph). Five balanced fault scenarios have been identified as points on the voltage-duration graph of Figure 2-14. Each point represents a rectangular voltage notch, which are shown are shown as voltage- and power-time traces in Figure 2-15a to e, representing scenarios 1 to 5.

a. Scenario 1

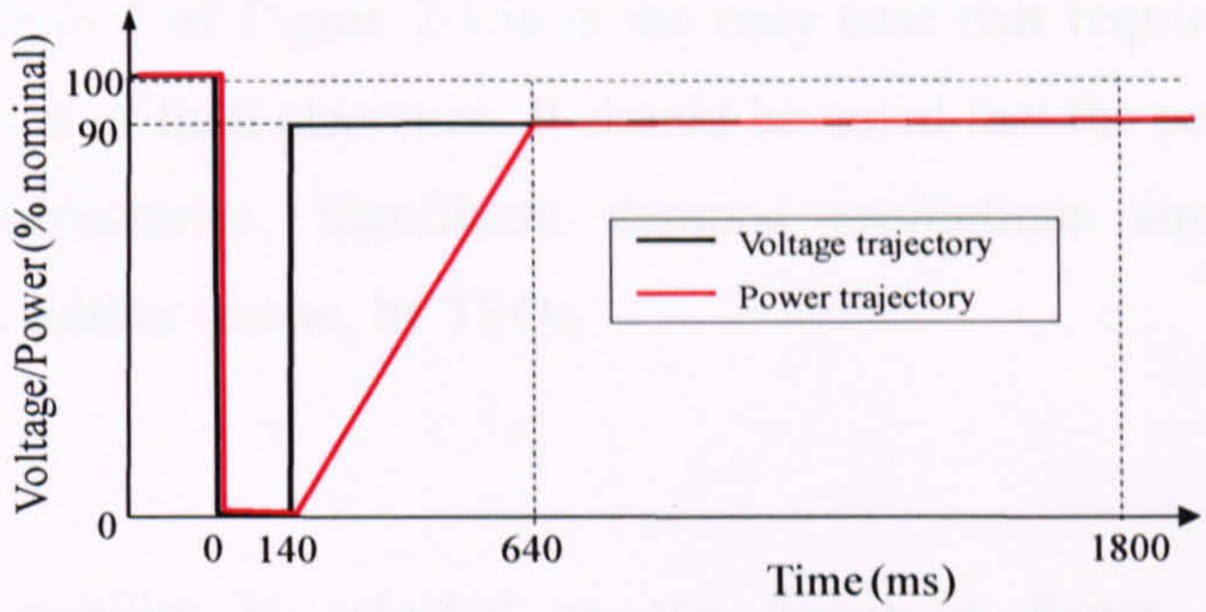

b. Scenario 2

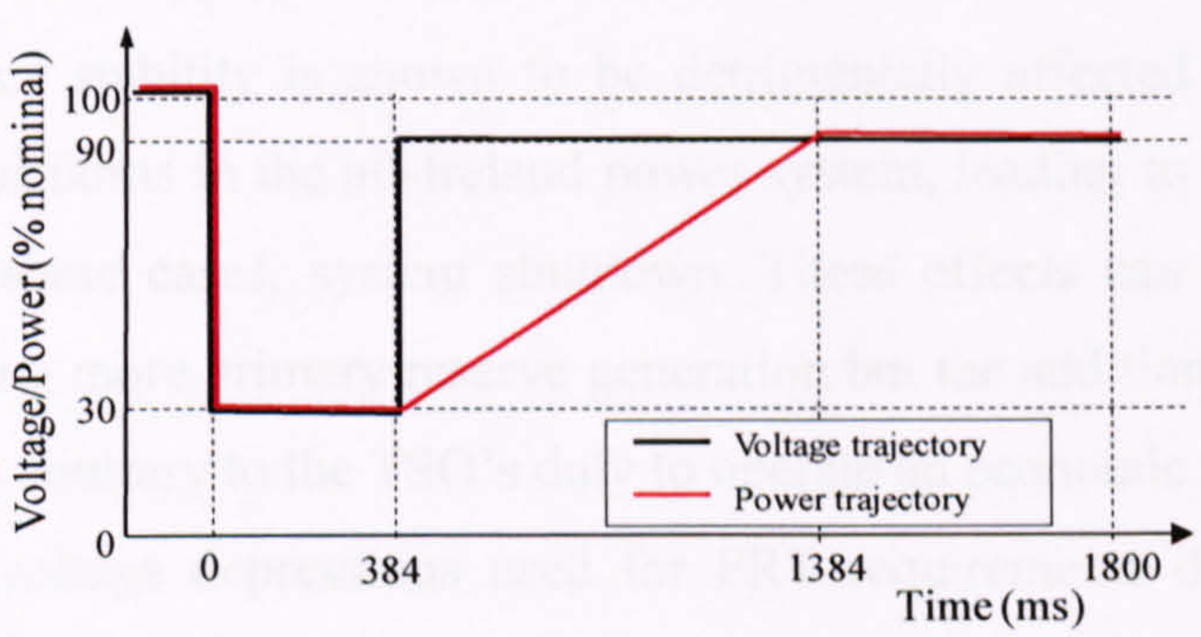

c. Scenario 3

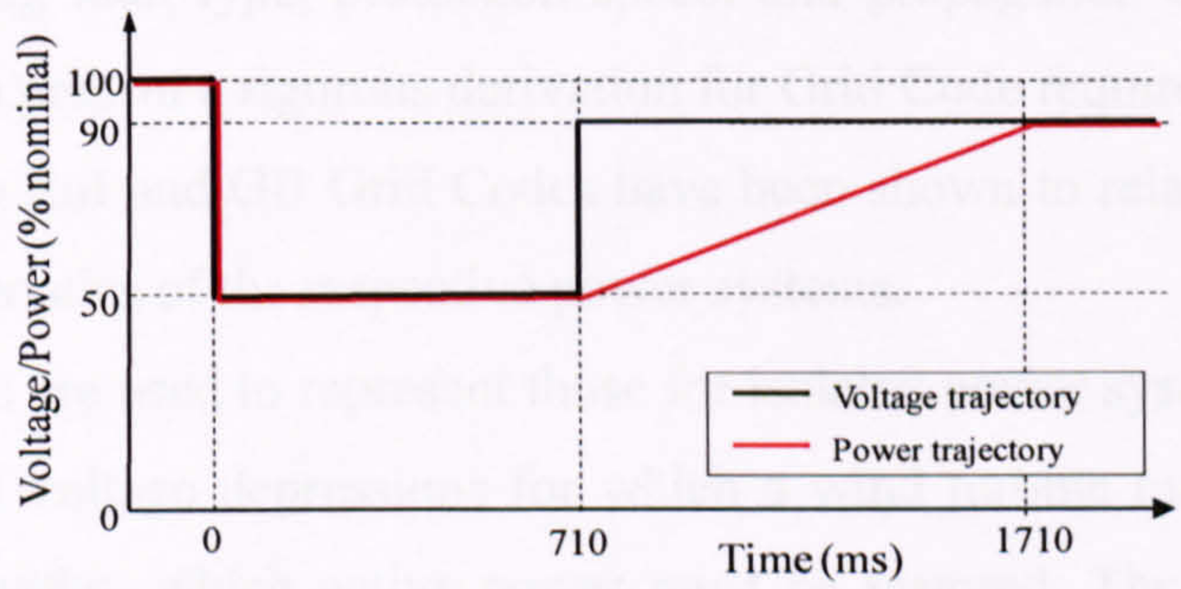

d. Scenario 4

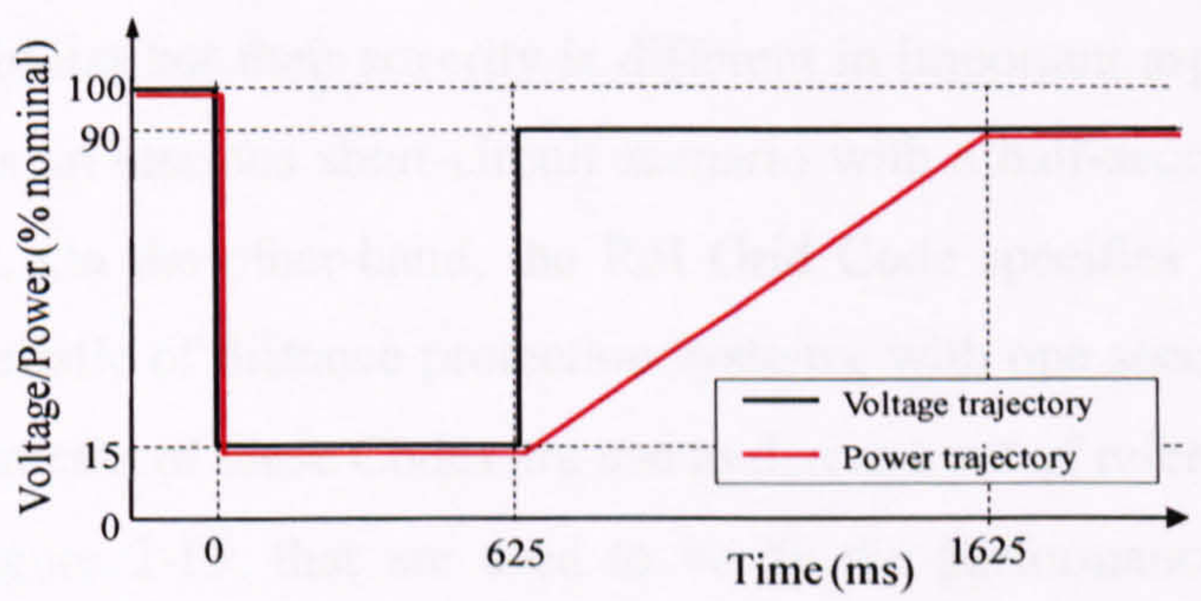

e. Scenario 5

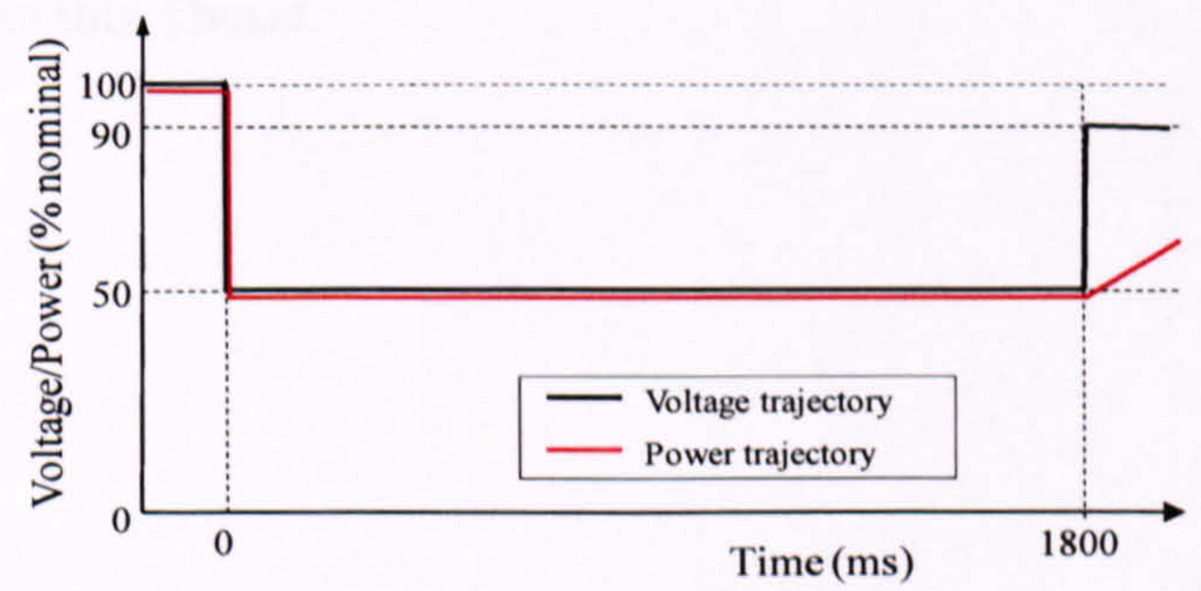

Figure 2-15: Voltage-time traces of selected five fault scenarios

It can be seen that scenario 1 of Figure 2-15a is the only case that requires power recovery within 0.5 second of fault clearance. It should be noted that the power-time traces show average trajectories. Significant damped oscillations about these trajectories are accepted, within reason, by TSOs.

2.8. Summary

Short-term frequency stability is selected as the dominant factor for FRT investigations. Frequency stability is shown to be detrimentally affected by fault-induced tripping of wind farms in the all-Ireland power system, leading to increased load shedding and, in some cases, system shutdown. These effects can be partly compensated by operating more primary reserve generation but the additional cost of this alternative option is contrary to the TSO's duty to operate an economic system.

The characteristics of voltage depressions used for FRT requirements depend on several factors, including fault type, protection speed, and propagation distance. It has not been possible to present a rigorous derivation for Grid Code requirements but differences between the RoI and GB Grid Codes have been shown to relate, in part, to the differing characteristics of the respective power systems.

RoI and GB Grid Codes are used to represent those for isolated power systems. Both Codes define ranges of voltage depressions for which a wind turbine must remain stable and timescales within which active power must be restored. The format of these requirements is similar but their severity is different in important aspects. The GB Grid Code specifies an onerous short-circuit scenario with a half-second power restoration requirement. On the other-hand, the RoI Grid Code specifies very long duration faults, characteristic of distance protection systems, with one second power restoration. The requirements of these Codes are use to derive a set of reference fault scenarios, shown in Figure 2-15, that are used to verify the performance of FRT technologies presented in this Thesis.

3. Technology review

3.1. Introduction

The wind industry has responded to Grid Code revisions by enhancing old technologies and developing new technologies to facilitate FRT compliance. FRT requirements have contributed to a substantial fall in the market share of FSWTs and the increasing dominance of VSWTs with DFIG, especially for large wind farms. The primary focus of current research and development has therefore shifted to improving the FRT performance of VSWTs, thereby reinforcing the dominance. In contrast, this Thesis focuses on improving the FRT performance of FSWTs, with the objective of extending the viability of this rugged and reliable technology.

This Chapter reviews current techniques and technologies that are used to improve the FRT performance of FSWT wind farms, with specific reference to GB and RoI Grid Codes requirements. Consistent with Chapter 2, this review focuses on the means by which these technologies improve the dynamic stability of wind farms and facilitate restoration of active power to the wider power system. Dynamic braking resistors (DBR) are included, in spite of not being currently applied, in order to introduce and compare the principles of dynamic braking with state-of-art technologies.

3.2. Wind Turbine and Farm Design Modifications

Although not a "technology" this first option is a possible contributing measure to improve FRT stability. Modifications can be made to mechanical, generator and/or electrical network characteristics that would improve dynamic performance. These modifications and their potential benefits are reviewed below and explored in greater detail by (Akhmatov 2003(a); Akhmatov 2005(b)).

3.2.1. Mechanical

Referring to Eq. 2.2, increasing drive train inertia would reduce drive train acceleration and thereby improve stability. This could be achieved by increasing the

blade section or by using heavier materials. This approach is unlikely to be adopted unless other economic benefits are derived by such modifications. Another mechanical change with smaller potential benefit is increasing the stiffness of the drive train coupling by shortening the low-speed drive shaft. The beneficial effect of these changes is quantified for a specific example in (Akhmatov 2005(b), Table 5.1) and further illustrated in Figure 3-1 using the representative wind farm model described in Chapter 4 and fault scenario 4 from Figure 2-15d.

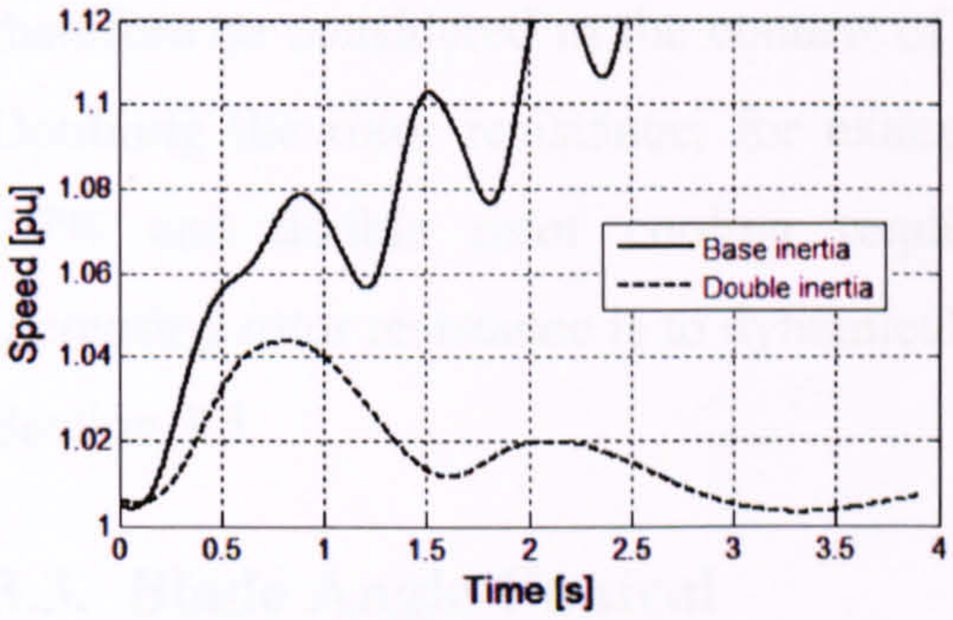

a. By increasing inertia

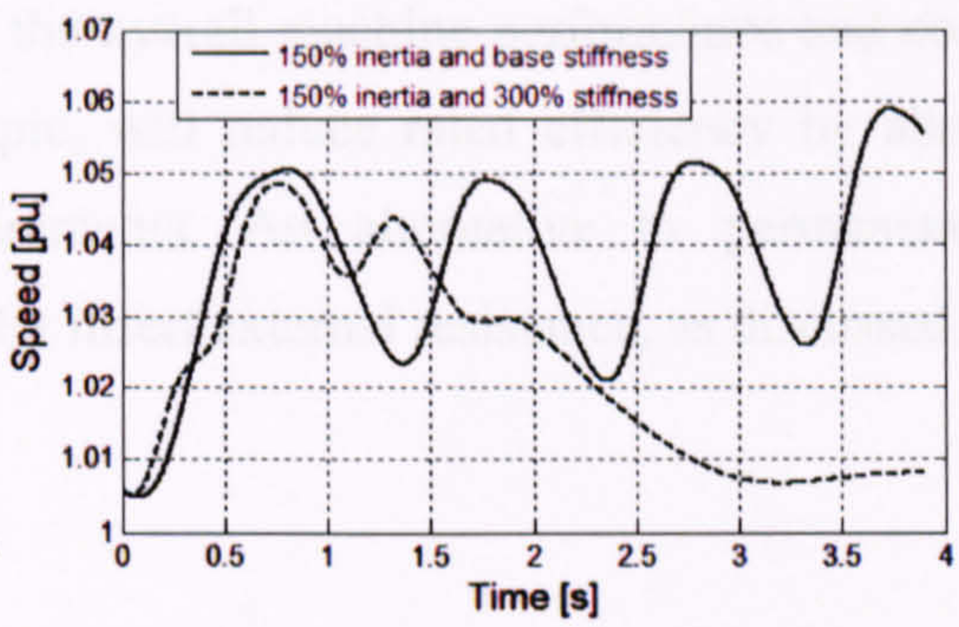

b. By increasing coupling stiffness

Figure 3-1: Improved stability by modifying mechanical parameters

Figure 3-1a shows that doubling drive train inertia has a very substantial stabilizing effect. Figure 3-1b shows how a three-fold increase in coupling stiffness can reduce the inertia necessary to achieve a similar a stability improvement.

3.2.2. Generator

Induction generator impedance can be modified to increase decelerating electrical torque at higher rotor speeds. Improvements can be made by reducing the stator or rotor leakage reactance or increasing rotor resistance (Akhmatov 2003(a), Fig 6.A.2). The effects of these improvements are shown in Figure 3-2 using the same base-case scenario as Section 3.2.1.

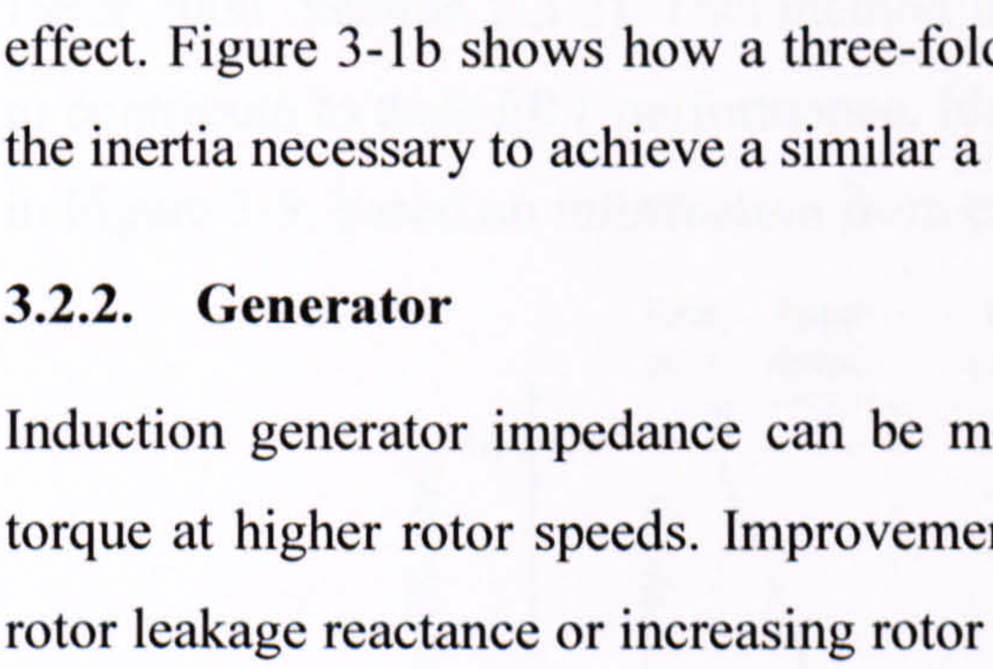

a. By reducing leakage inductance

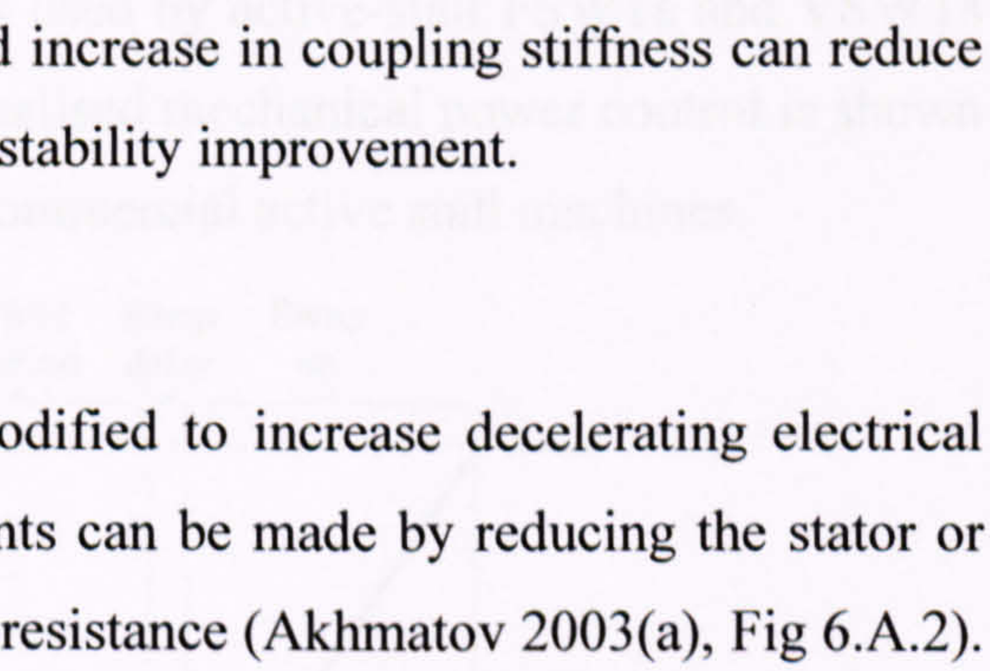

b. By increasing rotor resistance

Figure 3-2: Improved stability by modifying generator impedance

Figure 3-2a shows that a 15% reduction in stator and rotor leakage inductance can substantially improve FSWT recovery, despite persistent post-fault oscillation.
Figure 3-2b shows that a doubling of rotor resistance from 0.007 to 0.014pu makes a very positive impact on stability, leading to a rapid and damped recovery within 1.5 seconds of fault clearance.
However, these same parameters are optimised for other performance characteristics such as efficiency, inrush current and machine cooling. The above changes must therefore be considered in the context of the overall machine performance and cost. Doubling the rotor resistance, for example, will reduce rated efficiency by about 0.7% and double rotor cooling requirements. An alternative to permanently increasing rotor resistance is to dynamically insert external resistance, as discussed in Section 3.5.

3.3. Blade Angle Control

Stability can be substantially improved by temporarily reducing the mechanical power input by changing the rotor blade angle (Akhmatov 2005(b), Figure 5.21; Heier 2006, Section 2.3.2). This method is used by active-stall FSWTs and VSWTs to contribute to their FRT performance. Idealised mechanical power control is shown in Figure 3-3, based on information from commercial active stall machines.

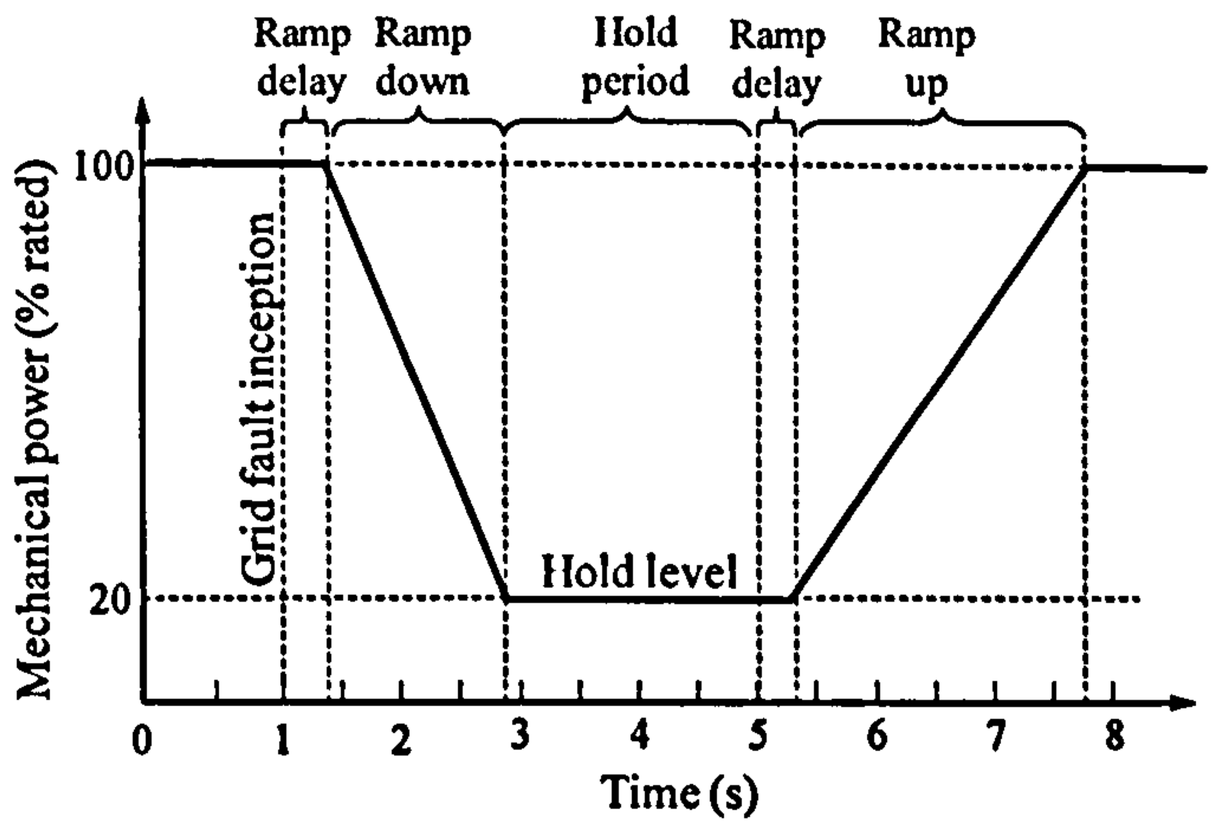

Figure 3-3: Idealised mechanical power ramping response

The initial *ramp delay* comprises actuation blade delay and aerodynamic lag between pitching and power reduction. The *ramp down* rate is limited by actuation speed and aerodynamic response. The *hold period* is governed by the speed of voltage recovery at the stator terminals. The minimum *hold level* is typically 20% but may be greater

if faster recovery times are required. The *ramp delay* before ramping up is primarily due to aerodynamic lag. The ramp up rate of about 2 seconds is typically limited by the maximum permissible axial loading on the wind turbine tower. In the example of Figure 3-3 full mechanical power output is restored several seconds after fault inception.

The simulated example in (Akhmatov 2005(b), Fig 5.24) shows power output recovery about four seconds after fault clearance. This compares unfavourably with the GB and RoI Grid Code requirement for one second recovery to 90%. Stability can be improved in some cases by increasing the hold level to about 60% as shown in Figure 3-4 for the base-case scenario of Section 3.2.1.

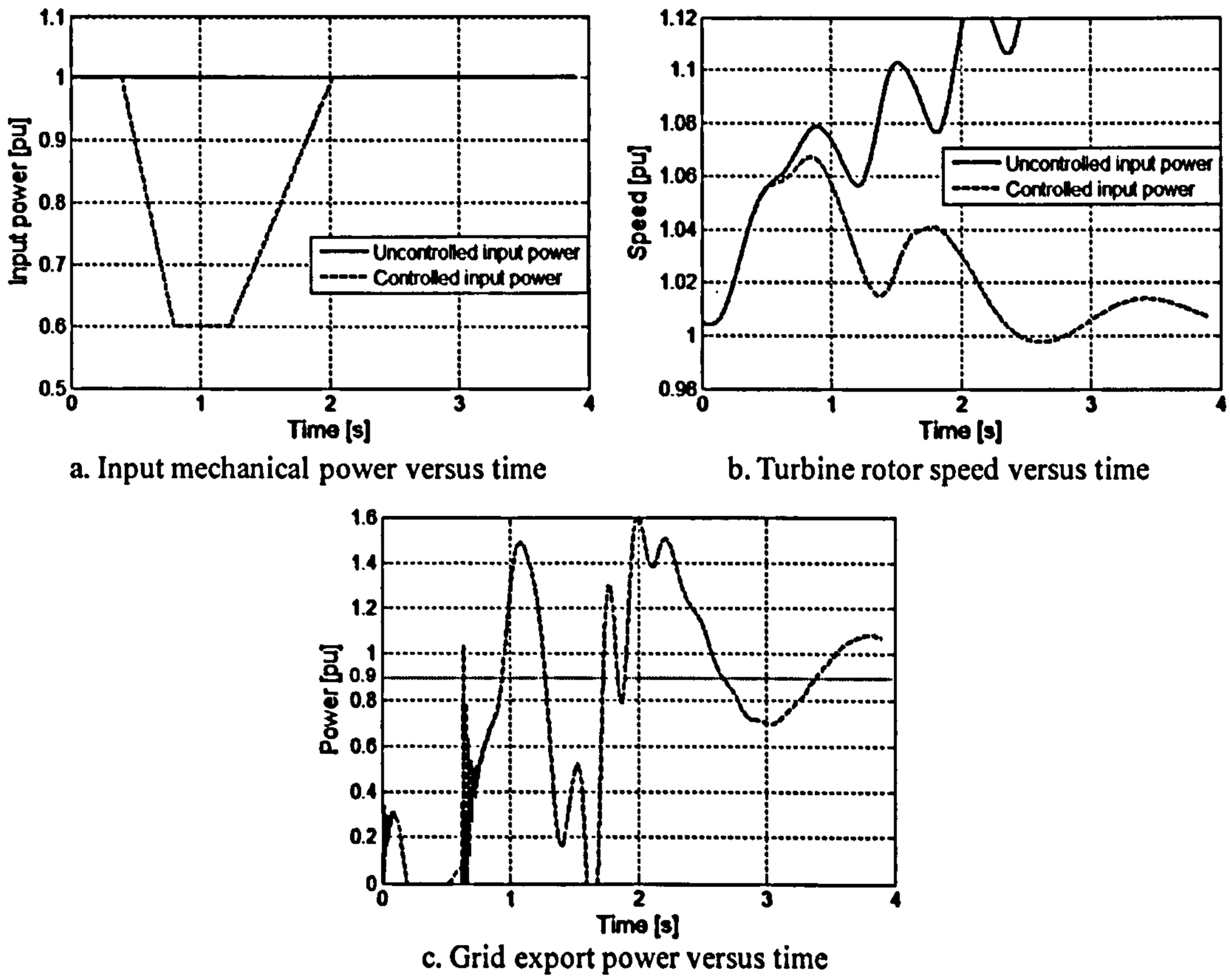

a. Input mechanical power versus time

b. Turbine rotor speed versus time

c. Grid export power versus time

Figure 3-4: Improved stability by blade angle control

Figure 3-4a shows an optimised mechanical power input characteristic applied to achieve the stable response of Figure 3-4b. Figure 3-4c shows the power exported to the grid which, despite significant oscillation, is restored to an average above 90% in just over one second.

3.4. Dynamic Reactive Power Compensation

3.4.1. Background

Dynamic Reactive Power Compensation (dRPC) improves the stability of FSWTs by partially supporting the heavy reactive power demand of the induction generator locally, thereby reducing the magnitude of reactive power supplied from the grid. Figure 3-5 illustrates why compensation of this type achieves improved stability.

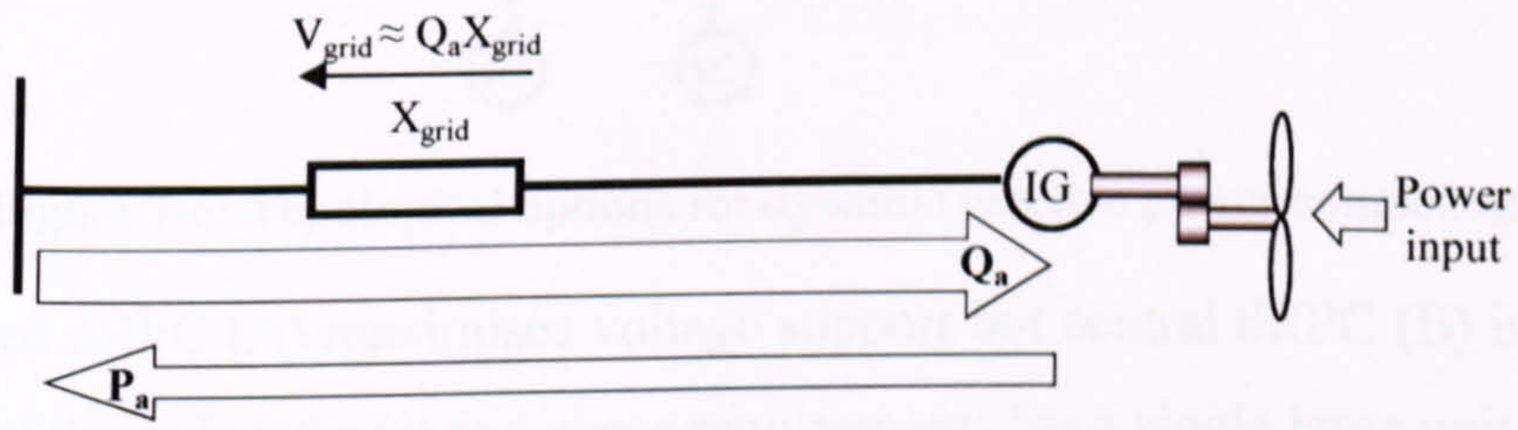

a. Reactive power demand without compensation

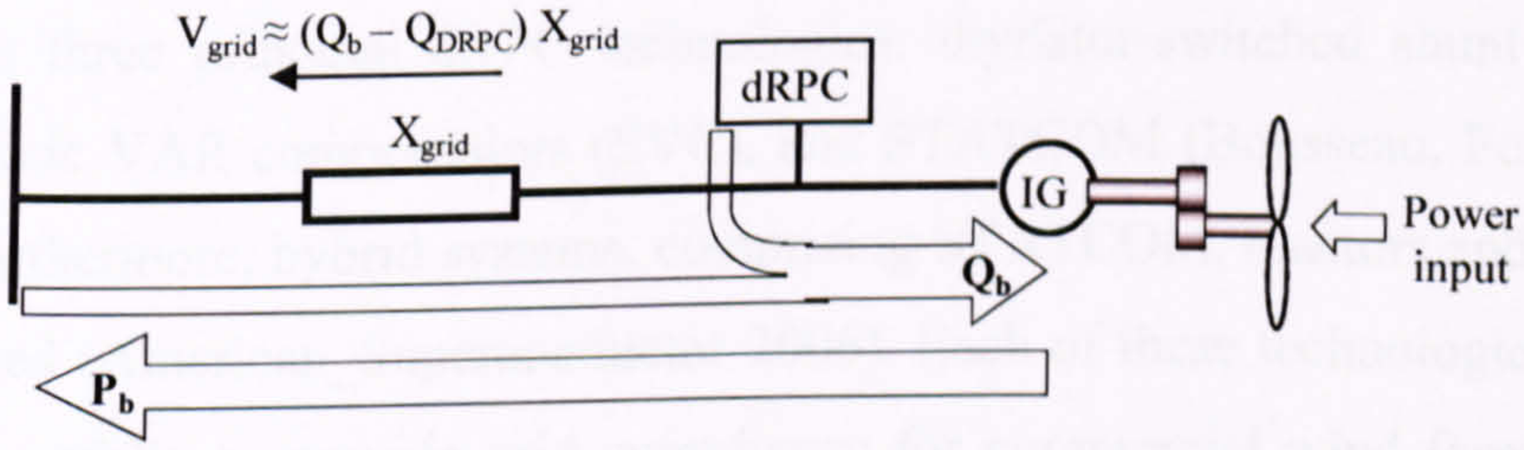

b. Reactive power demand with compensation

Figure 3-5: Effect of dynamical reactive power compensation

Figure 3-5a shows the full reactive power demand, Q_a, of the generator being drawn across the grid reactance, X_{grid}. In per unit form, the approximate voltage drop across the grid reactance is the product of reactive power flow and reactance, $Q_a X_{grid}$ (Jenkins, Allan et al. 2000, Eq. 3.15). Figure 3-5b shows how dRPC reduces reactive power transfer across the grid reactance thereby reducing voltage drop by $Q_{dRPC} X_{grid}$. This voltage support acts to increase the generator torque and electrical power output, P_b, because of the steady-state proportional relationship of torque to voltage squared (Fitzgerald, Kingsley et al. 2002). dRPC can be installed close to the generator terminals or at the substation busbar, as shown in Figure 3-6.

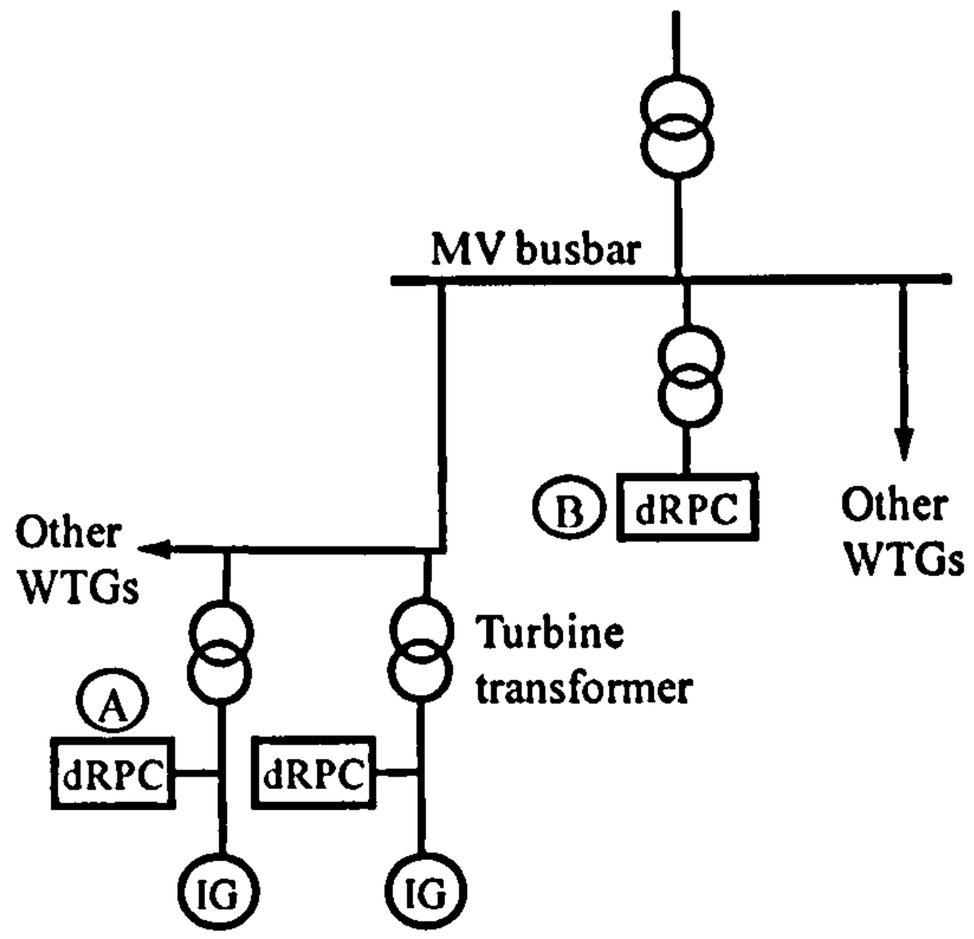

Figure 3-6: Topological options for dynamic reactive power compensation

Distributed dRPC (A) maximises voltage support but central dRPC (B) is often used because of the reduced cost and space requirements for a single large unit at the wind farm substation.

There are three principal dRPC technologies: thyristor-switched shunt capacitors (TSC), static VAR compensators (SVC), and STATCOM (Bousseau, Fesquet et al. 2004). Furthermore, hybrid systems, comprising STATCOM, reactors and capacitors can be used (American_Superconductor 2006). Each of these technologies has been used successfully to provide grid compliance for commercial wind farms installed within the past three years. Each provides the same product, reactive power, but they are distinguished by their cost, response, and voltage dependence, as discussed below.

3.4.2. TSC

Capacitors have been used for power factor correction of wind turbines for several decades. Conventionally these capacitors have been switched by mechanical contactors with response times in the order of a second. More recently thryristor-switching has been introduced to provide fast response for dynamic control. Siemens, for example, installs TSC on all its FSWTs. Figure 3-7 shows the stability improvement by increasing the capacitance from 0.4pu to 1.0pu, equivalent to adding 1.2MVAr compensation to each 2MW FSWT.

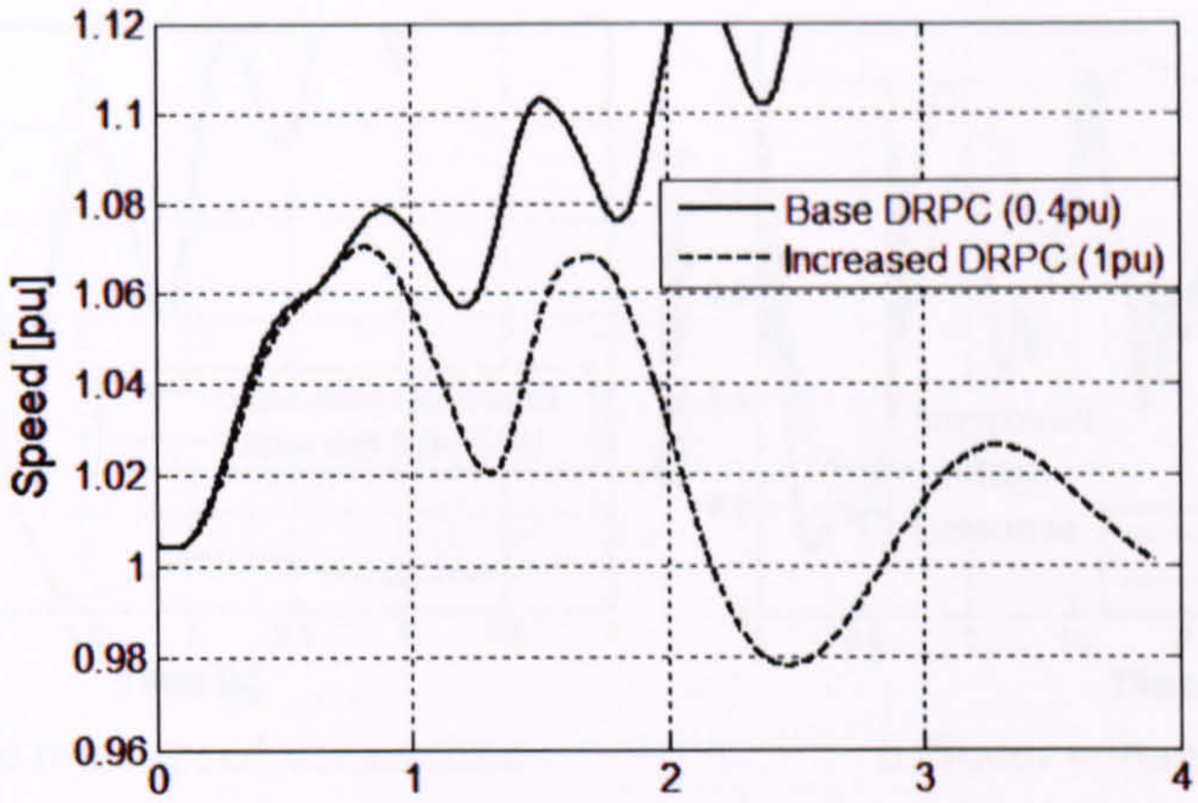

Figure 3-7: Improved stability using TSC

3.4.3. SVC

SVC comprises thyristor-switched inductors in parallel with switched capacitor banks. Although the topology and control is different from TSC described above, the response is very similar for purpose of FRT modelling. It can be inferred that the SVC capacity required for FRT stability is the same as shown for TSC above.

3.4.4. STATCOM

A STATCOM is a voltage source converter which is designed to source or sink reactive power. The benefit of STATCOM compared to TSC or SVC is that reactive power capability is proportional to voltage rather than voltage squared. This means that a 100MVAr- rated STACOM can source 50MVAr at 50% grid voltage whereas a TSC or SVC of the same capacity can source only 25MVAr. STATCOM is therefore particularly effective during periods of substantial voltage depression. The benefit of STATCOM in comparison with similarly rated TSC or SVC is shown in Figure 3-8. The simple transient STATCOM model, used for the analysis, is described in Chapter 4.

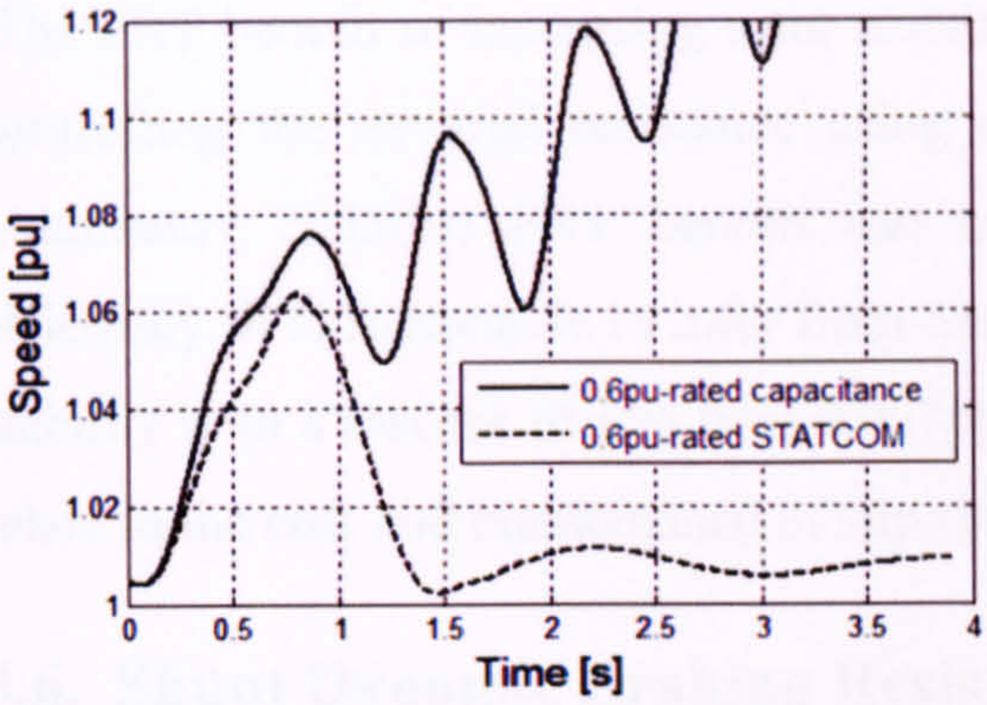

a. Turbine rotor speed versus time

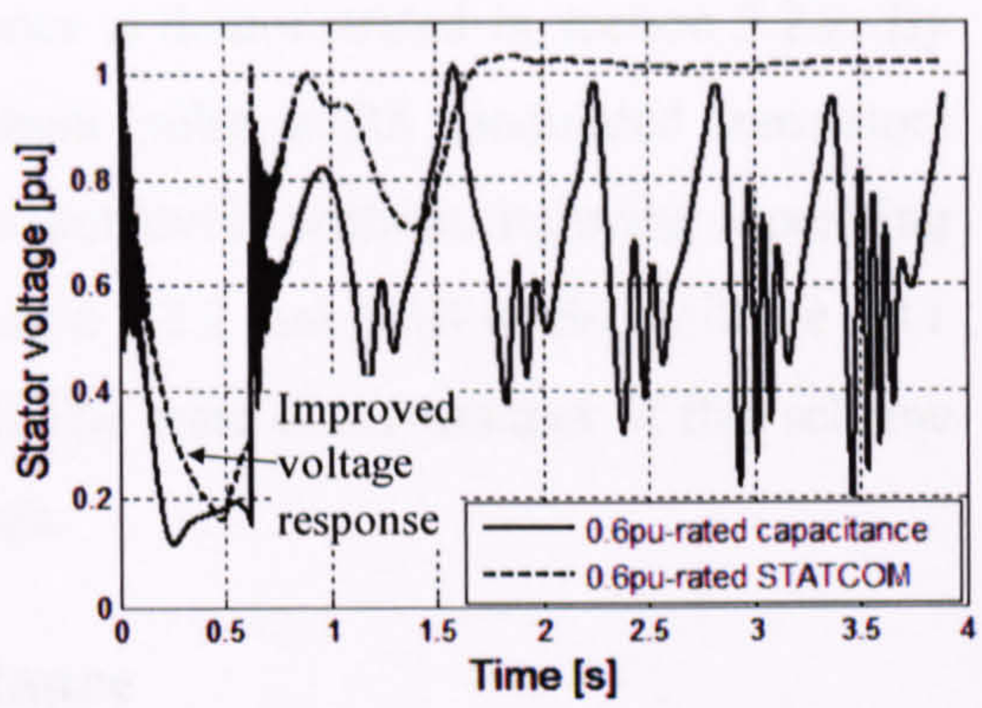

b. Stator voltage versus time

Figure 3-8: Comparison of FRT performance of SVC and STATCOM

Figure 3-8a shows the better dynamic response of STATCOM resulting from greater voltage support at the generator terminals, as show Figure 3-8b. Referring to Section 3.4.2 it can be noted that 1.0pu of TSC achieves similar stability to 0.6pu of STATCOM. Akhmatov's studies (Akhmatov 2003(a)), using different wind farm characteristics, concluded that the same stabilising effect could be achieved with 25% less STATCOM capacity. However, since the cost per MVAr of STATCOM is substantially higher than TSC or SVC, it may not be the least cost solution.

3.5. Dynamic Rotor Resistance

Dynamic rotor resistance (DRR) is a control method in which the rotor resistance of a wound rotor induction generation (WRIG) is supplemented by a controllable external resistance. This concept was initially applied several decades ago to soft-start industrial motors. More recently DRR has been applied by Vestas to FSWTs as a means of reducing electrical power output fluctuations and resulting flicker. The latter technology (*OptiSlip*^{R}) is shown in Figure 3-9.

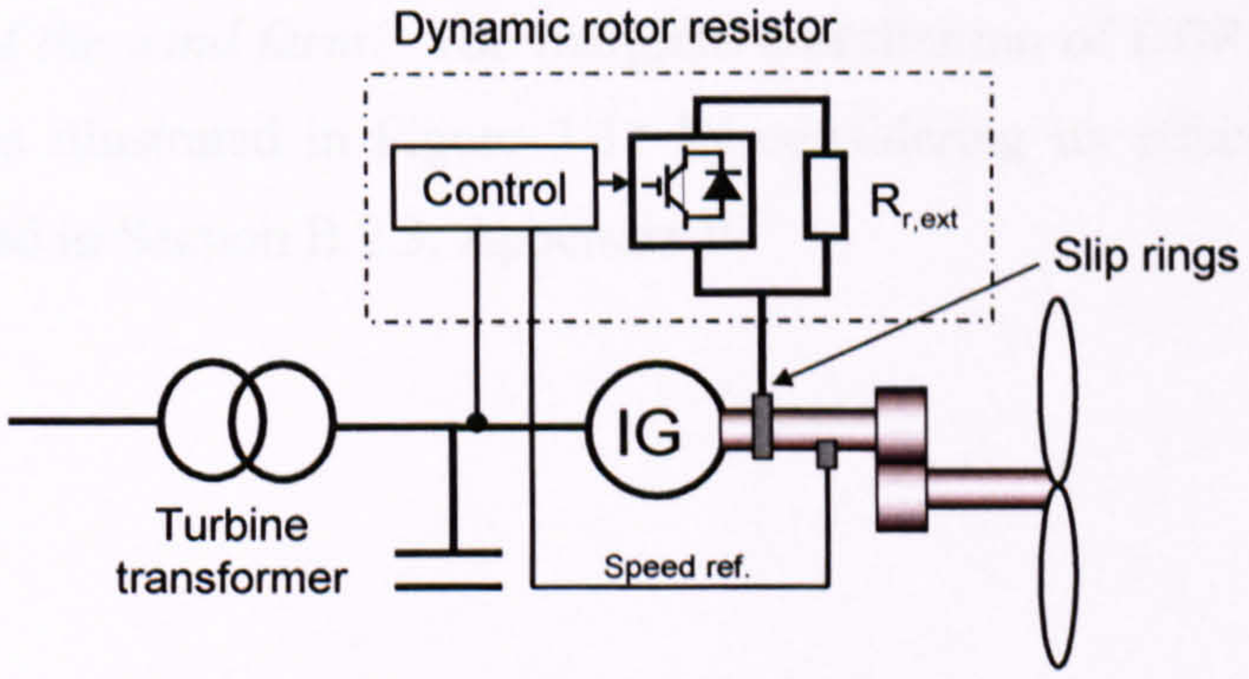

Figure 3-9: DRR schematic

The FRT benefit of increasing rotor resistance is demonstrated in section 3.2.2. By controlling the external resistance using shunt pulse width modulated transistors (Akhmatov 2005(b)) FRT benefit can be achieved without reducing operating efficiency. It is reasonable to infer from Section 3.2.2 that DRR could facilitate FRT stability with a resistor of less than 0.007pu. The main disadvantages of this scheme relate to the cost and maintenance of slip rings.

3.6. Shunt Dynamic Braking Resistance

Distributed (A) and centralised (B) topologies of shunt-connected dynamic braking resistors (DBR) are shown in Figure 3-10.

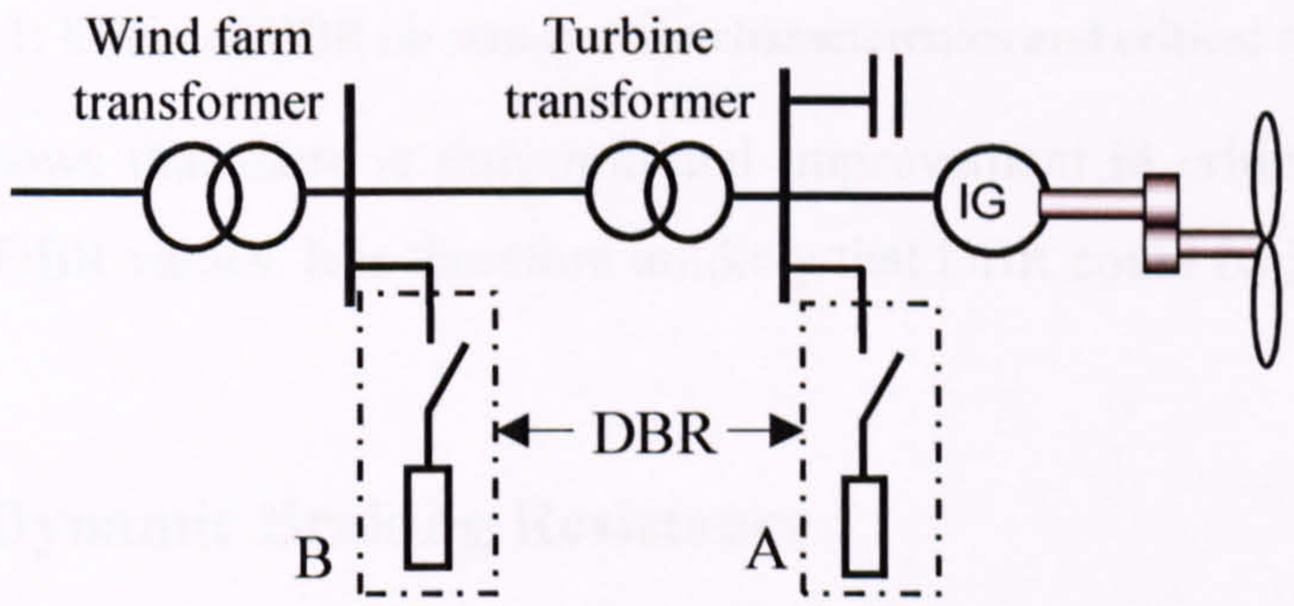

Figure 3-10: DBR topologies within a representative FSWT wind farm

DBR has been used to stabilise power swings on power transmission systems since the 1960s (Peelo, Hein et al. 1994). They have also been proposed to improve the stability of conventional synchronous generators (EPRI 1991) and FSWT wind farms (Wu, Arulampalam et al. 2003; Freitas, Morelato et al. 2004). A study of DBR in conjunction with STATCOM (Wu, Arulampalam et al. 2003) concluded that "*DBR could not significantly increase critical clearing time of the wind farm without the STATCOM. The DBR may be used together with the STATCOM for minor stability enhancement of the wind farm.*" The marginal contribution of DBR to FSWT wind farm stability is illustrated in Figure 3-11 by considering its effect on the critical speed, as defined in Section B.2.3, Appendix B.

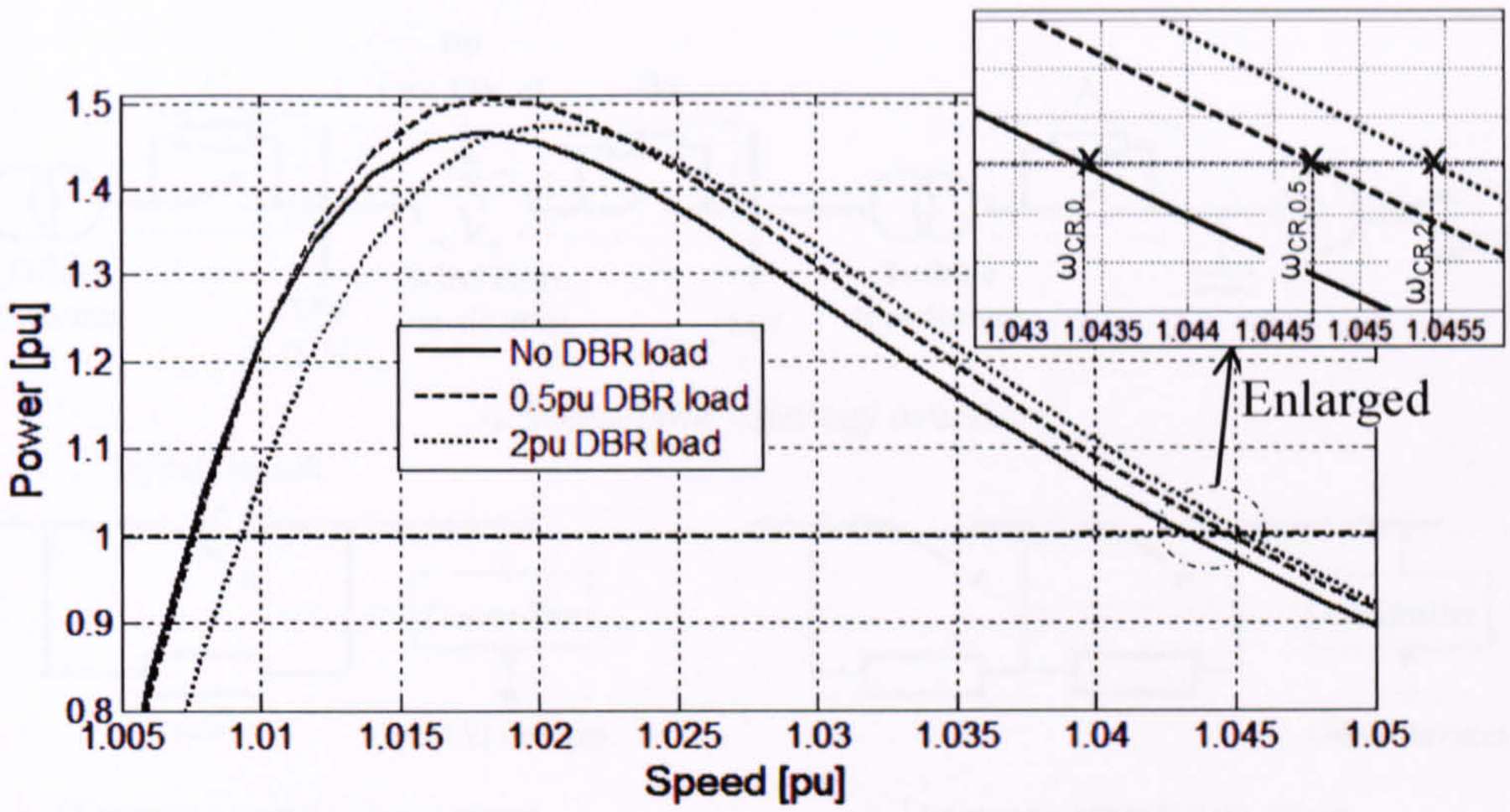

Figure 3-11: Effect of DBR on steady-state characteristics and critical speed, ω_{CR}

Figure 3-11 shows that there is only minimal improvement in critical speed for a wide range of DBR values. It is therefore unlikely that DBR could be justified in this application.

3.7. Series Dynamic Braking Resistance

3.7.1. General concept and arrangement

Series-connected Dynamic Braking Resistors (series-DBR) contribute directly to the balance of active power during a fault, with the potential to displace or eliminate the need for pitch control. It does this by dynamically inserting a resistor in the generation circuit, increasing the voltage at the terminals of the generator and thereby mitigating the depression of electrical torque and power during the fault period. The theory underpinning its beneficial effect is described in Chapter 5. Topologies of series-DBR are shown in Figure 3-12.

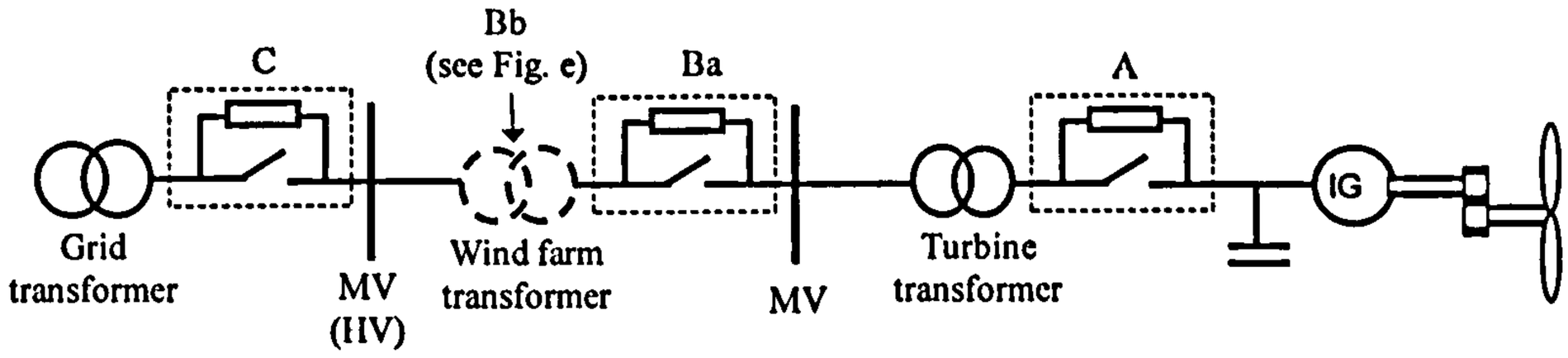

a. Series-DBR topology overview

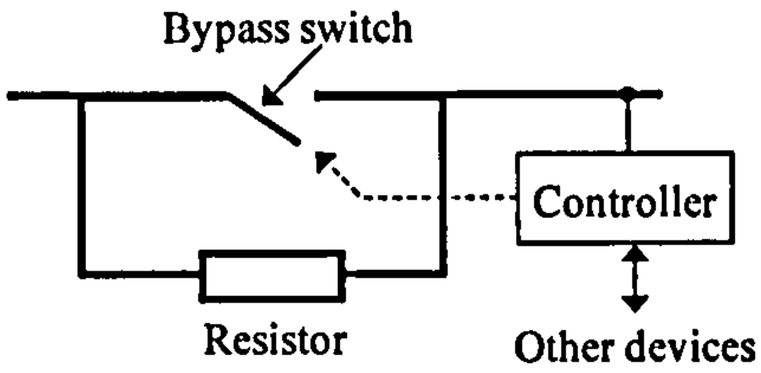

b. Discrete control: single stage

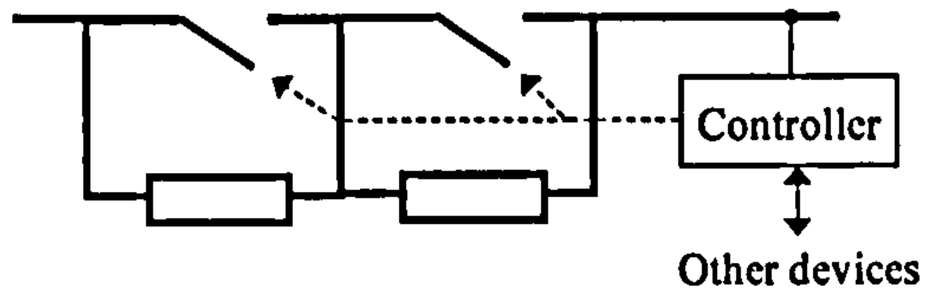

c. Discrete control: two-stage

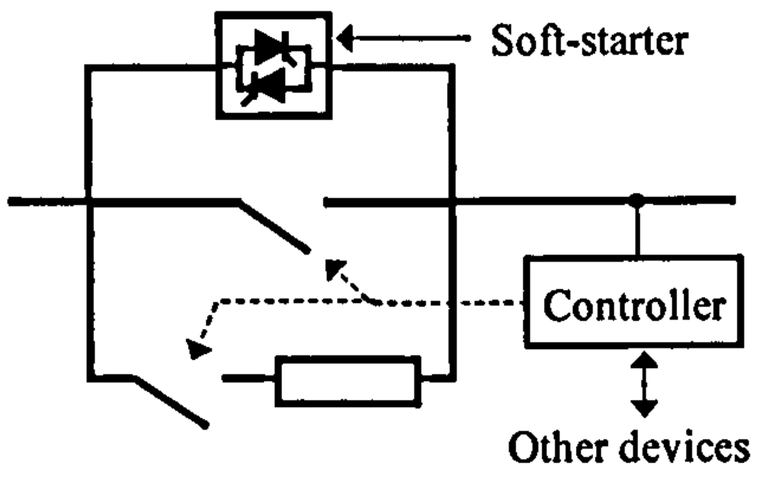

d. Continuous (variable) control

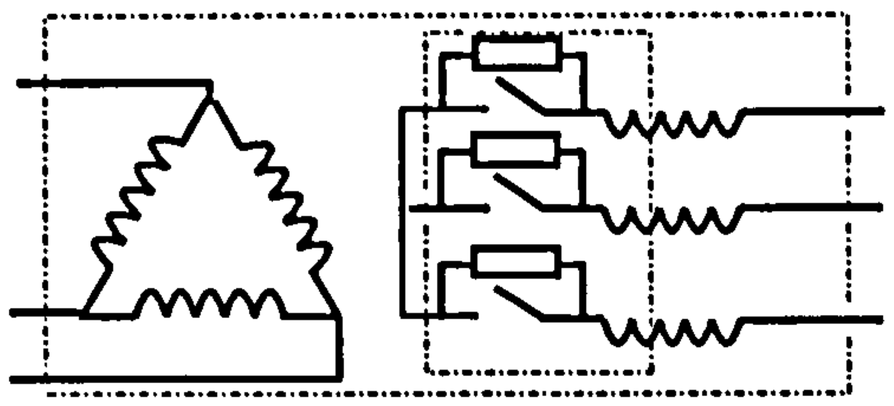

e. Detail for option Bb from Figure a.

Figure 3-12: series-DBR topologies within an FSWT wind farm

Series-DBR may be located at each wind turbine (A), at the wind farm substation (B) or embedded in the distribution system (C), as shown in Figure 3-12a. At each location, the scheme may comprise one, two or more stages of resistor/switch units, as represented by Figure 3-12b and Figure 3-12c. Figure 3-12d shows a possible arrangement at location A, using the soft-starter that is already applied for grid connection of FSWTs. The soft starter would allow continuous, optimised control of inserted resistance. The switching speed depends on the type (static or mechanical) and voltage (low, medium or high), as shown in Table 3-1.

Switching type	Opening time (ms)	Closing time (ms)
Low voltage contactor	20-40	100-150
Medium/high voltage breaker	70-100	-
Thyristor	10	10
IGBT	<1	<1

Table 3-1: series-DBR switching times

The series-DBR would operate with its bypass switch closed under normal conditions, bypassing the braking resistor. Voltage depression below a selected set-point would lead to near-instantaneous tripping of the switch. Current would then flow through the inserted resistor for the period of the fault and the initial post-fault recovery. When voltage recovered above a minimum reference level the switch would close and the circuit would be restored to its normal state. During the short insertion period energy would be dissipated in the resistor, raising its temperature.

Brief reference is made in (Kundur, Paserba et al. 2004) to series-DBR as an alternative to shunt-DBR for synchronous generator braking. In particular, Kundur refers to the configuration of Figure 3-12e (Barthold 1988) whereby the insulation voltage of the resistors and bypass switches can be reduced by insertion in the neutral of a star-connected transformer winding. This neutral-connection method could be applied at any of the locations shown in Figure 3-12 although the advantage is not significant for the low voltage option, A. In spite of these references, there is no published evidence of series-DBR being considered for the stability of induction machines or wind farms, prior to 2005. I started work on this concept in early 2005 following an extensive comparative investigation of a number of possible methods for improving the FRT stability of FSWTs. Having identified this concept as having strong potential benefits, I registered the "invention" with Newcastle University in May 2005, filed for a patent in December 2005 (Causebrook 2005) and presented a poster in February 2006 (Causebrook, Atkinson et al. 2006). A more rigorous presentation of the concept was published in August 2007 (Causebrook, Atkinson et al. 2007).

3.7.2. Transient Booster

Independently, ABB also carried out investigations on the use of a series-connected DBR device in 2005 leading to a poster presentation of their "Transient Booster™" concept in October 2005 (Gertmar, Christensen et al. 2005) and a conference paper in May 2006 (Gertmar, Christensen et al. 2006). The Transient Booster™ scheme is shown in Figure 3-13.

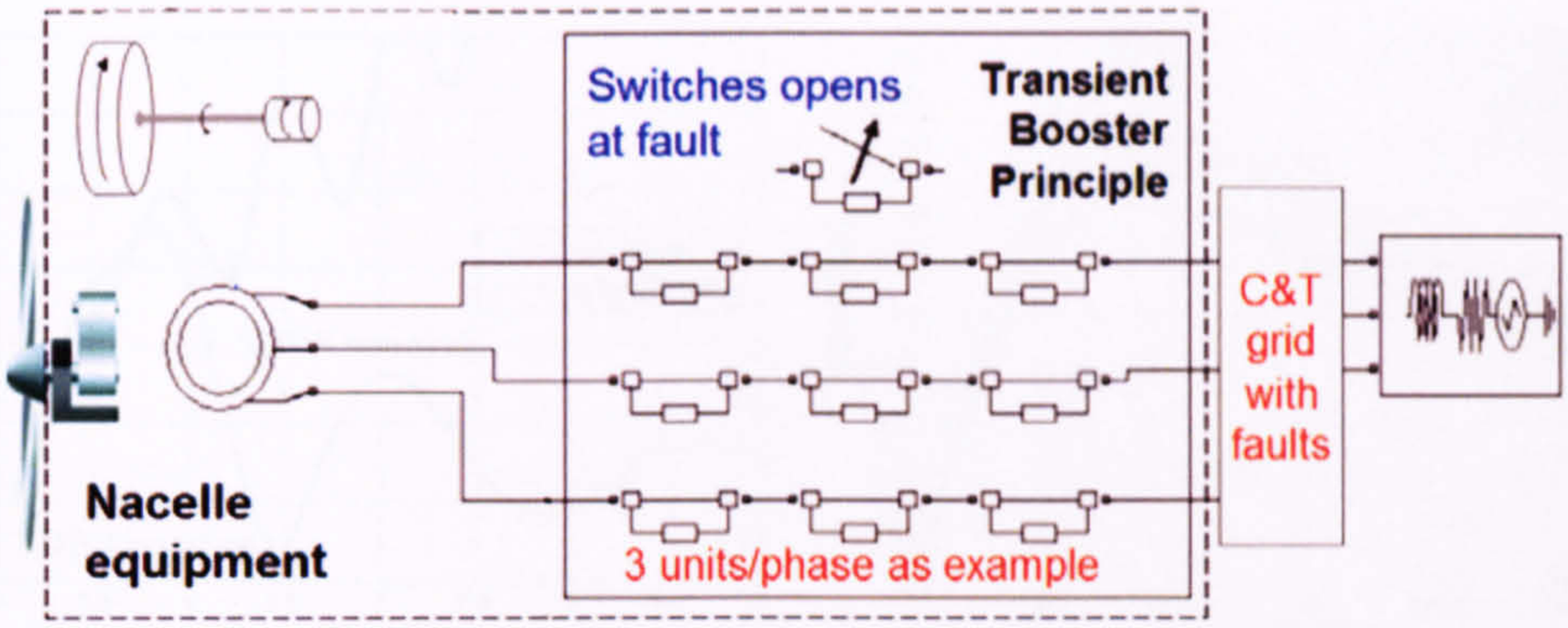

Figure 3-13: Transient Booster schematic (Gertmar, Christensen et al. 2005)

Although not explicitly stated, it is evident from the referenced paper that the inserted devices are resistors and therefore the scheme is one form of the series-DBR concept. An additional feature of the ABB scheme is that the resistors are independently controlled in each of the three phases, improving the scheme's performance during unbalanced grid faults.

I was unaware of the Transient Booster™ concept until December 2006 since neither of the above publications was accessible on electronic databases in that period. The potential conflict of intellectual property between these concepts is currently unresolved.

In order to distinguish my more general form of series-DBR from ABB's Transient Booster™, this Thesis focuses on the wind farm configuration of Ba in Figure 3-12 and refers to the concept as *sDBR*.

3.7.3. Preview analysis

The stability improvement of wind farm sDBR with a single 0.1pu resistance stage is previewed in Figure 3-14a using the fault scenario of Section 3.2.1 . The underlying basis for that improvement is shown in Figure 3-14b, with specific reference to critical speed.

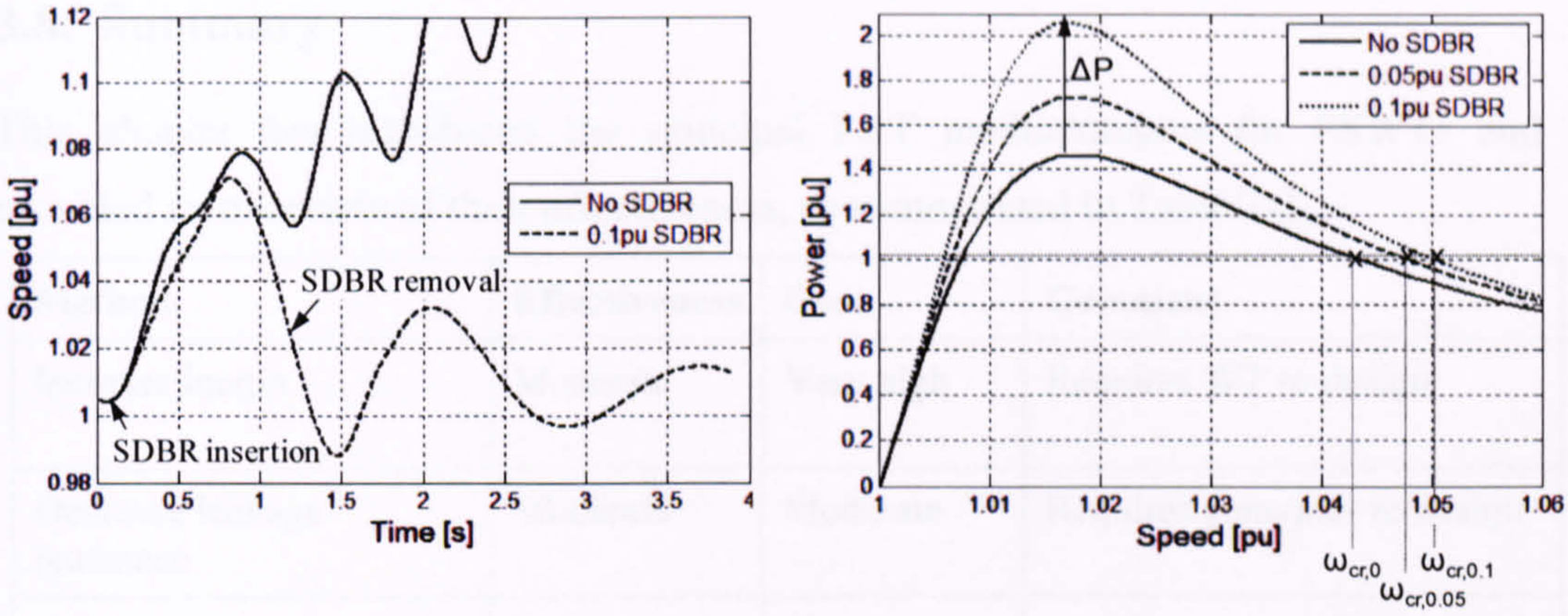

a. Improved FRT stablity b. Critical speed and peak power at 90% voltage

Figure 3-14: Effect of SDBR on FRT stability

Figure 3-14a shows the marked improvement by inserting sDBR 100ms after the fault inception for a period of 1.2 seconds. It can be seen that sDBR reduces the acceleration of the turbine rotor during the fault and increases deceleration in the initial period after fault clearance. The reason for this deceleration is illustrated by the steady-state characteristic of Figure 3-14b which shows a 0.7% increase in critical speed and a 45% increase in peak decelerating power. Quasi-steady-state and transient examinations of the sDBR-effect are covered in detail in Chapters 5 and 6.

3.8. Summary

This chapter has introduced the principal FRT methodologies for FSWTs and provided an overview of their effectiveness, as summarized in Table 3-2.

Method	Effectiveness	Cost	Comment
Increase inertia	Moderate	Very high	Requires WT re-design
Decrease leakage reactance	Moderate	Moderate	Requires generator re-design
Increase rotor resistance	Good	Higher losses	Feasibility depends on value of losses
Switched capacitors	Good	Moderate	Poor low voltage response
Static VAr compensator	Good	Moderate /High	Similar to switching capacitors
STATCOM	Very good	High/ Very high	Better low voltage response
Dynamic rotor resistance	Very good	High	Maintenance of slip rings
Shunt-DBR	Poor	Low	Marginal benefit
Series-DBR	Good	Low	Simple and effective at low cost

Table 3-2: Summary of FRT technologies

Of the technologies summarized in Table 3-2 *series-DBR* is chosen as the focus of this Thesis because of its strong potential to improve FRT stability of FSWTs at relatively low cost. This innovative technology could be installed at the substations of new wind farms or retrospectively applied to existing ones without affecting wind turbine design. The potential for retrospective application gives the technology a marketplace irrespective of the future rate of decline of the commercial FSWT sector.

4. Wind Farm Modelling

4.1. Introduction

The purpose of this Chapter is to derive an appropriate model and associated parameters for steady-state and transient FRT analysis of FSWT wind farms with sDBR and dRPC. Practical dynamics are highly complex due to wind variability, rotor aerodynamics, generator electromagnetics, and distributed impedance. This Chapter aims to reduce this complexity to the minimum level with sufficient accuracy for the stated purpose. This is achieved by considering the sensitivity of the overall system's dynamic response to each component of the wind farm system and the impact of its reduction or omission from the system model.

4.2. Typical Wind Farm System

Figure 4-1 shows a generalised single line diagram for a large wind farm system.

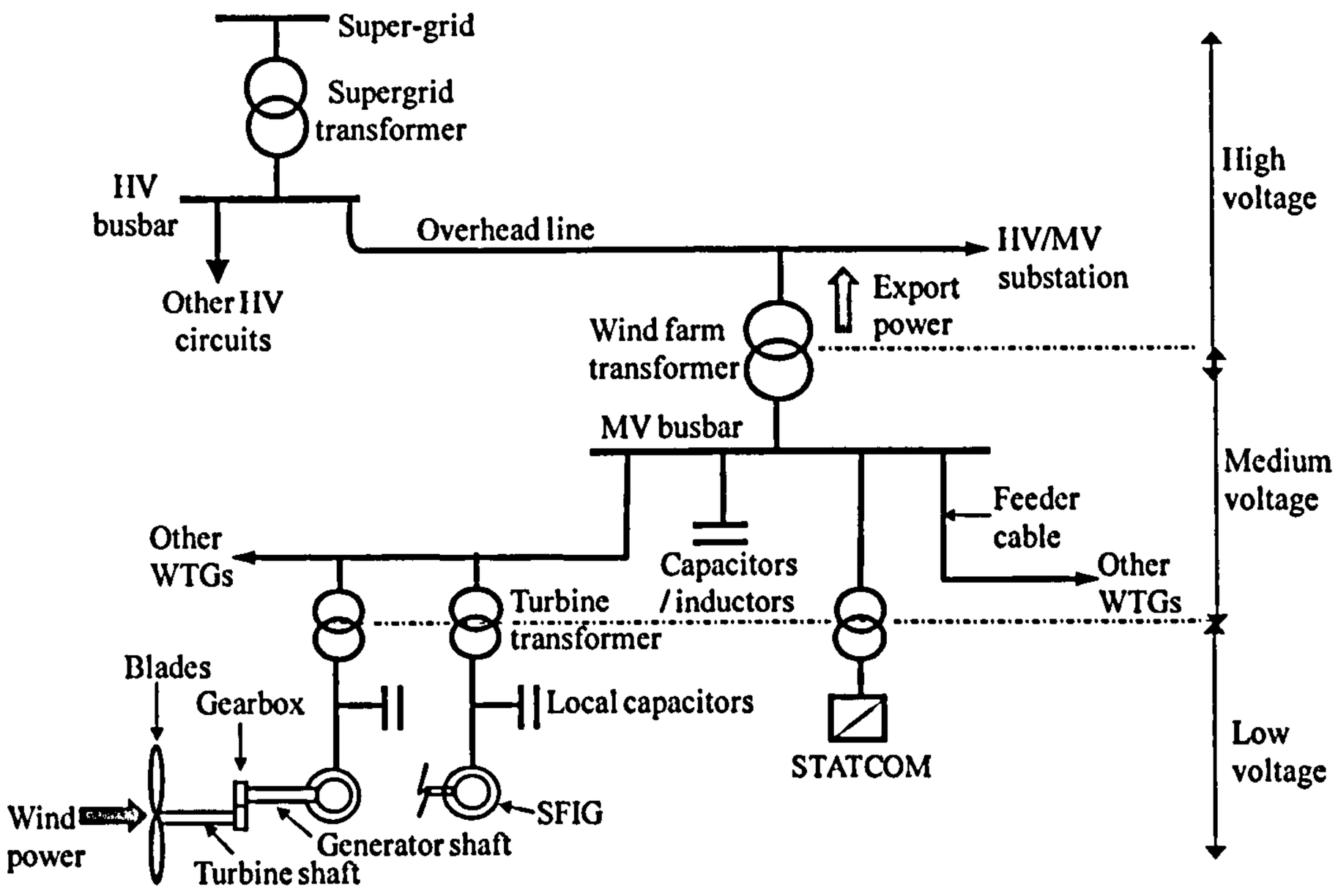

Figure 4-1: Single line diagram of generic FSWT wind farm system

Figure 4-1 includes the main components that influence system dynamic response but excludes items such as circuit breakers and relays which serve an important but

separate function. The topology of Figure 4-1 is applicable to most *large* wind farms. Variations usually relate to grid connection arrangement but these generally have a secondary effect on the fundamental system dynamics. The single line diagram of Figure 4-1 is represented in its simplest topological form in Figure 4-2 as a single electro-mechanical power train.

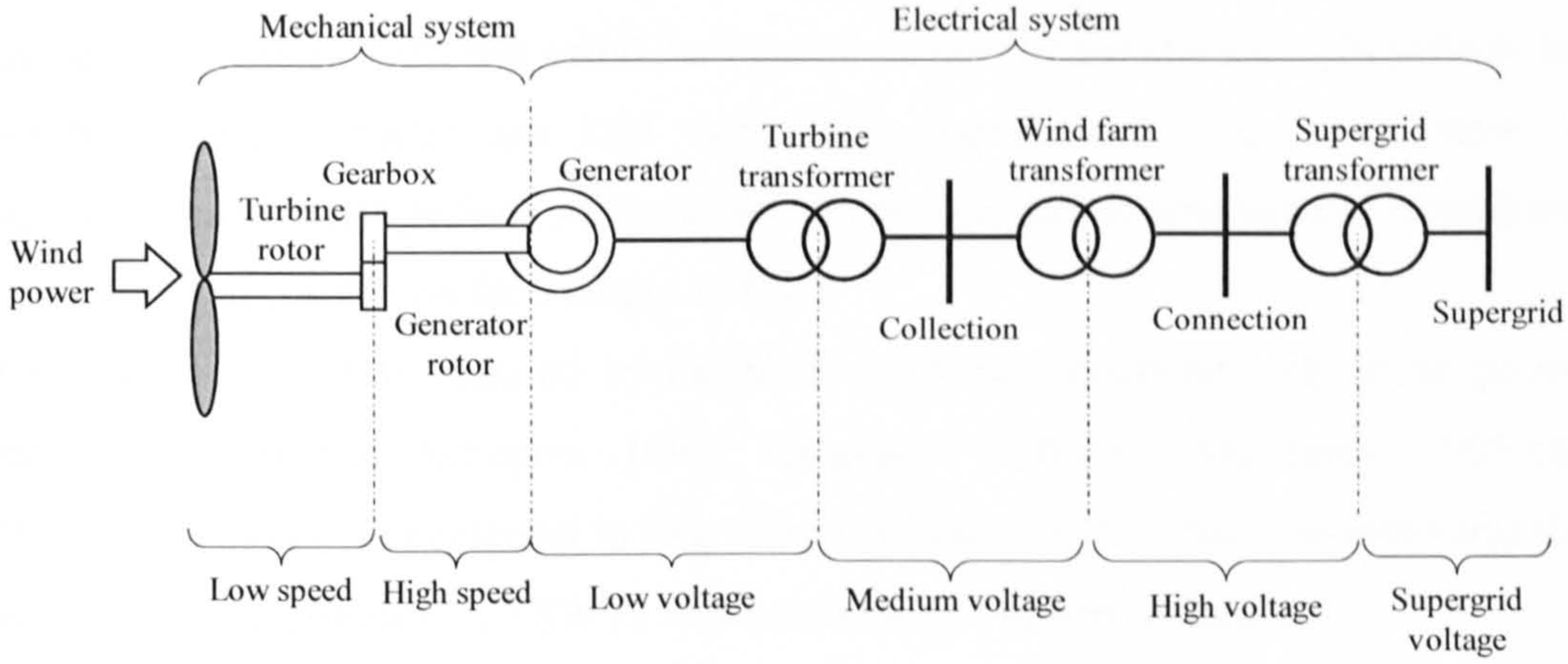

Figure 4-2: Simplified wind farm topology

4.3. Wind and Aerodynamic Modelling

Wind power is highly variable in several time domains (Freris 1990; Manwell, McGowan et al. 2002). Variations in each domain affect wind turbine performance and its effect on the power system. However, the scope of this Thesis is limited to deriving a value for mechanical input power that adequately represents the worst-case scenario for FRT. The steady-state power output of a wind turbine is represented by a power curve of type shown in Figure 4-3.

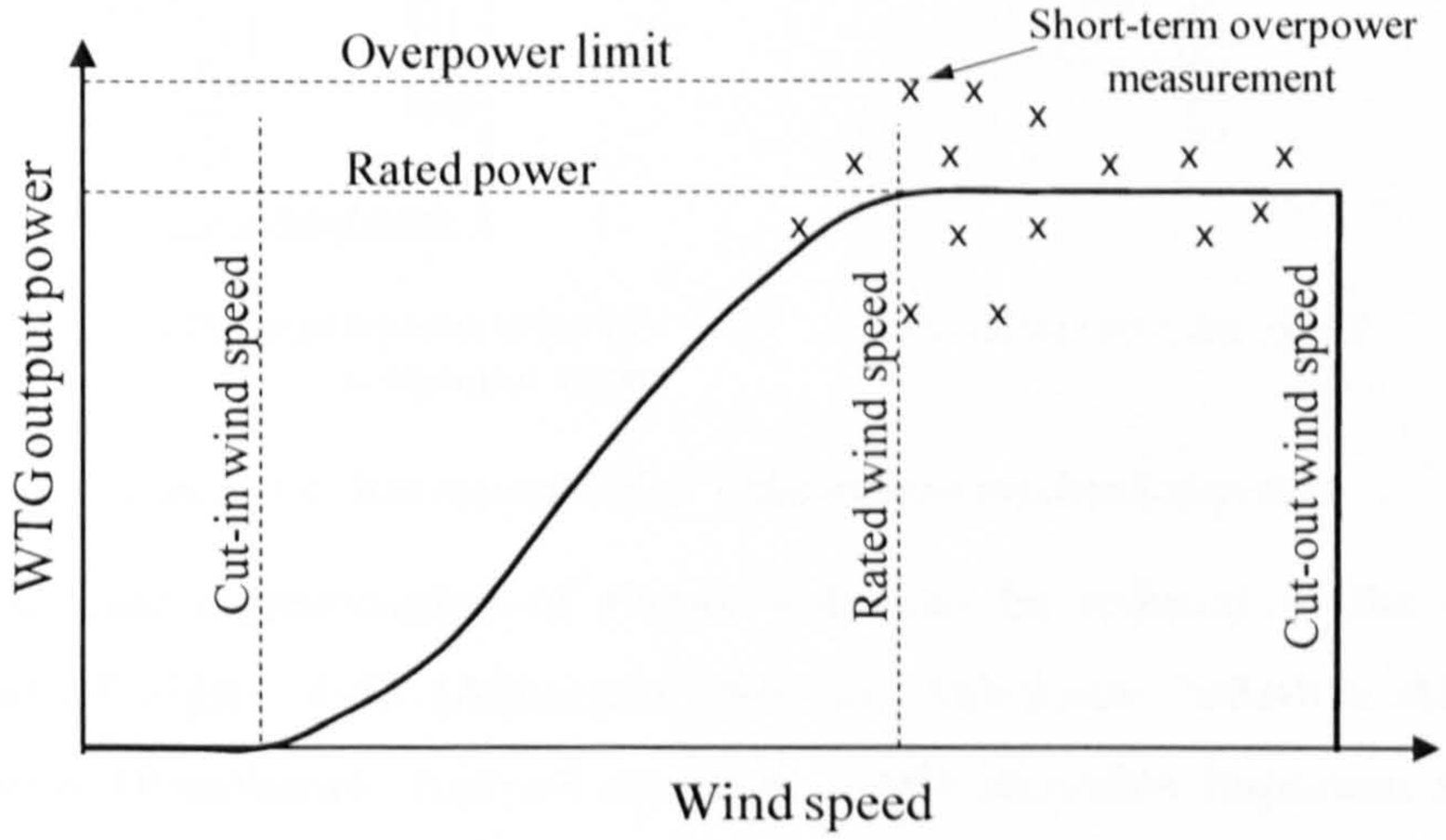

Figure 4-3: Wind turbine power curve

Unsteady aerodynamic flow conditions including *tower shadow and dynamic stall* (Manwell, McGowan et al. 2002, p136) give rise to substantial "*continuous operating*" power fluctuations (IEC 2001). These fluctuations, shown as crosses in Figure 4-3, are relevant to FRT because they can coincide with the fault events and therefore represent worst-case drive-train acceleration scenarios. IEC 61400-21 requires measurement of maximum wind turbine electrical power output over three averaging periods, 600s, 60s and 0.2s. Typical values for the 60s and 0.2s periods for multi-megawatt FSWTs are 1.05 and 1.4pu respectively. Since this Thesis is concerned with fault periods of the order of one second, an interpolated overpower level of 1.2pu is selected for a single WTG.

Unsteady-flow is also induced by the blade pitching associated with active power ramping (Snel and Schepers 1995; Akhmatov 2003(b); Akhmatov 2005(b)). However, this can be neglected in this Thesis because the FRT analysis compares the worst-case performance of FSWTs without the aid of power reduction.

4.4. Mechanical System Modelling

4.4.1. Multi-mass representation

The mechanical system of a wind turbine is shown in Figure 4-4.

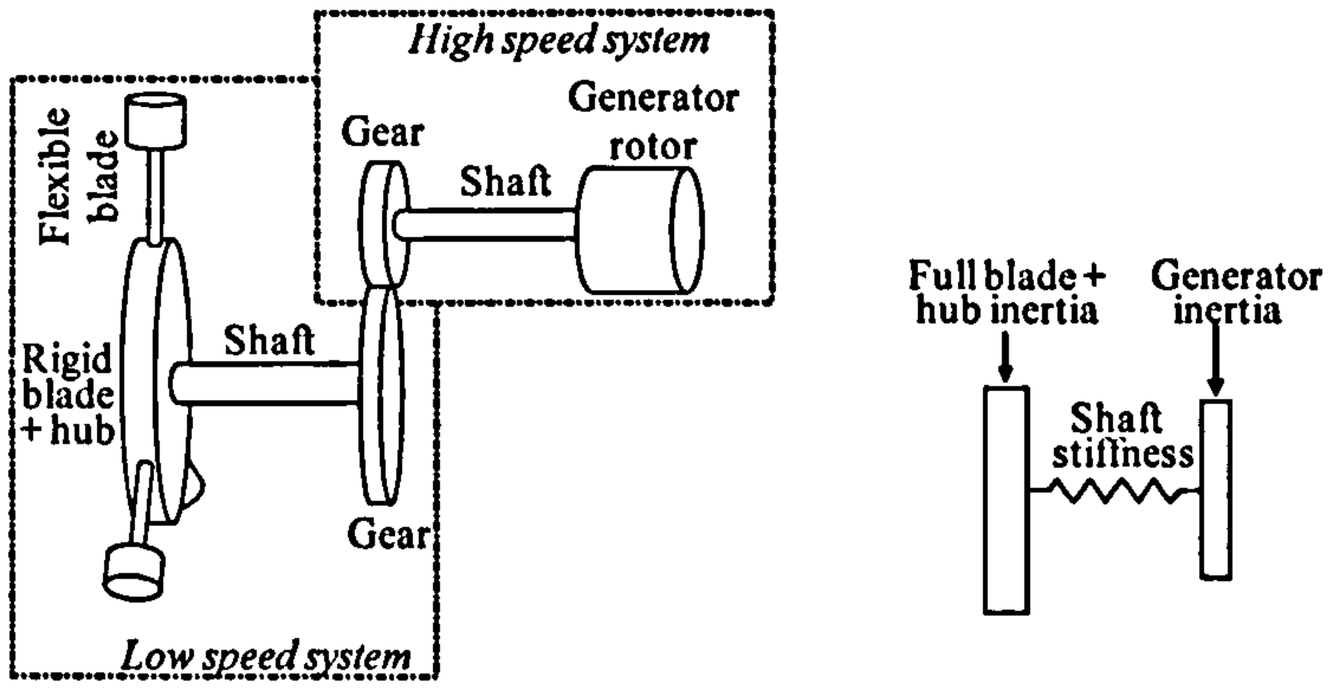

a. Physical representation of mechanical system

b. Equivalent two-mass model

Figure 4-4: Representation of wind turbine mechanical system

The multi-mass representation of Figure 4-4a can be reduced to the two-mass equivalent of Figure 4-4b (Akhmatov 2003(a); Akhmatov 2003(b)). Although a recent paper (Ramtharan, Anaya-Lara et al. 2006) identifies important secondary

oscillations using the three-mass model[4], the two-mass model is adequate for comparing the FRT technologies in this Thesis.

4.4.2. Drive-train inertia

There is significant divergence of opinion on typical inertia, J, for multi-megawatt wind turbines (Knudsen and Nielsen 2005; Morren, de Haan et al. 2006). In Figure 4-5, manufacturers' inertia data is plotted against machine rating for a small number of anonymous commercial WTGs (based on confidential information).

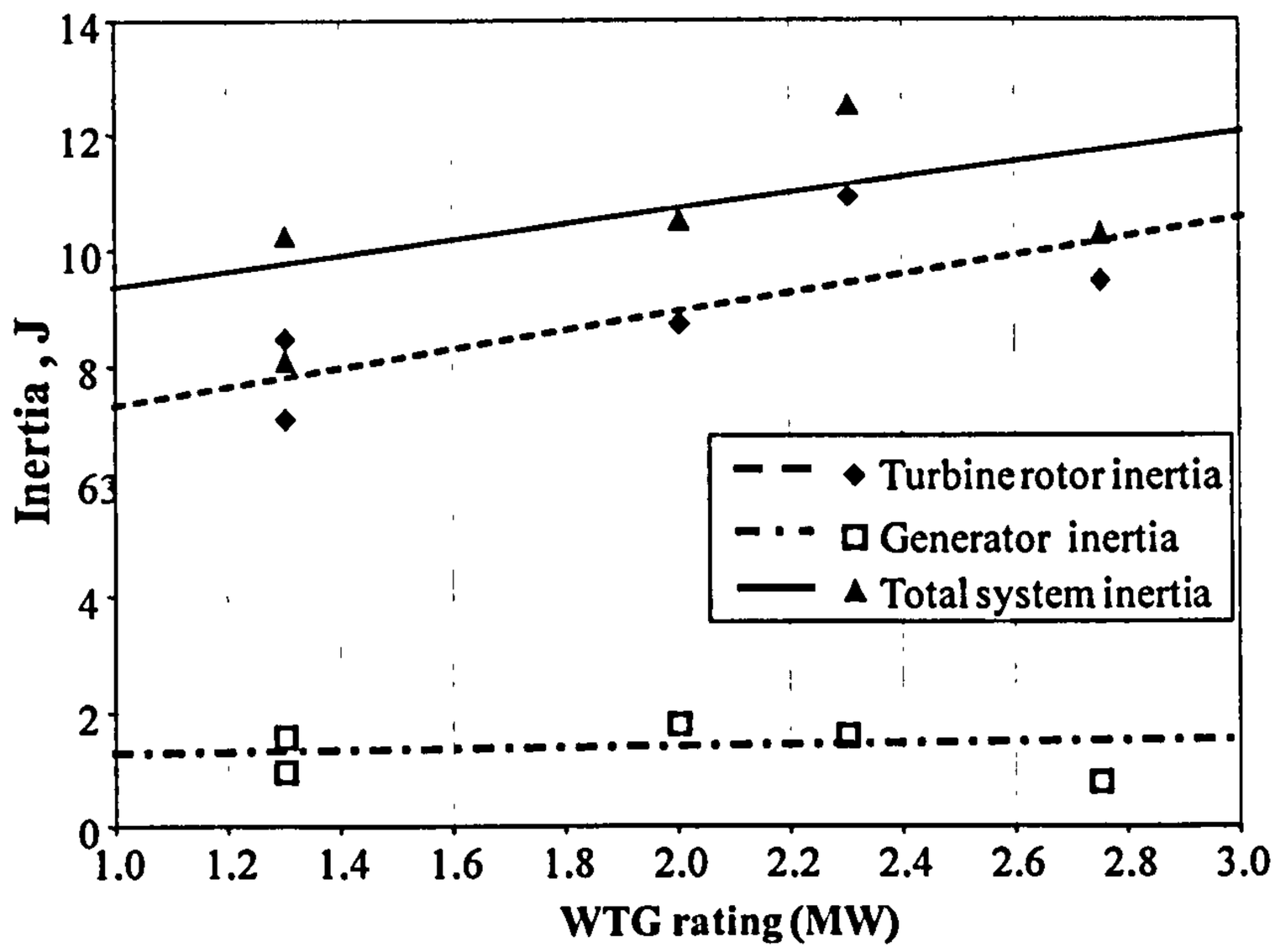

Figure 4-5: Mechanical system inertia from manufacturers' data

With reference to Figure 4-5, it is reasonable to assume turbine and generator rotor per unit inertias, J_t and J_g, of 8.0s and 1.0s respectively for analysis in this Thesis.

4.4.3. Drive-train stiffness

A distinctive characteristic of the FSWT drive-train is its low coupling stiffness, typically in the range 0.3 to 0.6 pu, using the *conventional* pu system, (Knudsen and Nielsen 2005) compared to values 30 to 100 greater for conventional plant such as steam turbine generators (Hinrichsen and Nolan 1982). This feature, combined with low generator rotor inertia, results in significant slip oscillations following electrical system disturbances. In view of the sensitivity of induction machine torque, current and power factor to slip, these oscillations have significant impact on the wind

---

[4] The third mass is formed to take account of the significant flexibility and inertia of the rotor blades

turbine's response and stability (Akhmatov 2005(b), Section 4.3.4). For the purpose of this Thesis a base case stiffness, K_c, of 0.45pu on conventional base has been selected (equivalent to 140pu on the unity time base used in this Thesis and described in Appendix A).

4.4.4. Drive-train damping

The turbine and generator friction coefficients, B_t and B_g, due to windage and bearing friction are set to zero because of its minimal significance for FSWT FRT studies. This is because the selected power input already takes account of friction at operating speed and speed variations during FRT are relatively small (<10%).

4.4.5. Transient modelling

In light of preceding sections, the transient model of a wind turbine can be reduced to a constant power input to a two-mass drive train. Constant *power* is chosen as the aerodynamic input in favour of constant *torque* in order to improve numerical stability and better reflect the physical behaviour of most wind turbines (Knudsen and Nielsen 2005). The transient response of this system can be simulated using

State Equations 4-1 to 4-4:

Input: $$\tau_{in} = \frac{P_{in}}{\omega_t} \quad (4\text{-}1)$$

Coupling: $$\omega_t - \omega_g = B_c \tau_c + \frac{1}{K_c}\frac{d\tau_c}{dt} \quad (4\text{-}2)$$

Turbine shaft: $$\tau_{in} - \tau_c = B_t \omega_t + J_t \frac{d\omega_t}{dt} \quad (4\text{-}3)$$

Generator shaft: $$\tau_c - \tau_e = B_g \omega_g + J_g \frac{d\omega_g}{dt} \quad (4\text{-}4)$$

Where P_{in} is input mechanical power, ω_t *and* ω_g are turbine and generator angular velocities respectively, τ_{in} τ_e *and* τ_c are mechanical input, electrical and coupling torque respectively and B_c is an intangible coupling "slip" parameter used only for numerical stability and set to 10-4 (sufficient for numerical stability but without affecting accuracy)

The equations are solved in Matlab-Simulink using the block model of Figure 4-6.

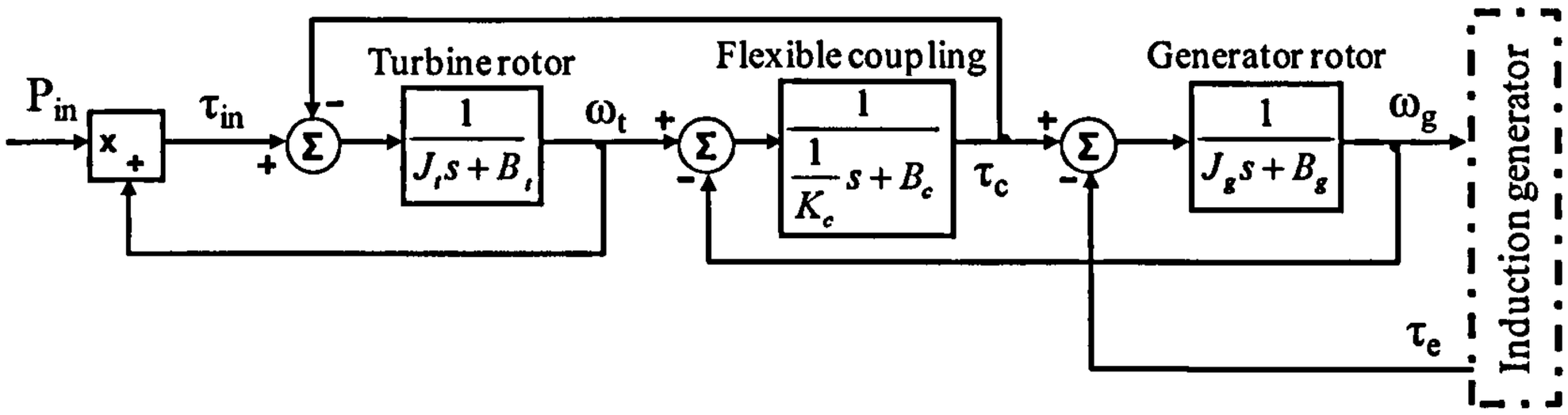

Figure 4-6: Block model of mechanical system

4.5. Generator System Modelling

4.5.1. Impedance

Multi-megawatt FSWTGs are generally squirrel-cage induction machines. Pu values of stator and rotor resistance (R_s and R_r), leakage inductance (L_{sl} and L_{rl}), and magnetising inductance (L_m) vary widely but some relevant values are quantified in Table 4-1.

	R_s	R_r	$\omega_s L_{sl}$	$\omega_s L_{rl}$	$\omega_s L_m$
Generic (Akhmatov 2005(b)))	0.01	0.005	0.12	0.20	5.0
Nordex N60 (1.3MW)	0.0060	0.0083	0.135	0.057	3.75
Siemens 1.3MW	0.0060	0.0057	0.12	0.096	3.71
Selected	0.0060	0.007	0.14	0.050	3.0

Table 4-1: Multi-megawatt FSWTG impedances (on MW rating base)

Table 4-1 shows generic pu impedance values, those of two commercially available FSWTs and those selected for analysis in the Thesis. The sensitivity of the stability to this selection is assessed in Chapters 5 and 6.

4.5.2. Shunt capacitance

Modern grid codes require wind farms to be capable of exporting reactive power, typically with a power factor of 0.95, measured at the *grid entry point,* with rated power output 95% grid voltage (EirGrid 2007, Figure WFPS1.4; National Grid Electricity Transmission (NGET) 2007, Clause 6.3.2c). The total capacitive compensation required to meet this steady-state condition is referred to as *base-case* compensation in this Thesis. A base-case compensation of 1.0 p.u is required for the selected generator of Table 4-1 and the selected electrical network of Section 4.6.

Additional compensation is termed *dynamic* since its purpose is to meet the dynamic requirements of FRT.

4.5.3. Saturation

The modelling of stator and rotor iron saturation is detailed by (Kundur 1993) and reviewed in (Akhmatov 2005(b), Sections 4.2.7 and 4.3.2.3). The conclusion of Akhamatov, with reference to studies by (Sorensen, Hansen et al. 2003), is that *"saturation effects in induction generators are not relevant in investigation of short-term stability"*. Saturation has therefore not been modelled in this Thesis.

4.5.4. Protection

Wind turbines and associated wind farm infrastructure are equipped with electrical relays and circuit breakers designed to protect the electrical equipment. This is an extensive subject covered in various texts (Jenkins, Allan et al. 2000). Their relevance to this Thesis is that these same relays must now be immune to tripping during FRT events. The principal changes required to ensure such immunity relate to undervoltage and overcurrent protection. Changes need to be carefully considered to ensure that the protective function is not compromised but my experience with one commercial FSWT and my wider judgement is that these changes can be accommodated.

Protection devices are not modelled in this Thesis because they introduce unnecessary complexity given low probability of them be the limiting factor for FRT.

4.5.5. Steady-state modelling

Steady-state modelling is performed with the conventional equivalent circuit of a squirrel-cage induction machine, as shown in Figure 4-7.

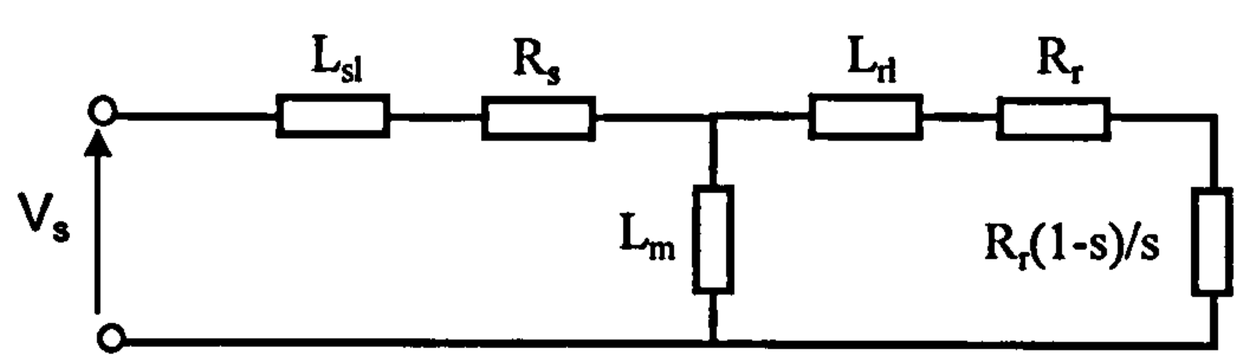

Figure 4-7: Equivalent circuit diagram of induction generator (where s = slip)

4.5.6. Transient modelling

The transient model of the induction generator is the space vector representation of electrical quantities with the *State Equations* 4-5 to 4-9 in the stator reference frame.

Stator flux linkage: $$\bar{\lambda}_s = L_m \bar{i}_r + L_s \bar{i}_s \quad (4\text{-}5)$$

Rotor flux linkage: $$\bar{\lambda}_r = L_m \bar{i}_s + L_r \bar{i}_r \quad (4\text{-}6)$$

Stator side voltage: $$\bar{v}_s = R_s \bar{i}_s + \frac{d\bar{\lambda}_s}{dt} \quad (4\text{-}7)$$

Rotor side voltage: $$\bar{v}_r = R_r \bar{i}_r + \frac{d\bar{\lambda}_r}{dt} - \omega_g \omega_b M \bar{\lambda}_r = 0 \quad (4\text{-}8)$$

Rotor torque: $$\tau_e = \omega_b L_m \bar{i}_s \otimes \bar{i}_r \quad (4\text{-}9)$$

where:

$L_s = L_m + L_{sl}$ and $L_r = L_m + L_{rl}$,

$\bar{i}_r$ *and* $\bar{i}_s$ are rotor and stator space vector currents respectively,

M is a 90^o rotation matrix and ω_g is generator angular velocity.

The symbol $\otimes$ in Equation 4-9 is the cross product. Equations 4-5 to 4-8 are represented by the transfer block model of Figure 4-8:

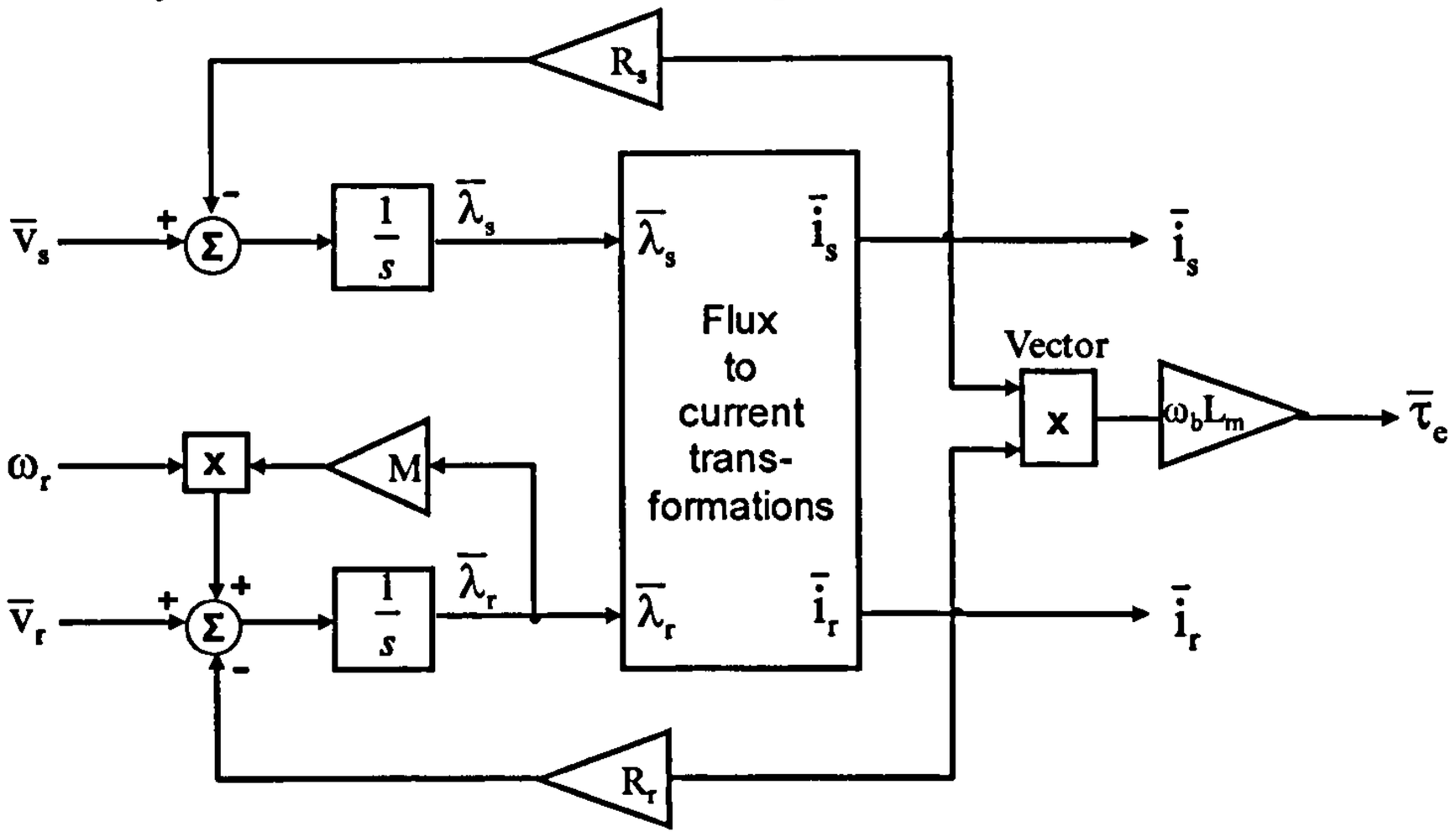

Figure 4-8: Block model of induction generator

Where the flux to current transformations are given by Eq. 4-10 to 4-12:

$$A = L_m L_{sl} + L_m L_{rl} + L_{sl} L_{rl} \quad (4\text{-}10)$$

$$\bar{i}_s = \bar{\lambda}_s \frac{L_r}{A} - \bar{\lambda}_r \frac{L_m}{A} \quad (4\text{-}11)$$

$$\bar{i}_r = \bar{\lambda}_r \frac{L_s}{A} - \bar{\lambda}_s \frac{L_m}{A} \quad (4\text{-}12)$$

4.6. Electrical Network Modelling

This Section uses the representative electrical network topology of Section 4.2.

4.6.1. Transformers

The representative wind farm system includes three transformations between the FSWT and the supergrid. The steady-state and dynamic response of each transformer is determined primarily by its impedances. The full model of a transformer is identical to the induction generator model of Section 4.5 with zero rotor speed. However, because of the very high magnitude of magnetising inductance (typically >100pu), it is common to reduce the transformer model to series inductance and resistance. This reduced representation is used in Chapters 5 and 6. Typical ranges of these parameters are shown in Table 4-2.

Transformer	Typical rating (MVA)	Reactance	Resistance
Turbine	1-4	0.06-0.08	0.07-0.1
Wind farm	30-150	0.1-0.2	0.05-0.08
Super-grid	500-2000	0.2	0.05-0.06

Table 4-2: Typical transformer impedances (on MVA rating base)

4.6.2. Wires

The representative wind farm includes low voltage (LV) cables at each wind turbine, medium voltage (MV) cables between the turbine transformers and the wind farm substation and high voltage (HV) overhead lines and/or cables from the wind farm substation to the super-grid substation. Cables and lines comprise series reactance and resistance and shunt capacitance. However, the effect of shunt capacitance on comparative dynamic studies is small is therefore neglected in this Thesis.

Typical series pu reactance and resistance values are given in Table 4-3.

Wiring system	Reactance	Resistance
LV cables	<0.005	<0.005
MV cables	0.01	0.01
HV overhead line	0.02	0.005
Total	0.05	0.02

Table 4-3: Typical cable and line impedances (pu on wind farm MW rating base)

4.6.3. Wind farm dRPC

TSC is used as the primary dRPC through-out this Thesis. However, a simple STATCOM model is also described below and used in Chapter 3 to compare its performance with TSC.

4.6.4. TSC

TSC is modelled as fixed shunt capacitance connected directly to the wind farm system without the inclusion of an interposing transformer. TSC capacitance, C_{dRPC}, is controlled between minimum and maximum capacity, C_{min} and C_{max}, using the control system of Figure 4-9.

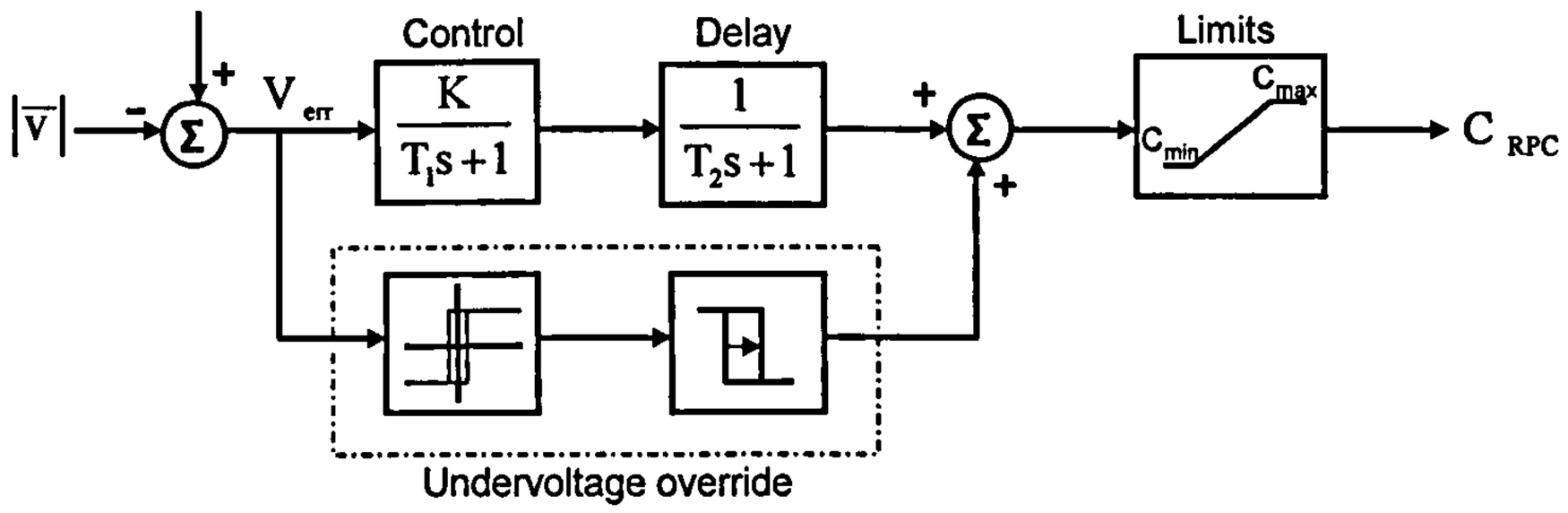

Figure 4-9: TSC controller

The gain, K, and time constants, T_1 and T_2, in Figure 4-9 are optimised in Chapter 6. The undervoltage override allows the TSC to step up to its maximum capacitive output within 20ms on fault inception.

4.6.5. STATCOM

The simple STATCOM model used for comparative purpose in Chapter 3 is identical to TSC except for the addition of a voltage magnitude term which transforms its steady-state reactive response from proportionality with voltage squared to proportionality with voltage, as shown in Eq. 4-13.

$$\bar{i}_{in} - \bar{i}_{out} = \frac{1}{R}\bar{v}_c + \frac{C}{|\bar{v}|}\frac{d\bar{v}_c}{dt} \qquad (4\text{-}13)$$

Where R is shunt resistance and $|\bar{v}|$ is the magnitude of space vector voltage, $\bar{v}_c$, across the capacitor.

4.6.6. sDBR

The selected configuration and location of sDBR selected for further detailed analysis is the single-stage resistor at the wind farm substation (Ba), as shown in Chapter 3, Figure 3-12. A medium circuit breaker is assumed as the switching device, with a total opening time of 80ms.

4.6.7. Transient modelling

The reduced electrical network is shown schematically in Figure 4-10.

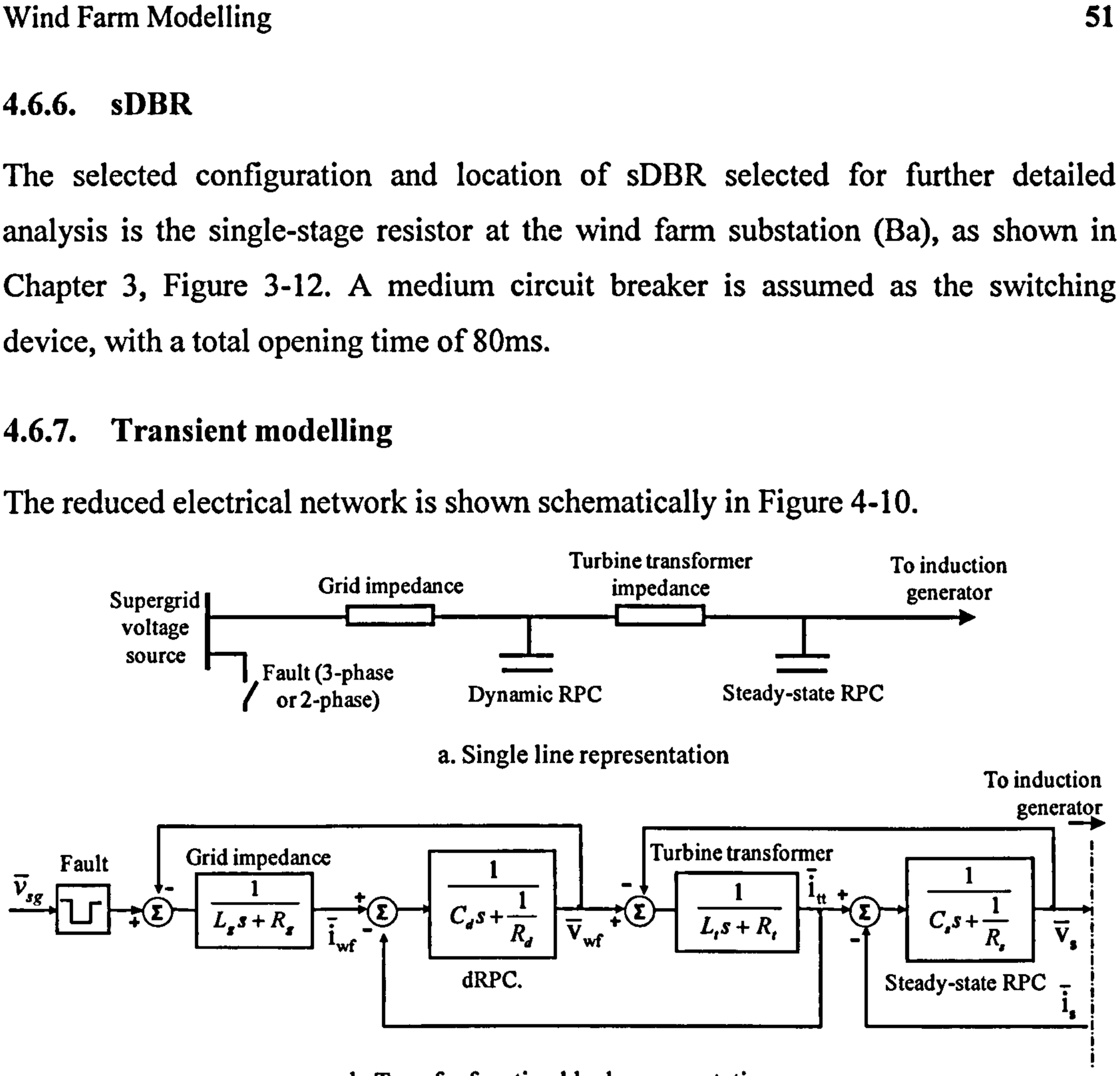

Figure 4-10: Basic electrical network in single line and transfer block diagram forms

The state equations and associated transfer functions for impedance and RPC are analogous to inertia and coupling respectively of Section 4.4.5. The supergrid voltage, $\bar{v}_{sg}$, is a unit space vector rotating at synchronous speed. The fault block of Figure 4-10b applies time-sequence multipliers to modify the vector according to the required fault scenario. For balanced faults, the multiplier reduces the vector magnitude symmetrically whereas for phase to phase short-circuit faults, the multiplier is applied only to the q-axis of vector space, reducing the voltage trajectory to a straight line. sDBR is inserted by simply adding the braking resistor magnitude to the grid resistance parameter during the insertion period.

4.7. Model Reduction

Previous Sections have defined suitable models and parameters for each component of the wind farm system. A typical large wind farm may comprise 50 wind turbines.

It would be unreasonable to apply a 50-turbine model for analysis of a power system. The objective of this Section is therefore to reduce the complexity of the wind farm system by justifying the use of lumped equivalents.

4.7.1. Circuit reduction

A typical wind farm comprises N identical WTGs connected in parallel via differing lengths of MV cables, as represented by the equivalent circuit of Figure 4-11a.

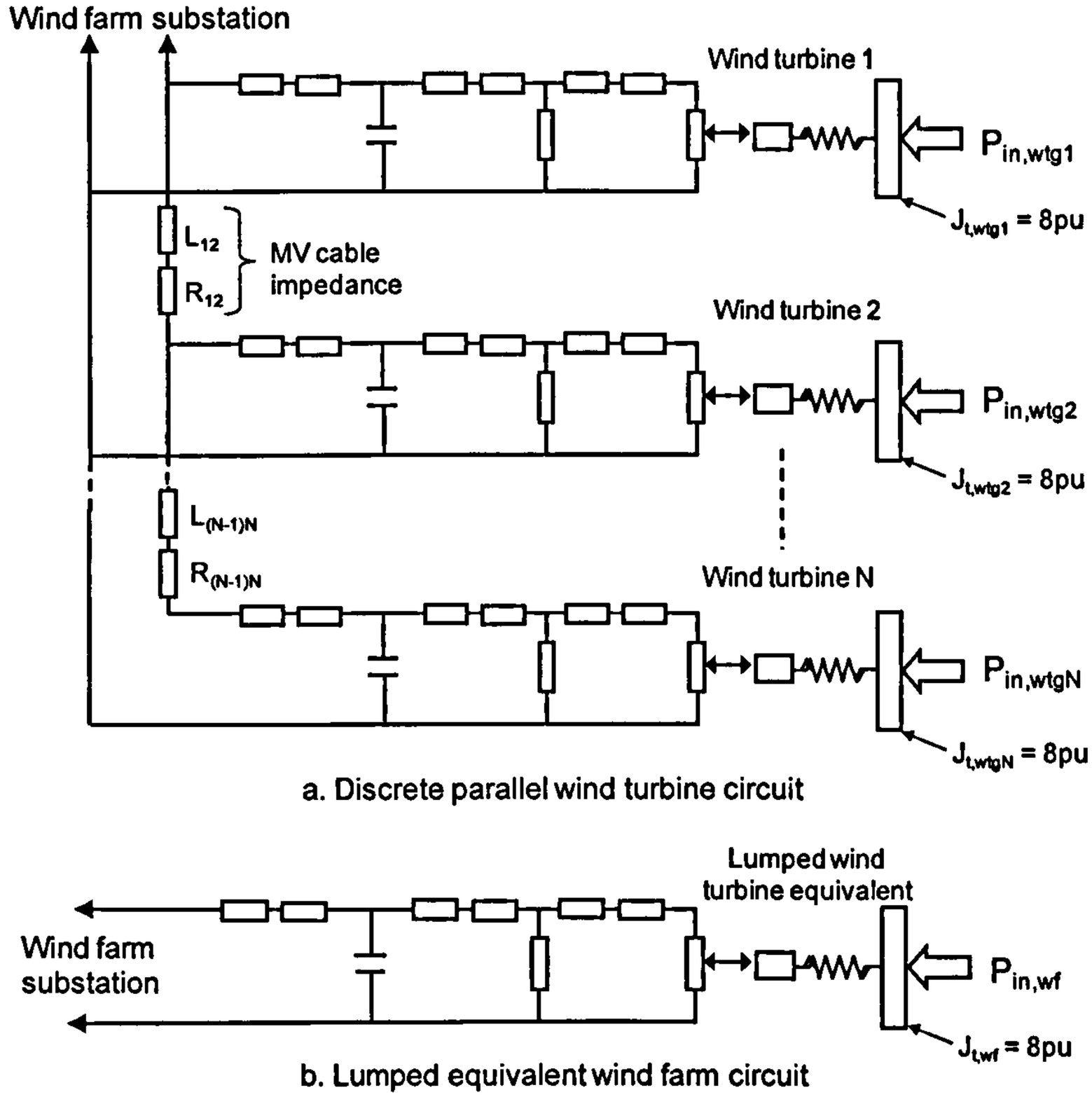

Figure 4-11: Reduction of N-wind turbine circuit to equivalent wind farm circuit

From basic circuit theory, N identical parallel sub-systems with parameters defined in pu on the sub-system rating base can be substituted by a single equivalent system with the same pu values on a base N times the sub-system base. In order to reduce the wind farm system in this manner, as shown in Figure 4-11, it is necessary to justify that any differences between the parallel wind turbines sub-systems are small enough to prevent significant reduction error.

The first dissimilarity is that effective MV cable impedance is different for each turbine, as illustrated by Figure 4-11. However, the total magnitude of cable impedance is typically about 0.01pu compared to turbine transformer impedance of

0.06pu and total generator impedance of nearly 0.2pu. The discrepancy is therefore very small in the context of the overall sub-system and can reasonably be neglected.

The second dissimilarity is that input power, Pin, varies significantly across a wind farm in the FRT time-frame. With reference to Section 4.3, it is possible for 0.2-second averaged power to vary between about 0.7pu and 1.4pu. Since a FRT compliance criterion is that all turbines must remain connected, it is not possible to confirm compliance using only the wind farm equivalent. However, the wind farm equivalent alone is sufficient to achieve the objective of this Thesis, namely to assess the comparative performance and sensitivities of FRT technologies.

4.7.2. Aggregation of overpower

An important feature of the short-term overpower of individual WTGs is that it does not occur simultaneously across a wind farm site. This *independence* gives rise to substantial smoothing over a large wind farm, as applied to flicker (Jenkins, Allan et al. 2000, Section 5.1). Equation 4-14 quantifies the smoothing of wind farm overpower, $P_{in,wf}$, for a site comprising N WTGs with individual overpower, $P_{in,wtg}$.

$$P_{in,wf} = 1 + \frac{P_{in,wtg} - 1}{\sqrt{N}} \qquad (4\text{-}14)$$

Given that this Thesis covers wind farms in the range 30-150MW, a reasonable minimum number of turbines is 15. Substituting N=15 and the worst-case single-WTG overpower, $P_{in,wtg}$, from Section 4.3, into Eq. 4-14 gives an overpower of 1.05pu, as used for analysis in the remainder of this Thesis.

4.8. Full Model

Figure 4-12 and Table 4-4 show the reduced wind farm system and the parameter values selected for steady-state and transient analysis in Chapters 5 and 6.

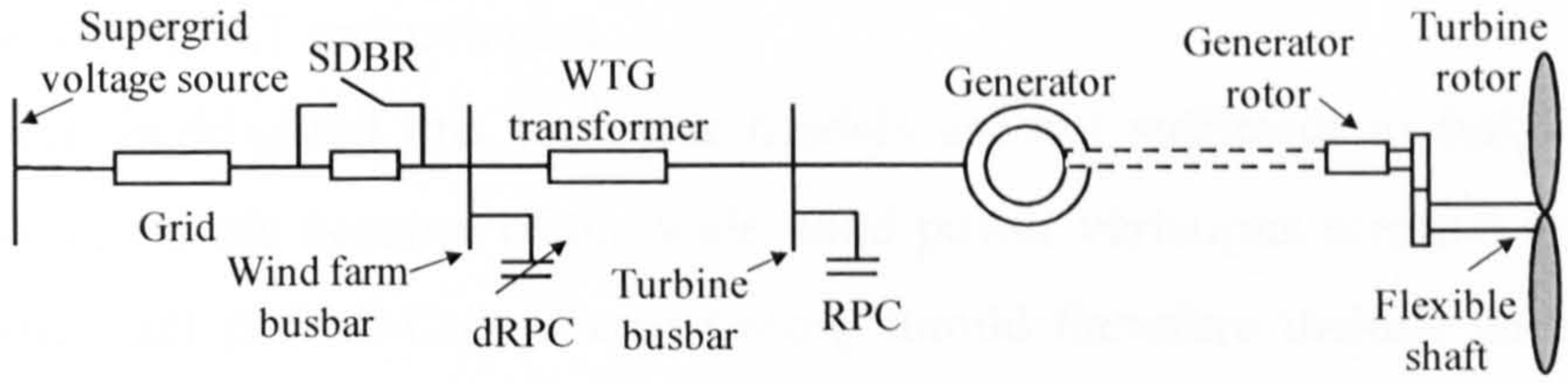

a. Single line representation of reduced wind farm model

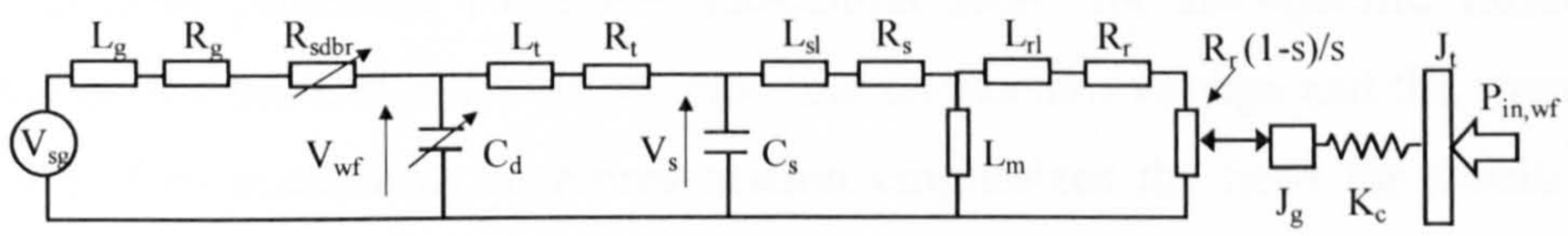

b. Equivalent circuit representation of reduced wind farm model

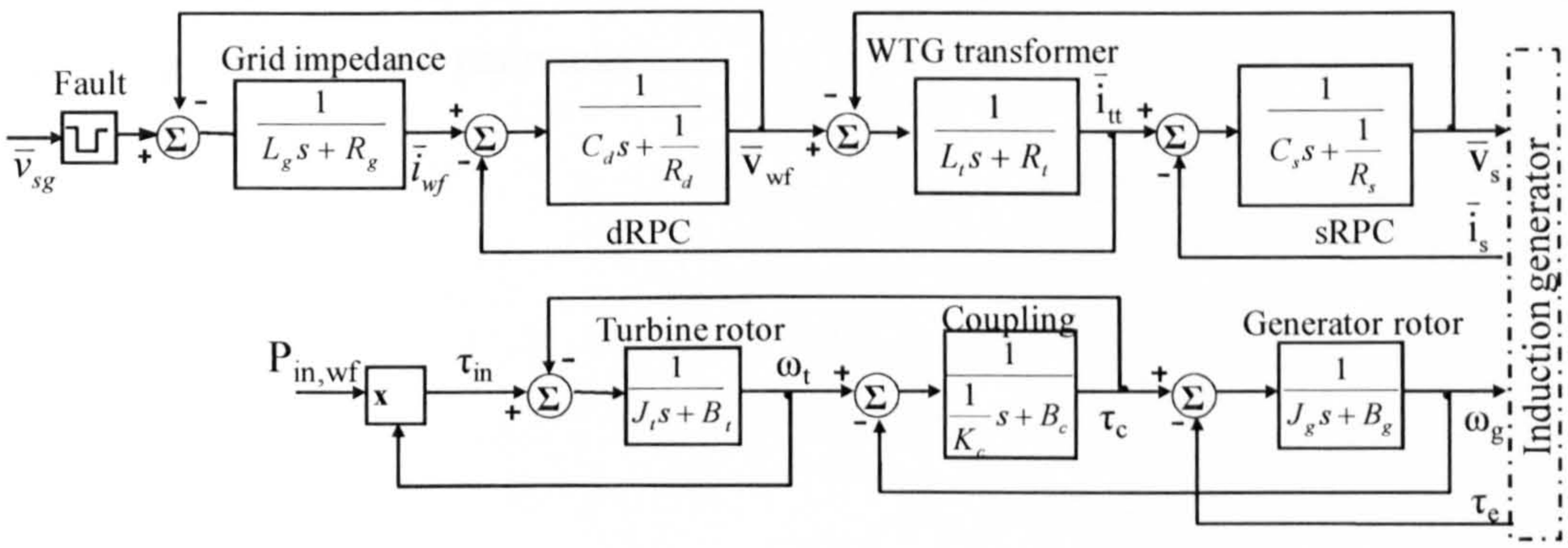

c. Block diagram of reduced transient wind farm model

Figure 4-12: Representations of wind farm system

Elec. parameter	Sub-script	X	R	Mech.parameter	Ref	J	B
Grid	g	0.13	0.02	Gen rotor	g	1	0
Dynamic RPC	d	tbc	0	Drive coupling	c	140	10^{-4}
WTG transformer	t	0.07	0.02	Turbine rotor	t	8	0
Steady-state RPC	s	-1.0	10^3	Note: Values of X are given which are equivalent to $\omega_b L$ where ω_b s synchronous speed (314 rad/s)			
Gen stator (leakage)	s(l)	0.14	0.006				
Gen rotor (leakage)	r(l)	0.05	0.007				
Gen magnetisation	m	3.0	0				

Table 4-4: Selected wind farm parameters (pu on WF rating base)

4.9. Summary

This chapter has defined a representative wind farm system and derived reduced steady-state and transient models with sufficient accuracy for comparing the performance of FRT technologies.

It has been highlighted that the same models are not sufficient to fully test FRT compliance, mainly because of the wide wind power variations across a typical site during the fault period. Compliance testing should therefore include an additional sub-model for a WTG under worst-case overpower conditions.

Each wind farm parameter value has substantial scope for site-specific variation depending on the particular WTGs selected, the connection voltage and the strength of the grid. This uncertainty in representation emphasizes the need for sensitivity analysis, as carried out in Chapters 5 and 6, to ensure that the extent of beneficial effect or comparative advantage of a FRT technology is not limited to a relatively small range of base-case parameters.

5. Steady-State Characterisation

5.1. Introduction

This Chapter uses the equivalent circuit derived in Chapter 4 to characterise the steady-state behaviour of a representative wind farm and thereby infer the comparative FRT performance of dRPC and sDBR technologies.

Steady-state stability analysis of induction generators is well established in determining the stability limit for FSWT wind farms operating for short periods of seconds or minutes at reduced grid voltages (Holdsworth, Jenkins et al. 2001). For an event of this duration, the system could be assumed reach a new steady-state operating point during the voltage dip. An extension of this technique to dynamic stability is presented by Akhmatov (Akhmatov, Knudsen et al. 2000; Akhmatov 2003(a)) and applied to FSWTs. This extended approach is assessed comprehensively and justified in Appendix B and designated *quasi-steady-state (QSS) analysis*. Although *QSS analysis* does not provide a precise prediction of FRT performance it does identify the underlying characteristics of FSWT stability and facilitate comparison of FRT techniques. It also allows extensive sensitivity analysis without the laborious process of carrying out a large number of transient simulations.

5.2. QSS Methodology

QSS is described in detail in Appendix B and it is recommended that the reader refers to the Appendix to become familiar with this technique. Given its importance for this Chapter, this section also provides an introductory summary of QSS methodology.

The starting assumption for QSS analysis is that the dynamic process can be approximated as two QSS stages, described as *fault* and *recovery*. The voltage is assumed to be constant during each stage, and the system response can therefore be characterised with reference to two steady-state power curves. Figure 5-1a identifies five points during a generalised fault scenario that are used to trace the dynamic trajectory of the wind farm system for two inertia scenarios in Figure 5-1b.

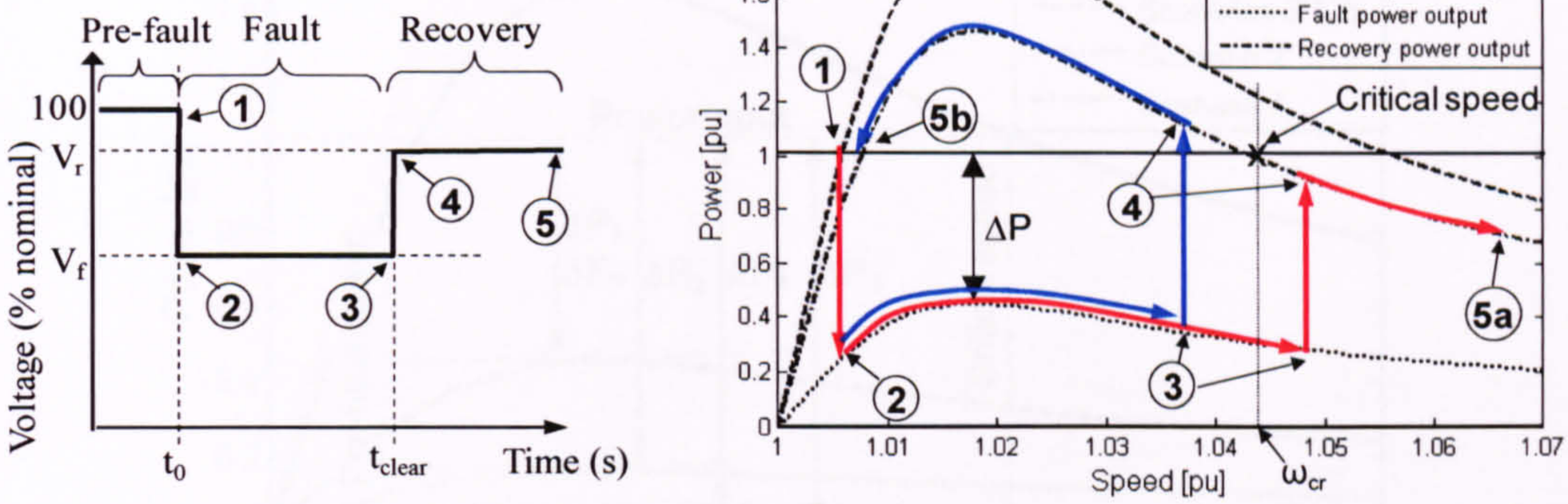

a. Grid voltage trace b. Power-speed trajectory

Figure 5-1: Quasi steady-steady response during a generalised fault scenario

Point 1 is the steady pre-fault state, lying at the intersection of the power input and pre-fault (100% voltage) power output curves of Figure 5-1b. Point 2 lies on the fault-power output curve at rated speed. The dynamic trajectory then follows the fault-power output curve as speed increases due to the net accelerating power, ΔP. At fault clearance the trajectory transfers from point 3 to point 4 on the recovery-power output curve. At point 4 the net power either causes the drive train to accelerate towards point 5a and eventually trip (red trajectory) or decelerate towards stable point 5b (blue trajectory). It can be concluded, by inspection, that the system stability limit, *critical speed*, ω_{cr} (Akhmatov 2005(b))), is at the intersection of the power input and recovery power output curves, as shown by the cross on Figure 5-1b. A characteristic critical speed can be defined for any given wind farm system (including its grid connection) at specified recovery voltage and mechanical power input.

5.3. Base-Case Stability Assessment

This Section uses QSS analysis to assess stability of the representative wind farm system of Figure 4-12 for the five balanced FRT scenarios of Figure 2-15, assuming a lumped drive train with inertia, J_r, of 9pu.

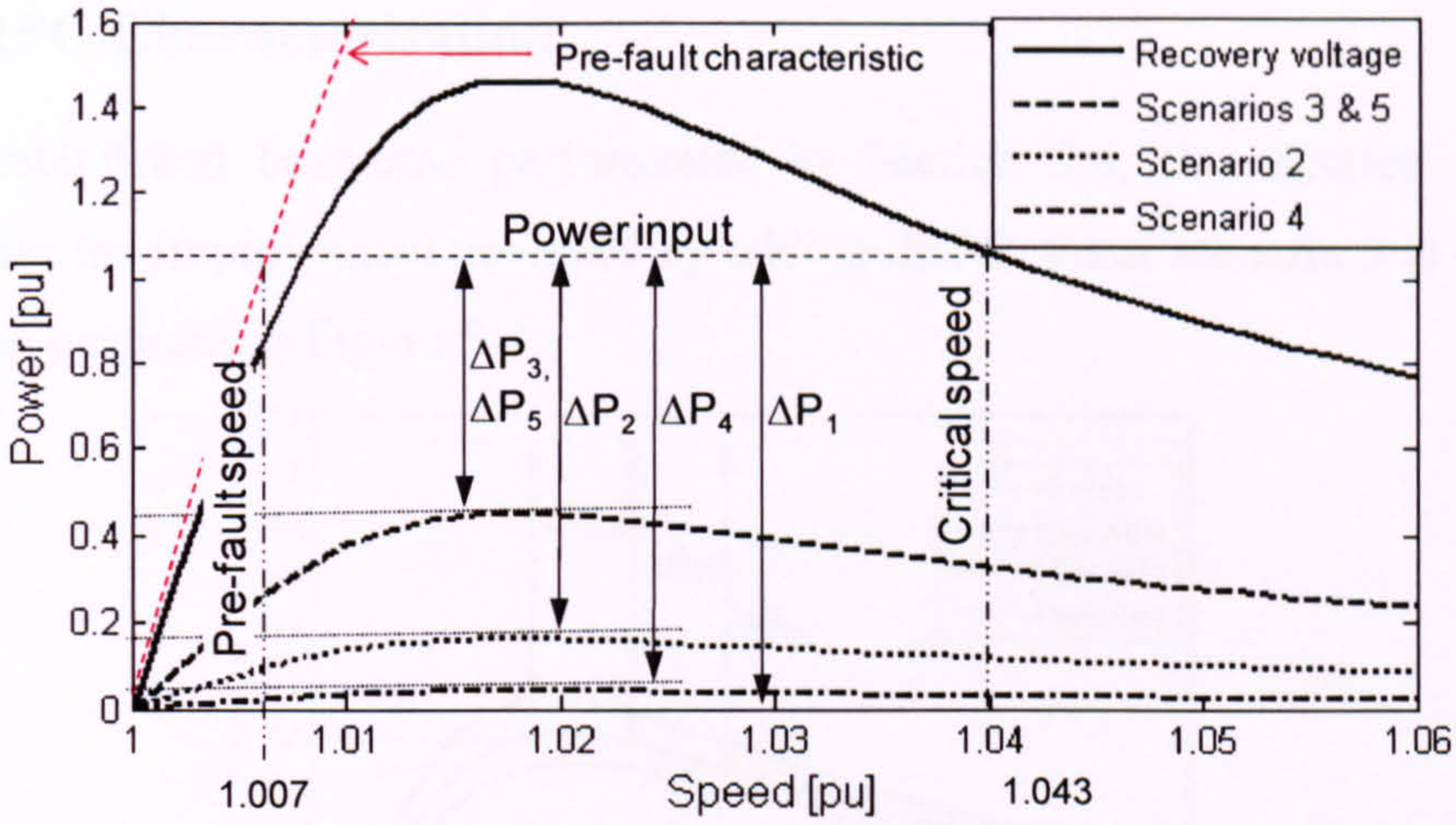

Figure 5-2: Power-speed characteristics associated with fault scenarios

The QSS stability criterion is that the rotor, starting at its pre-fault operating speed, ω_i, does not exceed the critical speed shown in Figure 5-2. The minimum accelerating power, ΔP_1 to ΔP_5, during each fault scenario is shown in Figure 5-2. The most optimistic assessment assumes this minimum accelerating power throughout the fault period, t_f. With this assumption, Eq. 5-1 is used to derive the rotor speed, ω_c, at fault clearance for each scenario.

$$\omega_c = \sqrt{\frac{2\Delta P_n t_f}{J_r} + \omega_i^2} \qquad (5\text{-}1)$$

Substituting the appropriate values into Equation 5-1 for each scenario gives the clearance speeds given in Figure 5-3.

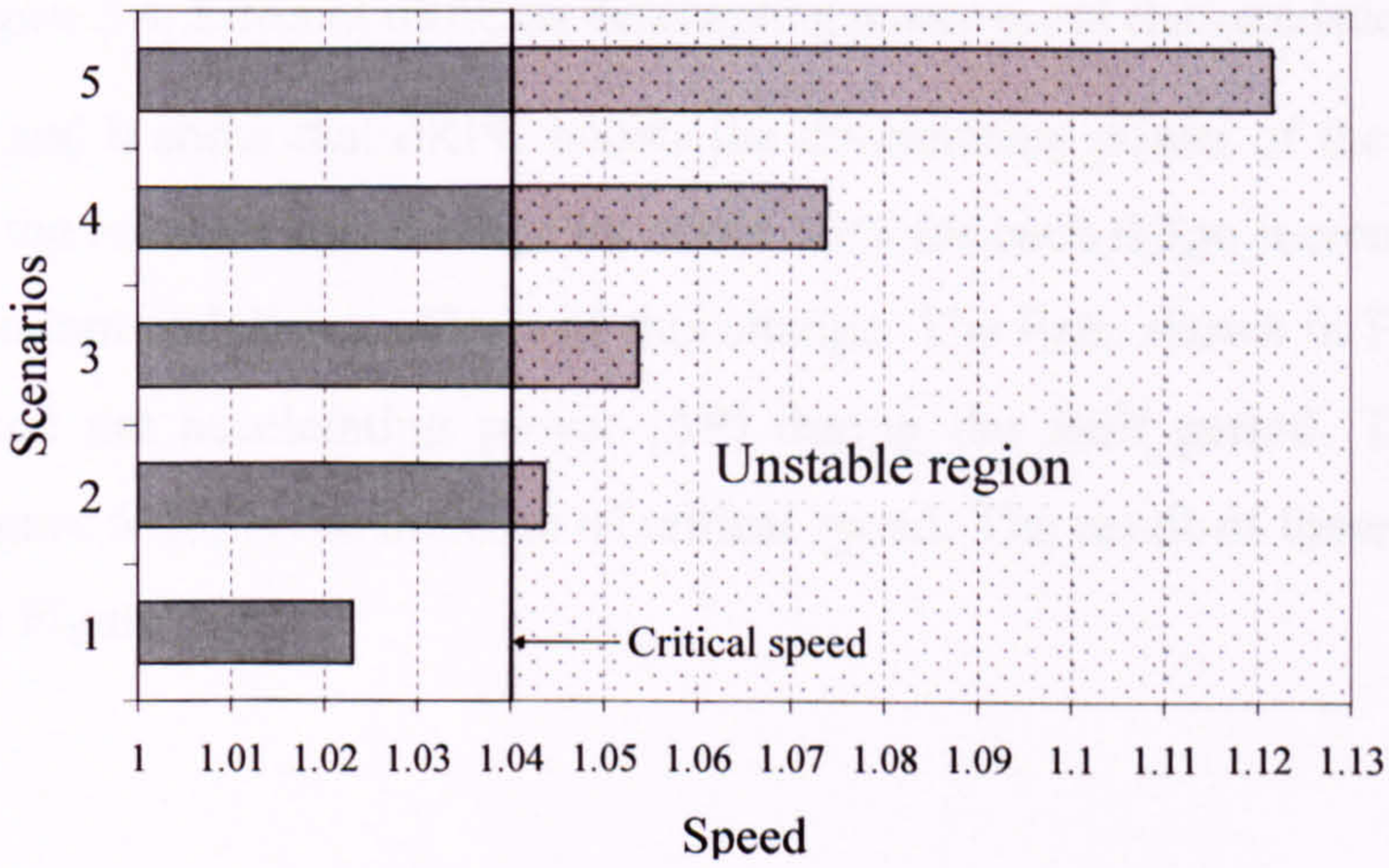

Figure 5-3: Clearance speeds and inferred stability of wind farm system for base-case

Figure 5-3 shows that the wind farm is only inferred to be stable for fault scenario 1.

5.4. dRPC Characterisation

Having established base-case performance in Section 5.3, this Section aims to characterise the improvement achieved by adding dRPC. Fault scenario 3 is used for illustration purposes in Figure 5-4.

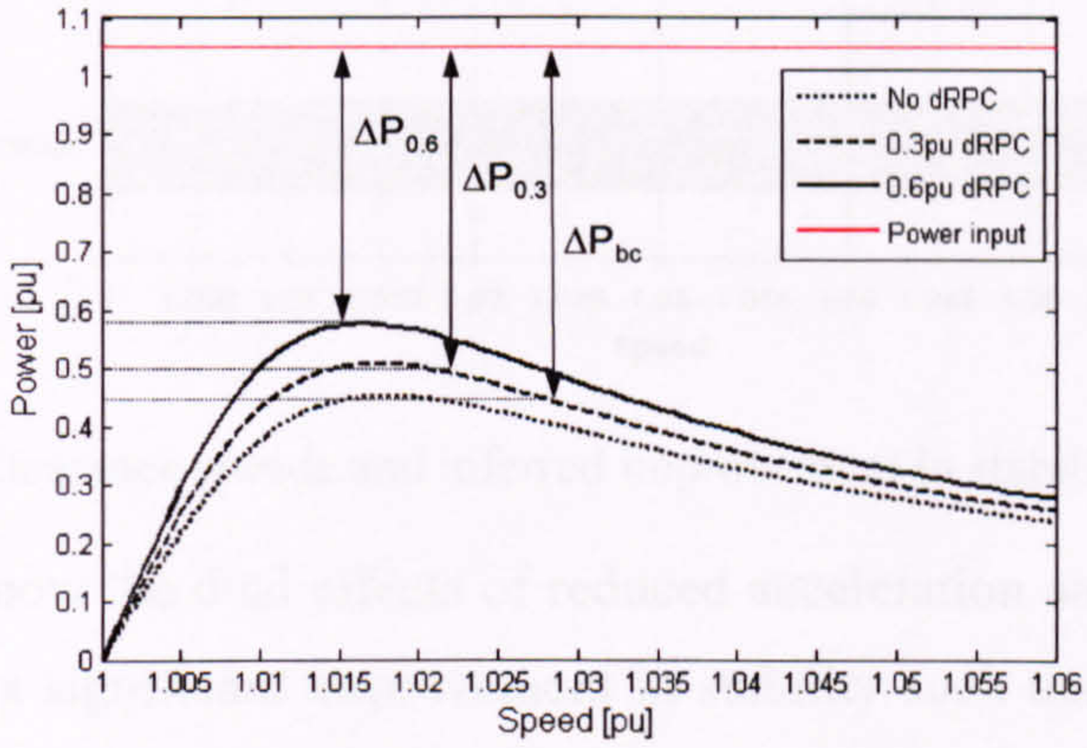

a. Effect on net accelerating power

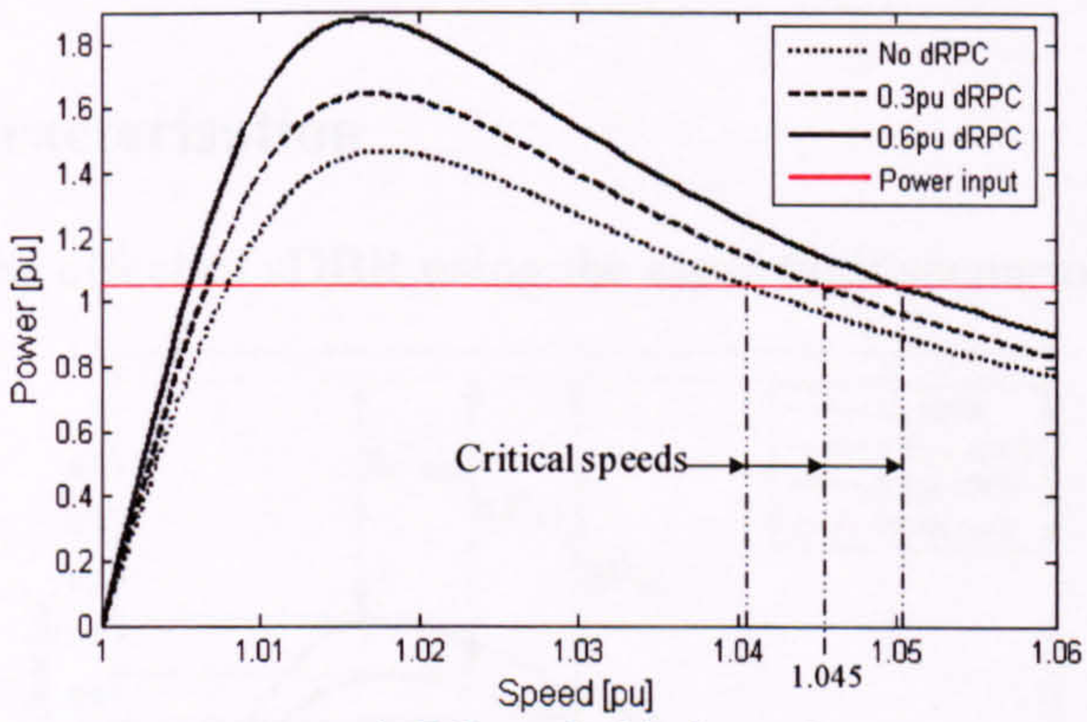

b. Effect of critical speed

Figure 5-4: Effect of dRPC on decelerating power-speed characteristics

Figure 5-4a and b show that dRPC boosts the decelerating power of the wind farm through-out the relevant speed range by about 15% for each 0.3pu increment. There are two important stabilising effects of this change. The first, shown in Figure 5-4a, is the reduced net accelerating power (ΔP) during the fault period. The second, shown in Figure 5-4b, is the increase of critical speed. The result of these changes is illustrated in Figure 5-5.

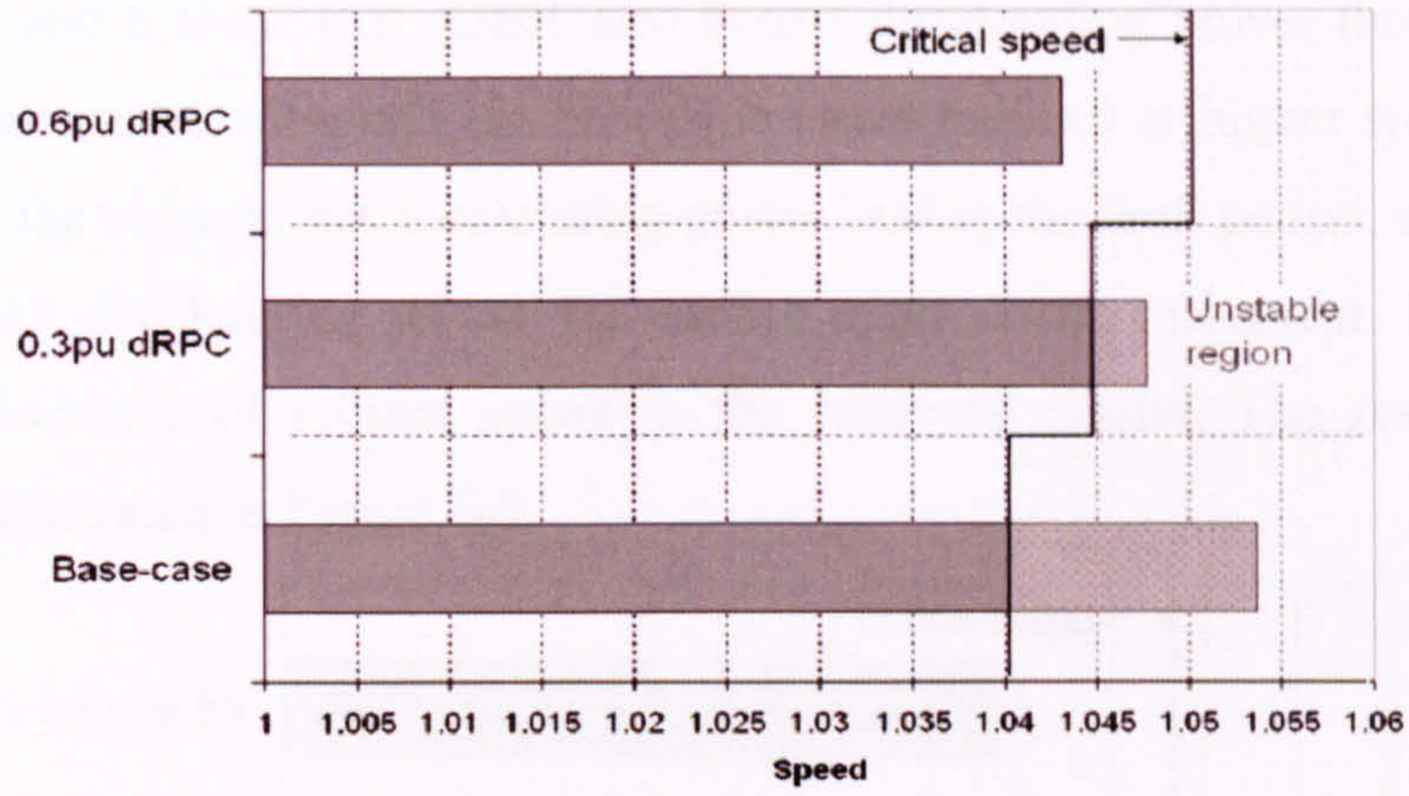

Figure 5-5: Clearance speeds and inferred improvement in stability with dRPC

Figure 5-5 shows how the dual effects of reduced acceleration and increased critical speed give rise to a significant improvement in stability such that, according to this optimistic approach, stability should be achieved with 0.6pu dRPC..

5.5. sDBR Characterisation

Figure 5-6 shows the effect of sDBR using the same fault scenario as above.

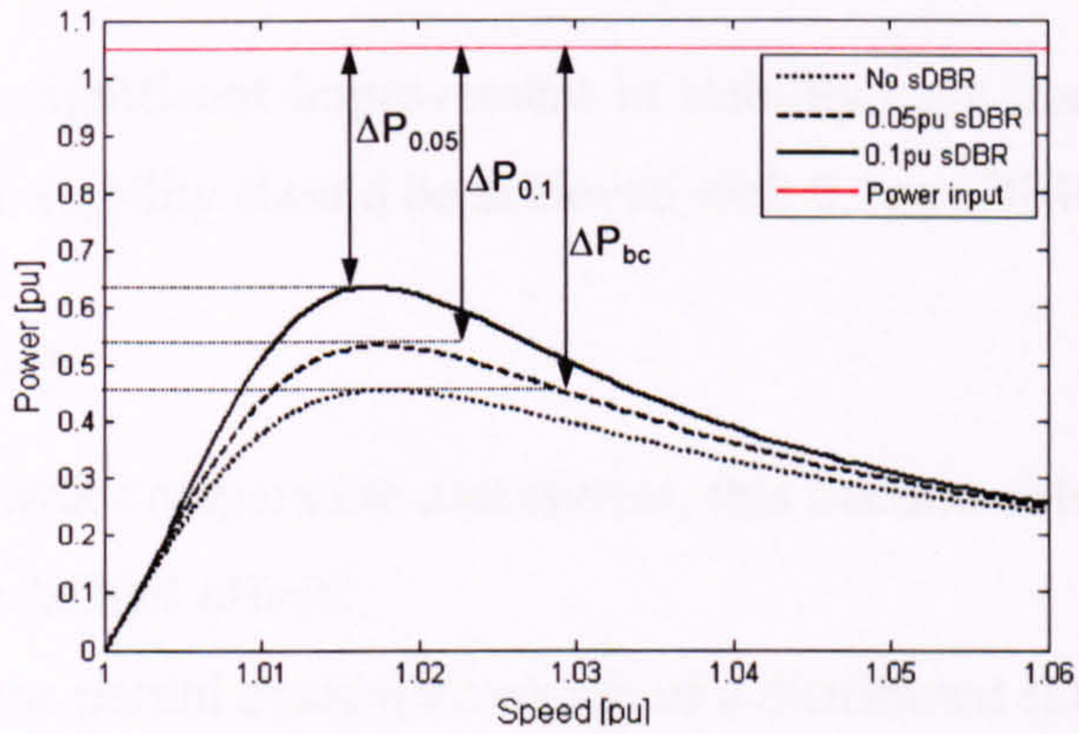

a. Effect on net accelerating power

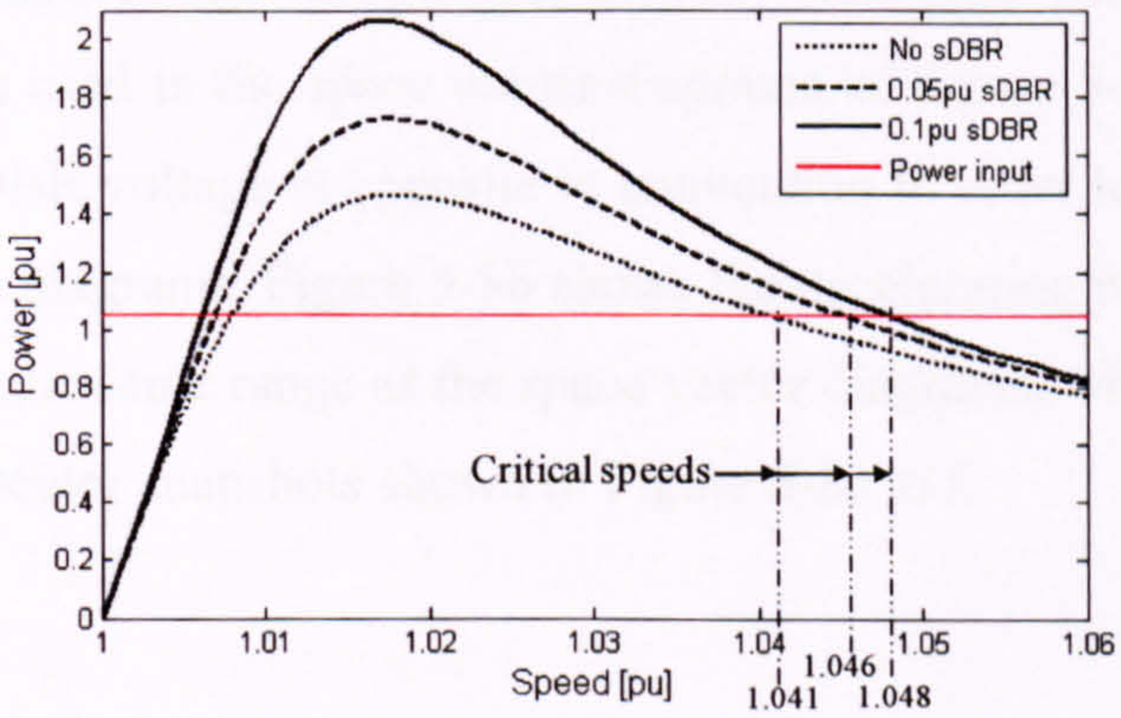

b. Effect of critical speed

Figure 5-6: Effect of sDBR on decelerating power-speed characteristics

Figure 5-6a and b show that sDBR also boosts decelerating power through-out the relevant speed range, although the benefit is much reduced at higher speeds. Figure 5-6a, shows the reduced net accelerating power during the fault period, due to a 20% boost in peak decelerating power for each 0.05pu sDBR increment. Figure 5-6b, shows the increase of critical speed in the recovery period. The result of these changes is illustrated in Figure 5-7.

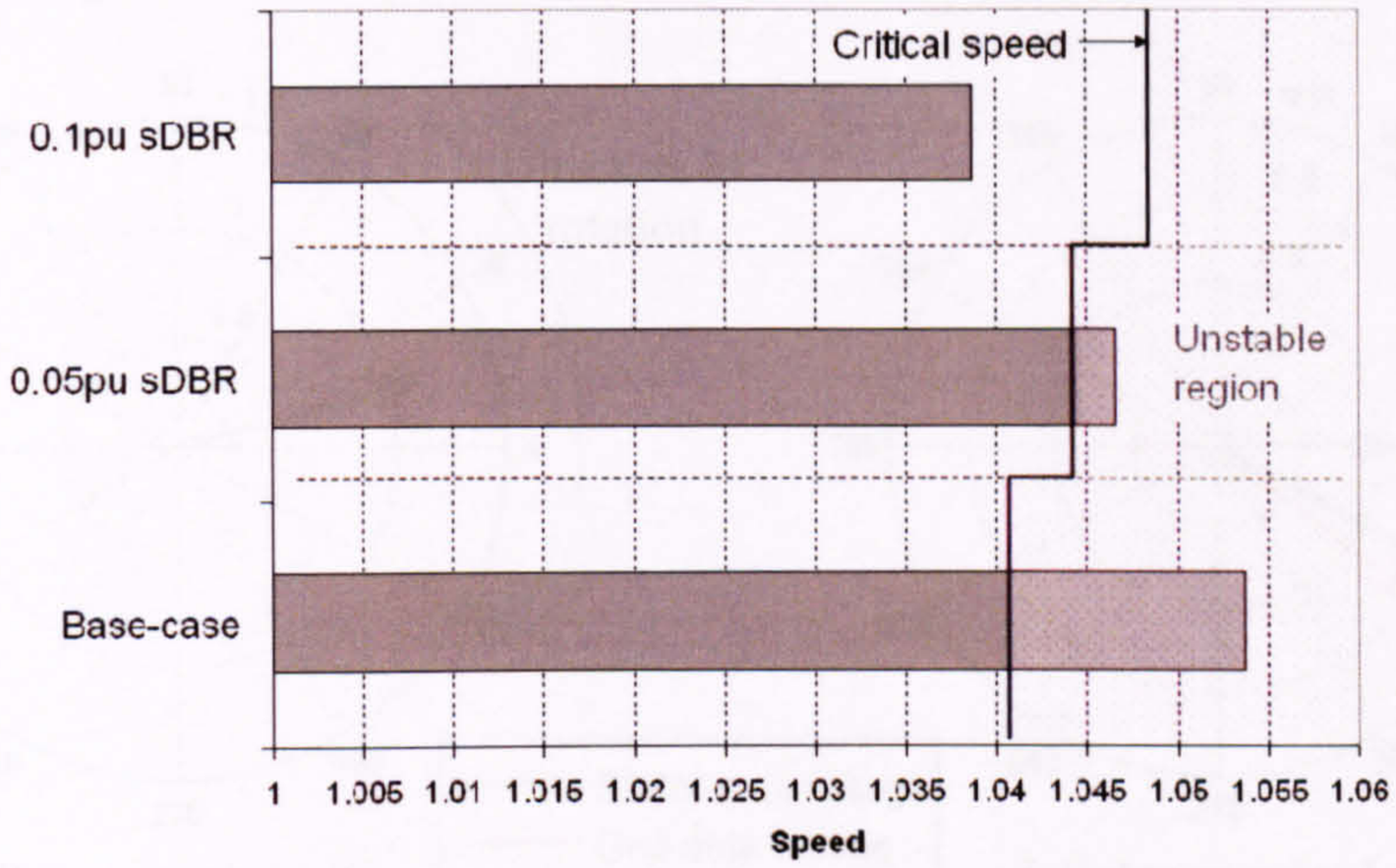

Figure 5-7: Clearance speeds and inferred improvement in stability with sDBR

Figure 5-7 shows a significant improvement in stability such that, according to this optimistic approach, stability should be achieved with 0.1pu sDBR.

5.6. sDBR Theory

Before proceeding with comparative assessment, this Section extends the theoretical underpinning of the "sDBR effect".

Figure 5-8a shows the partial equivalent circuit of a distributed sDBR device (located on the generator side of the turbine transformer) annotated with the current and voltage parameters used in the space vector diagrams of Figure 5-8c to f. Note that the direction of sDBR voltage is opposite to convention in order to reduce cluttering of the space vector diagrams. Figure 5-8b shows the decelerating power versus speed characteristic over the same range as the space vector diagrams, with a cross marking each of the space vector snapshots shown in Figure 5-8c to f.

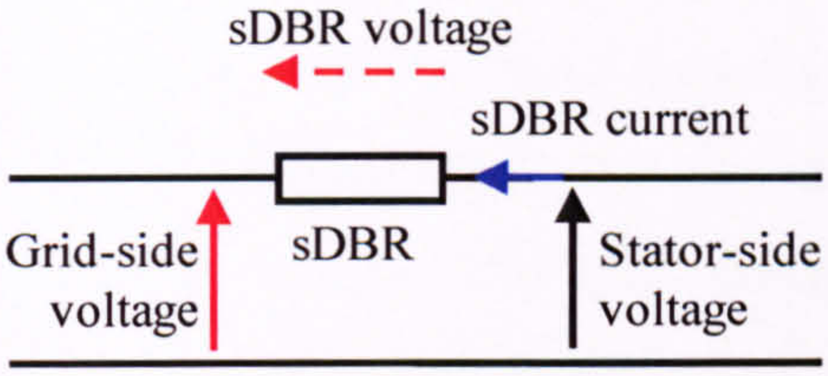

a. sDBR voltage and current parameters

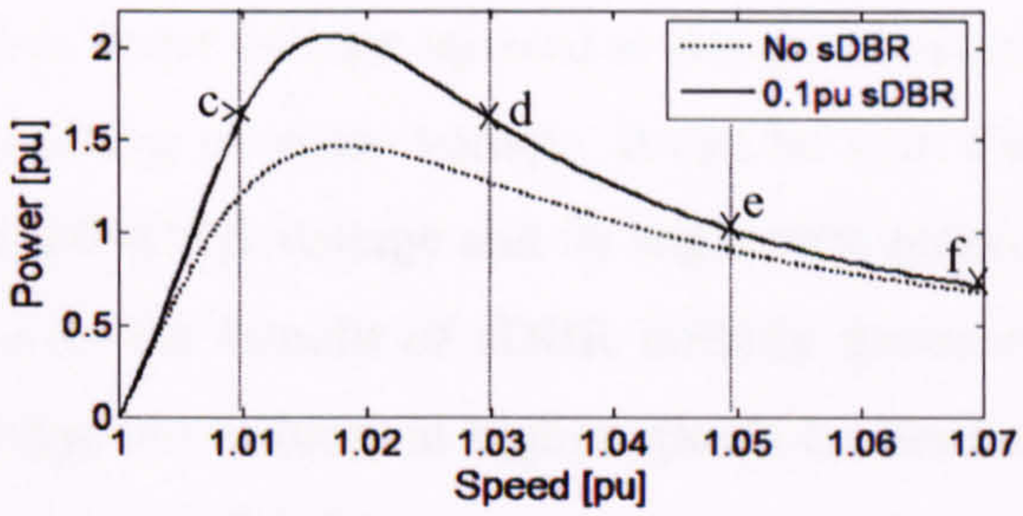

b. Decelerating power versus speed

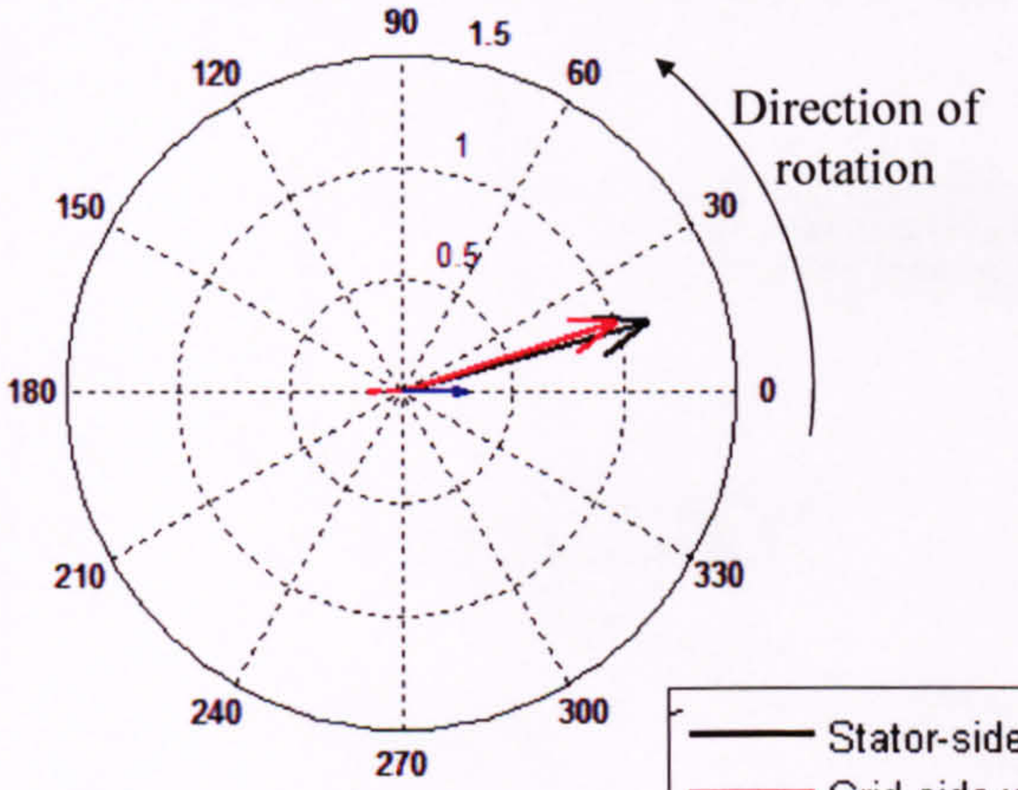

c. Rotor speed = 1.01

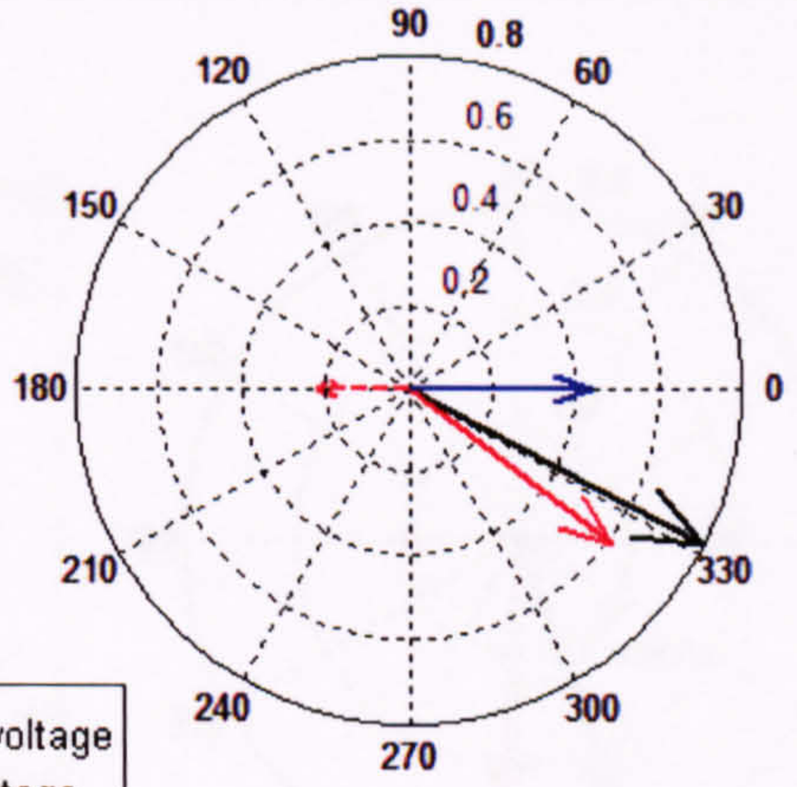

d. Rotor speed = 1.03

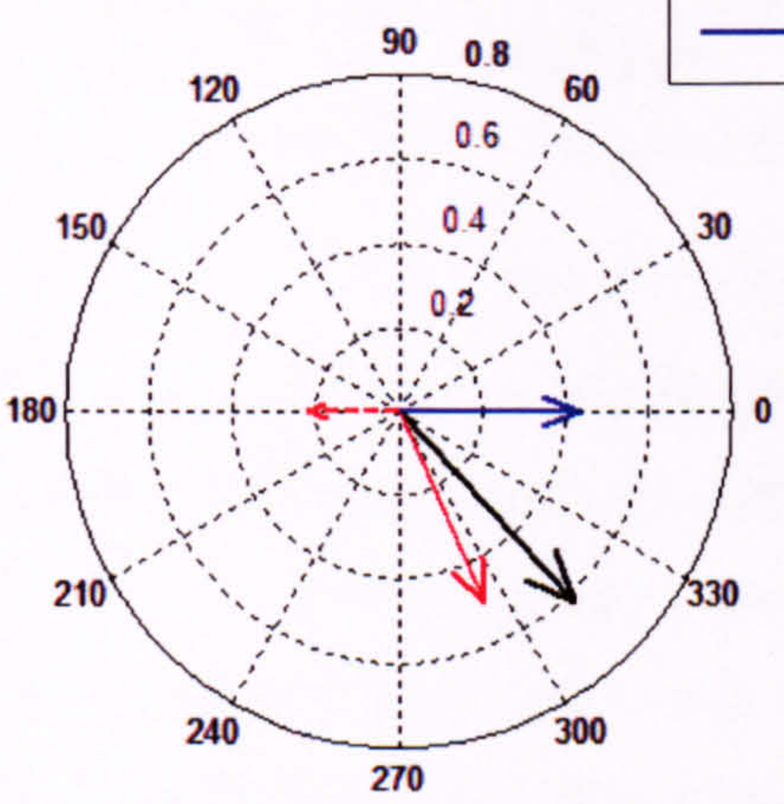

e. Rotor speed = 1.05

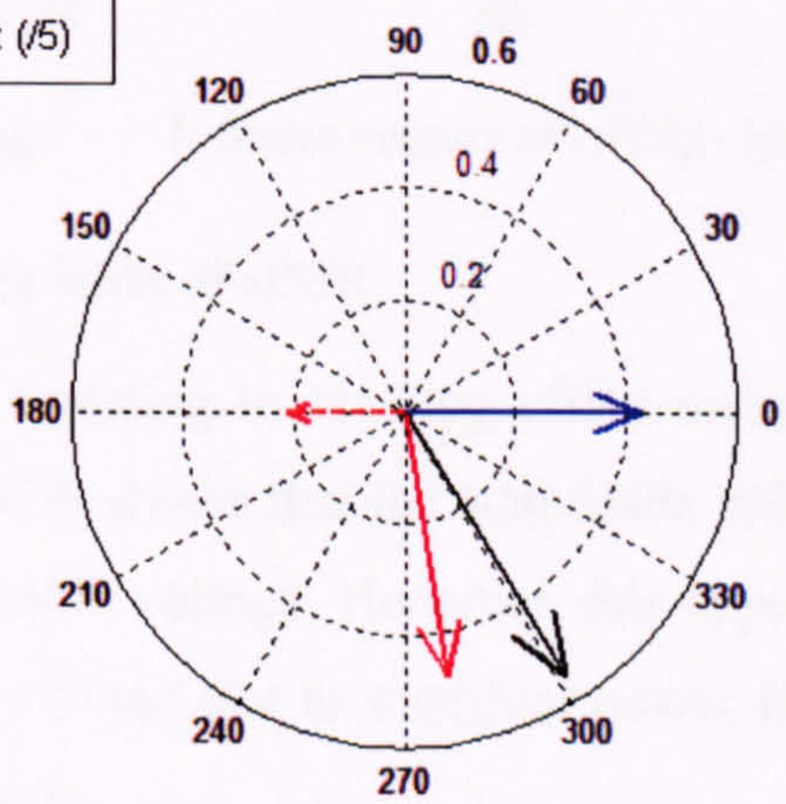

f. Rotor speed = 1.07

Figure 5-8: Phasor diagrams illustrating sDBR effect

Figure 5-8c to f show the voltage space vectors associated with the sDBR device of Figure 5-8a with respect to sDBR current at four speeds in the range 1.01pu to 1.07pu. As expected for a resistive device, sDBR voltage is always in phase with sDBR current (shown as anti-phase only because of inversion) and has a magnitude equal to the product of sDBR current and resistance. Both grid and stator-side voltages lead sDBR current at 1.01pu speed because of excess VAr supplied by the steady-state RPC but lag current with progressively larger angles as speed increases.

Since decelerating power is proportional to stator voltage squared at any given speed, the benefit of sDBR derives from the boosting of stator voltage. It can be seen that voltage boosting relates to the magnitude of sDBR voltage and its angle with respect to grid-side voltage. From this perspective, the benefit of sDBR initially increases due to increasing sDBR current and voltage but reduces at higher speeds because of the increasing phase angle between sDBR and grid voltage.

As rotor speed increases still further the beneficial effect reduces to zero, as shown in Figure 5-9a.

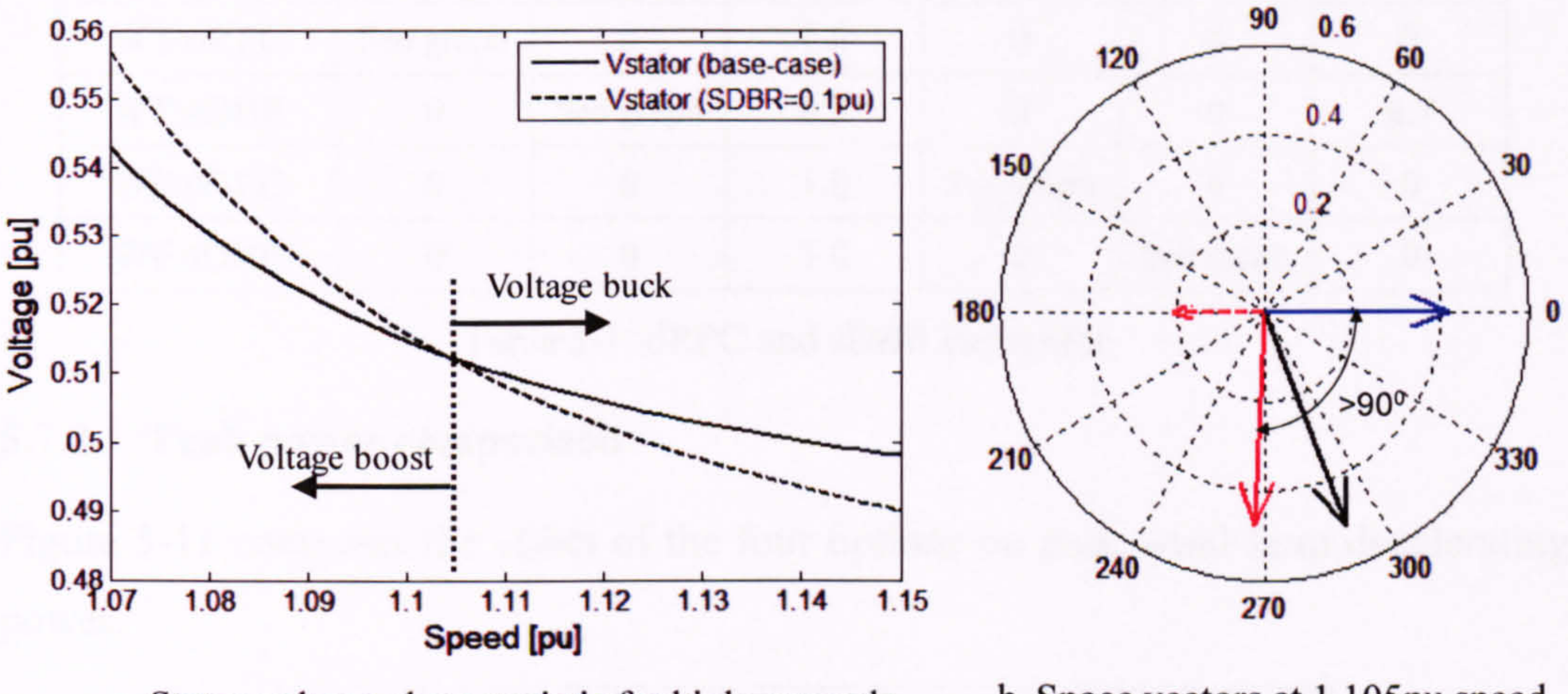

a. Stator voltage characteristic for higher speeds b. Space vectors at 1.105pu speed

Figure 5-9: Voltage boosting limits of sDBR

Figure 5-9a shows that the transition from a boosting to bucking effect on stator voltage is at a rotor speed of 1.105pu. Figure 5-9b shows that the stator-side voltage magnitude is still marginally greater than grid-side voltage. However, this apparent gain is negated by the depression of grid-side voltage due to modified power flows across the turbine transformer and grid impedances.

5.7. Comparative Assessment

5.7.1. Options

Sections 5.4 and 5.5 have shown the inferred beneficial effects of dRPC and sDBR on wind farm FRT stability. This Section compares the effect of dRPC and sDBR options on the key stability parameters, peak decelerating power and critical speed. The four options are shown in Figure 5-10 with associated dRPC, sDBR and steady-state (ss) RPC capacities specified in Chapter 4.

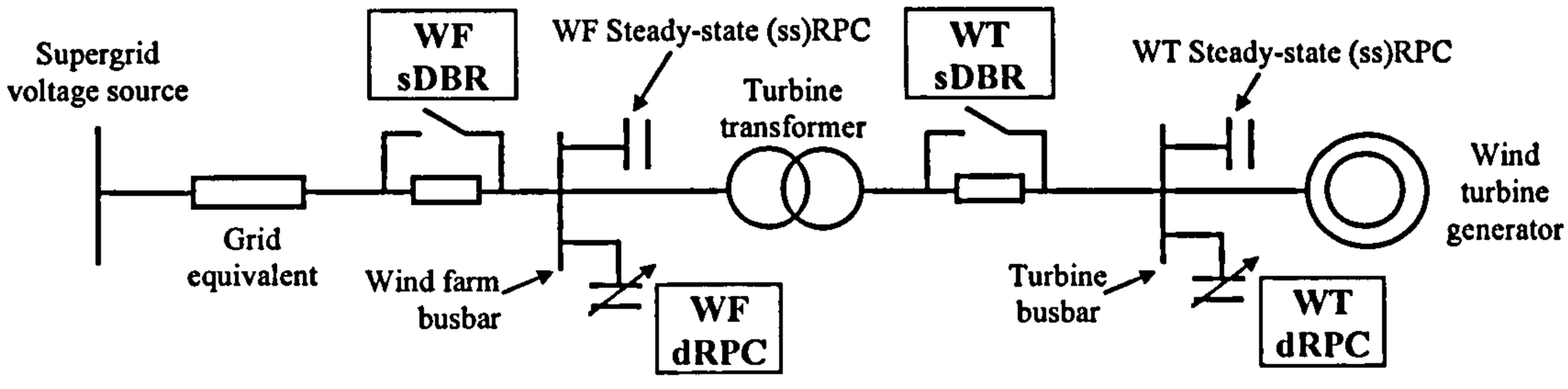

Figure 5-10: dRPC and sDBR options for comparative analysis

Option	WT dRPC	WT sDBR	WT ssRPC	WF dRPC	WF sDBR	WF ssRPC
WT dRPC	See graph	0	1.0	0	0	0
WT sDBR	0	See graph	**0.3**	0	0	**0.7**
WF dRPC	0	0	1.0	See graph	0	0
WF sDBR	0	0	1.0	0	See graph	0

Table 5-1: dRPC and sDBR capacities

5.7.2. Peak power comparison

Figure 5-11 compares the effect of the four options on peak wind farm decelerating power.

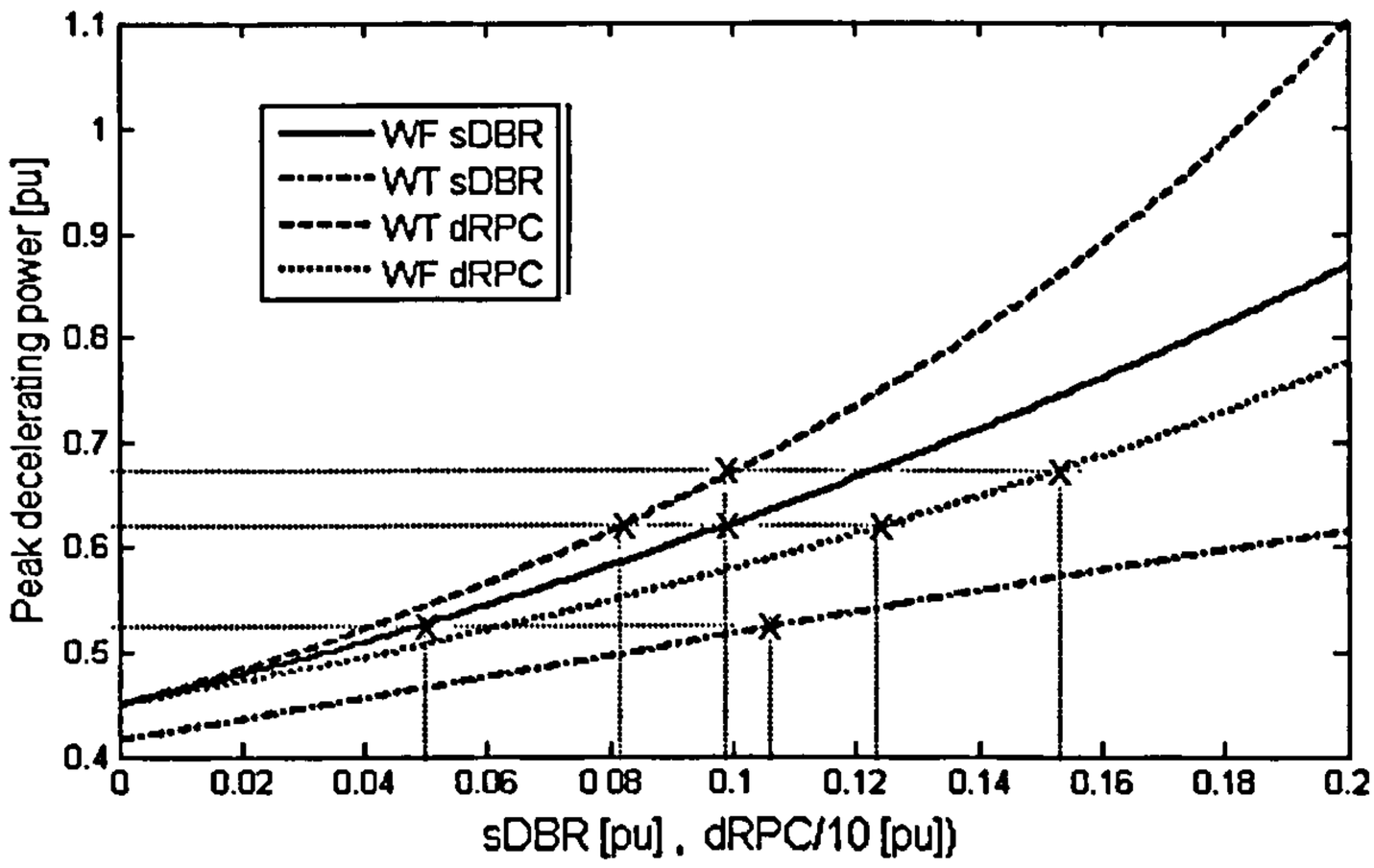

Figure 5-11: Effect of dRPC and sDBR on peak decelerating power

The options from Figure 5-11 are compared in pairs below:

WT versus WF dRPC:

WT dRPC and WF dRPC both significantly boost peak power. For example, 1pu WT dRPC is equivalent to 1.53pu WF dRPC, both achieving a 50% increase in peak power. The 50% greater stabilising effect of WT dRPC arises from compensating for reactive power demand close to its source, reducing the *voltage depression* effect of

reactive power flowing through the turbine transformer. This significant benefit is counteracted by the commercial, installation and control benefits of installing a single dRPC at the wind farm substation rather than several smaller ones at each wind turbine. WF dRPC is therefore still common despite its theoretical disadvantage.

WT versus WF sDBR:

WF sDBR and WT sDBR both significantly boost peak power. For example, 0.05pu WF sDBR is equivalent to 0.11WT sDBR, both achieving a peak power of 0.53pu. This comparison of the two methods unfairly represents the WT sDBR option because it is uniquely disadvantaged by having 70% of its steady-state RPC located at the wind farm substation. This handicap, explained above, is illustrated by the 7% greater peak power of WF sDBR in the base-case (sDBR = 0). However, it is evident from the gradient of the two characteristic curves that the incremental effect of WT sDBR is also substantially less than WF sDBR. The inferior performance of WT sDBR in this example[5] is due to the poorer power factor across the braking resistor, resulting in a reduced voltage-boosting effect. The dependence of sDBR's beneficial effects on power factor was previously shown in Figure 5-8.

WF sDBR versus WF dRPC:

WF dRPC and WF sDBR both significantly boost peak power with 0.1pu WF sDBR being equivalent to 1.25pu WF RPC. It is clearly difficult to make meaningful comparison of these techniques without investigation of relative costs and practical considerations for installation on a real wind farm.

5.7.3. Critical speed comparison

Figure 5-12 compares the effect of the four options on critical rotor speed.

---

[5]However, it should be emphasised that the performance of WF and WT sDBR are identical if the allocation of RPC is the same in both cases.

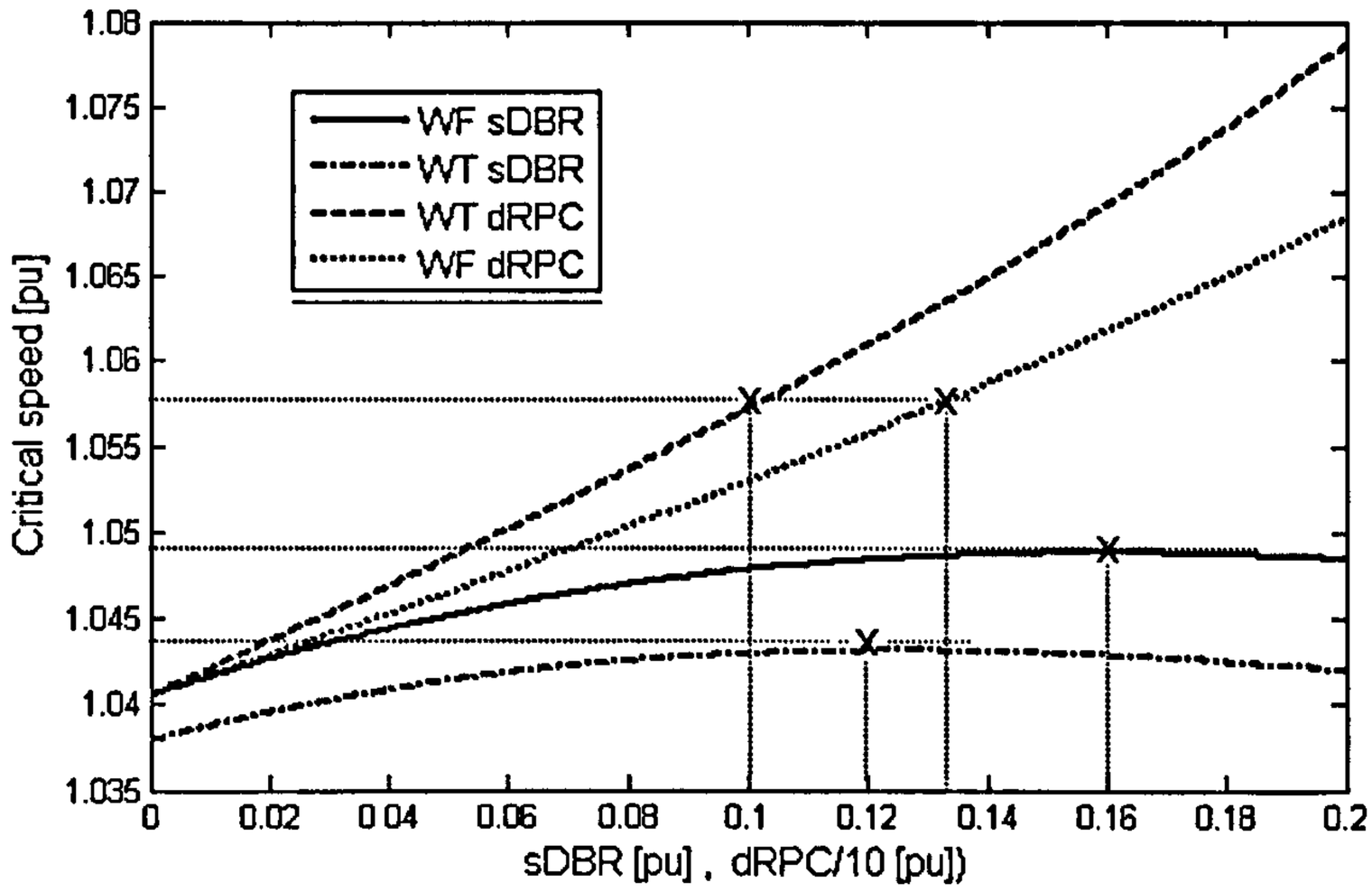

Figure 5-12: Effect of dRPC and sDBR on critical rotor speed

The characteristic curves of Figure 5-12 are compared in the same manner as peak power above.

WT versus WF dRPC:

WT dRPC and WF dRPC both increase critical speed with progressively increasing gradient. For example, 1pu WT dRPC is equivalent to 1.33pu WF dRPC, both achieving a 0.9% increase in critical speed. The 33% greater stabilising effect of WT dRPC is for the same reason given in Section 5.7.2.

WT versus WF sDBR:

WF sDBR and WT sDBR both increase critical speed for small magnitudes of resistance. However, this effect weakens with increasing sDBR magnitude resulting in maxima at 0.12pu for WT sDBR and 0.16pu for WF sDBR.

WF sDBR versus WF dRPC:

WF dRPC has a stronger beneficial influence on critical speed, especially at higher values of inserted capacity.

5.7.4. Comparison of combined stabilising effect

Figure 5-13 uses the technique of Section 5.3 to compare the inferred stability speed margins of the four options for fault scenario 3.

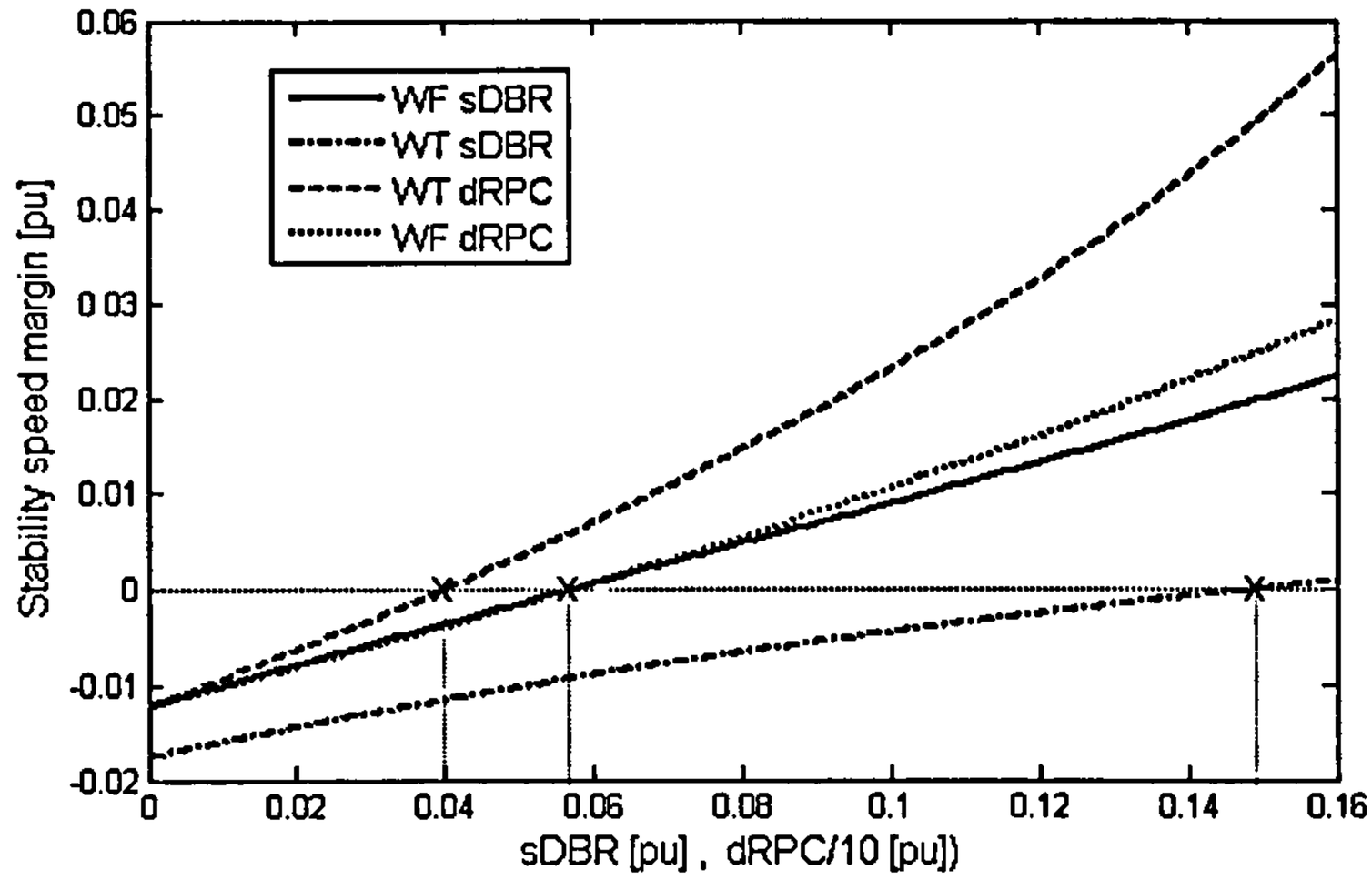

Figure 5-13: Effect of dRPC and sDBR on inferred wind farm stability

It can be seen from Figure 5-13 that with each option it should be possible to achieve stable operation following fault scenario 3.

Finally, Figure 5-14 compares performance during the worst case fault scenario, 5.

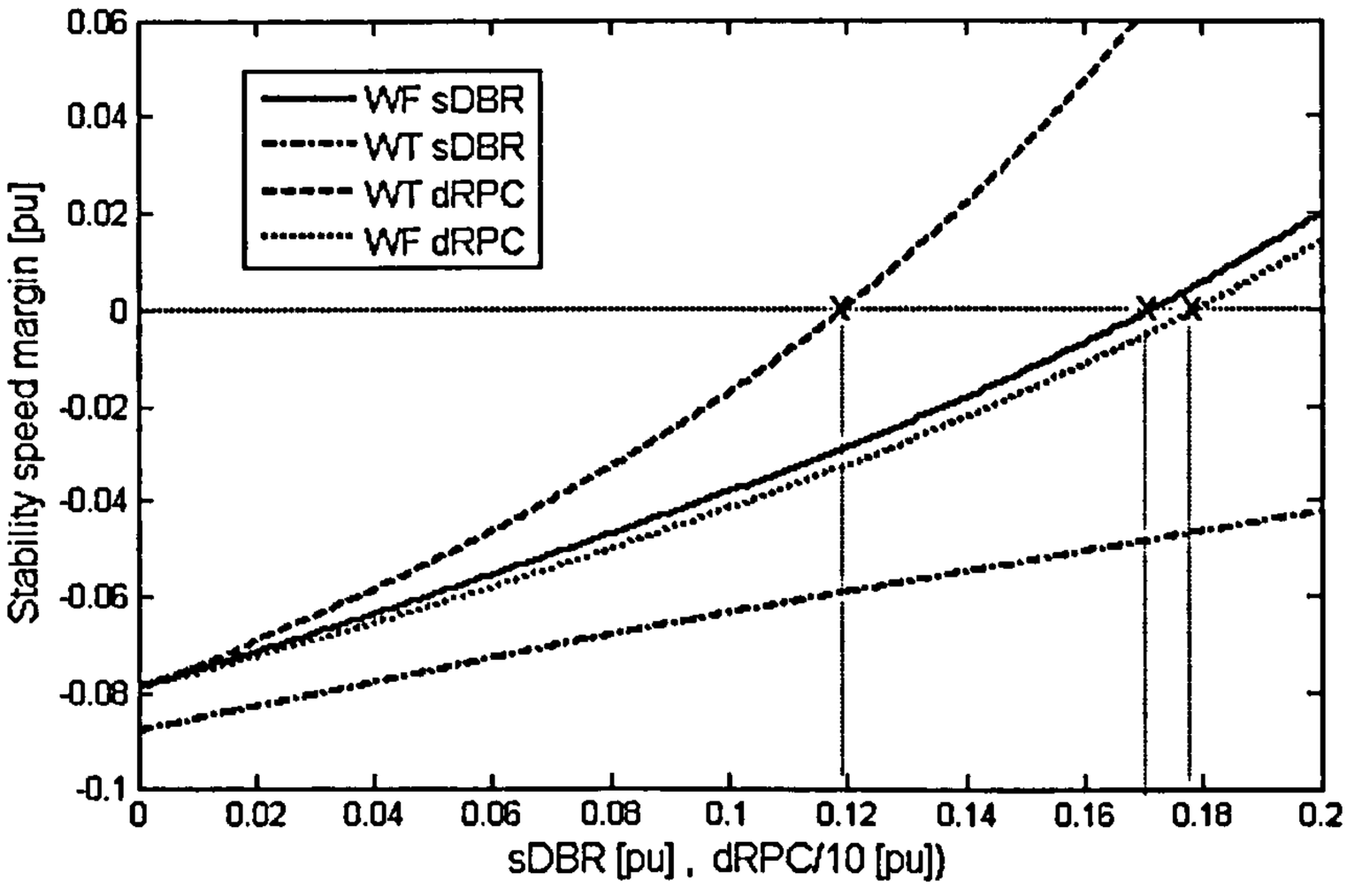

Figure 5-14: Effect of dRPC and sDBR on inferred wind farm stability

Figure 5-14 shows that compliance with even the most onerous grid code requirements in GB and RoI should be possible with all options except WT sDBR.

5.8. Sensitivity Analysis

Section 5.7 infers that the particular representative wind farm should be able to be made compliant with GB and RoI Grid Codes given suitable application of sDBR or dRPC technology. In reality, each wind farm will have unique characteristics which may differ significantly from the ones chosen as representative. The purpose of this Section is therefore to test the sensitivity of the stability to impedance values of a specific wind farm. This sensitivity study is performed using fault scenario 3 and the representative wind farm system as the base-case. The study compares the sensitivity of 0.1pu WF sDBR and 0.95pu WF dRPC on the basis that each achieves an equal, positive stability margin (see Figure 5-13) in the base-case.

Figure 5-15a shows the sensitivity of stability speed margin to changes in selected impedance values in order to clarify the derivation of sensitivity gradients used in Figure 5-15b to compare the sensitivity of dRPC and sDBR.

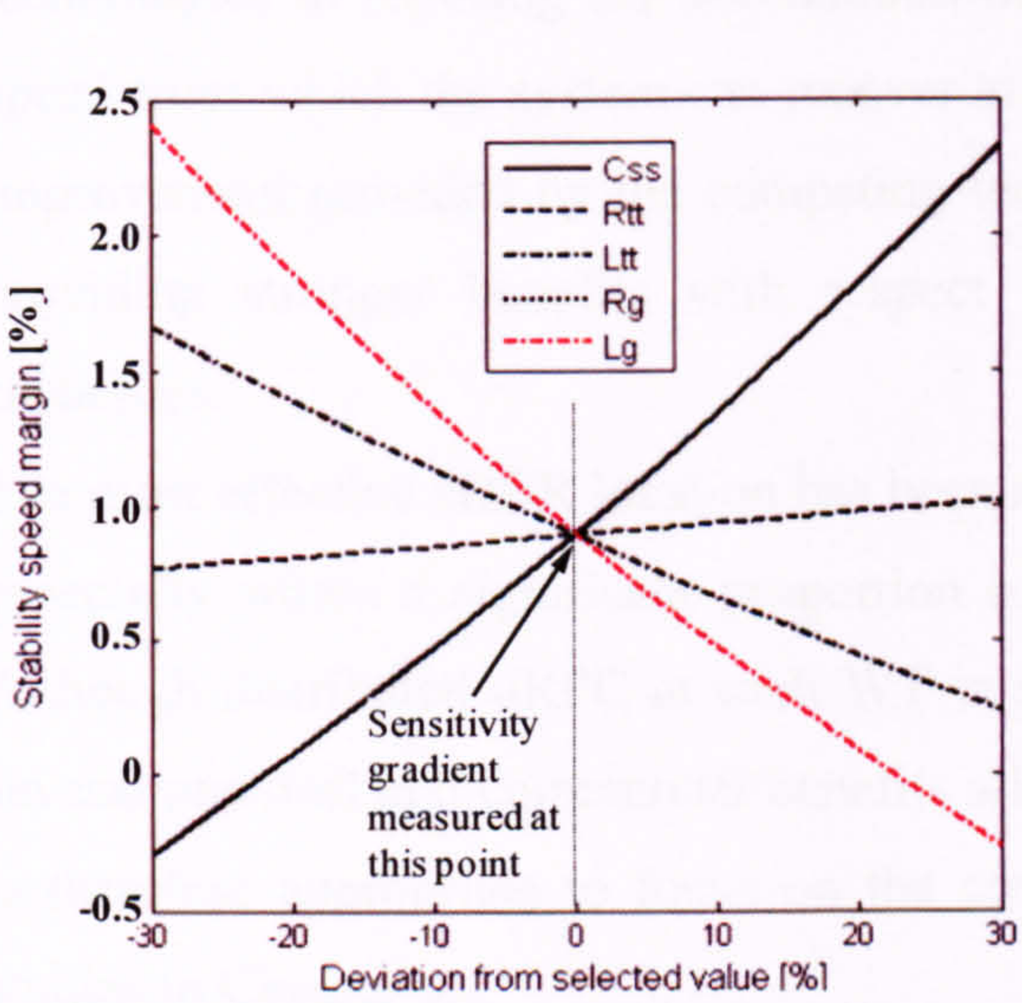

a. Sensitivity of RPC & grid parameters (WF sDBR option)

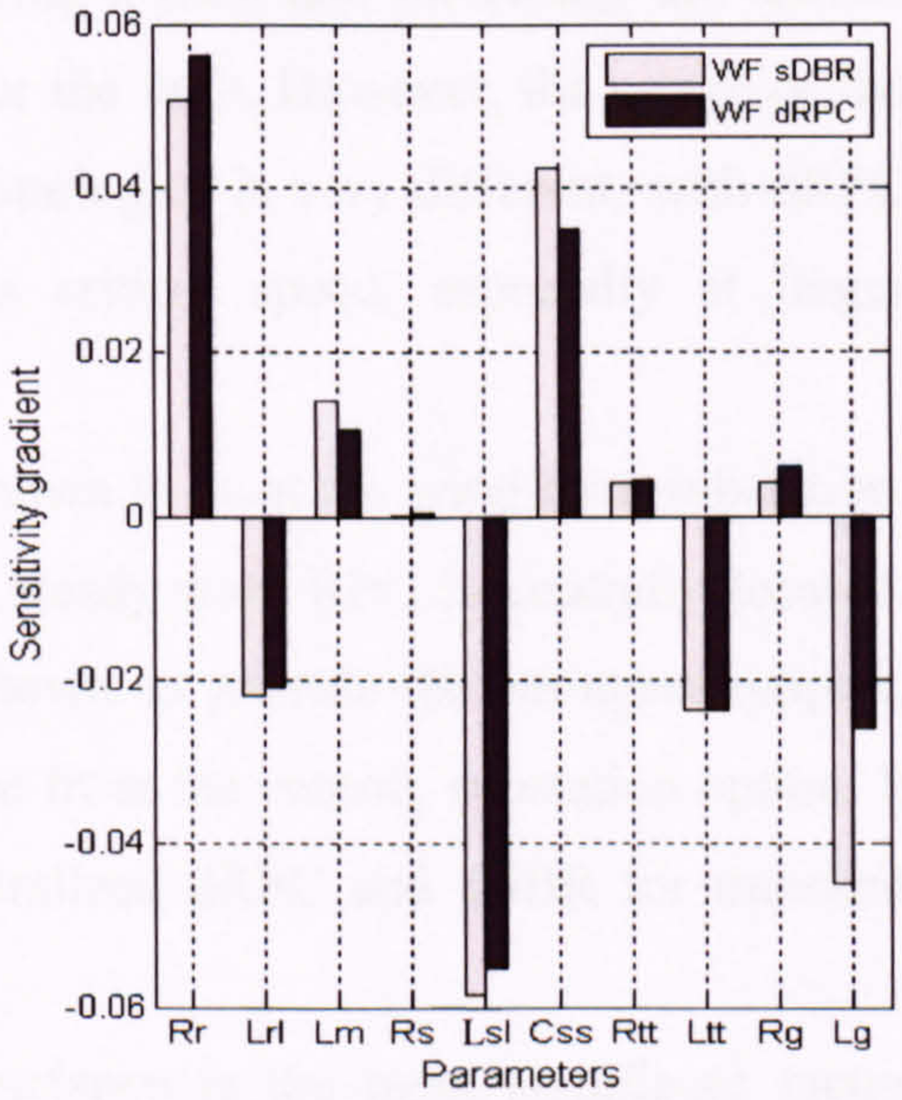

b. Comparative sensitivities for sDBR & dRPC options

Figure 5-15: Sensitivity of stability speed margin with changing wind farm parameters

Figure 5-15a shows the sensitivity of stability margin to changes to wind farm and grid impedance parameters in the range of +/-30% of the base-case. The *sensitivity gradient* for each parameter is derived at the base-case parameter value (0% deviation). These gradients are used in Figure 5-15b to compare sensitivity of stability with dRPC and sDBR technologies to changes in impedance parameters associated with the representative wind farm. It can be seen that stability is highly

sensitive to stator inductance, rotor resistance, grid inductance and steady-state RPC and insensitive to stator, turbine transformer and grid resistance. Sensitivity to series inductance and rotor resistance highlights the importance of selecting components with optimum parameter values and ensuring that parameter tolerances are accounted for in carrying out stability studies.

It is important to note that the WF sDBR option is nearly twice as sensitive to changes in grid inductance. This implies that larger values of grid impedance would be detrimental to WF sDBR's stability in comparison with WF dRPC.

5.9. Summary

This Chapter shows that both dRPC and sDBR can significantly improve the base-case FRT stability characteristic of the representative FSWT wind farm derived in Chapter 4. Stability improvement is shown to derive from the contribution of both technologies to reducing the acceleration during a fault and increasing the critical speed from which the system can recover after the fault. However, the nature of the improvement provided by the competing technologies is very different, with dRPC providing stronger benefits with respect to critical speed, especially at larger capacities.

The most effective sDBR location has been shown to be at the wind farm substation, especially where a significant proportion of steady-state RPC is centrally located. Although distributed dRPC at each WT is shown to provide the strongest support, several practical and commercial benefits arise from the central, substation option. It is therefore appropriate to focus on the centralized dRPC and sDBR for transient studies in Chapter 6.

Sensitivity analysis highlights that grid inductance is the most significant factor influencing the *relative* performance of dRPC and sDBR. Increasing grid inductance has a more detrimental effect on stability with sDBR. The base representative value of 0.13pu selected for grid inductance is on the mid- to high-side of a typical range for large wind farms. However, this does suggest that any comparative advantage of sDBR may diminish for very weak grid connections, especially those connected via high impedance grid transformers.

6. Transient Simulation

6.1. Introduction

The purpose of this Chapter is to analyse and compare the FRT performance of sDBR and dRPC technologies under the full range of fault scenarios defined in Figure 2-15.

The representative transient model of a wind farm system, developed in Chapter 4, is used to perform this analysis. The results of base-case FRT simulations using this model are validated and compared to the stability performance inferred from QSS analysis in Chapter 5. The absolute and comparative effects of dRPC and sDBR on FRT performance are investigated using the validated model. Finally, the sensitivity of those results is tested to ensure that results are not limited to a narrow band of wind farm parameters.

6.2. Base-Case Assessment

The purpose of this Section is to validate and compare the results of base-case transient wind farm simulations with reference to the QSS analysis in Section 5.2.

6.2.1. Steady-state characteristics

The transient wind farm electrical model is validated by running numerical simulations with very slowly accelerating rotor (α=0.0002pu) in order to produce effective steady-state characteristics in the speed range of 1.00 to 1.06pu. The decelerating power characteristics at recovery voltage (90%) are then compared with the steady-state characteristics calculated from their respective equivalent circuits, as shown in Figure 6-1.

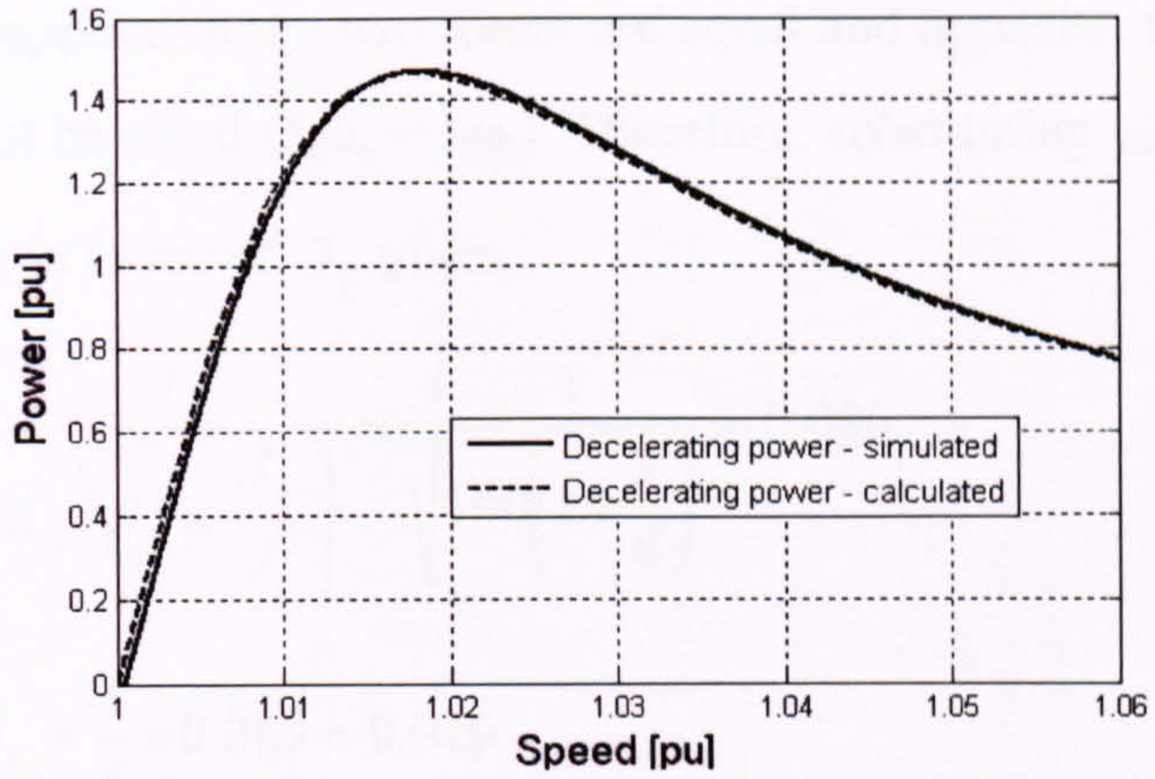

Figure 6-1: Comparison of steady-state wind farm characteristics at 90% supergrid voltage

Figure 6-1 confirms very close correlation between simulated and calculated results.

6.2.2. Dynamic response

Having validated the electrical side of the transient wind farm model simulations against steady-state characteristics, this section validates its mechanical response. As introduced in Chapter 4, the oscillatory response of a two-mass drive train with soft coupling has very significant influence on the dynamics and stability of a typical wind farm. Figure 6-2 shows the unconstrained oscillation of the representative drive train initially at rest with a coupling torque, T_{k0}, of 1.0pu.

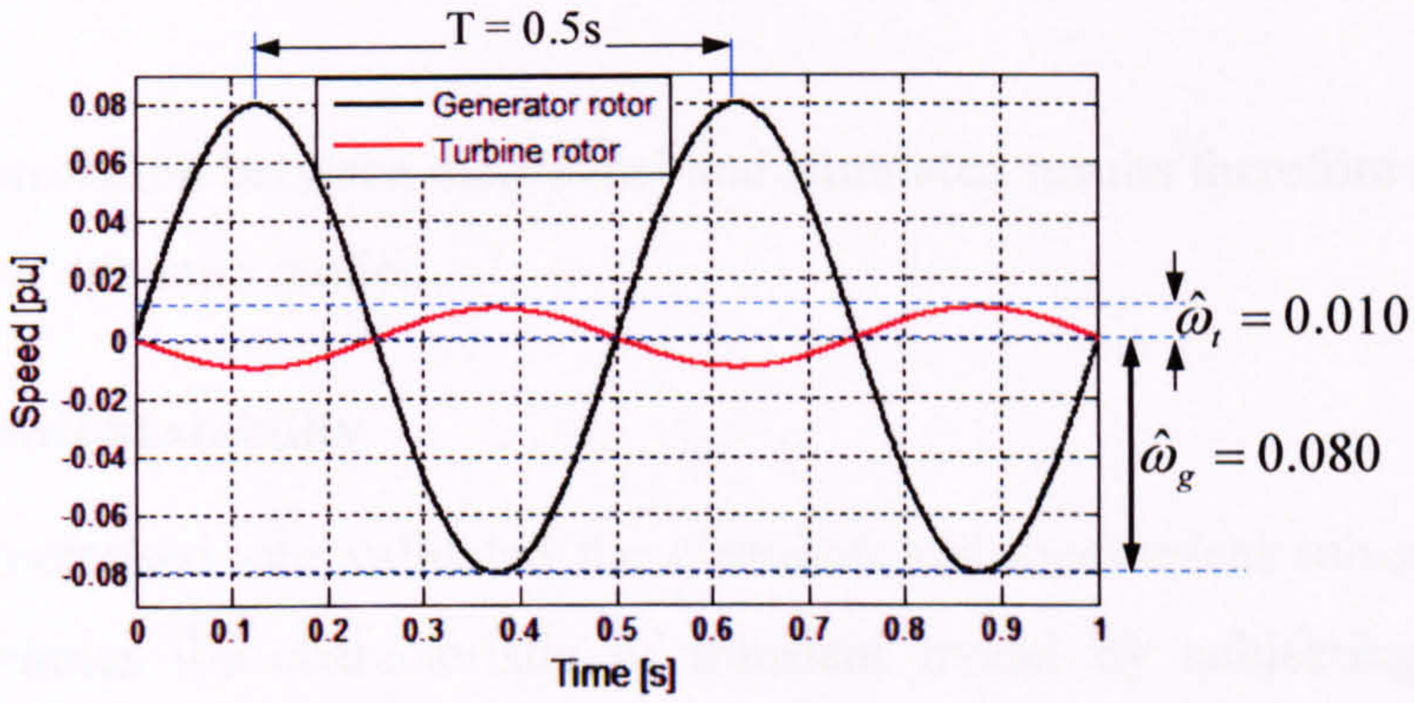

Figure 6-2: Dynamic response of representative two-mass wind turbine drive train

Figure 6-2 shows the simulated amplitude and period of oscillation. Equation 6-1 expresses the total system energy, E_{sys}, initially stored in the coupling then transferred to the inertial energy of the rotors after a quarter of a cycle.

$$E_{sys} = \frac{T_{K0}^{\ 2}}{2K_c} = \frac{1}{2}\left(J_g\hat{\omega}_g^2 + J_t\hat{\omega}_t^2\right) \qquad (6\text{-}1)$$

Since the torques applied to the two rotors are equal and opposite, the momentum of the two rotors must be equal ($J_g\omega_g = J_t\omega_t$). Therefore, substituting $\hat{\omega}_g$ for $\hat{\omega}_t$ in Eq. 6-1 and re-arranging in terms of $\hat{\omega}_g$ gives,

$$\hat{\omega}_g = T_{K0}\sqrt{\frac{1}{K_c J_g\left(1+\frac{J_g}{J_t}\right)}} = \sqrt{\frac{1}{140\left(1+\frac{1}{8}\right)}} = 0.080 \qquad (6\text{-}2a)$$

$$\hat{\omega}_t = \frac{J_g}{J_t}\cdot\hat{\omega}_g = \frac{1}{8}\times 0.080 = 0.010 \qquad (6\text{-}2b)$$

Equation 6-2a shows the inversely proportional relationship of oscillation amplitude to the square root of coupling stiffness, K_c, and generator inertia, J_g. This means that lower values of K_c and J_g increase speed excursions during the fault, reducing stability, as demonstrated in Chapter 3.

Equation 6-3 expresses the period of oscillation.

$$T = 2\pi\sqrt{\frac{J_{eff}}{K_c}} = 2\pi\sqrt{\frac{0.89}{140}} = 0.50s \qquad (6\text{-}3)$$

Where $J_{eff} = \frac{J_g J_t}{J_g + J_t} = \frac{1\times 8}{1+8} = 0.89$

The close correlation between theoretical and simulated results therefore supports the validity of the dynamic model.

6.2.3. Transient stability

Having characterised and validated the electrical and mechanical sub-systems, this Section examines the characteristic of transient model by subjecting it to fault scenario 3 of Figure 2-15c. The simulation results are shown in Figure 6-3.

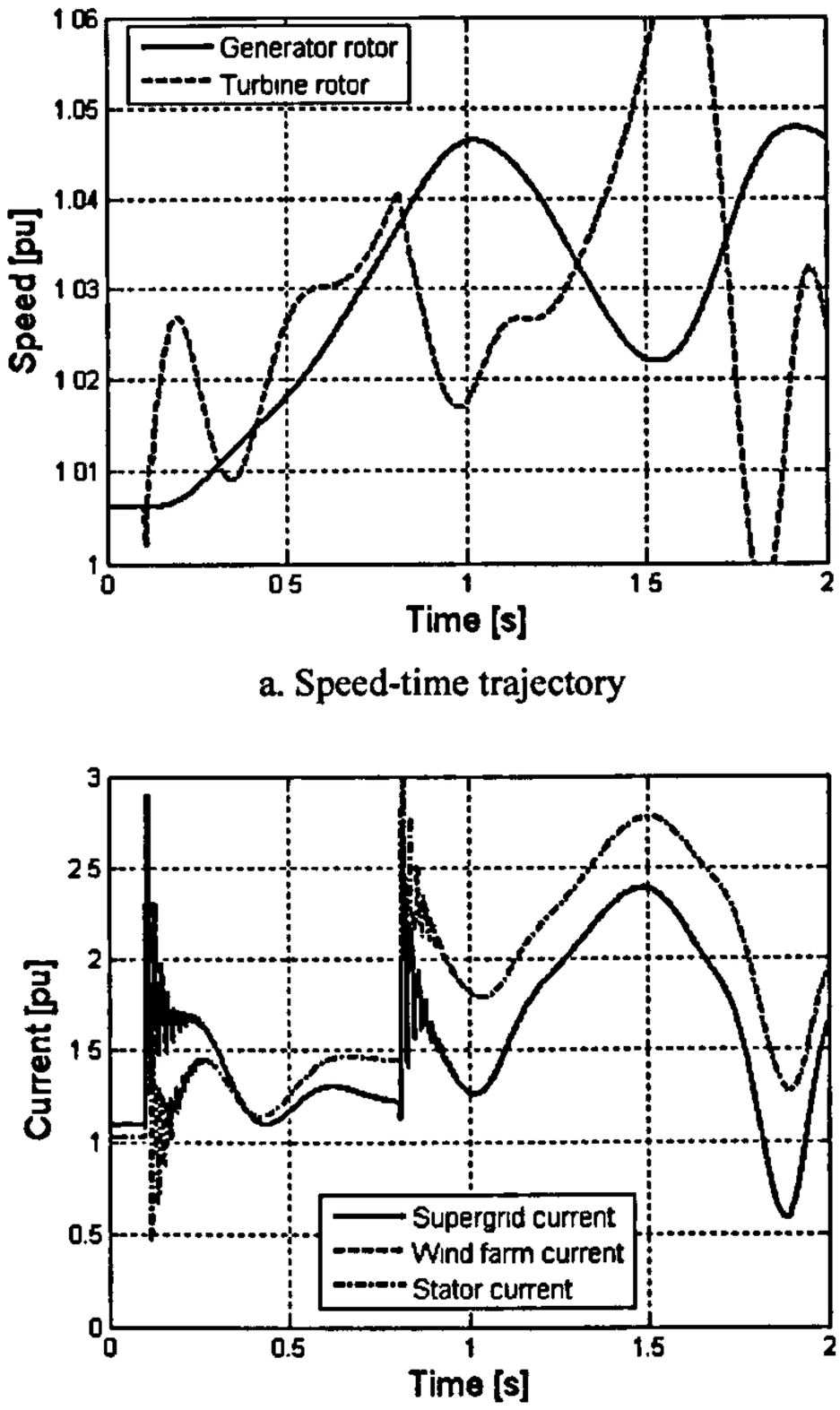

a. Speed-time trajectory

b. Voltage-time trajectory

c. Current-time trajectory

d. Active power-time trajectory

Figure 6-3: Detailed simulation results for reduced wind farm model

The speed-time response of Figure 6-3a highlights pronounced oscillation of the generator rotor, initiated by fault inception and reinforced by fault clearance. As expected, the amplitude and period of natural oscillation are significantly modified by the residual decelerating torque. The rotor speed at the time of fault clearance is just above 1.04pu compared to 1.053pu inferred from QSS analysis. This direction of error implies that the beneficial effect of the voltage transition from the pre-fault to faulted states outweighs the optimistic assumption for decelerating power used in the QSS analysis. The relevance of QSS term *critical speed* is further explored in Figure 6-4 by comparing simulation results for one- and two-mass drive-trains with identical overall inertia.

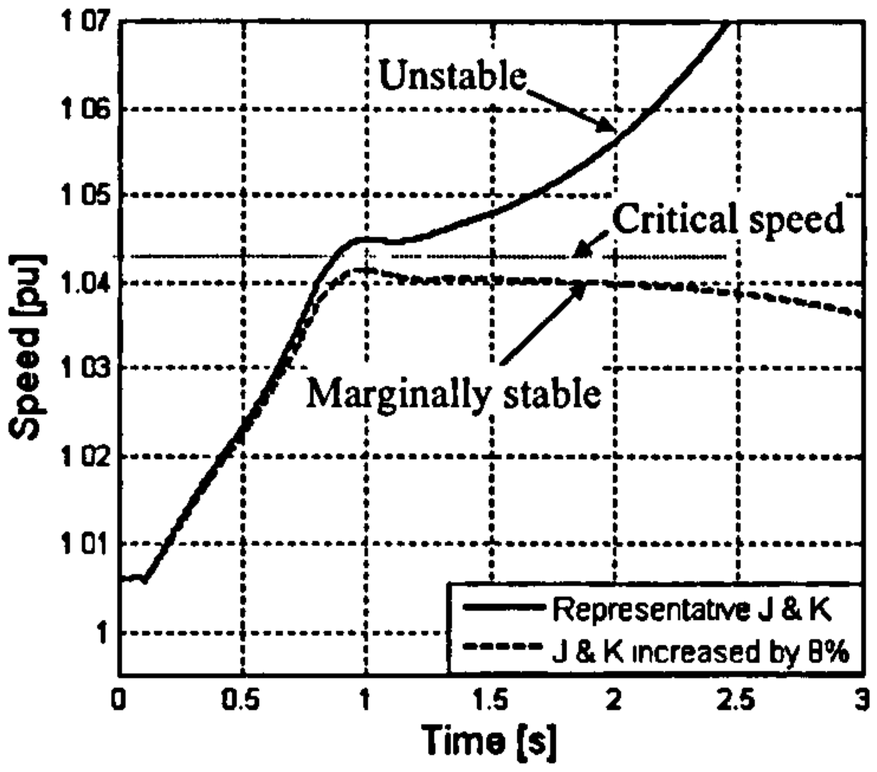

a. Speed-time trajectory with 1-mass model

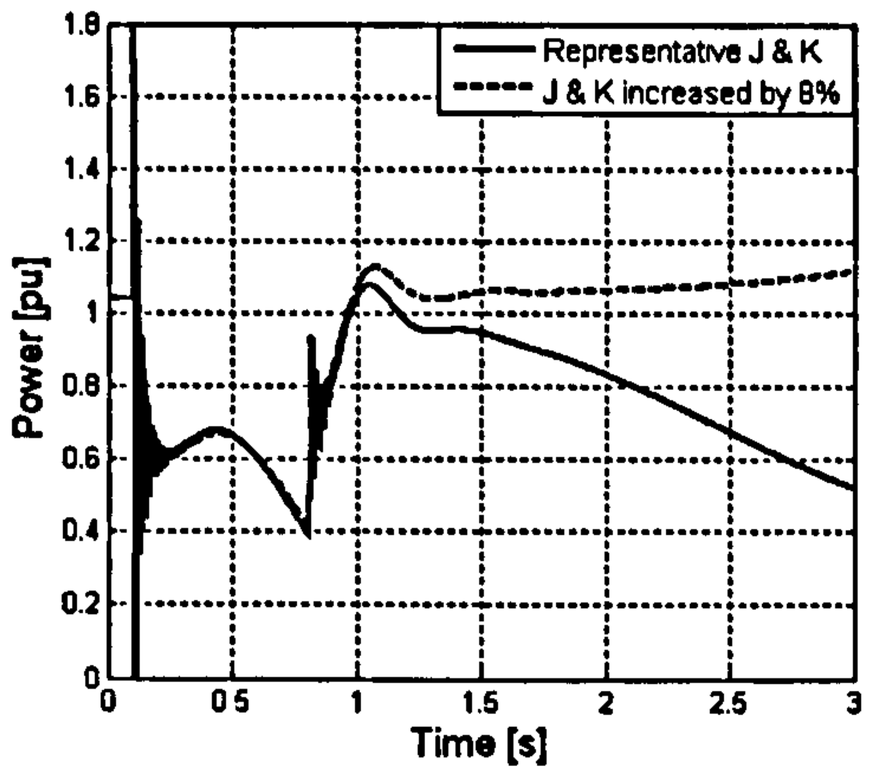

b. Power-time trajectory with 1-mass model

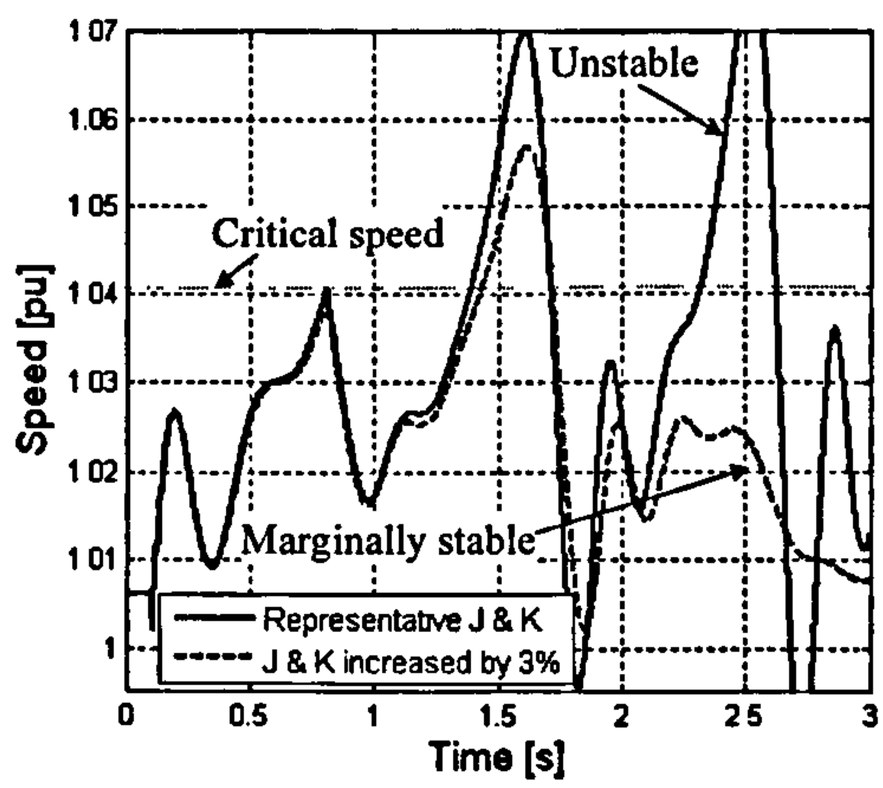

c. Speed-time trajectory with two-mass model

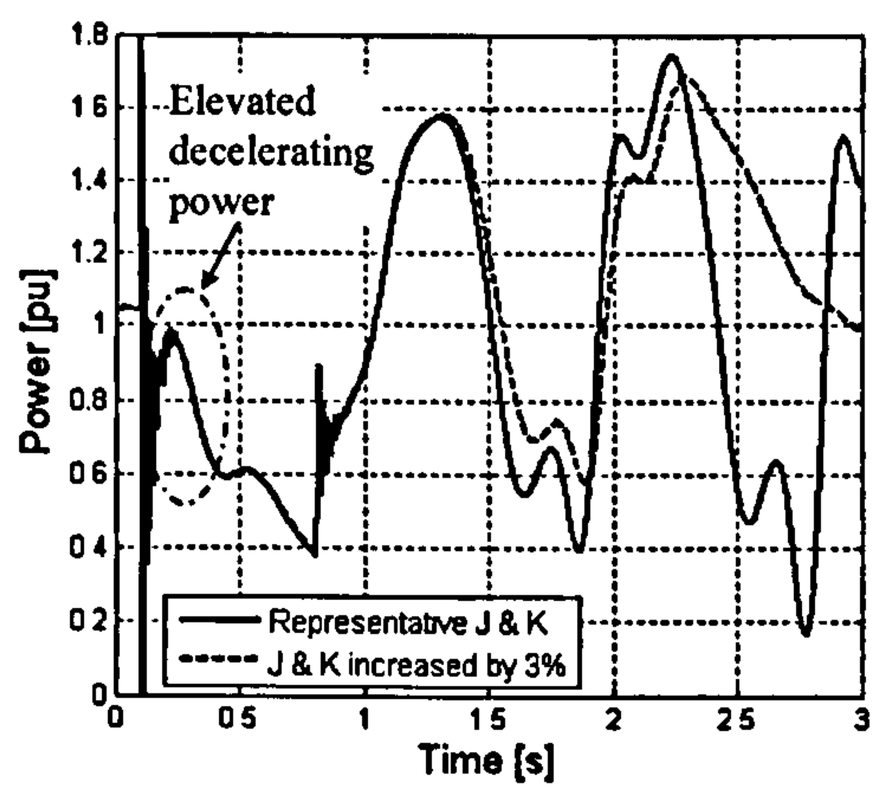

d. Power-time trajectory with two-mass model

Figure 6-4: Stability limits for one- and two-mass models

Figure 6-4a and c both show the speed-time trajectories for two fault scenarios distinguished only by the differences in inertia and stiffness. Figure 6-4b and d show the decelerating power-time trajectories associated with the corresponding speed-time graphs. These scenarios highlight two important points:

i. Critical speeds for the one-mass and two-mass simulations are 1.042pu and 1.038pu respectively compared to the 1.040pu predicted by QSS analysis.
ii. The two-mass case is marginally more stable than the one-mass case under this fault scenario. The reason for this is highlighted in Figure 6-4d as the elevated decelerating power during the initial fault period due to higher rotor speeds.

6.2.4. Comparative stability for selected FRT scenarios

Figure 6-5 shows the dynamic response of the representative one- and two-mass wind farms models to the five fault scenarios of Figure 2-15.

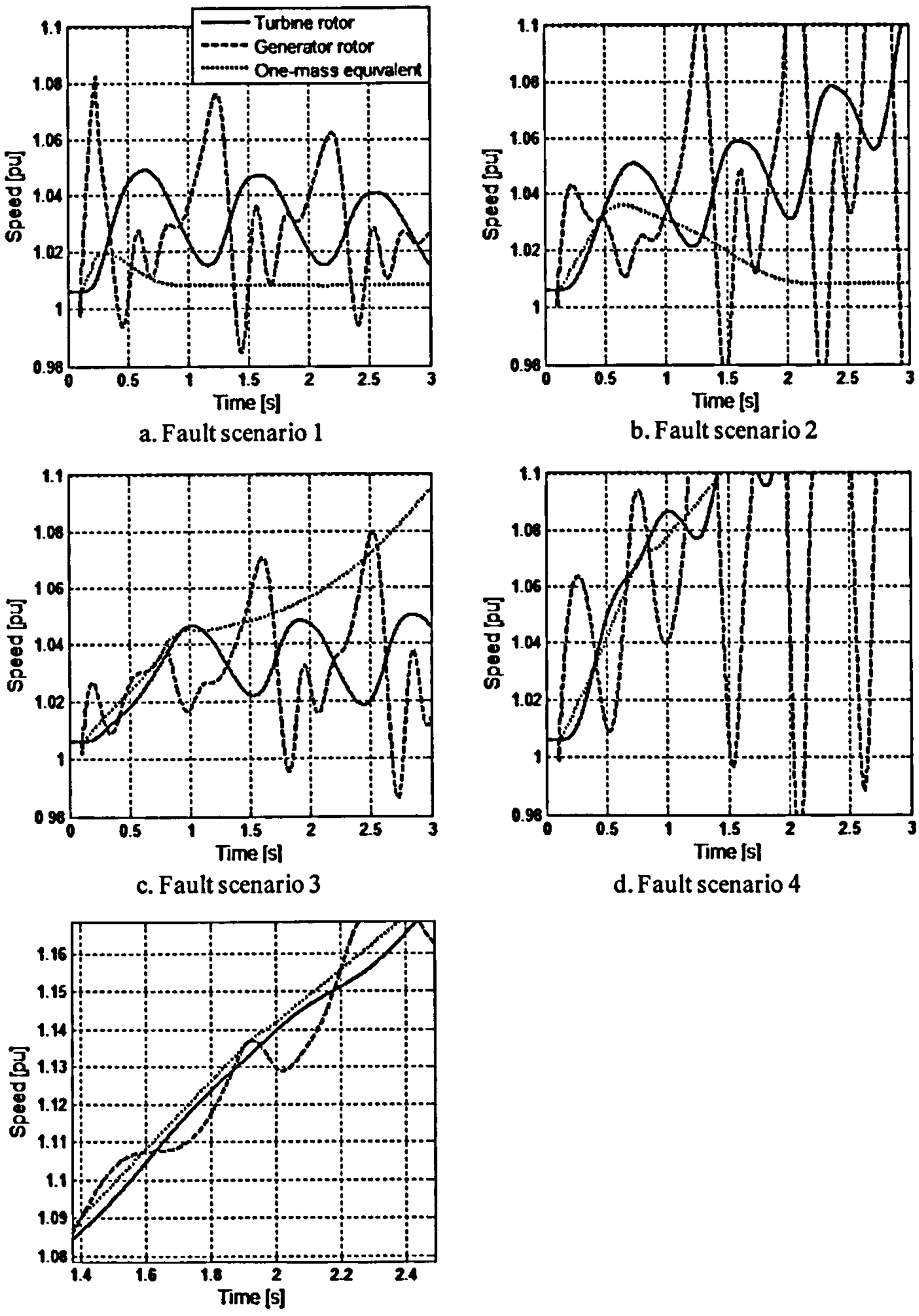

Figure 6-5: Simulation results for five FRT scenarios

Figure 6-5a shows the dynamic response of the representative one- and two-mass wind farms models to fault scenario 1 (zero voltage for 140ms). The one-mass response is evidently more stable than the two-mass response in spite of having the same total inertia and electrical characteristics. The reason for the longer recovery time is the very substantial speed excursions and the relatively low decelerating torque applied at high and low speed regions of the oscillation cycle (refer to Figure C-5). This destabilising effect is shown with greater contrast in Figure 6-5b where it

makes the difference between stable and unstable response to fault scenario 2 (30% voltage for 384ms). The stable response of the one-mass model with speed peaking at 1.036pu contrasts with the QSS prediction, from Figure 5.2, of 1.043pu peak speed and marginal instability. The reason for this better-than-predicted response is the significant transient support offered during shorter fault periods (180ms time constant in the context of a 384ms fault). Figure 6-5c to e confirm the increasingly unstable response predicted by QSS analysis. The full correlation of QSS predictions and the transient results are summarised in Figure 6-6.

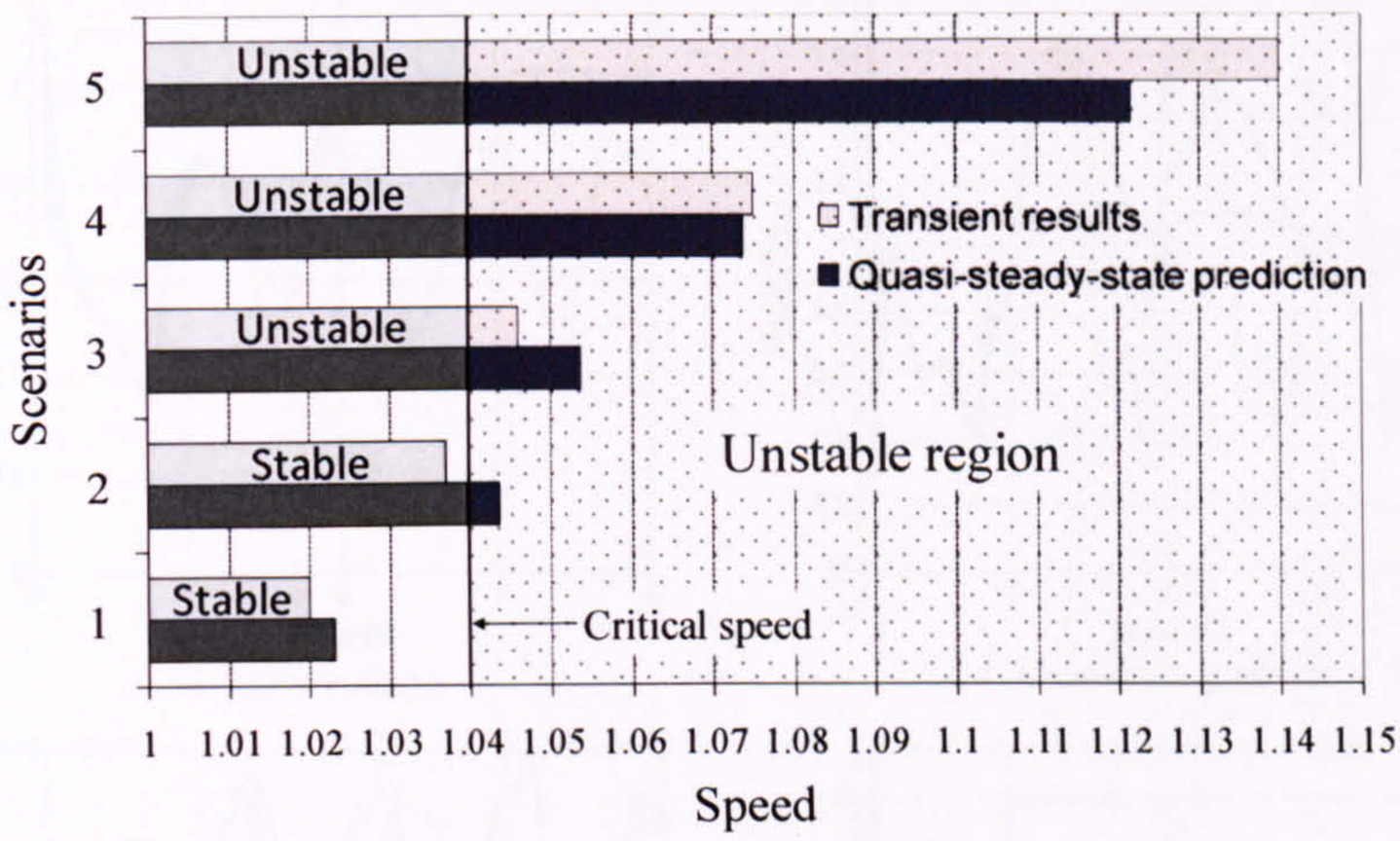

Figure 6-6: Comparison of QSS predictions with transient results

Figure 6-6 confirms that QSS predictions underestimate stability for short faults by neglecting transient support during the fault period and overestimate stability during long faults by assuming peak decelerating power through-out the fault period.

6.3. dRPC Simulation

This section examines the effect of dRPC on wind farm stability by initially using fault scenario 3 as a detailed example and then identifying the magnitude of dRPC required to achieve stability for all fault scenarios.

6.3.1. Analysis of fault scenario 3

FRT response with two levels of dRPC is compared with the base-case in Figure 6-7.

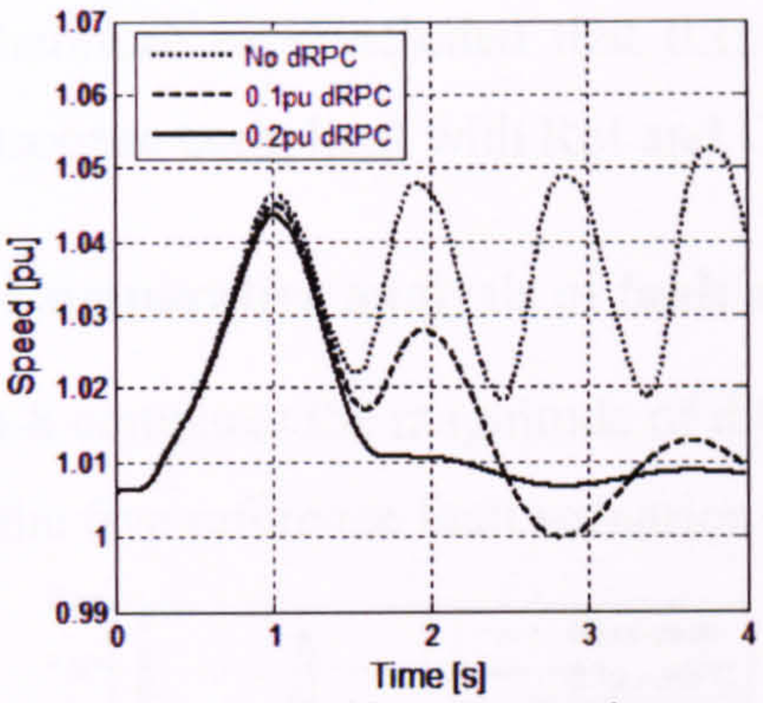

a. Turbine rotor speed

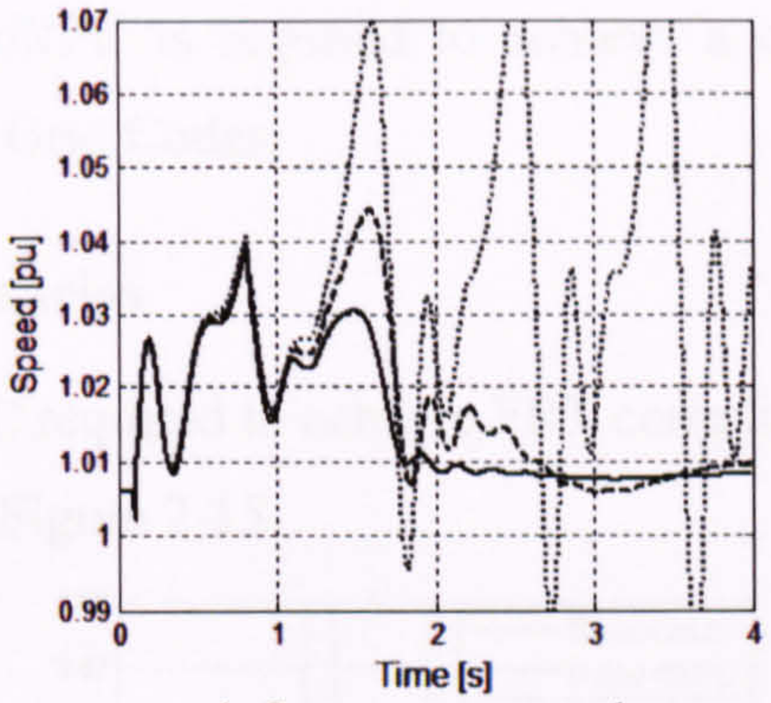

b. Generator rotor speed

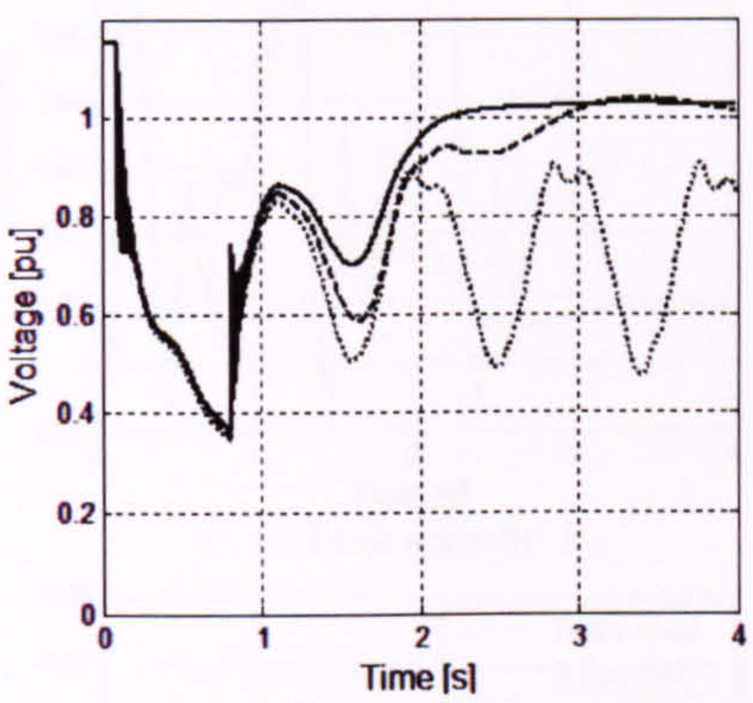

c. Stator voltage

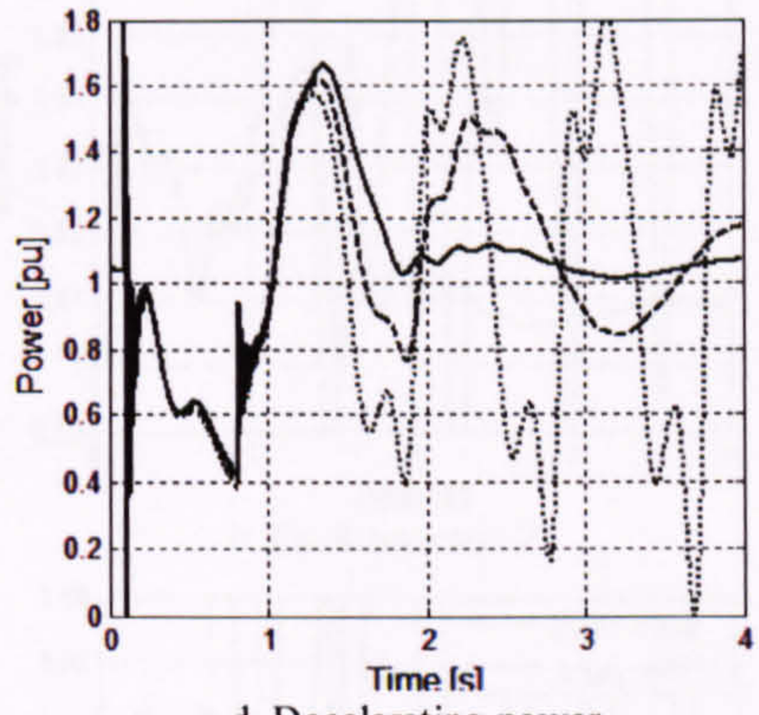

d. Decelerating power

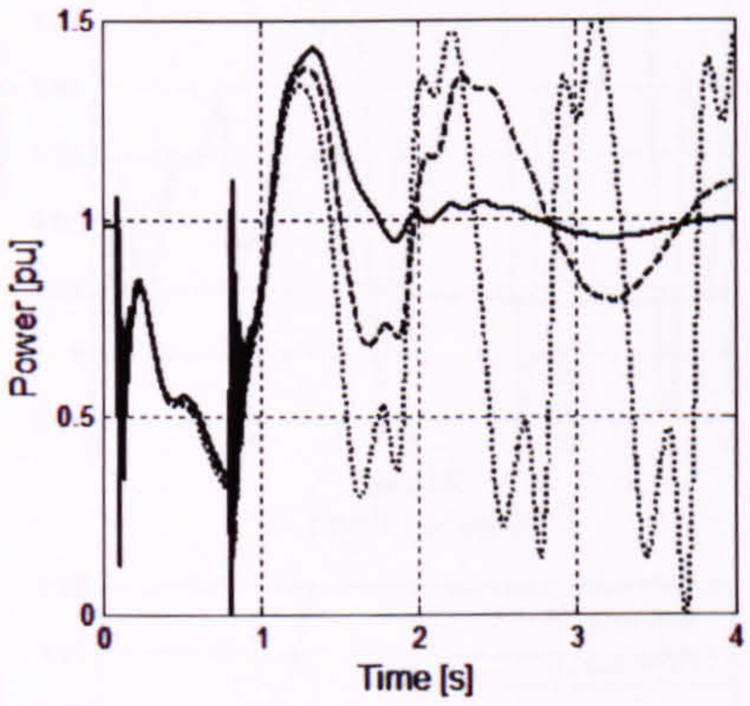

e. Export active power

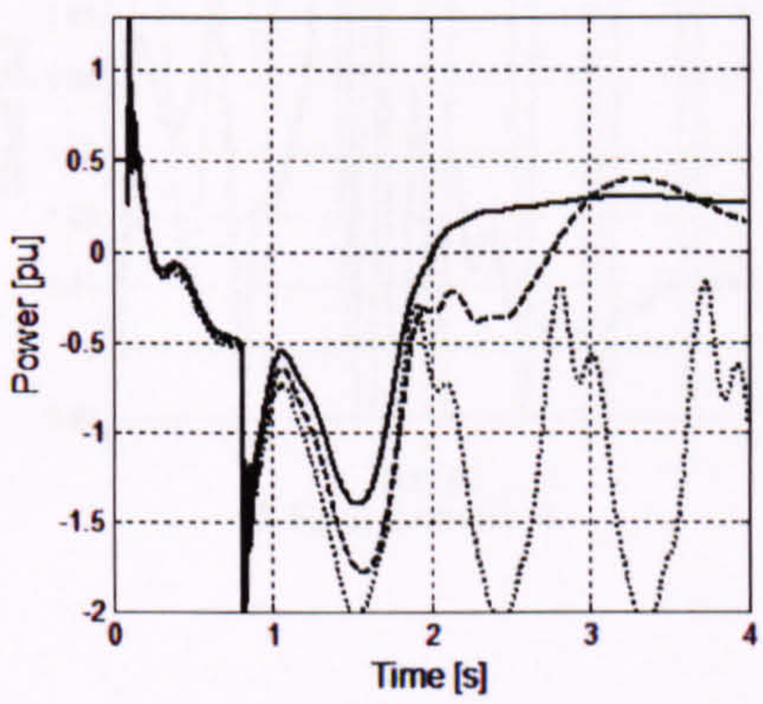

f. Export reactive power

Figure 6-7: Effect of dRPC on wind farm response to fault scenario 3

Figure 6-7a and b show that 0.1pu dRPC is sufficient to stabilise the wind farm although 0.2pu provides more rapid and damped restoration. Figure 6-7c shows the voltage boosting effect of dRPC which results in the elevated decelerating power response shown in Figure 6-7d. Figure 6-7e shows that the RoI and GB Grid Codes requirements for active power export recovery defined by Figure 2-15 are easily met with 0.2pu dRPC. Figure 6-7f shows that 0.2pu dRPC reduces the reactive power import during the initial second after fault clearance and results in a reactive power export by about 1.2 seconds after fault clearance.

It can therefore be concluded that 0.1pu dRPC is required to achieve a clear-cut stable response compliant with RoI and GB Grid Codes.

6.3.2. Comparative analysis of fault scenarios

Figure 6-8 compares the magnitude of dRPC required to achieve FRT compliance for each of the five reference fault scenarios of Figure 2-15.

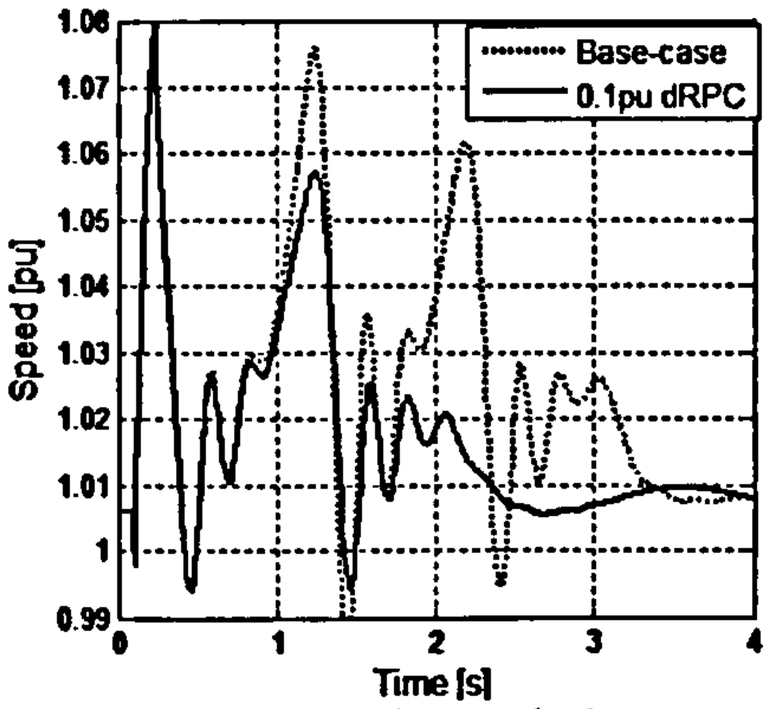

a. Fault scenario 1

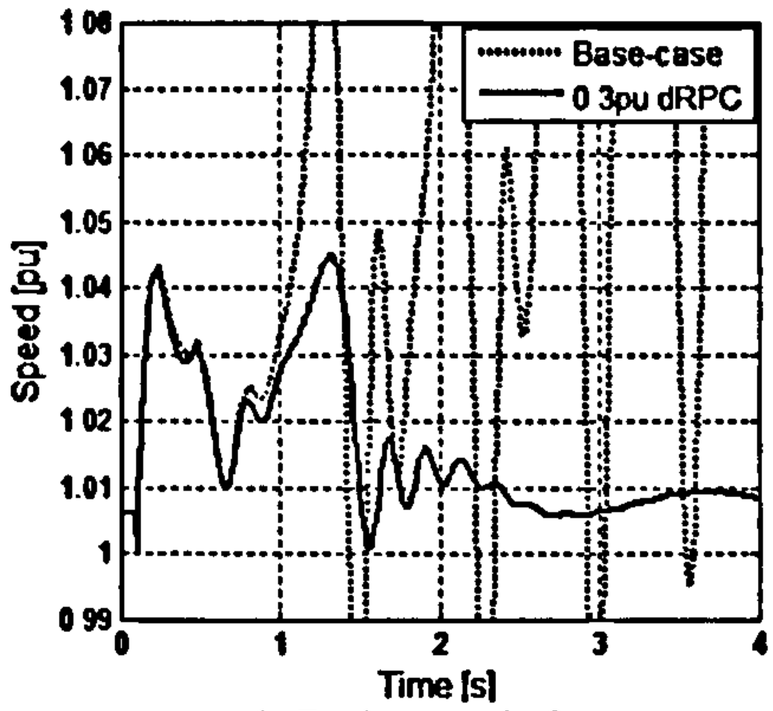

b. Fault scenario 2

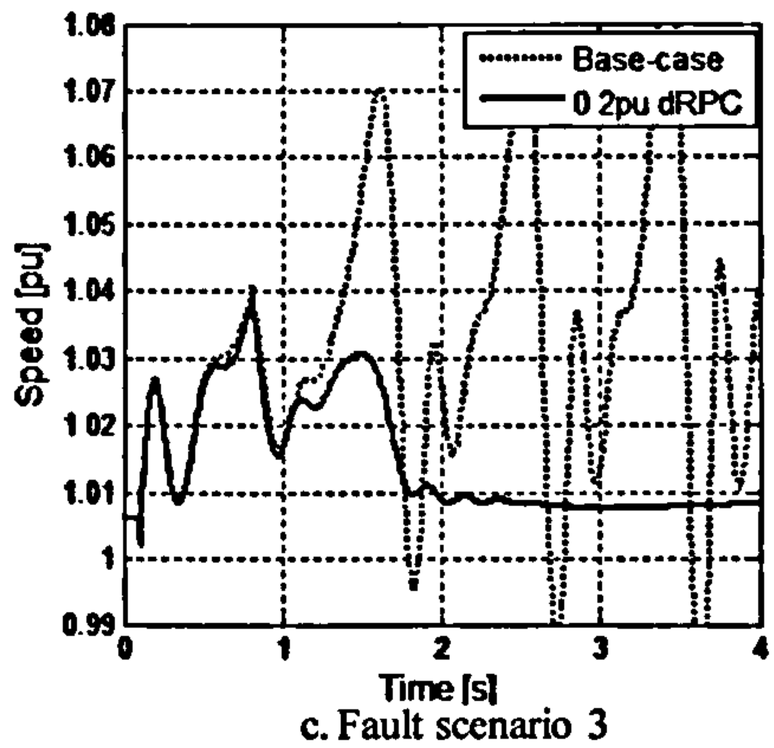

c. Fault scenario 3

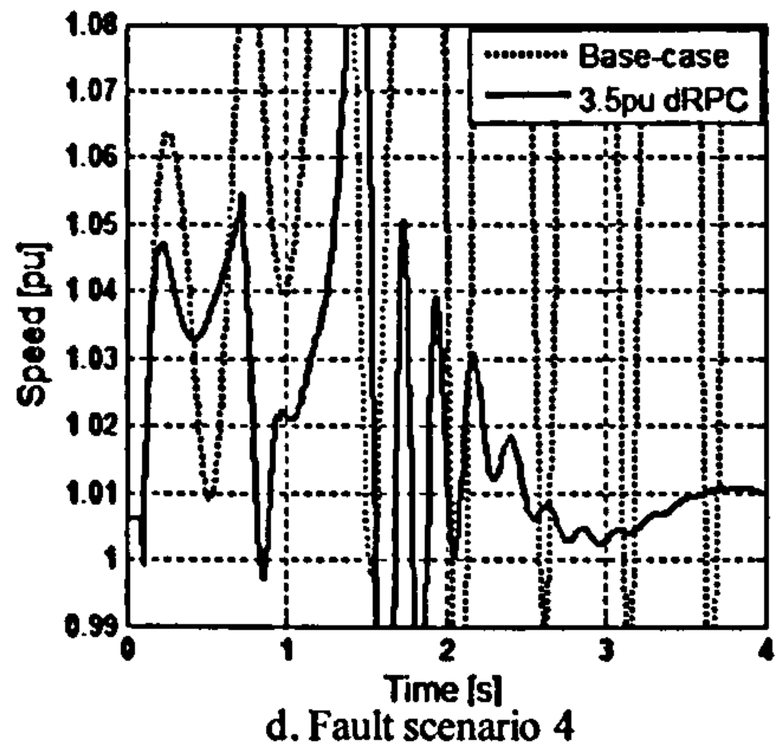

d. Fault scenario 4

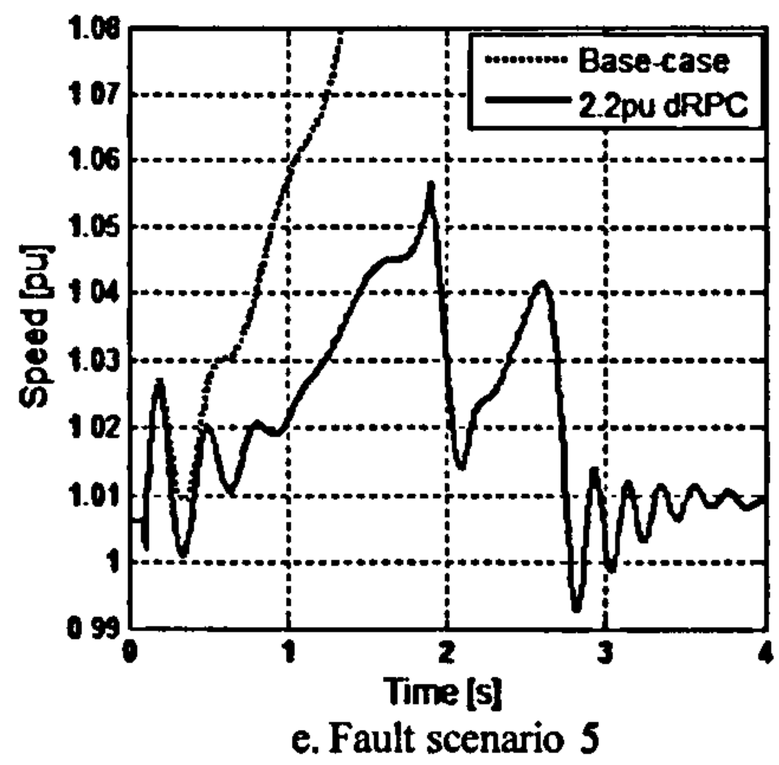

e. Fault scenario 5

Figure 6-8: Application of dRPC to achieve stability for selected fault scenarios

It can be seen that 0.3pu dRPC is sufficient to achieve compliance for the GB Grid Code scenarios in Figure 6-8a, b, c and f. However, the RoI Grid Code scenarios in Figure 6-8d and e require 3.5pu and 2.2pu dRPC respectively to achieve stability.

This magnitude of dRPC would probably be uneconomic for most wind farm projects.

6.4. sDBR Simulation

This section examines the effect of sDBR, in the same manner as performed on dRPC in Section 6.3.

6.4.1. Analysis of fault scenario 3

FRT response with two levels of sDBR is compared with the base-case in Figure 6-7.

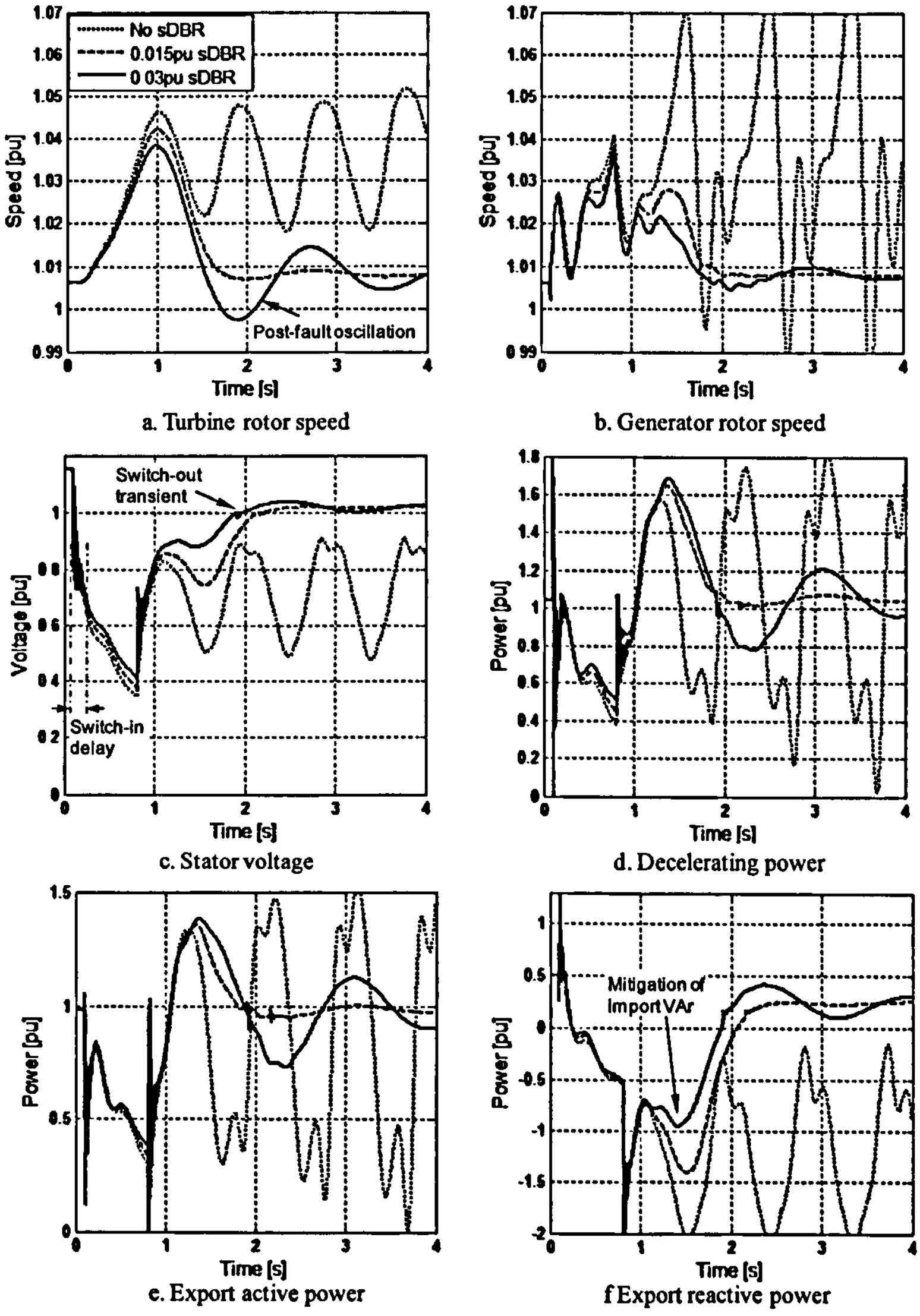

a. Turbine rotor speed

b. Generator rotor speed

c. Stator voltage

d. Decelerating power

e. Export active power

f Export reactive power

Figure 6-9: Effect of sDBR on wind farm response to fault scenario 3

Figure 6-9a and b show that 0.015pu sDBR is sufficient to stabilise the wind farm and restore pre-fault export power within 0.5 seconds. Increasing sDBR to 0.03pu provides faster deceleration and improved reactive power response (Figure 6-9f) but also introduces post-fault oscillations. Figure 6-9c shows the improved voltage response with sDBR which results in the elevated decelerating power response shown in Figure 6-9d. Furthermore, the switching in and out of sDBR can be observed by the point of initial divergence of the three trajectories (about 0.1 second after fault initiation) and the small voltage transients as the trajectories pass through 1pu (just over one second after fault clearance). Figure 6-9e shows that the RoI and GB Grid Codes requirements for active power are met more effectively with 0.015pu sDBR because of the post-fault power oscillations introduced by increased resistance.

It can therefore be concluded that 0.015pu sDBR is the optimal resistance for FRT compliance of the representative wind farm with for fault scenario 3.

6.4.2. Comparative analysis of fault scenarios

Figure 6-10 compares the magnitude of sDBR required to achieve FRT compliance for each of the five reference fault scenarios.

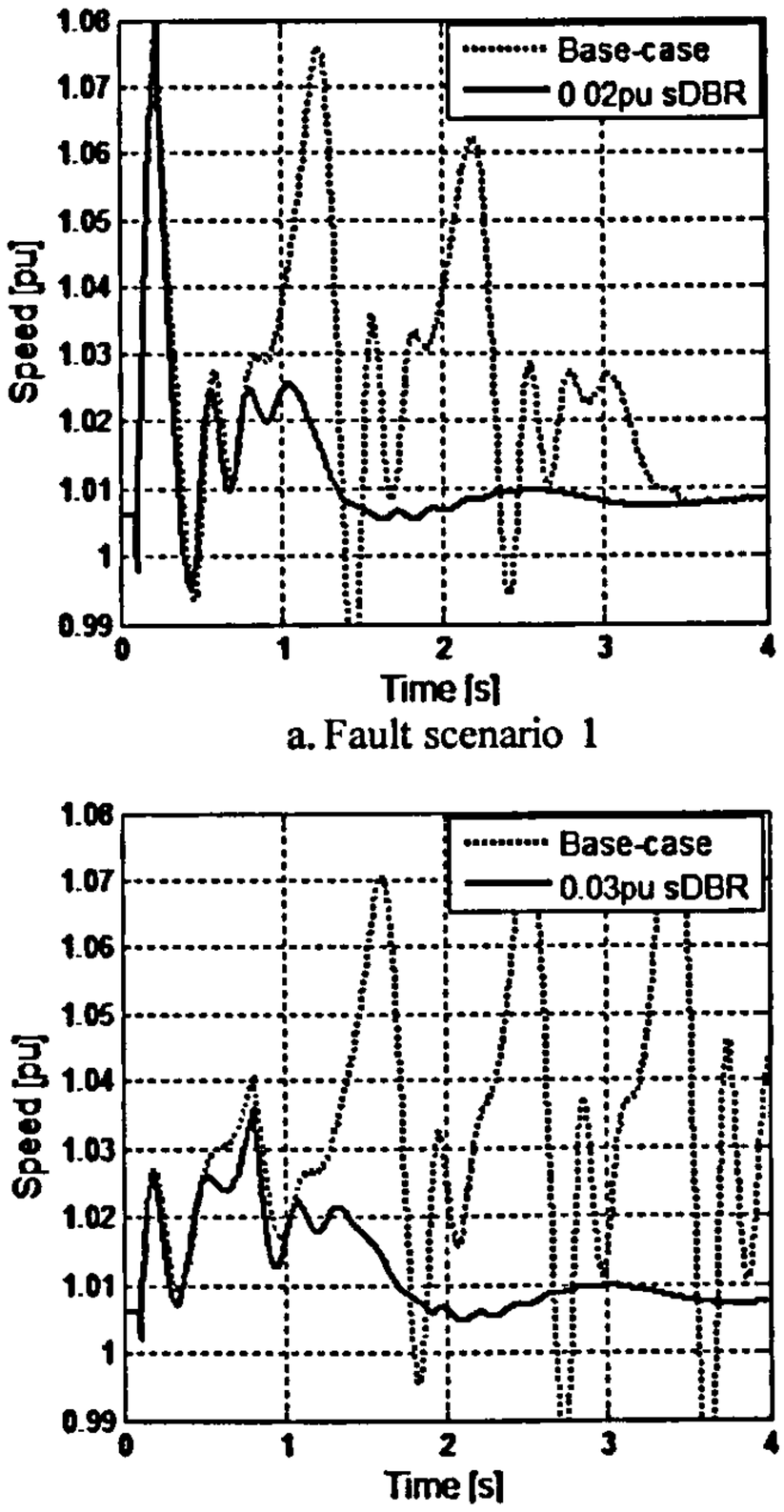

a. Fault scenario 1

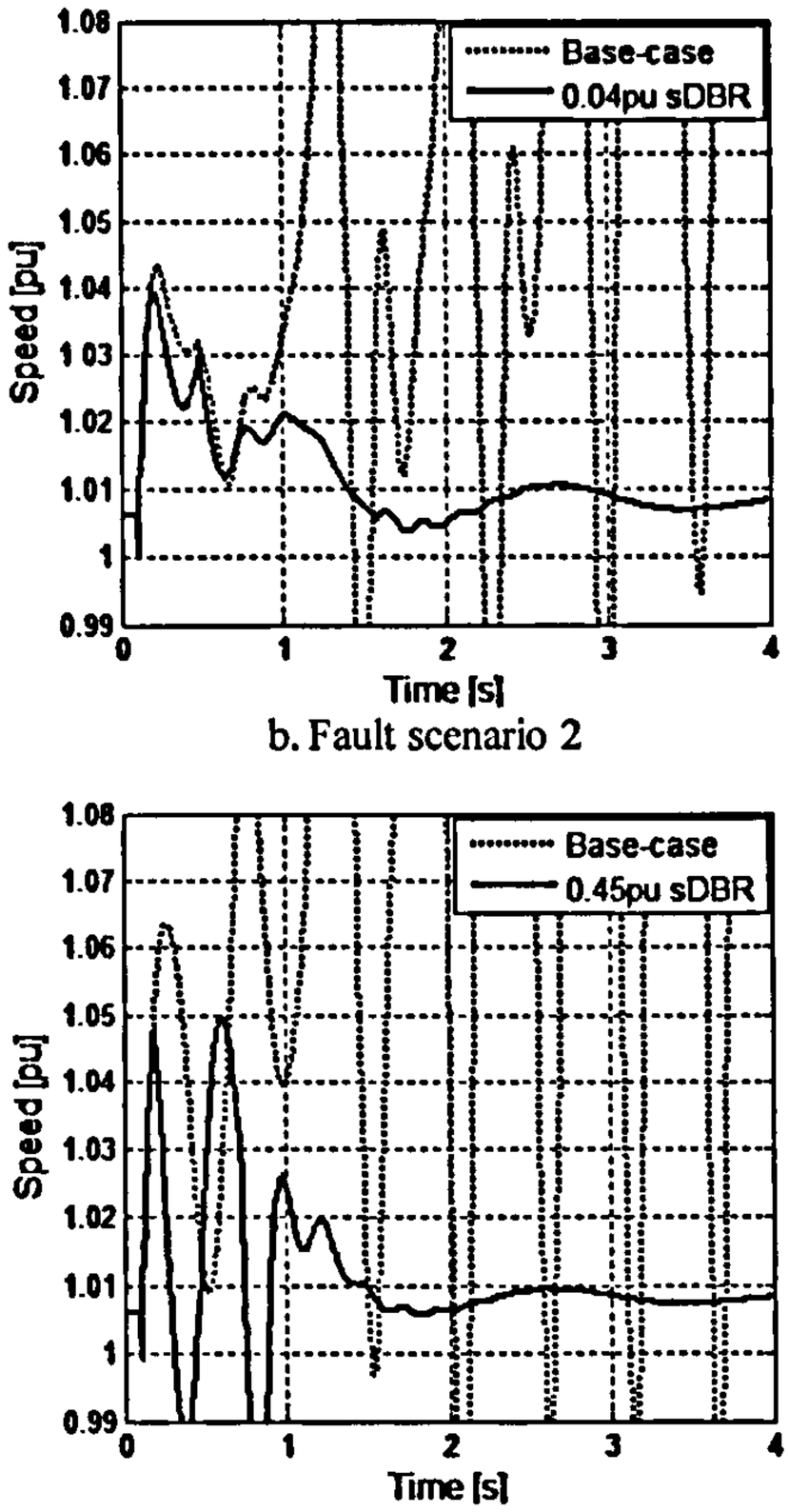

b. Fault scenario 2

c. Fault scenario 3

d. Fault scenario 4

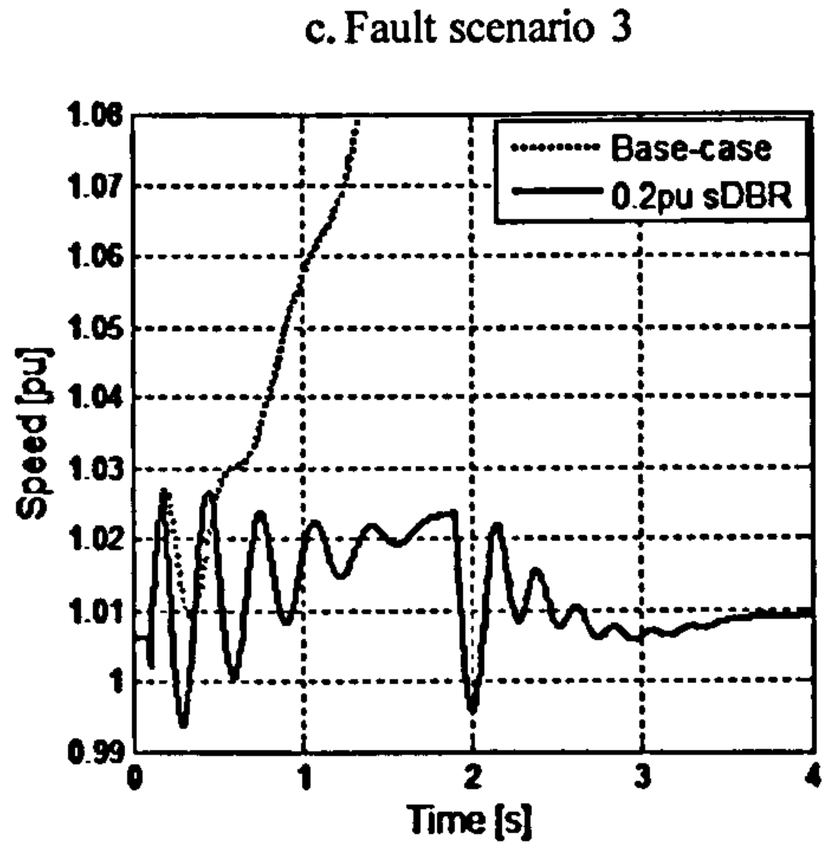

e. Fault scenario 5

Figure 6-10: Application of sDBR to achieve stability for selected fault scenarios

It can be seen that 0.04pu sDBR is sufficient to achieve compliance for the GB Grid Code scenarios in Figure 6-10 a, b, c and f. However, the RoI Grid Code scenarios in Figure 6-10d and e require 0.45pu and 0.2pu sDBR respectively to achieve stability. This magnitude of sDBR would result in a substantial increase in the heat dissipated and the resulting size and cost of the resistor bank.

6.5. Comparison of FRT Technologies

6.5.1. Comparison of dRPC and sDBR magnitudes

Table 6-1 summarises the results from Sections 6.3 and 5.5, comparing the magnitudes of dRPC and sDBR required to achieve stability for each of the reference fault scenarios derived from GB and RoI Grid Codes.

	Fault scenarios (and national code from where scenario derives)					
	1(GB)	2 (GB)	3 (GB)	4 (RoI)	5 (RoI)	6 (GB)
dRPC magnitude (pu)	0.1	0.3	0.2	3.5	2.2	0.2
sDBR magnitude (pu)	0.02	0.04	0.03	0.45	0.2	0.02
Ratio of dRPC to sDBR	5	7.5	6.7	7.8	11	10

Table 6-1: Summary minimum dRPC and sDBR magnitudes required for FRT stability

Table 6-1 shows that the minimum required magnitude of dRPC to achieve stability is between five and eleven times greater than the required magnitude of sDBR. It is also notable that both dRPC and sDBR magnitudes need to be greater by a factor of about ten for the RoI scenarios.

6.5.2. Comparison of dRPC and sDBR response

Figure 6-11 reproduces the turbine rotor responses of Figure 6-7a and Figure 6-9a in order to compare the effect of dRPC and sDBR on wind turbine response.

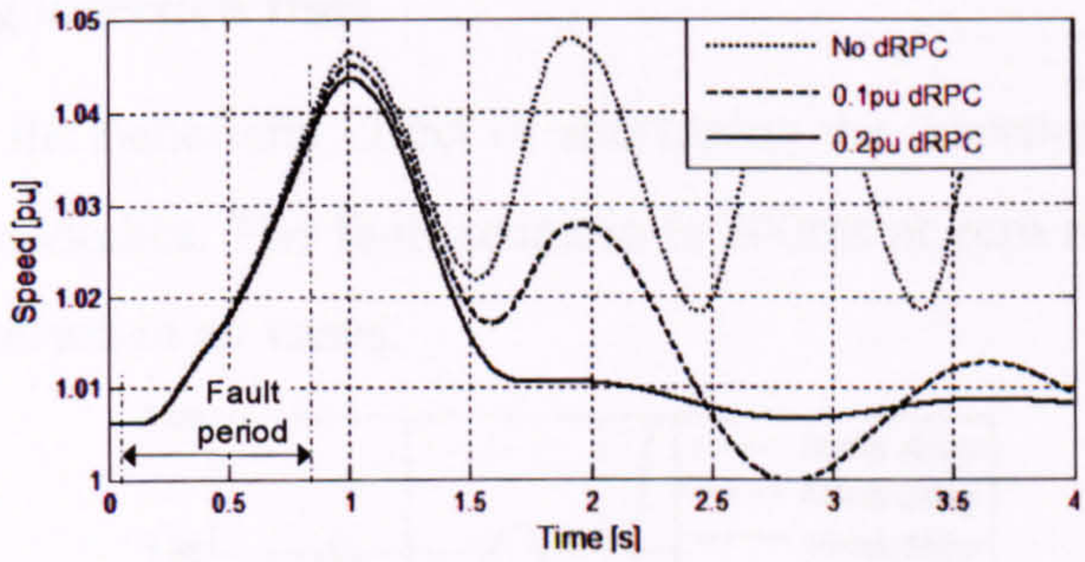

a. dRPC response

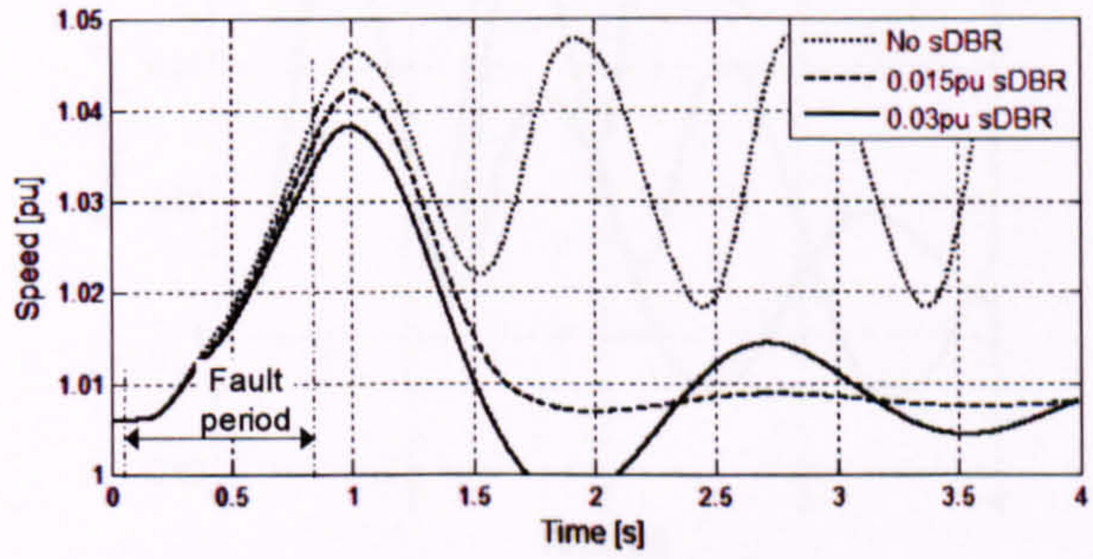

b. sDBR response

Figure 6-11: Comparison of effect of dRPC and sDBR on FRT response

The first notable difference is that although sDBR responds more slowly than dRPC (80ms compared to 10ms) the effect is much more pronounced during the fault period. As a result, the reduction of speed at fault clearance is 0.007pu for 0.03pu sDBR but only 0.002pu for 0.2pu dRPC. The much greater effectiveness of sDBR during the fault period arises from the fact that its voltage boosting effect relates to current and is therefore magnified by the high transient currents. In contrast, the voltage boosting effect of dRPC relates to the square of voltage and is therefore greatly diminished in the fault period. The effect of dRPC is seen to apply strongly after fault clearance when the wind farm voltage rises and its voltage-boosting reactive power contribution rises with its square.

The second notable difference is that increasing dRPC results in a more damped speed restoration whereas increased sDBR tends to cause an over-swing with resulting post-fault oscillations. A major reason for this difference is that dRPC has near-continuous and instantaneous thyristor control whereas sDBR is switched as a single discrete unit.

6.6. Advanced sDBR Control

The purpose of this Section is to give an indication of the possible stability improvements that may be achieved using more sophisticated sDBR control.

6.6.1. Shortening insertion time

Figure 6-12 shows the beneficial effect of shortening the insertion time of sDBR by using faster acting switches. The fault scenario is 200ms at zero residual voltage and 0.05pu sDBR is inserted in all cases.

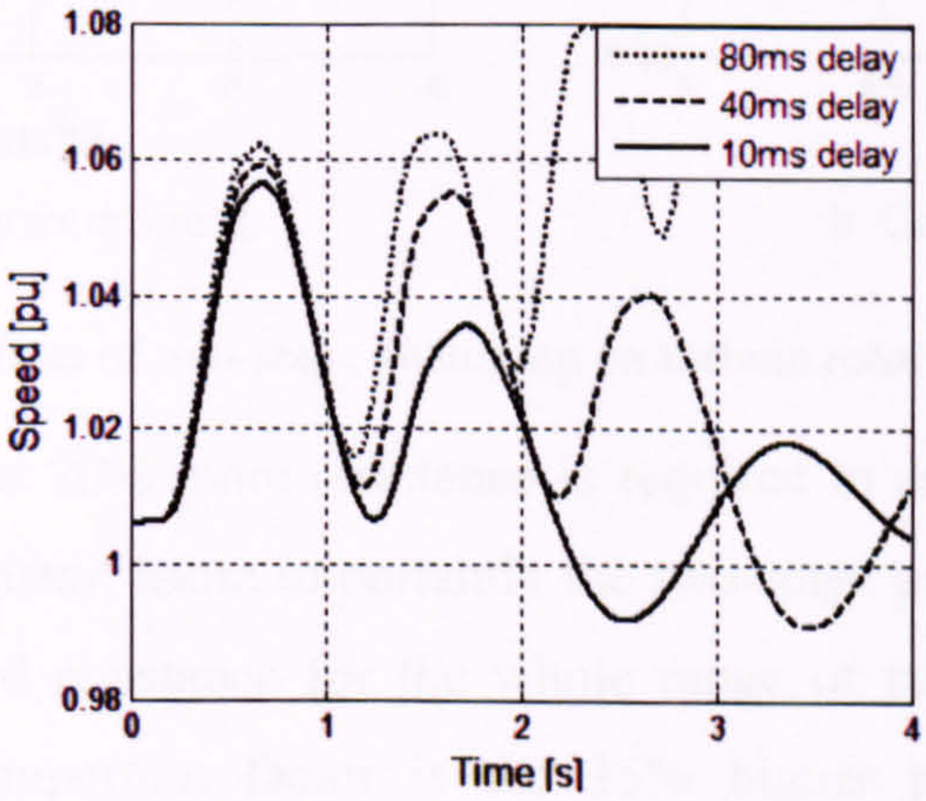

Figure 6-12: Effect of shortening insertion time on turbine rotor speed recovery

6.6.2. Multi-stage resistors

Multistage sDBR allows a high value of resistance to be inserted initially and reduced as the voltage recovers. This is particularly helpful for longer fault scenarios. Figure 6-13 shows a two-stage braking resistor configuration with bypass switches, S1 and S2, controlled independently by a voltage-dependent controller.

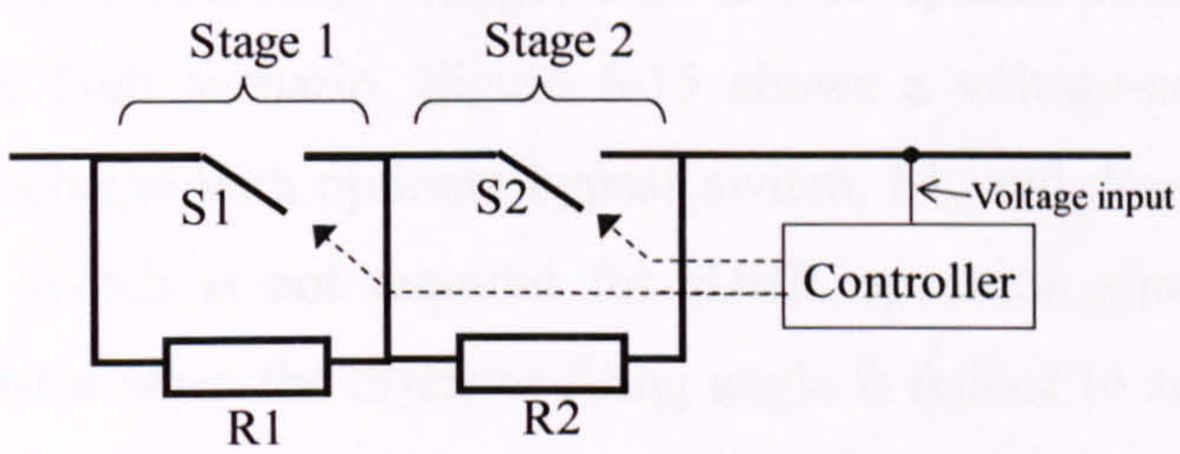

Figure 6-13: Two-stage switching scheme

Figure 6-14 compares the two-stage sDBR scheme, with resistances of 0.09pu and 0.19pu, with two single stage schemes with resistances of 0.34pu and 0.28pu respectively in response to fault scenario 4. The two-stage control scheme switches out the larger resistance at 0.96pu voltage and the smaller resistance at 1.04pu voltage whereas the singe-stage scheme both switch-out at 1.04pu voltage.

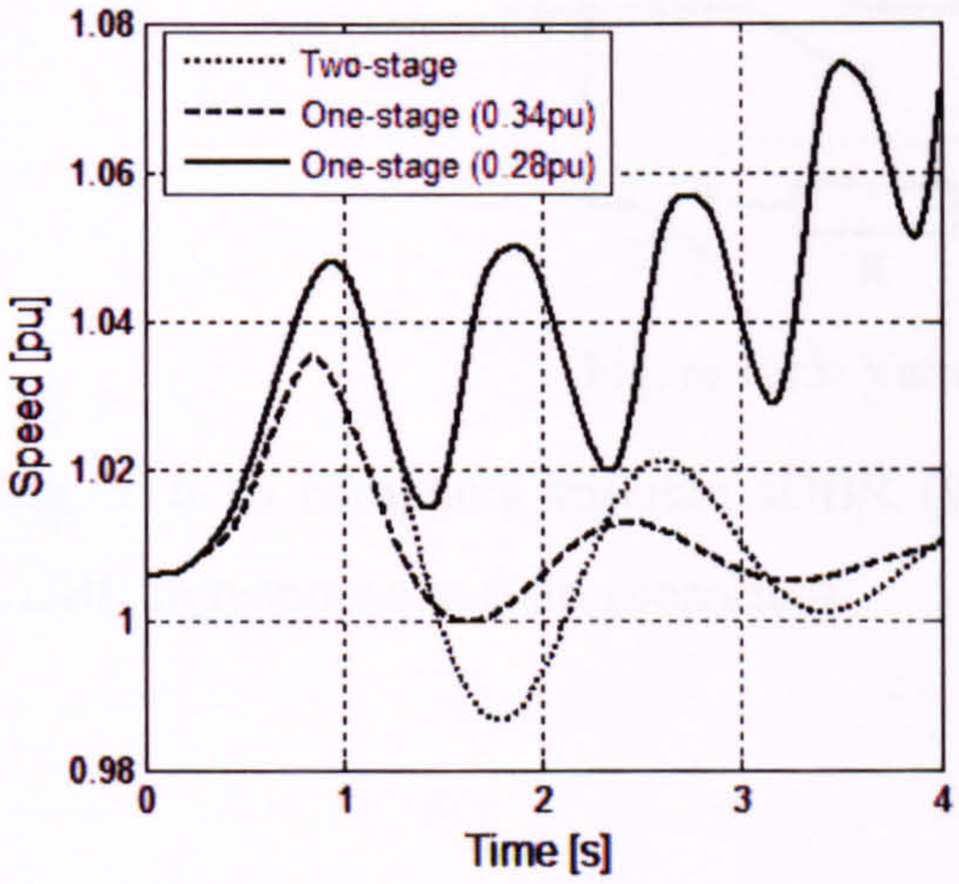

a. Turbine rotor speed

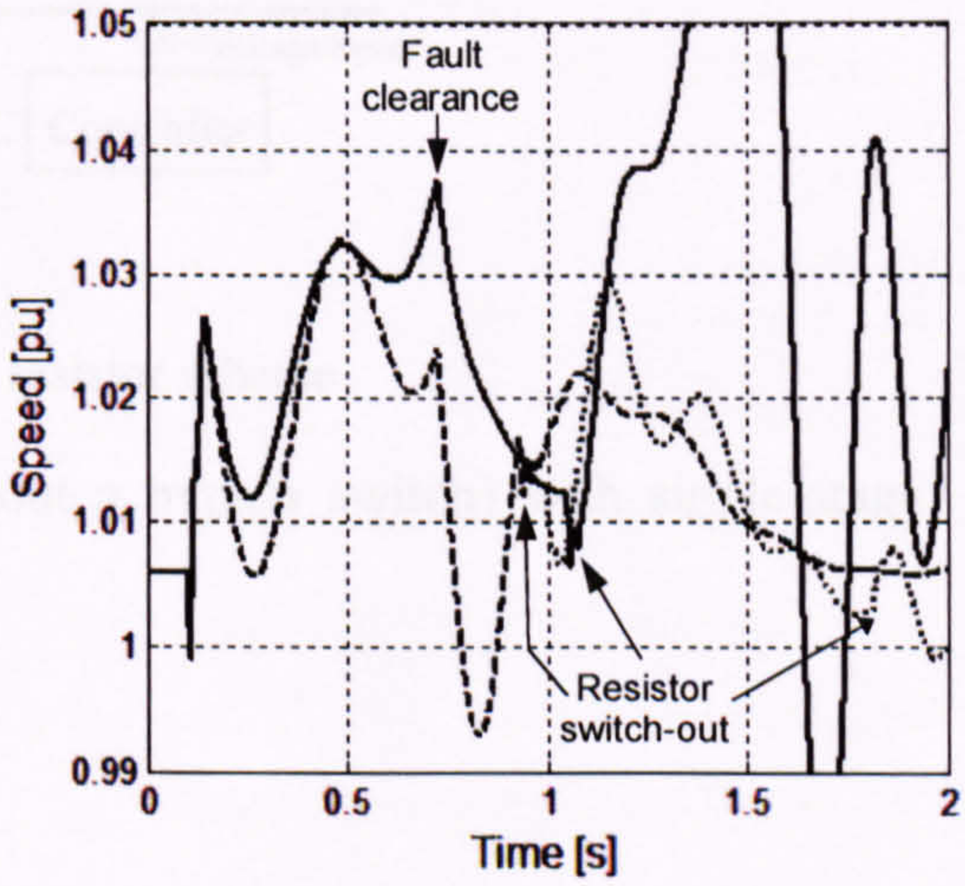

b. Generator rotor speed

Figure 6-14: Effect of two-stage switching on turbine rotor speed recovery

Figure 6-14 shows that 20% more resistance is required to achieve similar stability with a single stage resistor. More importantly the two-stage give more flexibility for optimising the inserted resistance for the whole range of possible fault scenarios. Another potentially important factor is the 15% higher peak torque switching transient arising when bypassing the larger single resistor.

Multistage resistors increase the cost and complexity of sDBR and, as a result, single stage sDBR in conjunction with variable dRPC may be a preferred solution.

6.6.3. Variable resistance

Variable resistance sDBR allows the value of inserted resistance to be continuously varied in response to recovery voltage. This allows optimisation of the scheme's response for any fault scenario. Figure 6-15 shows a voltage-controlled variable braking resistor scheme with optional bypass switch, S1, and disconnection switch, S2. The bypass switch is not required for sDBR operation since the soft-starter bypasses the resistor when the thyristor firing angle is reduce to zero. However, the bypass switch does reduce the operational loss of the scheme albeit with the significant disadvantage of delaying sDBR insertion by about 30ms. Switch S2 allows the resistor to be disconnected when using the soft starter in its more common role of reducing the inrush transient during FSWTG grid connection.

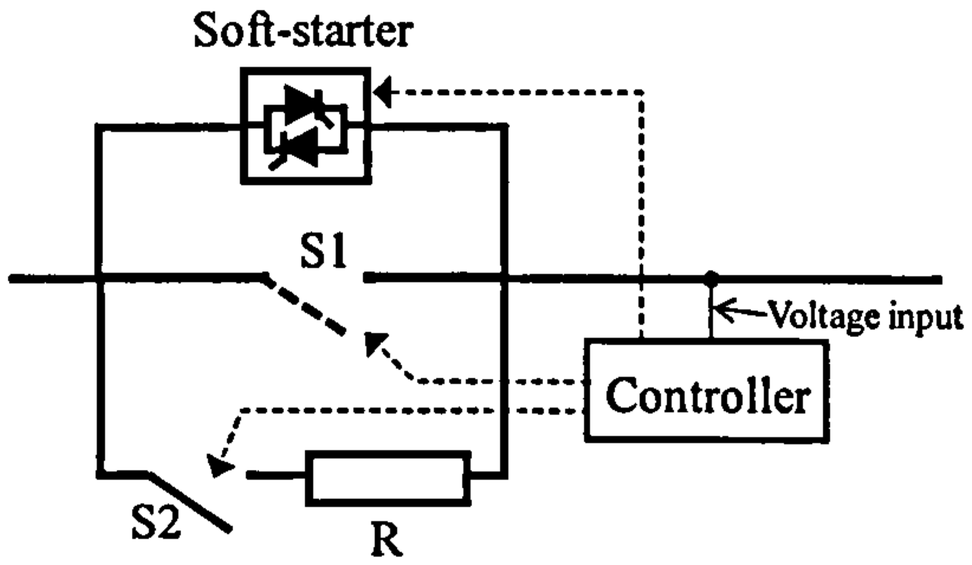

Figure 6-15: Variable resistor scheme

Figure 6-16 compares variable sDBR (without a bypass switch) with single-stage sDBR in response to fault scenario 4.

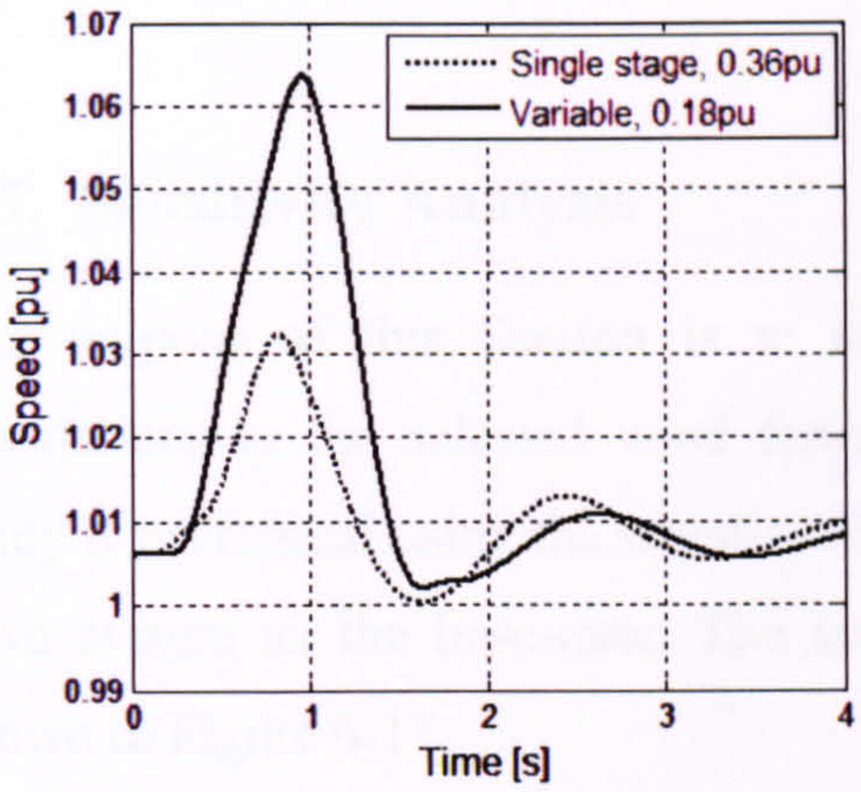

a. Turbine rotor speed

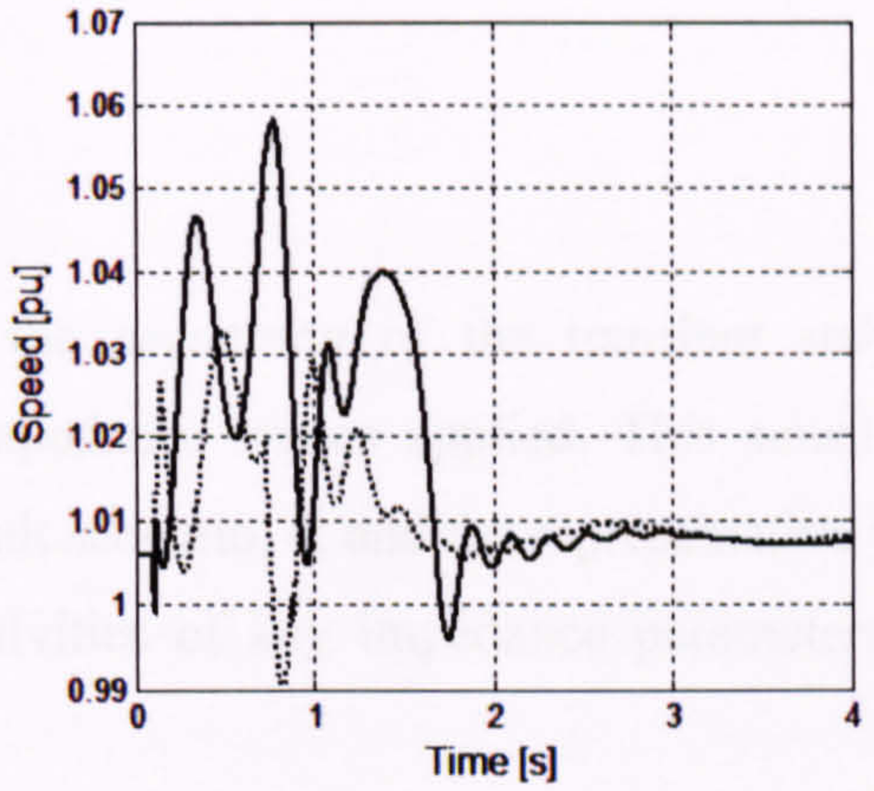

b. Generator rotor speed

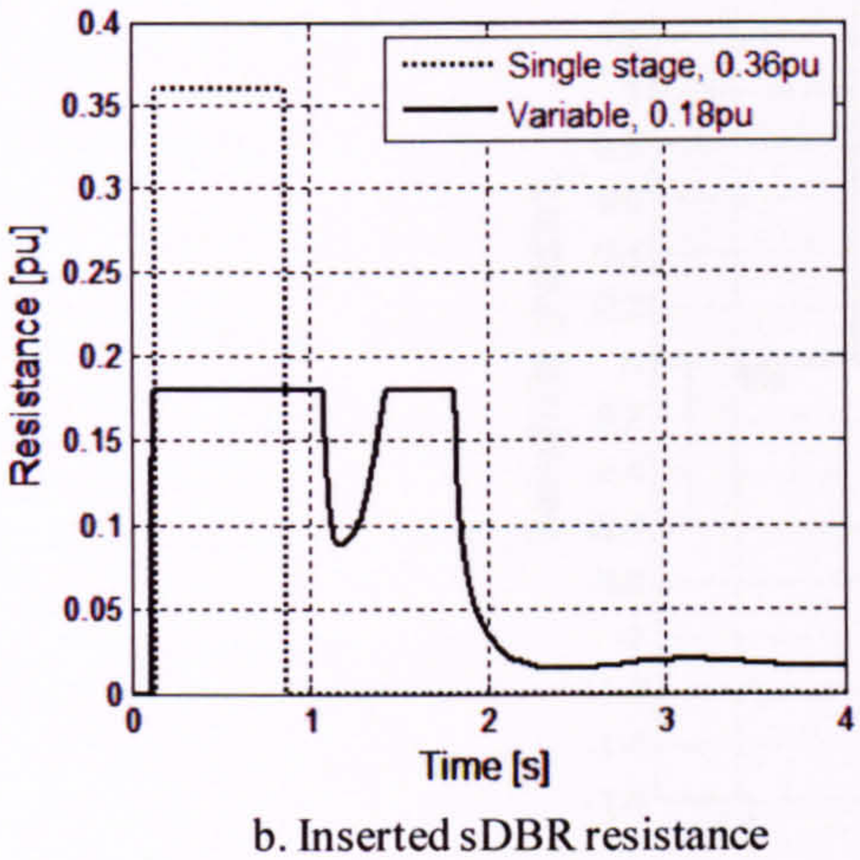

b. Inserted sDBR resistance

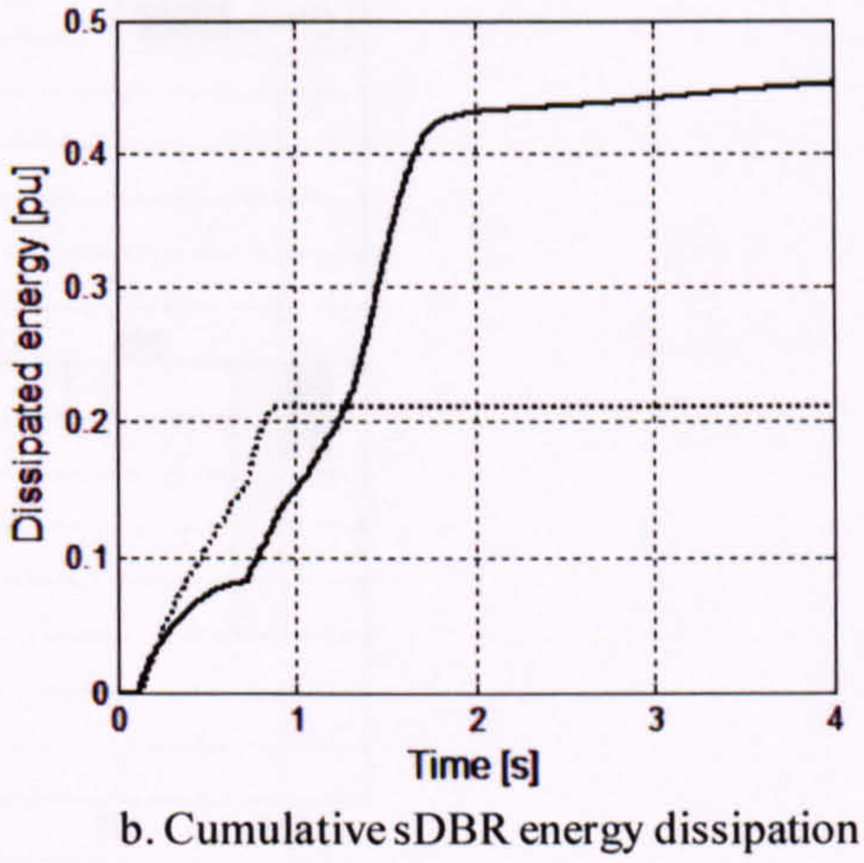

b. Cumulative sDBR energy dissipation

Figure 6-16: Effect of variable resistance on speed recovery and sDBR energy dissipation

Figure 6-16a and b show that comparable FRT stability is achieved by a variable scheme with only 50% of the resistance of a fixed scheme. Figure 6-16c shows the variation of inserted resistance during the fault and recovery period. Figure 6-16c shows that the reduced resistance does not, however, result in reduced overall energy dissipation because of the extended insertion time required for the variable scheme to achieve stability. The main advantage of variable sDBR is to reduce the peak and transient torques imposed by sDBR and allow optimised response to a wide range of faults. The disadvantage lies in the significantly increased complexity and cost of the scheme.

6.7. Sensitivity Analysis

The purpose of this Section is to test the sensitivity of the transient stability simulations to the selected wind farm impedance values applied. This sensitivity study is performed using the worst-case fault scenario, 4, and the representative wind farm system as the base-case. The sensitivities of key impedance parameters are shown in Figure 6-17.

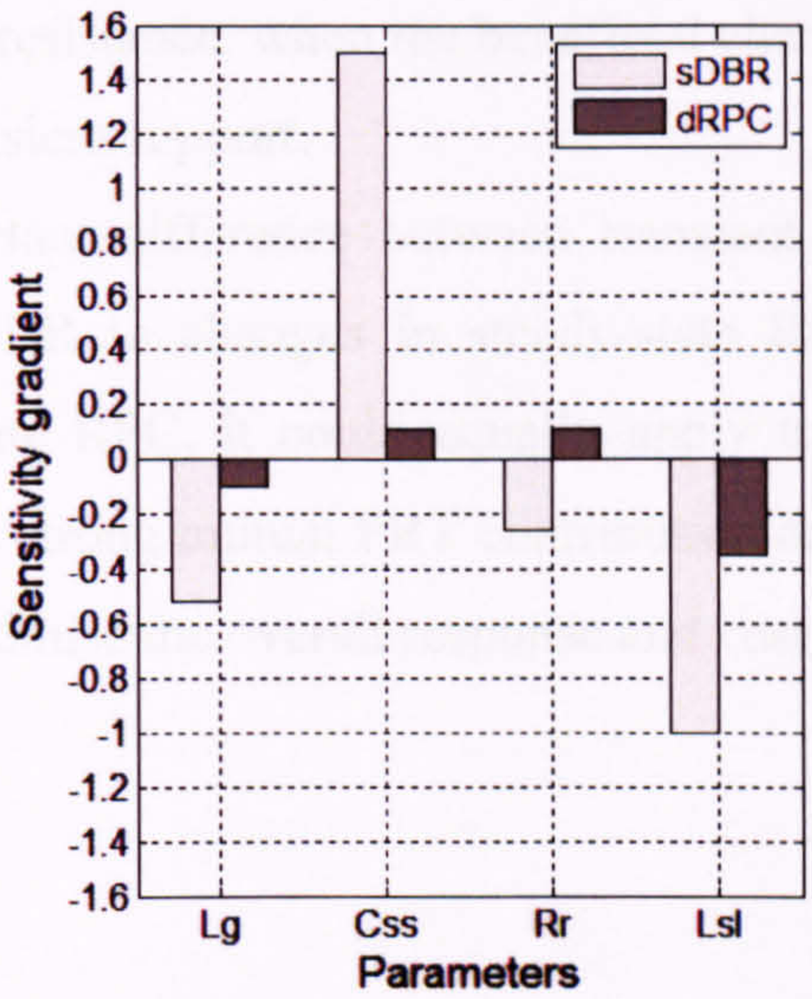

Figure 6-17: Sensitivity gradients

The sensitivity gradients of Figure 6-17 are very different to those used for QSS sensitivity in Figure 5-14. It is not possible to define a stability speed margin for transient simulations. Sensitivity gradients for the transient results are therefore defined by Eq. 6-4.

$$Grad = -\frac{\Delta(sDBR_{\min})}{\Delta(L_g)} \qquad (6\text{-}4)$$

Where $\Delta(sDBR_{min})$ is the change in minimum magnitude of sDBR required to achieve stable operation and $\Delta(L_g)$ is the change in grid inductance that brought about the change in $sDBR_{min}$.

It can be seen from Figure 6-17 that sDBR magnitude is more sensitive to fractional change than dRPC. However, this is not a highly significant comparison because the cost sensitivity of sDBR to changes in magnitude is much less than dRPC. A more meaningful way of comparing technologies for future work would be to use a cost rather than magnitude sensitivity function.

By comparing the transient and QSS sensitivity gradients of Figure 6-17 and Figure 5-15b respectively, it is evident that the relative magnitude of sensitivities to the selected parameters is broadly similar, with the notable exception of the sensitivity of sDBR to rotor resistance. The negative sensitivity to rotor resistance relates to the change in transient time constant of Eq. D-1. The shortening transient time constant with increasing rotor resistance results in reducing decelerating power during the fault period, offsetting the benefits of an increasingly stable QSS characteristic. However, it should be noted that this sensitivity becomes strongly positive at higher base-case values of rotor resistance, when the beneficial change in QSS characteristic outweighs the loss of transient support.

A less severe but important difference between transient and QSS results is the greater sensitivity of sDBR to changes in steady-state RPC (Css). Although the analysis refers steady-state RPC, it could equally apply to dRPC, suggesting that sDBR and dRPC provide strong mutual FRT contribution and should be treated as a single FRT scheme to optimise the overall response and cost.

6.8. Summary

This Chapter demonstrates that the benefits of dRPC and sDBR, inferred from QSS analysis, are realised by transient simulation. It is shown that dRPC and sDBR can each improve the FRT performance of the base-case representative wind farm to achieve compliance with both GB and RoI Grid Codes. However, both technologies are severely challenged by the onerous RoI fault scenarios and compliance would be economically challenging for dRPC and technically challenging for sDBR.

Improvements to the FRT performance of the basic single-stage sDBR, are shown to arise by shortening its insertion time or varying its resistance, either by multi-stage or continuous control. These options would incur additional costs and would only be applied if justified by the particular compliance requirements. Proving the technical and commercial viability of these advanced techniques would require further work.

Wind farm stability with sDBR is shown to be adversely affected by increasing rotor resistance, contrary to the inference of QSS sensitivity analysis (Section 5.7) and dynamic rotor resistance (Section 3.5). sDBR may therefore be disadvantaged in comparison to dRPC by increasing rotor resistance because of the weakening of transient deceleration benefits that sDBR provide during the fault period.

The sensitivity analysis also highlights the large sensitivity of sDBR to the presence of RPC. This sensitivity highlights that the relationship between sDBR and dRPC is mutually enhancing rather than competitive. A FRT scheme should therefore integrate the control of sDBR and dRPC to ensure minimum cost and maximum stability.

7. Experimental Demonstration

7.1. Introduction

The transient analysis of Chapter 6, with the support of QSS analysis in Chapter 5, is the primary means of demonstrating the performance-enhancing effects of sDBR in this Thesis. The simplicity of the mechanically switched sDBR scheme means that simulation results provide a high-level of confidence in the concept and the approximate magnitude of its beneficial effects. A large-scale demonstration site would be the most appropriate next step in demonstrating the concept. However, in the absence of a suitable large-scale site, the purpose of the experimental work in this Chapter is to illustrate the sDBR concept using a very small-scale representation of a wind farm and grid system. The experimental work had to be completed within a very limited time and cost budget using an existing, non-optimal generator and drive. The substantial part of the challenge of this experimental work was therefore to obtain a representative demonstration of the effects of sDBR on the FRT performance of a large-scale wind farm system with limited resources.

7.2. Modelling Overview

In order to simplify the test rig, a lumped representation of a FSWT wind farm with distributed sDBR was used, as shown schematically in Figure 7-1.

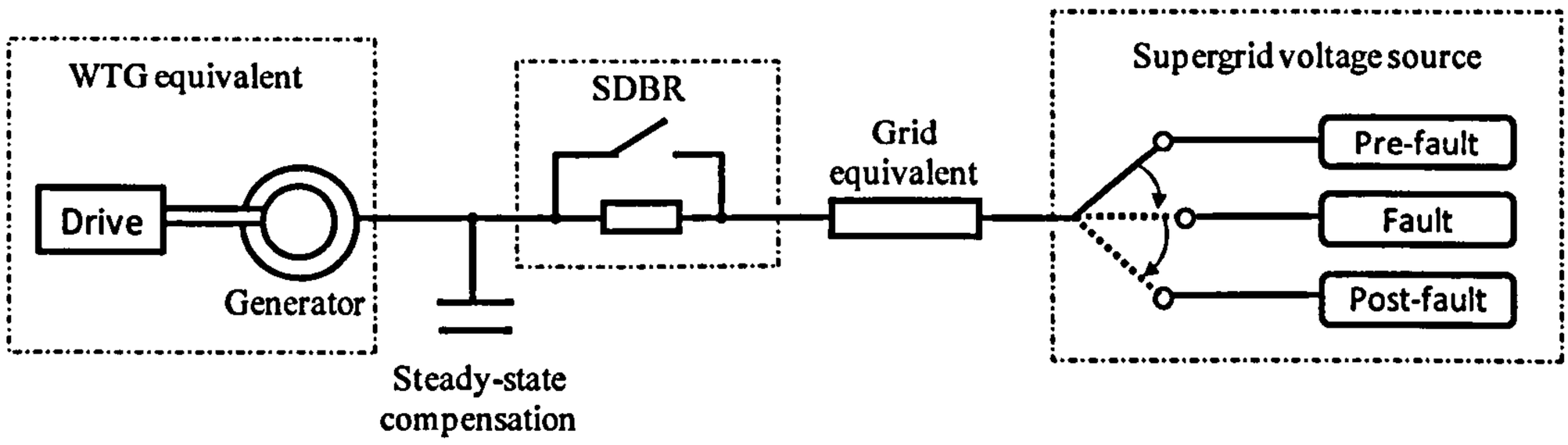

Figure 7-1: Schematic representation a FSWT wind farm with distributed sDBR

The following sections briefly describe in the design, construction and testing of the small-scale rig based on the representative wind farm of Figure 7-1.

7.3. Rig Design and Characterisation

7.3.1. Representation

This Section describes the test rig design with specific reference to the representative wind farm of Figure 7-1. The representational validity of each rig component is considered and divergences are discussed. The scale of the rig was determined by the availability of an existing 7.5kW, 415V, 4 pole induction generator and controllable 10kW drive. Pu bases for all quantities given in this section are therefore derived from the generator's rated power, 7.5kW, rated voltage, 415V, and synchronous speed, 1500rpm.

7.3.2. Supergrid

The Supergrid, as defined by Grid Codes, is effectively a three-phase voltage source switched between fixed pre-fault, fault and post-fault levels, as illustrated schematically in Figure 7-1. An experimental equivalent can be derived by switching between the output of three variacs or by suitable control of a voltage source converter. The former option, shown in Figure 7-2, was selected on the basis that it provided adequate representation with reduced complexity and cost.

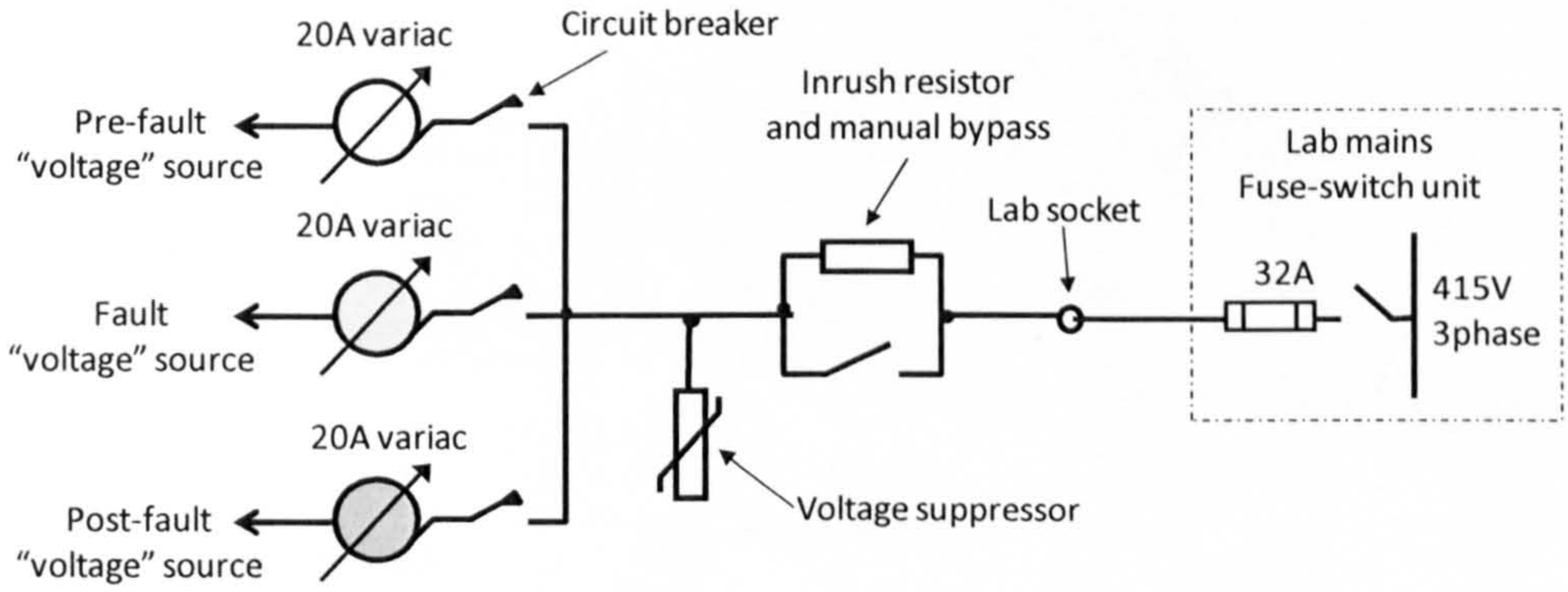

Figure 7-2: Single line diagram of experimental Supergrid equivalent

The total impedance of the supply circuit of Figure 7-2 was calculated to be (0.01+j0.025)pu from measurement of variations of the output voltage under known loading conditions. This source impedance is accounted for in steady-state and transient simulations by equating the "grid" equivalent impedance of Figure 7-1 with the sum of source and inductor impedances. Voltage variations due to independent external loads on the same supply were corrected by adjusting the variacs before

each test. Inrush resistors were inserted to reduce the inrush current during energisation of the variacs, thereby avoiding weakening or blowing of the 32A fuse.

7.3.3. Transfer switching

The Supergrid equivalent of Figure 7-2 outputs three near-constant voltages that can be manually adjusted to levels representing balanced pre-fault (100%), fault (variable) and post-fault (90%) states. This Section describes the means of switching the wind farm equivalent between these outputs, as shown in Figure 7-3.

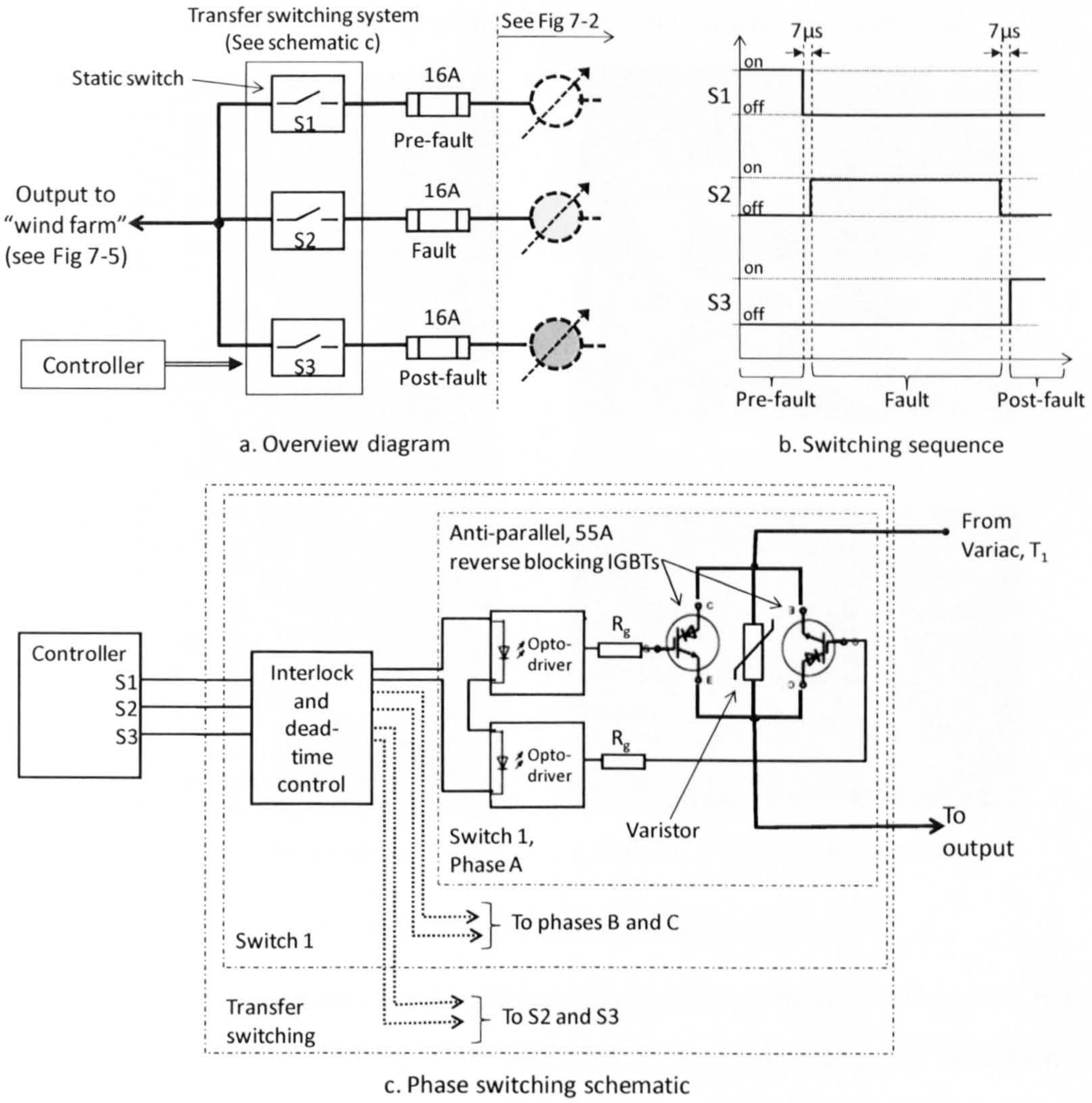

Figure 7-3: Experimental equivalent of fault switching

Figure 7-3a shows a single line overview of the transfer switching scheme comprising three static three-phase switches, S1 to S3, each partially-protected by 16A semi-conductor fuses. Figure 7-3b illustrates the switching sequence associated with an FRT event including a dead-time of 7µs, selected to be greater than the worst

case IGBT switching time by a safe margin. The dead-time and hardware interlocking were introduced to minimise the likelihood of damaging the thermally sensitive IGBTs by short-circuiting variac outputs. Figure 7-3c shows the switching schematic for a single phase switch. The control signals for the switches are sourced from the programmable rig controller, processed by the on-board protection control unit and used to drive anti-parallel reverse-blocking IGBTs. The parallel varistor across each IGBT pair prevents damaging inductive switching voltage transients as the IGBTs open.

The physical layout of the transfer switching system is shown in Figure 7-4.

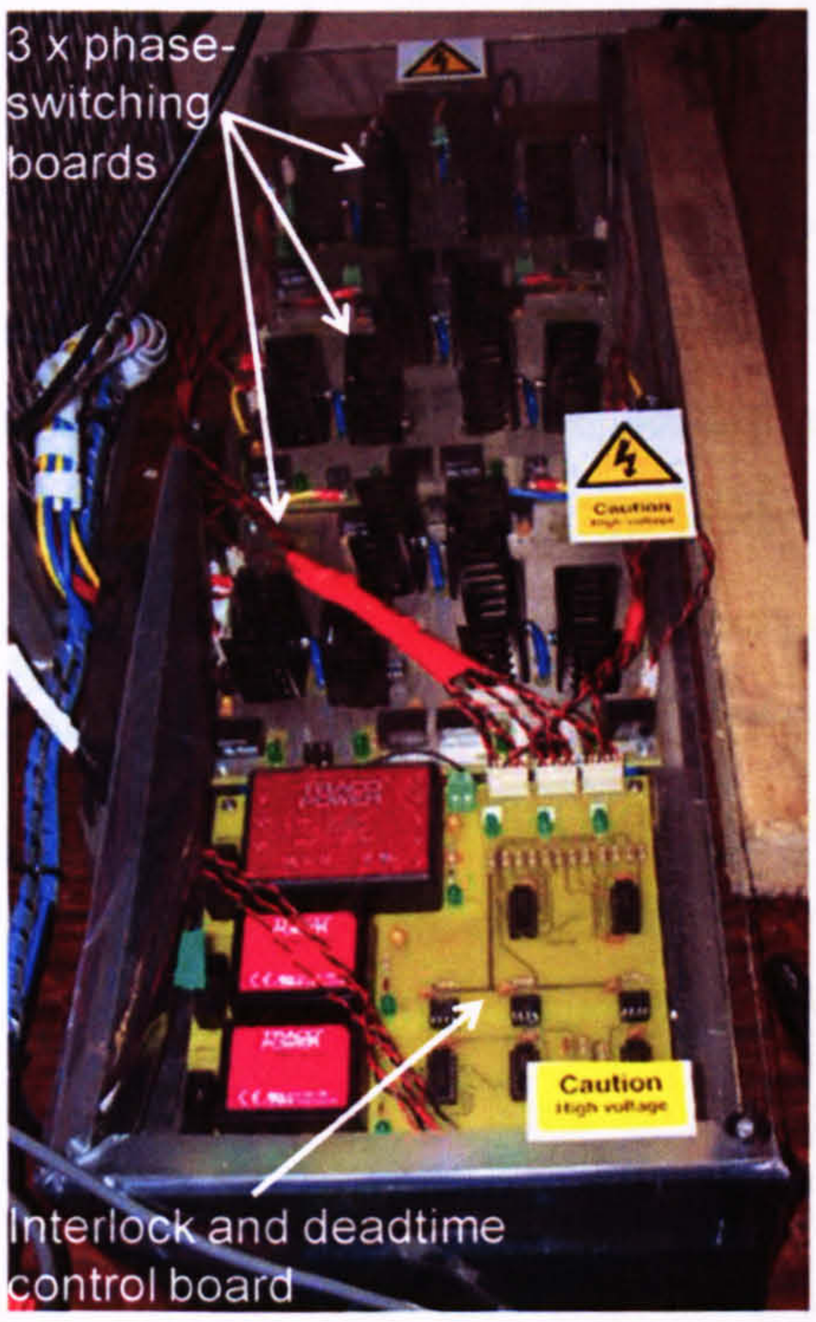

a. Complete transfer switching board

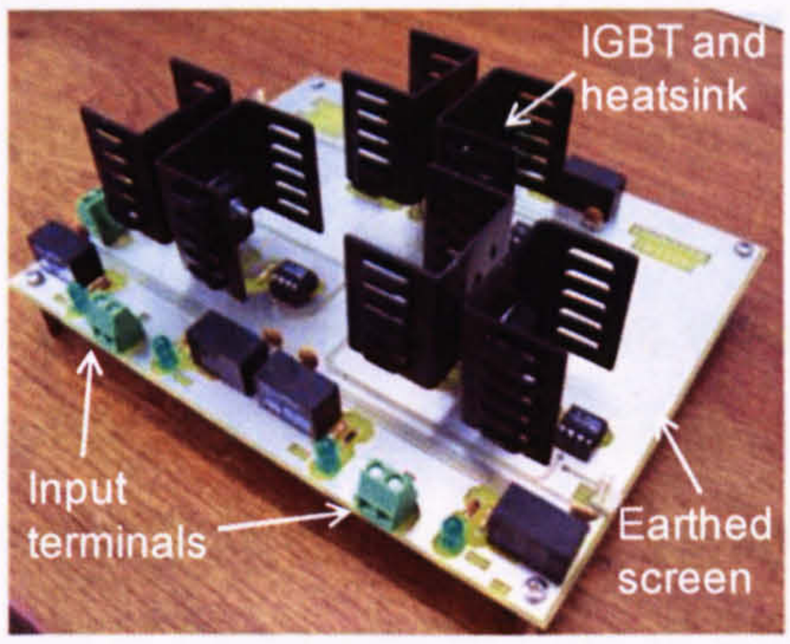

b. 1 phase, 3-switch sub-board: Top

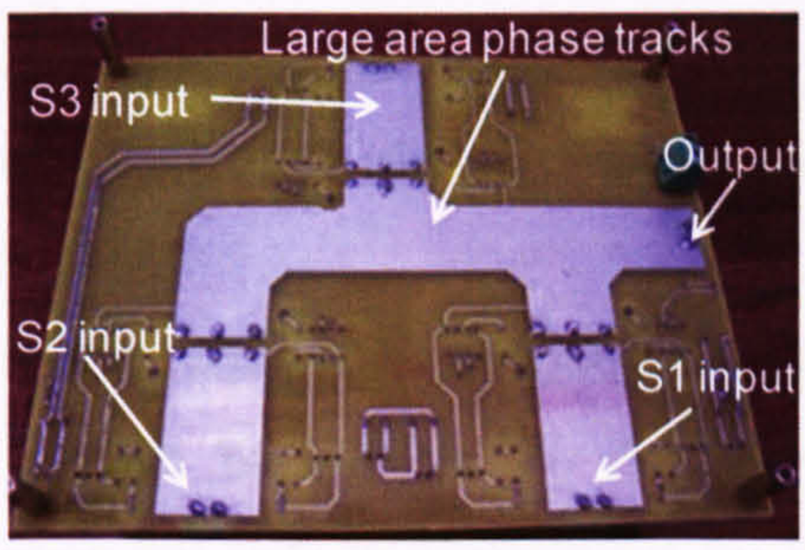

c. 1 phase, 3-switch sub-board: Bottom

Figure 7-4: Photos of transfer switching system

The principle design criteria of sub-millisecond switching, thermal robustness, noise immunity and voltage isolation were achieved by careful rating and selection of components, segregation of voltages and sizing of power tracks and IGBT heatsinks. Figure 7-4 identifies some of these key design features.

7.3.4. Grid and wind farm electrical network

Figure 7-5 shows the single line diagram of the grid and wind farm network from the transfer switch output to the generator terminals.

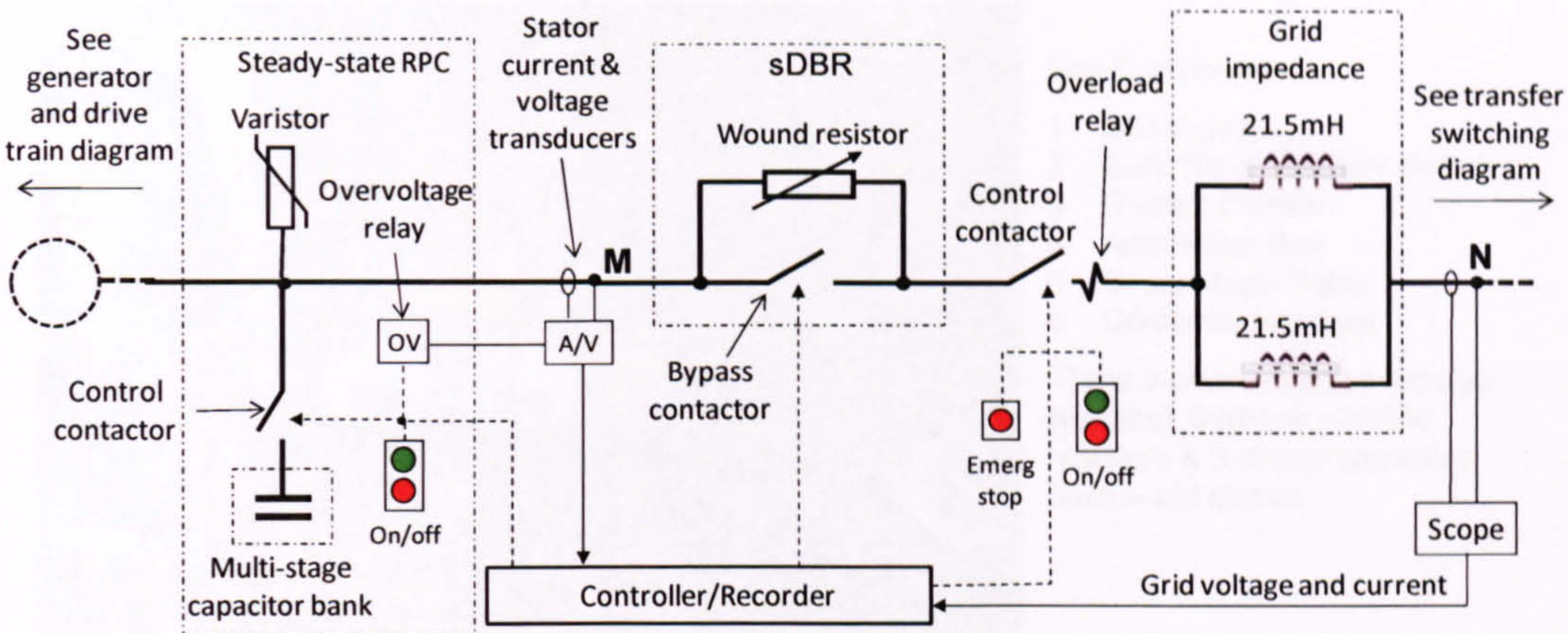

Figure 7-5: Single line diagram of grid and wind farm electrical network

Six 21.5mH, 5A, iron-cored inductors are used in parallel pairs for each of three phases, as shown in Figure 7-5. The parallel inductor impedance of 10.75mH (0.147pu) added to the source impedance gives a total "grid" equivalent impedance of 0.167pu compared to the representative value of 0.20pu used for theoretical analysis. The total experimental grid resistance of 0.03pu, comprising the inductor, contactor, IGBT and source resistance, compared to representative value of 0.04pu.

The experimental sDBR scheme comprises a variable wire-wound resistor in each phase with a range of 0-10Ω (0-0.44pu) and a bypass contactor. The normally closed contactor opens 40ms after initiation of the fault. The closing time is variable according to the recovery response of the drive train.

A multi-stage capacitor bank is used to select an equivalent magnitude of steady-state RPC at the generator terminals, as shown in Figure 7-5. A steady-state capacitance of 0.54pu was selected for the recorded tests to compensate for the no-load reactive power demand of the generator at operating power. Although less than the 1pu capacitance used for theoretical studies, this compensation was considered adequate for experimental purposes and small enough to reduce the risk of self-excited over-voltage to a very low level. The risk of over-voltage was further reduced by applying a fast-acting overvoltage protection scheme and heavy-duty varistors, as shown in Figure 7-5.

The hardware for the transfer switching, grid equivalent and hardware controls are shown in Figure 7-6.

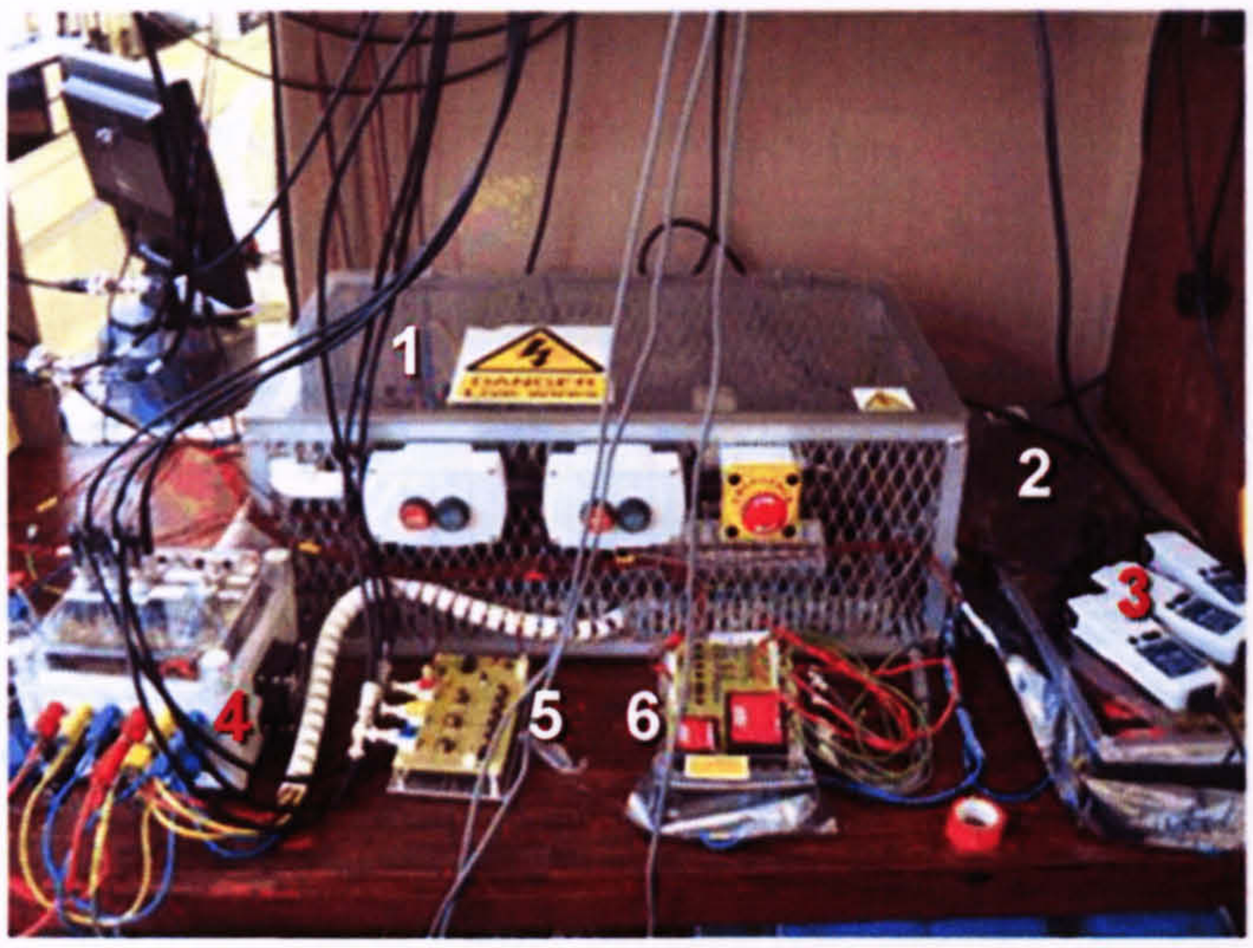

Key Components;

1 Switchgear
2 Solid State Transfer Switch
3 Current Probes
4 Acquisition Box
5 Overvoltage Relay
6 Contactor Interface

Three 3-phase voltage supplys (variacs), 3-phase variable resistors & 3-phase capacitor bank – not shown

Figure 7-6: Transfer switching, grid equivalent and hardware controls

7.3.5. Generator and drive system

Figure 7-7a shows the single line diagram for the experimental generator and drive system and Figure 7-7b illustrates the test rig drive train

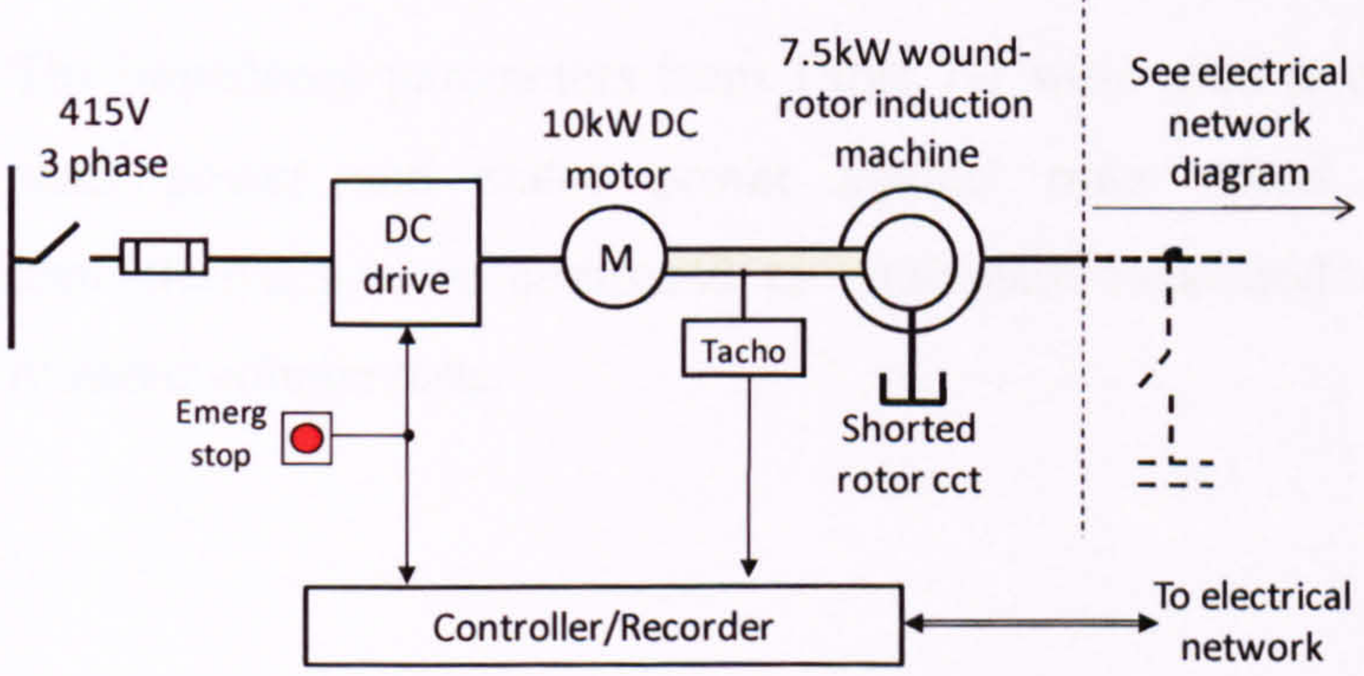

a. Generator and drive schematic diagram

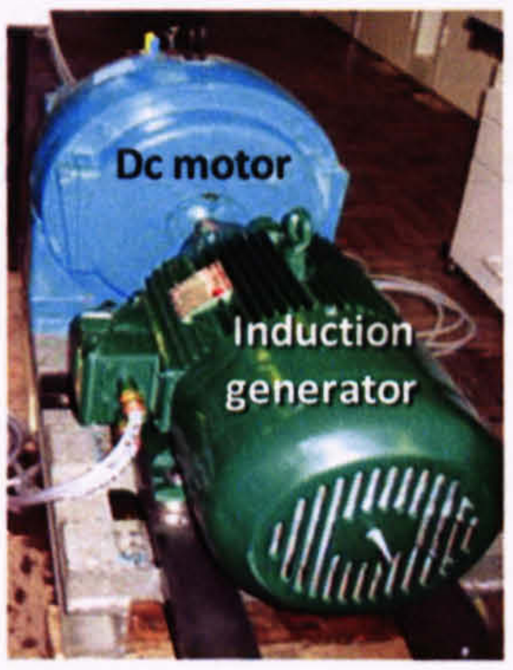

b. Generator and dc motor

Figure 7-7: Single line diagram of generator and drive system

The induction generator parameters in Table 7-1 were derived from reduced voltage locked rotor tests (LRT), dc resistance measurements (DCR), synchronous speed tests (SST) and rotor acceleration tests (RAT). The rotor values are reflected to the stator side accounting for the 0.31 stator/rotor turns ratio.

Parameter	Test	Value	Parameter	Test	Value
Stator resistance	LRT+DCR	0.026	Stator leakage reactance	LRT	0.062[2]
Rotor resistance	LRT+DCR	0.027[1]	Rotor leakage reactance	LRT	0.062[2]
Magnetising reactance	SST	2.1	No. of poles		4
Drive train inertia	RAT	1.25	Drive train friction	SST	0.127

Notes:

1. *Rotor resistance ranges between 0.024pu (dc) and 0.027 (ac, 50Hz). The locked rotor value is selected to best represent the machine at critical rotor speeds of 1.2pu.*
2. *Leakage reactance is at locked rotor. This is typically 10-20% less than reactance at rated speed. Locked rotor values are judged to be more representative of conditions during FRT.*
3. *Values are stated with an experimental margin of error of +/-2%.*

Table 7-1: Induction generator parameters

The impedance parameters from Table 7-1 were used to calculate characteristics for shaft power and stator power against rotor speed at rated voltage. These characteristics were compared to equivalent measured quantities scaled up from reduced voltage tests.

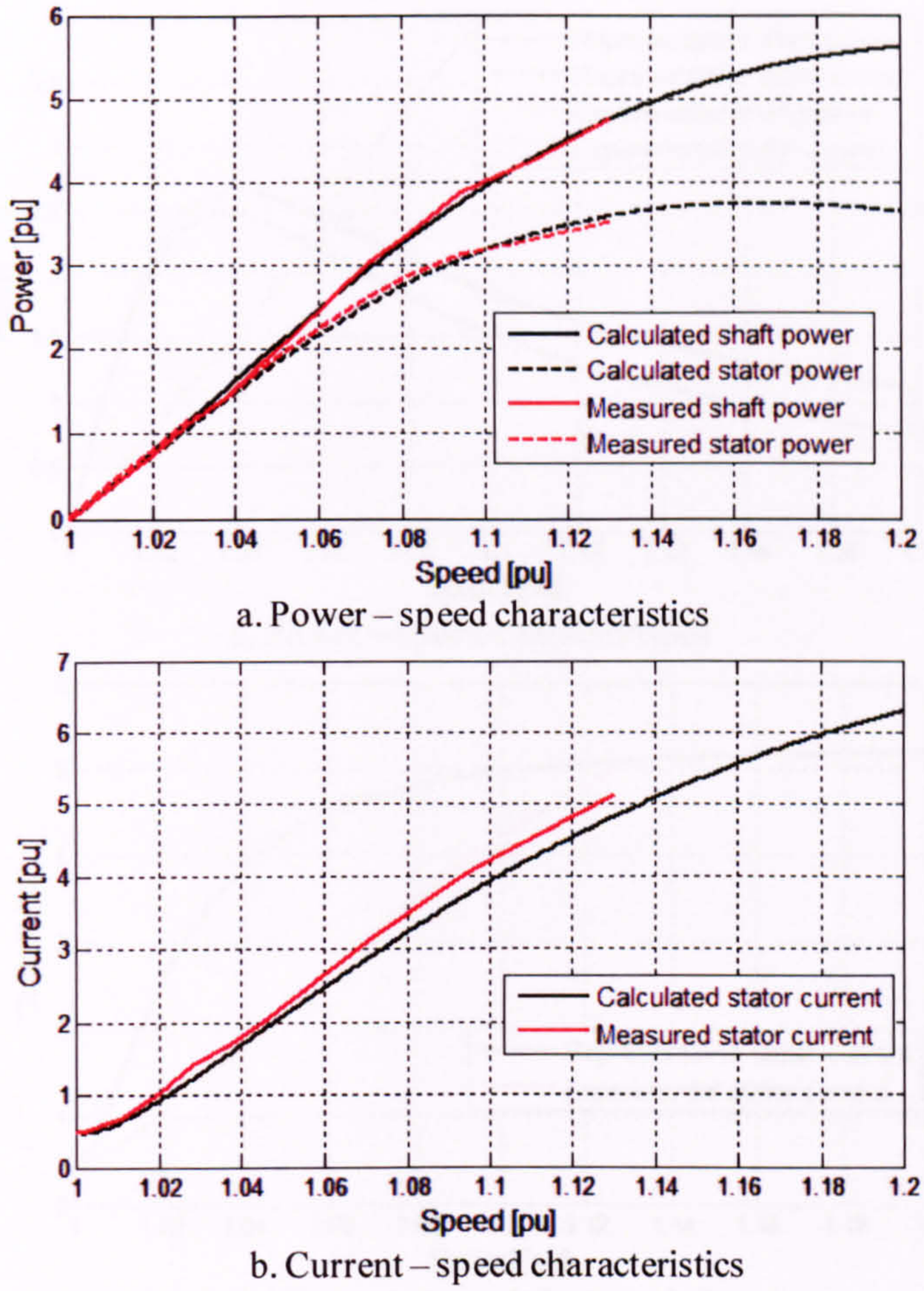

a. Power – speed characteristics

b. Current – speed characteristics

Figure 7-8: Comparison of calculated and measured power-speed characteristics

Figure 7-8a shows good correlation (+/-2% divergence) of calculated and measured shaft and stator power. Figure 7-8b also shows reasonable correlation (+4% divergence) of calculated and measured stator current. However, the substantial discrepancy of experimental and representative full-scale generators (as defined in Chapter 4) is shown by Figure 7-9.

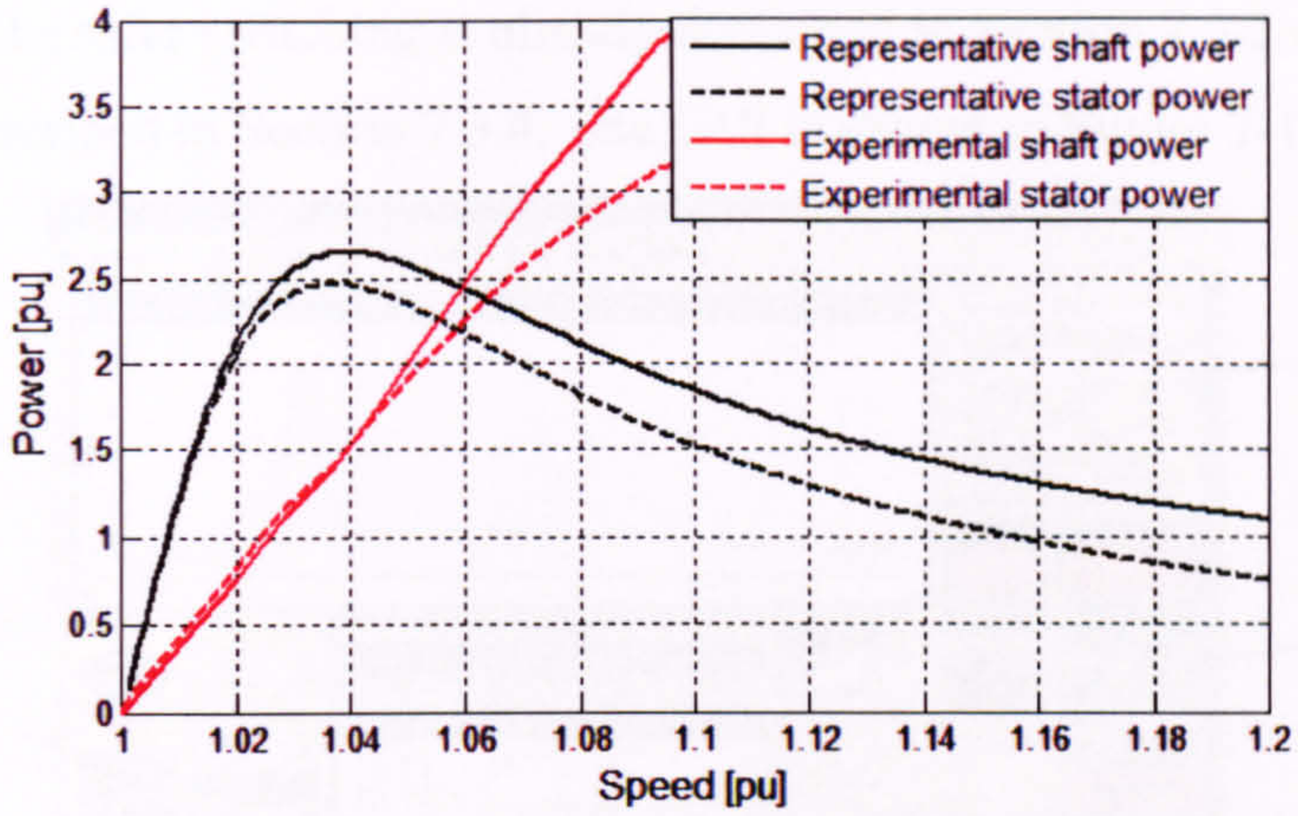

a. Power – speed characteristics

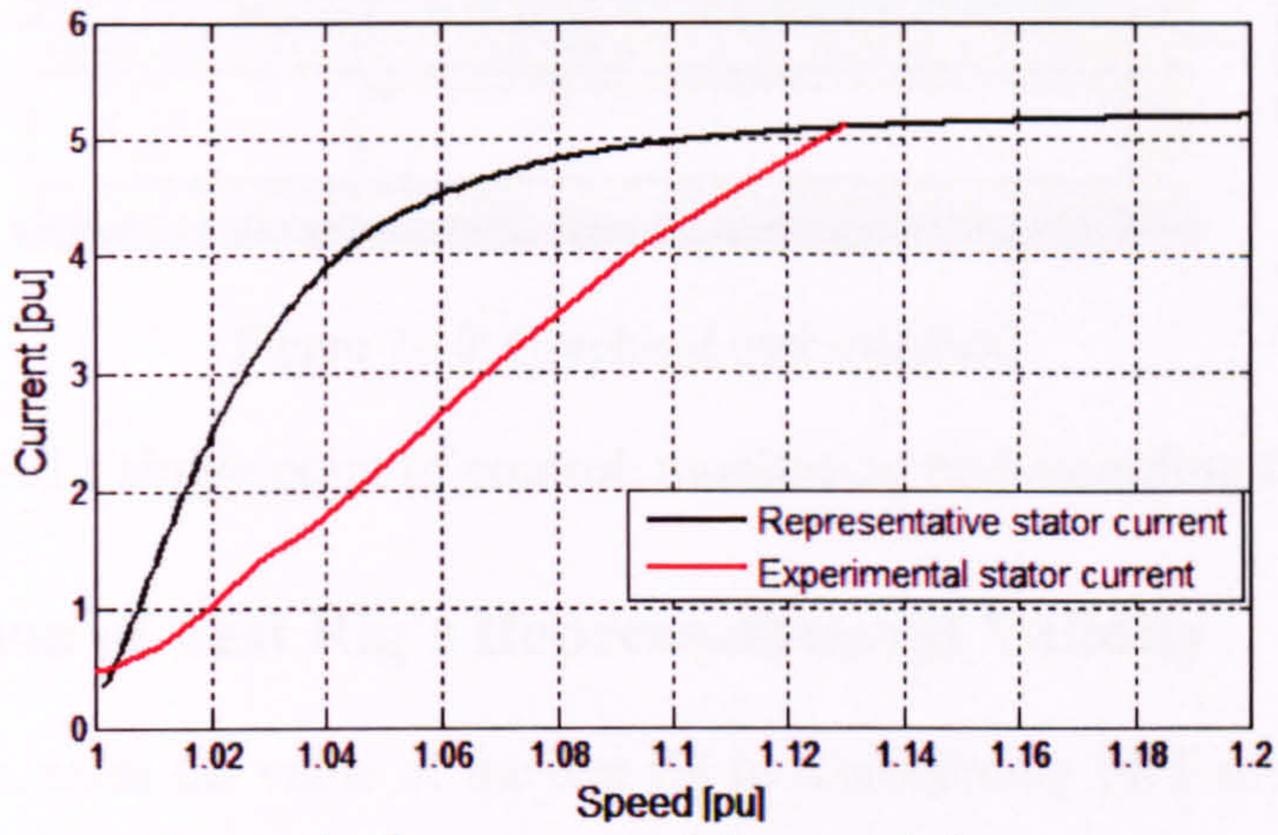

b. Current – speed characteristics

Figure 7-9: Comparison of experimental and representative full-scale generator

Figure 7-9 highlights the extreme divergence of experimental and representative generator characteristics. The most significant differences are due to the very high experimental generator resistances (four times greater). This shifts the speed at which peak shaft power occurs from 1.04pu to 1.2pu resulting in a very substantially more stable system under fault conditions.

7.3.6. Control and recording system

Control, recording and secondary protection of the experimental rig were performed by a programmable controller. It is not the purpose of this Chapter to describe the controller or its detailed functions. The basic controller structure and graphical user interface (GUI) was programmed by Graham Pannell, a PhD student working on an independent project focussing on DFIGs FRT. We extended the programme to include an FRT and sDBR sequence controller and GUI for this test rig. The

sequencing of transfer switching is already described in Section 7.3.3 and the control of sDBR is described in Section 7.3.4. The GUI is shown in Figure 7-10.

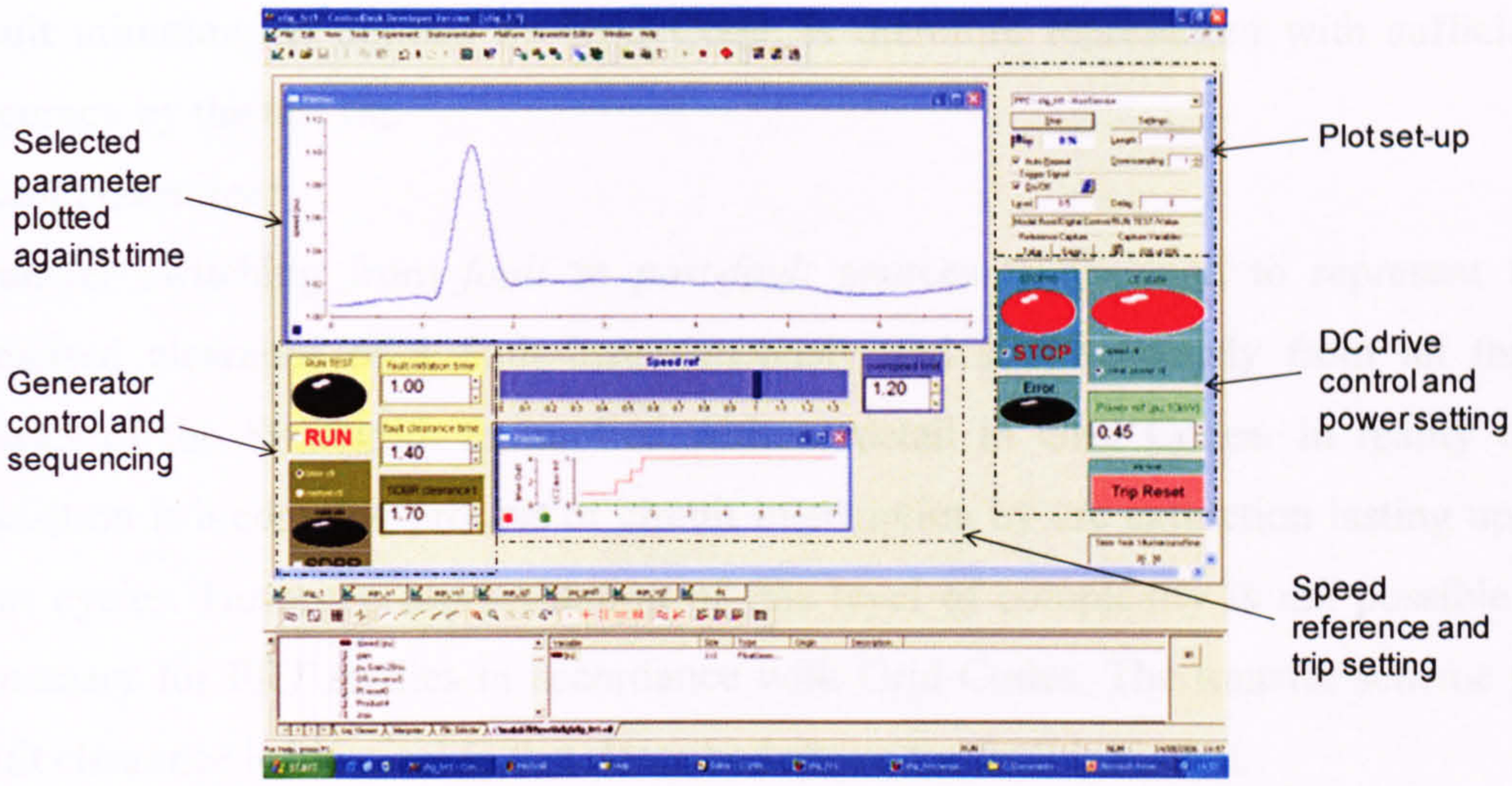

Figure 7-10: Graphical user interface

The GUI provided a single point of control, monitoring and recording for FRT tests.

7.4. Discussion of Test Rig's Representational Validity

This section discusses the value of the test rig in representing FRT scenarios of full-scale wind farms, as defined by GB and RoI Grid Codes.

7.4.1. Fault representation

Fault initiation:

Transfer switching from *pre-fault* to *fault* sources is designed to represent the initiation of an idealised fault instantaneously and simultaneously applied to all three phases of the Supergrid, as implied, without detail, in Grid Codes. The transfer switching scheme is therefore designed such that the IGBTs in each of the three phases of the *pre-fault* switch open simultaneously within 1μs. If the IGBTs open while the through-inductive current is non-zero then a transient voltage builds up across the collector-emitter until the current diverts through the parallel varistor. The varistor carries the diverted current, dissipating inductive energy in a similar manner to the arc across separated contacts, for the dead-time of 7μs. After this dead-time an alternative lower impedance path is created by closure of the *fault* switch. The complete transfer from *pre-fault* to *fault* sources is therefore complete within 10μs, a

negligible time period within the context of a 20ms cycle and circuit time constants greater than one cycle.

Fault initiation, as defined by Grid Code, is therefore represented with sufficient accuracy by the test rig.

Fault clearance:

Transfer switching from *fault* to *post-fault* sources is designed to represent the idealised clearance of a fault instantaneously and simultaneously from all three phases of the Supergrid, as implied without detail in Grid Codes. In reality this transition is a complex process of circuit interruption by arc extinction lasting up to four cycles. However, representation of this level of complexity is not possible or necessary for FRT studies in accordance with Grid Codes. The transfer scheme for fault clearance is identical to that described above for fault initiation.

Fault clearance, as defined by Grid Code, is therefore represented with sufficient accuracy by the test rig.

7.4.2. Network representation

The representational validity of lumping of network impedance as a single series inductor and neglecting stray shunt capacitance is already covered in Chapter 4. The steady-state shunt capacitance at the terminals of the generator is fully representative and also requires no discussion. sDBR is therefore the focus of this section.

A copper-wound variable resistor with low inductance is used to represent a power resistor, which may be of grid design. The only material difference would be the inductive component of impedance which, in both cases causes only a negligible effect in delaying the transfer of current from the bypass switch to the resistor. The contactor was selected to have fast operating time (55ms closing, 20ms opening), the opening time being the critical representational factor. The coil control circuit was then designed to achieve an overall operating time (fault initiation to contact opening) of 40ms, described as typical for a 690V contactor in Chapter 4. In order to simplify the rig construction, the contactor was opened by a timed signal from the central controller, as set by the GUI rather than an under-voltage or other detection device. Although not representative of a real scheme, this discrepancy is not significant given the objective of proving the sDBR concept rather than refining its operation.

7.4.3. Induction generator representation

The divergence of experimental and full-scale generator steady-state characteristics is illustrated by Figure 7-9. This section discusses the implications of this discrepancy on the representation validity of FRT tests using the rig. Figure 7-11 compares the experimental and full-scale shaft power characteristics at 90% recovery voltage for the complete "wind farm" system.

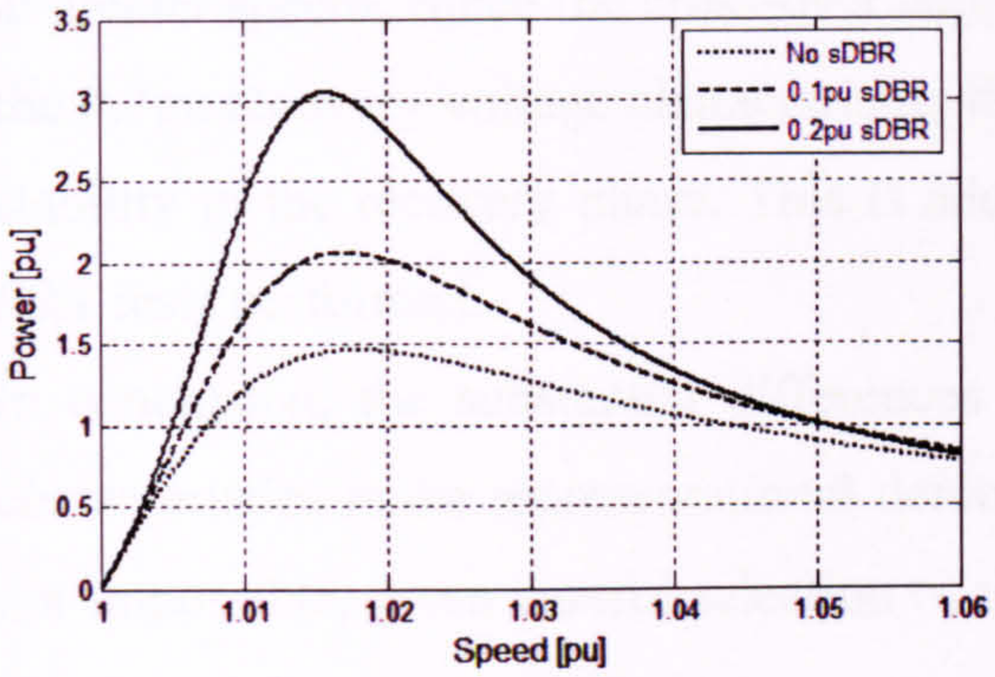

a. Full-scale power

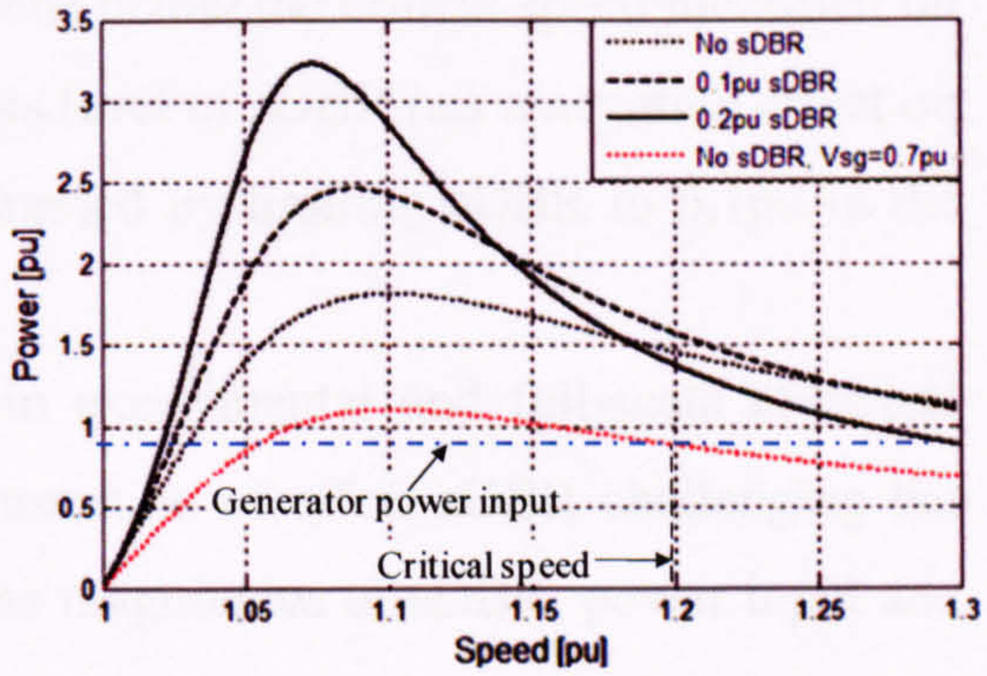

b. Experimental power

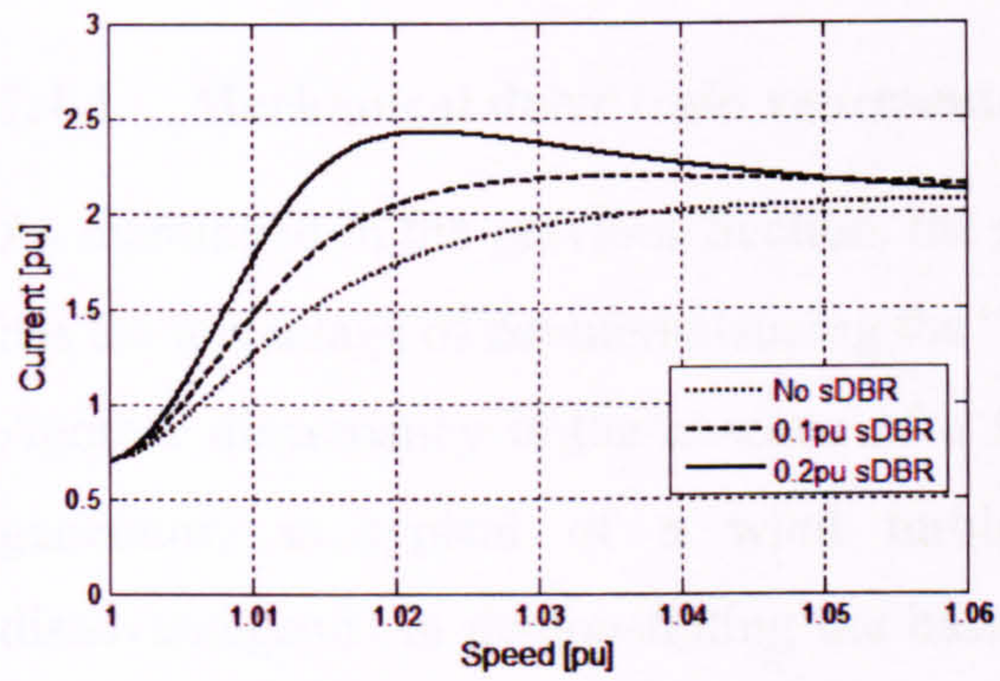

c. Full-scale current

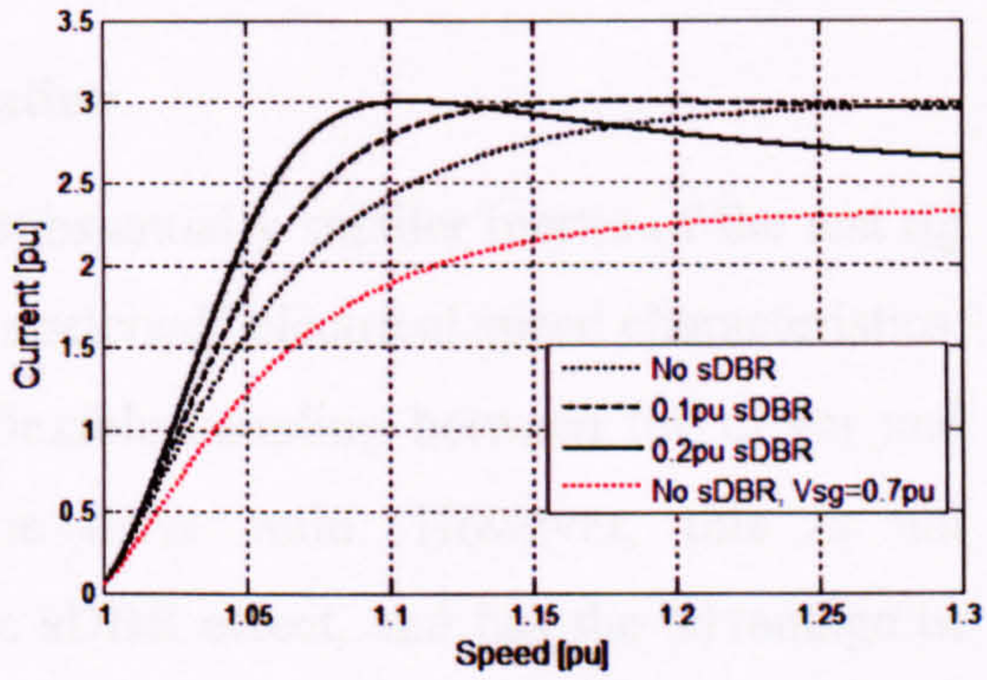

d. Experimental current

Figure 7-11: Comparison of full-scale and experimental system characteristics

The most striking difference between the full-scale and experimental characteristics is the speed scale, as referred in Section 7.3.5. However, this is not an insurmountable obstacle to the use of the test rig as a representation of a full-scale system because it is counterbalanced by the substantially smaller experimental inertia, which results in proportionately greater acceleration during the fault period.

A more significant difference is the elevated shaft power, which remains above rated power even at rotor speeds as high as 1.3pu. A limitation of 1.0pu on dc motor output power, equating to a net generator input power (after frictional losses) of 0.87pu at operating speed, further exacerbates the difficulty of demonstrating relative FRT performance. These discrepancies were compensated for by reducing the recovery

voltage to 0.7pu, as shown in Figure 7-11b and Figure 7-11d, to produce a base-case recovery characteristic with a critical speed of 1.2pu.

Another important difference is the relative effect of 0.2 pu sDBR on the two characteristics. In the full-scale case of Figure 7-11a the base-case shaft power is elevated through-out the illustrated speed range. However, in the experimental case of Figure 7-11b the shaft power is elevated up to about 1.18pu speed and depressed at greater speeds. Since the cross-over happens below the critical speed identified on the 0.7pu recovery voltage characteristic, this level of sDBR has a negative effect on stability in the recovery phase. This is addressed by limiting sDBR to 0.1pu in the FRT tests performed.

In conclusion, the substantial differences in experimental and full-scale electrical characteristics make representational demonstration of effect sDBR challenging but not impossible, given careful selection of the magnitudes of sDBR, power input and recovery voltage.

7.4.4. Mechanical drive train representation

As mentioned in the previous Section, the substantially smaller inertia of the test rig has the advantage of counterbalancing the "stretched" electrical speed characteristics. Another discrepancy is the absence of a flexible coupling between the driver and generator, as typical of a wind turbine drive train. However, this is not disadvantageous in demonstrating the basic sDBR effect, and has the advantage of reducing the complexity of the results.

7.4.5. Prime mover representation

The dc motor, as prime mover, provides a constant power output in the manner recommended for modelling purposes in Chapter 4. However, practical commutator deformation resulted in sparking and reduced efficiency such that it was not possible to deliver rated input power to the generator for sufficient time to carry out reliable tests. This limitation was compensated in the manner described in Section 7.4.3.

7.5. Experimental Method

Prior to energisation, the settings of Table 7-2 were applied for the two selected demonstration tests. All settings, except for sDBR resistance, were applied through the GUI of Figure 7-10. sDBR resistance was set by manually adjusting the variable resistor slider for each phase.

Test no.	Power input(2)	Fault duration	Residual voltage	Recovery voltage	sDBR resistance	sDBR switch-in	sDBR switch-out
1	1.0	0.45	0.3	0.7	0	N/A	N/A
2	1.0	0.45	0.3	0.7	0.1	t_f +0.04s(2)	t_f+ 1.55s(2)

Notes:

1. *"Power input" relates to the dc motor output and must therefore be reduced by (0.13ω) pu, where ω is pu speed, to allow for frictional losses.*
2. *Switch-in and switch-out times are stated with reference to the fault initiation time, tf.*

Table 7-2: Settings for test scenarios

The drive was then energised and used to accelerate the dc motor to synchronous (1pu) speed before energising the generator from the *pre-fault* variac, set at 1pu in both cases. The drive was then switched from *constant speed* to *constant power* control and the preset FRT sequence was initiated as soon as the preset power level was reached. When the FRT response was complete the drive was switched back to synchronous speed control before de-energising the generator and saving the data.

7.6. Experimental Results

7.6.1. Raw measured data

Raw voltage and current measurements are shown in Figure 7-12 for the purpose of highlighting experimental distortions which have a bearing on the derived data shown in Figure 7-13. The data is derived from the sDBR scenario but the issues are almost identical in both scenarios.

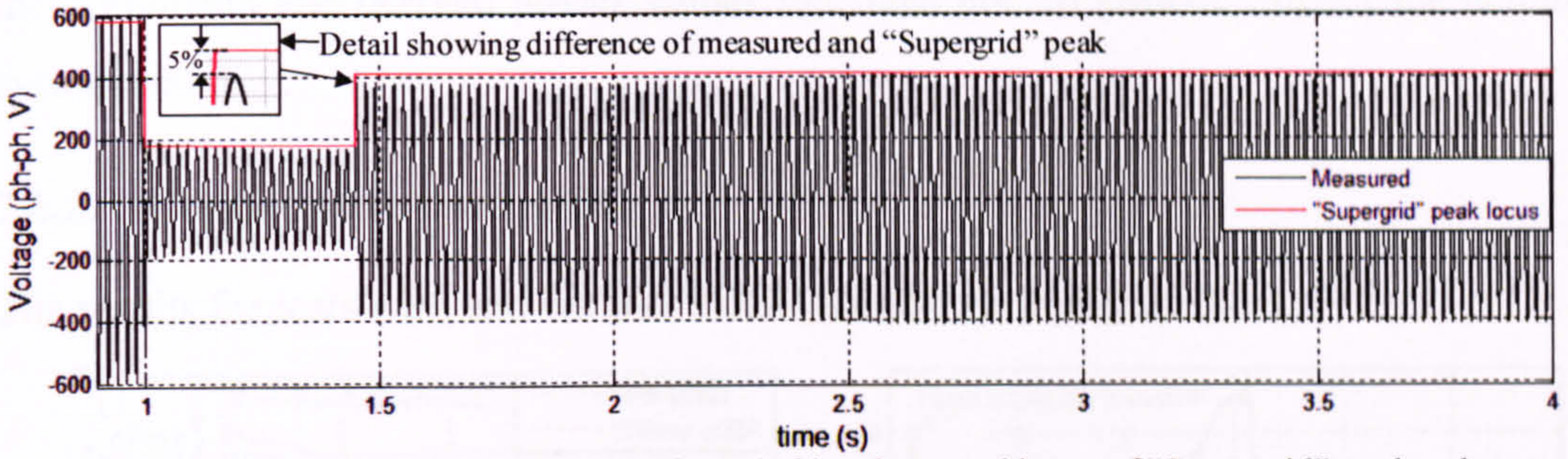

a. Transfer switch output phase-to-phase (a-b) voltage and locus of "Supergrid" peak voltage

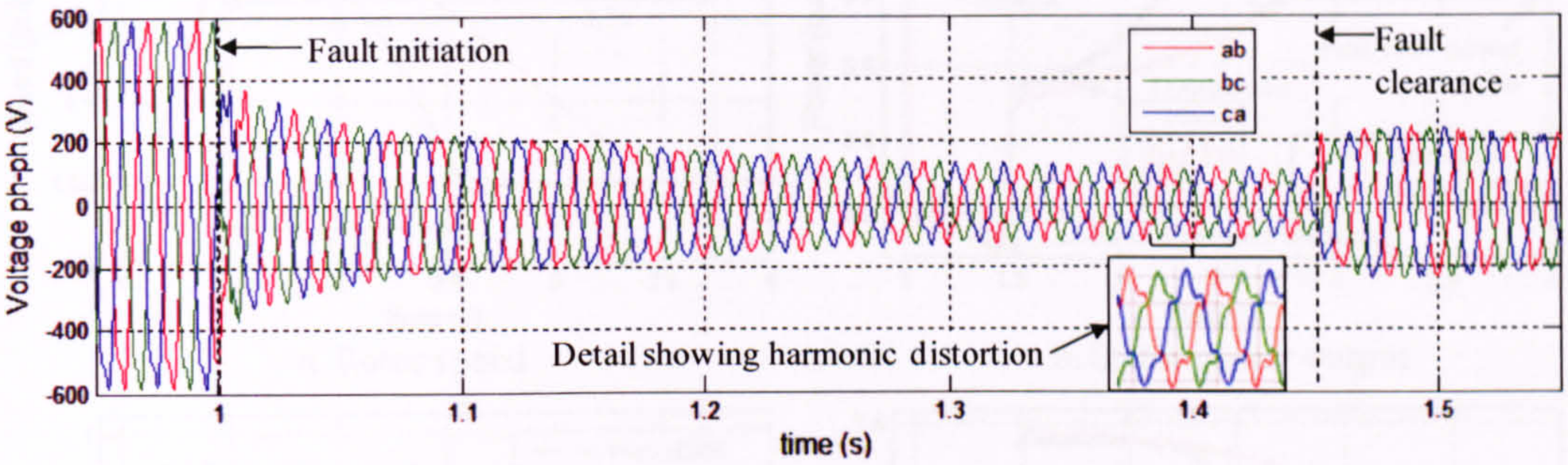

b. Stator phase-to-phase voltages

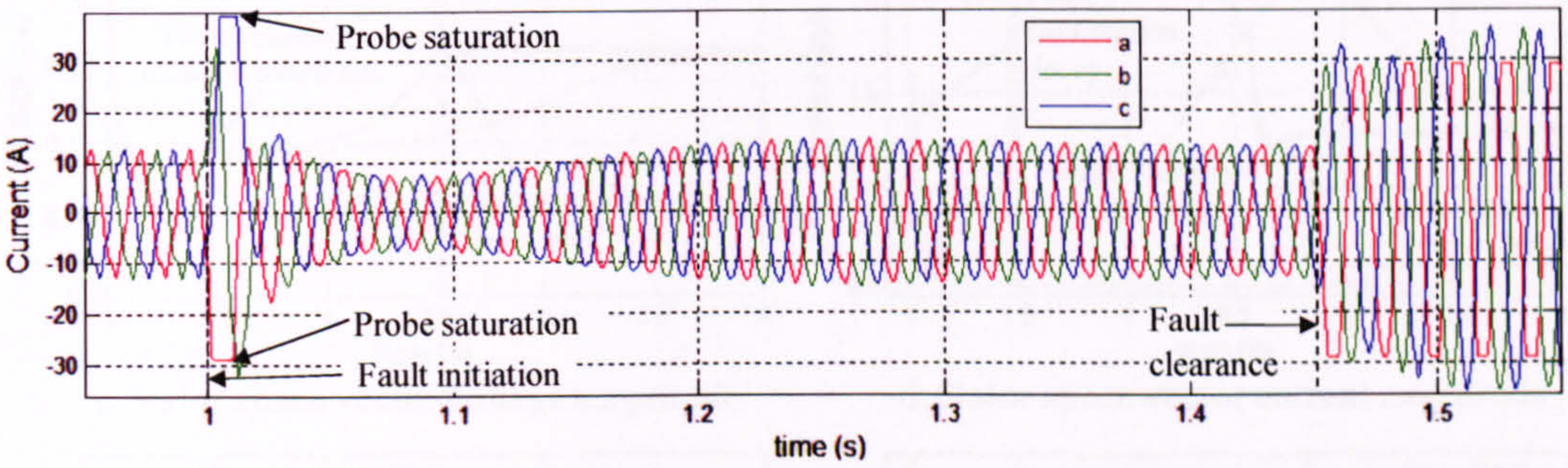

c. Stator currents

Figure 7-12: Measured voltage and current data with sDBR inserted

Figure 7-12a shows the phase-to-phase grid voltage measured at location N in Figure 7-5. It shows a peak voltage of +/-600V (1.0pu) stepping down to near +/-170V (0.3pu) and back up to near +/-400V (0.7pu) after 0.45s. The Figure also shows the locus of intended "Supergrid" positive peak magnitudes. The discrepancy of up to 5% between voltage measured at N and the "Supergrid" voltage is due to the current of up to 2.4pu (see Figure 7-12c) flowing through the 2% source impedance.

Figure 7-12b shows the stator voltage data measured at location M in Figure 7-5. It highlights the harmonic distortion imposed by the supply source. Harmonics have only a small effect on system stability, possibly contributing to the higher than predicted measured current shown in Figure 7-9b.

Figure 7-12c shows the stator current data measured at location M in Figure 7-5. It highlights the current probe saturation that subdues the transient current

measurements and derived power values but does not, of course, impact the actual system stability.

7.6.2. Comparative test results

The results for tests with and without sDBR are shown in Figure 7-13.

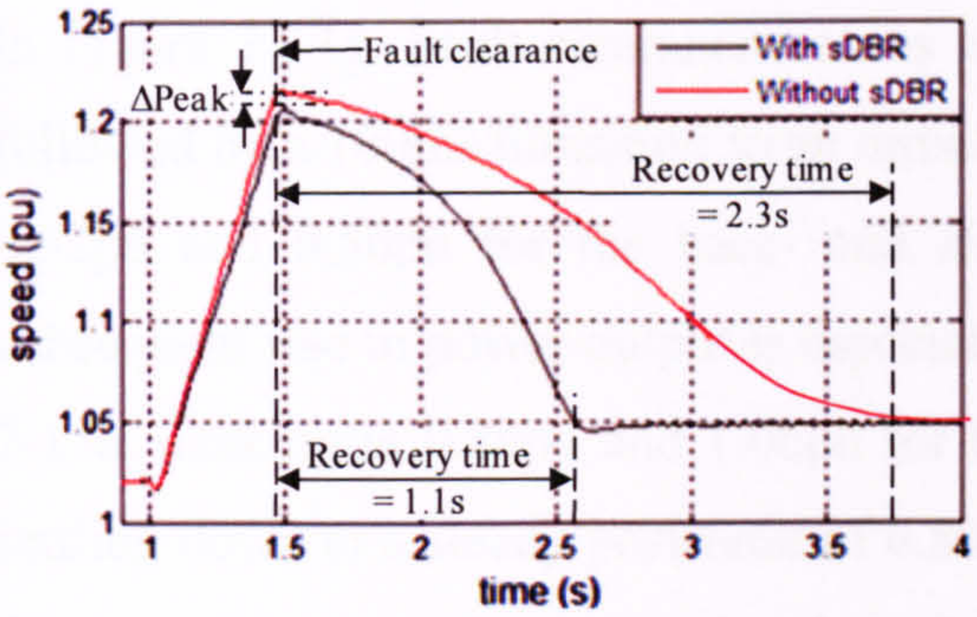

a. Rotor speed

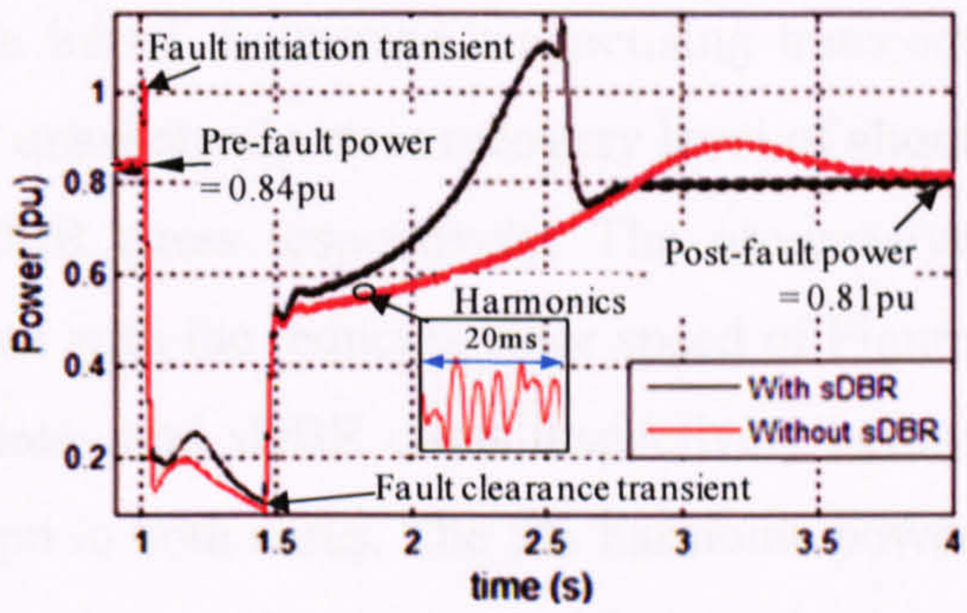

b. Stator power output

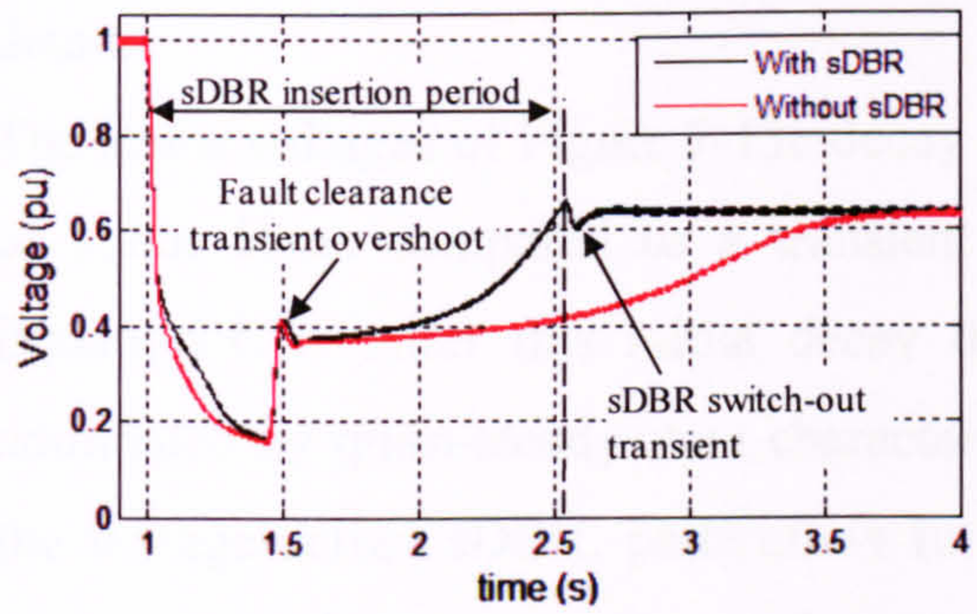

c. Stator space vector voltage magnitude

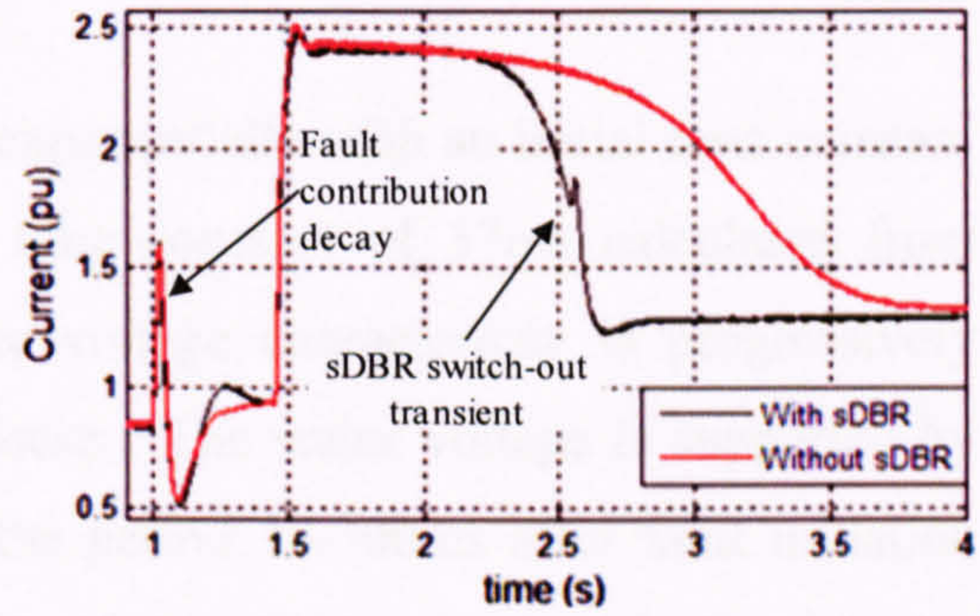

d. Stator space vector current magnitude

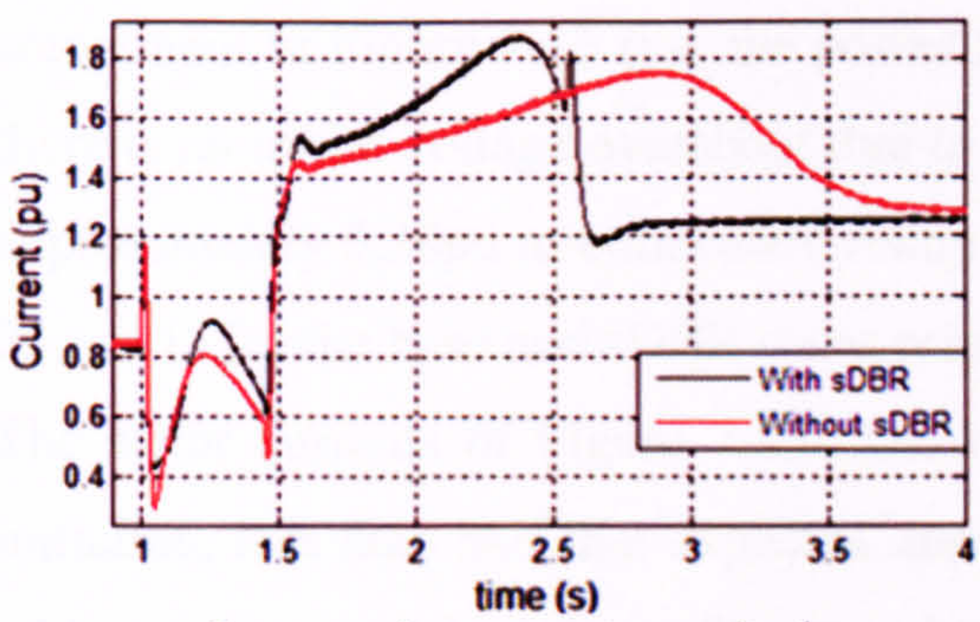

e. Stator active current magnitude

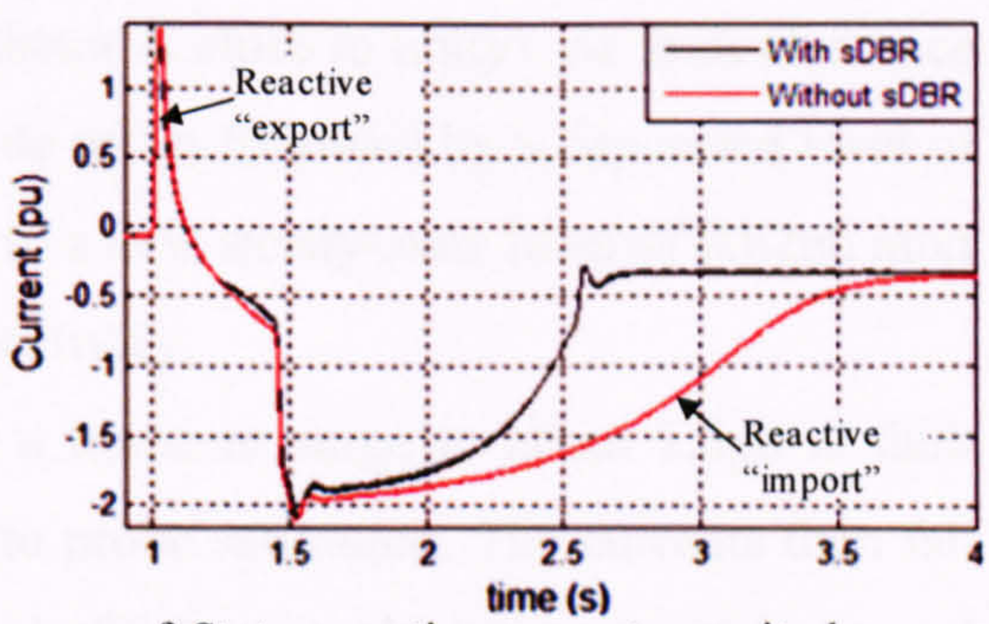

f. Stator reactive current magnitude

Figure 7-13: FRT results for both test scenarios

Figure 7-13a shows a small decelerating impulse at fault initiation arising from the transient overpower of Figure 7-13b. This is followed by a period of near-constant acceleration of 0.41pu for the base-case and 0.40pu for the sDBR case. After fault clearance, the rotors peak quickly at 1.22pu and 1.21pu for the base- and sDBR cases respectively before decelerating and recovering to a common steady post-fault speed

of 1.05pu, 2.3s and 1.1s after fault clearance for the base- and sDBR cases respectively.

The stator power outputs of Figure 7-13b show an initial upwards transient before decaying to about 0.2pu in 50ms. The sDBR case benefits from an elevated power level during the fault period leading to the reduced acceleration and peak speed seen in Figure 7-13a. Fault clearance causes an initial downward magnetising transient followed by a 100ms transition to an initial quasi-steady-state recovery level of about 0.52pu and 0.56pu for the base- and sDBR cases respectively. The progressive subsequent rise in power output is associated with the reducing rotor speed of Figure 7-13a, peaking at 0.84pu and 1.06pu for base- and sDBR cases respectively before settling down to a steady post-fault of 0.80pu in both cases. The 5% harmonic power fluctuations arising from the supply voltage harmonics are magnified in the inset detail.

The stator voltages of Figure 7-13c decay exponentially with an initial time constant of about 50ms compared to a transient time constant of 37ms calculated from Equation C-1. After this initial decay the voltage characteristic is progressively dominated by quasi-steady-state characteristics. The stator voltage is supported by the voltage across sDBR, particularly in the period 10-300ms after fault initiation when the active component of current in Figure 7-13e dominates the reactive component in Figure 7-13 (i.e. the power factor is close to unity). At fault clearance there is an initial voltage overshoot due to dc offset followed by a depressed level of approximately 0.38pu in both cases, rising to a new steady-state level of 0.62pu after 2s and 1s for the base and sDBR cases respectively.

The stator currents of Figure 7-13d show a transient surge to about 1.6pu at fault initiation, less than half that expected due to probe saturation. The currents then fall with a time constant of about 50ms to a level of 0.5pu, at which time the rising speed superimposes a steady-state current component, derived from Figure 7-11d, which dominates in the latter fault period. The increased current in the sDBR case can also be explained with reference to the same Figure. On fault clearance there is a subdued dc transient overshoot followed by an initial near-steady current of 2.4pu, compared to 2.3pu in Figure 7-11d, which falls to a steady post-fault value of 1.3pu, compared to 1.25pu at 1.05pu speed in Figure 7-11d. There is a small sDBR switch-out transient at 2.54s

The active and reactive current trajectories of Figure 7-13e and f are informative in-so-far as they support the basis for the beneficial effect of sDBR in extracting more active power from the generator during and after the fault and mitigating the reactive power demand in the first two seconds after fault clearance.

7.7. Comparative Transient Simulations

The transient model of Chapter 4 was used to compare experimental and simulated performance with and without sDBR. The test rig parameters of Table 7-1 and fault scenario settings of Table 7-2 were applied to the simulation.

7.7.1. Comparison of results without sDBR

The base-case experimental and simulation results are compared in Figure 7-14.

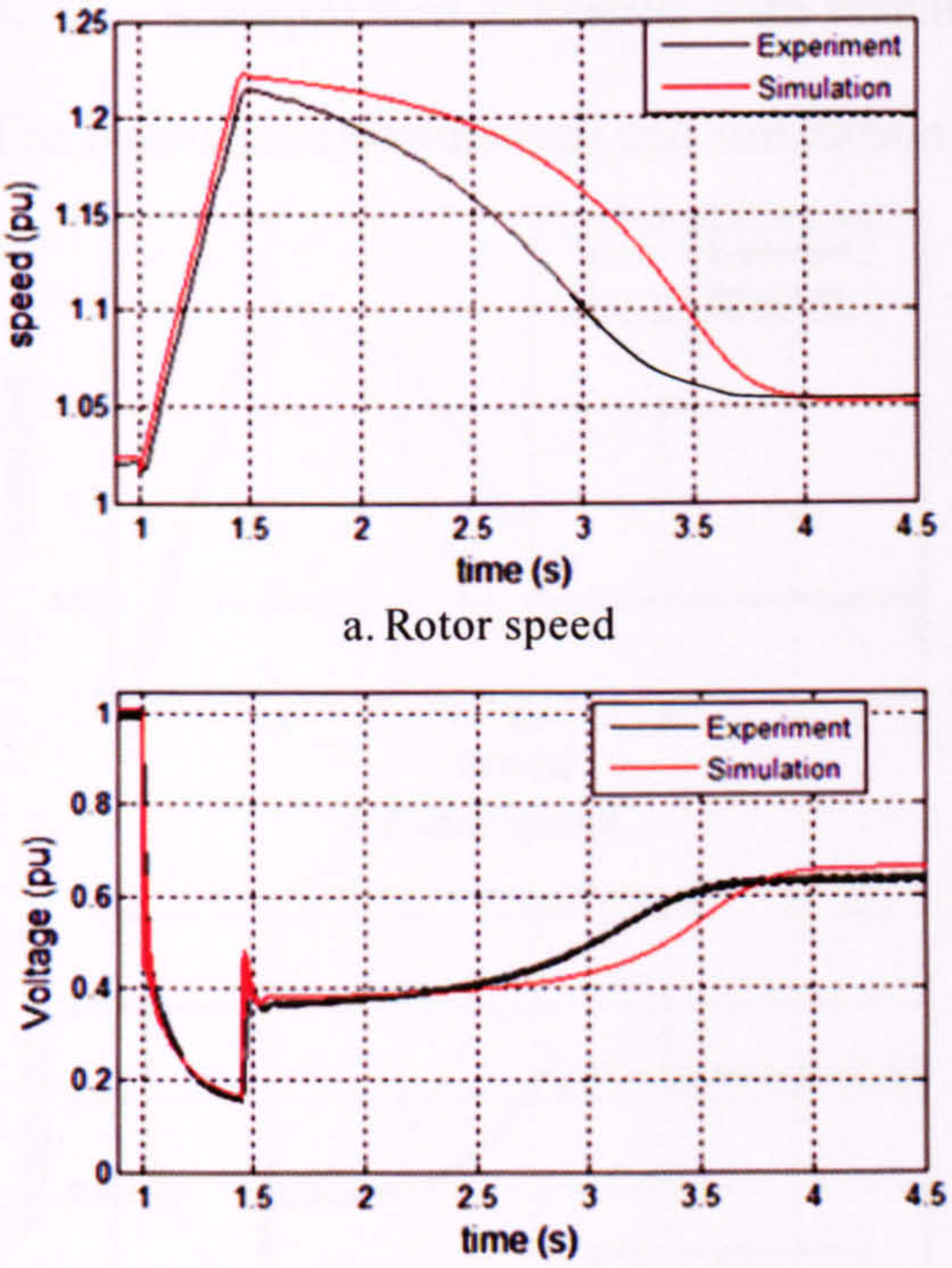

a. Rotor speed

b. Stator power output

c. Stator space vector voltage magnitude

d. Stator space vector current magnitude

Figure 7-14: Comparison of experimental and simulation results without sDBR

Figure 7-14a to d show that, ignoring transients, the acceleration, stator power voltage and current trajectories differ by less than 2% in the pre-fault and fault period. The substantial simulated transients at fault initiation and clearance are absent from the experimental results. There are a number of possible reasons for this transient discrepancy including the switching operation (some transient energy is dissipated in varistors in experimental case), current probe saturation and actual

machine saturation. However, these possible causes are not explored further in this Thesis because the differential effect is not dynamically significant.

The discrepancy between results is greater in the post-fault period, resulting in a slower recovery for the simulated case, as illustrated explicitly in Figure 7-14a. The initial recovery conditions, shown in Figure 7-14a-d, are similar but diverge with time as simulated recovery lags experimental recovery. It should be noted that the difference in recovery time is eliminated by only a 2% increase in simulated rotor resistance or a 1% decrease in simulated leakage reactance. These discrepancies are well within the margins of experimental error.

The 5% difference in recovery current in Figure 7-14d is similar to the steady state divergence noted in the steady-state characterisation of Figure 7-8b.

7.7.2. Comparison of results with sDBR

The base-case experimental and simulation results are compared in Figure 7-15.

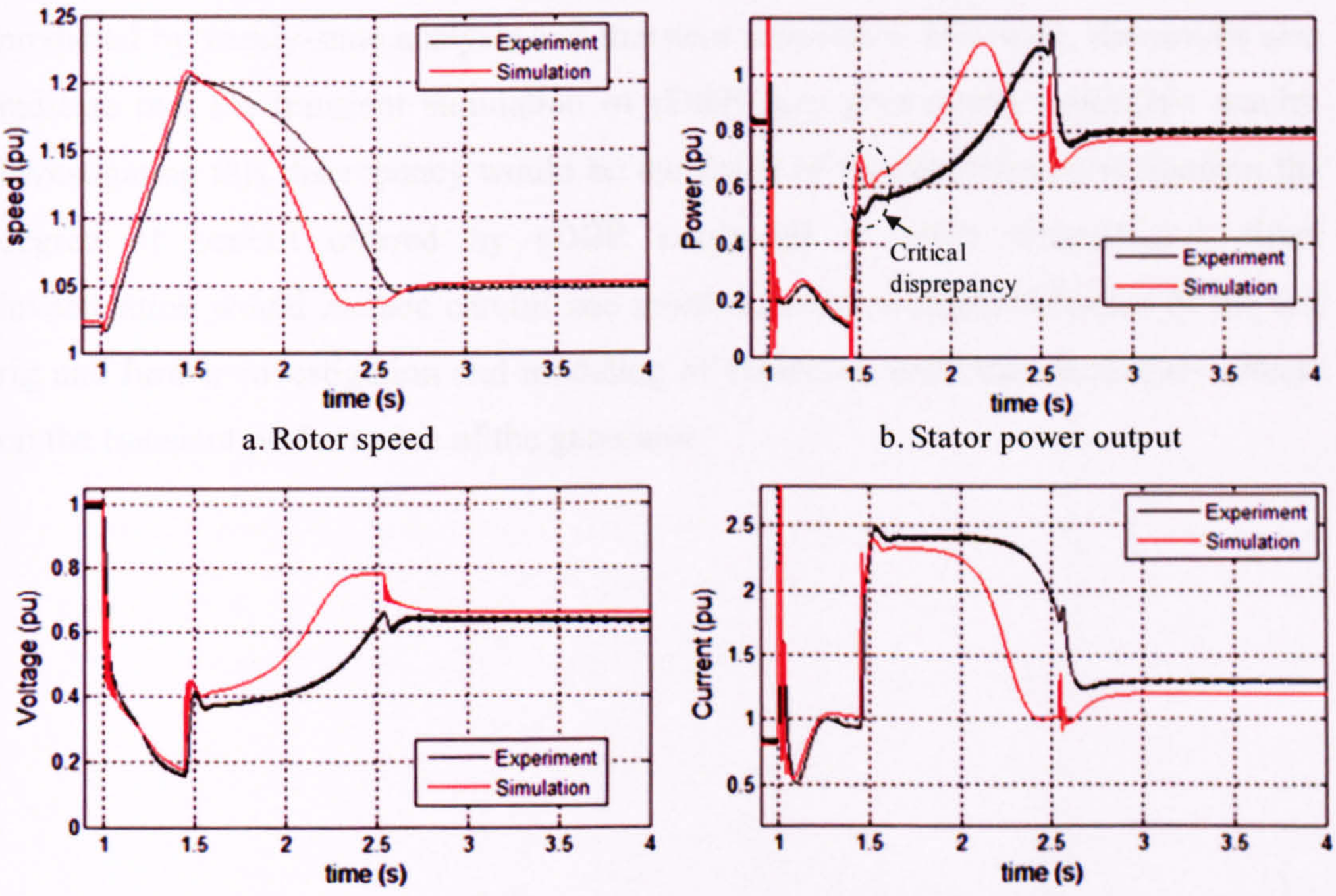

a. Rotor speed

b. Stator power output

c. Stator space vector voltage magnitude

d. Stator space vector current magnitude

Figure 7-15: Comparison of experimental and simulation results with sDBR

As for the base-case scenario, Figure 7-15a to d show that, ignoring transients, the experimental and simulated responses differ by less than 2% in the pre-fault and fault period. The discrepancy between results is again greater in the post-fault period, however in this case the simulated recovery is faster, as illustrated in Figure 7-15a. A

particularly visible discrepancy arises in the first 100ms after fault clearance, when there is significantly more decelerating power in the simulated case. This discrepancy may be due to the switching operation and/or saturation effects. However, the speed difference caused in this period is small and it is not therefore the most significant discrepancy. It is more difficult to adjust the simulation parameters to replicate the experimental result in this case. Further measurements, tests and simulations would be required to better understand and resolve this discrepancy.

7.8. Summary

Very large differences between the characteristics of the small-scale test rig and a large wind farm system have been highlighted. However, by adapting the fault scenario parameters accordingly it has been possible to derive experimental results that provide strong support for the sDBR-induced improvements in FRT stability predicted by steady-state analysis and transient simulation. However, the results also indicate that the transient simulation of sDBR may give overly optimistic results. Investigating this discrepancy would be the focus of further research to confirm the degree of benefit offered by sDBR compared to other technologies. Such investigation would include careful and more accurate re-characterisation of the test rig and further investigation and modeling of saturation and other secondary effects on the transient performance of the generator.

8. Conclusions and Recommendations

8.1. Conclusions

The series Dynamic Braking Resistor (sDBR) is the core innovation of this Thesis. The success of this Thesis therefore hinges on the potential for a valid contribution of sDBR to improving the FRT capability of FSWTs and the effectiveness of theoretical, analytical and experimental evidence presented to support this. The following points offer key evidence in favour of the successful contribution of this Thesis to relevant technological advancement and academic knowledge in this field:

1. The diminishing but still significant position of FSWT in the world wind turbine market is established in Chapter 1. This supports the validity of pursuing contributory technologies that have the potential to extend the viable application of this old but reliable turbine technology.

2. The fundamental requirement for FRT and the importance of rapid power restoration of wind power, especially in smaller power systems, are established in Chapter 2. This supports the pursuit of a technology that contributes to FRT in general with particular emphasis on rapid power recovery.

3. A review of state-of-art FRT technologies in Chapter 3 identifies the range and characteristics of technologies currently applied or proposed. This review identifies a gap for sDBR as a simple, low cost technology with potential for effective contribution to FRT compliance of FSWTs.

4. The careful development of a representative wind farm model in Chapter 4 and sensitivity analysis in Chapters 5 and 6 ensure that the simulation and experimental work of Chapters 6 and 7 provide strong evidence of FRT contribution to a broad range of real wind farm projects.

5. The quasi-steady-state (QSS) analysis of Chapter 5, supported by Appendix B, provides an unprecedented critique and justification of a technique used more loosely in previous papers and texts on wind farm stability. QSS provides

valuable under-pinning of the sDBR concept and reasonable correlation with comparative transient simulations in Chapter 6.

6. Transient analysis of Chapter 6 shows the strong performance of sDBR in direct comparison with the state-of-art FRT technology, dynamic reactive power compensation (dRPC). This relative performance is summarised in Table 6-1, showing that wind farm sDBR can deliver GB FRT compliance with very small resistances, in the same order as total equivalent resistance of the wind farm system. Equivalent compliance with dRPC requires 5 to 10 times greater pu magnitudes of reactive power compensation at significantly greater cost.

7. Compliance with RoI Grid Code requirements is shown in Table 6-1 to be substantially more onerous for both sDBR and dRPC. The use of either technology is therefore unlikely to achieve compliance in isolation. Evidence for strong complimentary benefits of the two technologies is provided by sensitivity analysis of Section 6.7. Furthermore, sDBR and dRPC have the potential to be used in conjunction with blade pitching to practically ensure compliance with RoI requirements.

8. The experimental work of Chapter 6 carefully mitigates the substantial discrepancies between the characteristics of a small (7.5kW) test rig and a large (50MW) wind farm by careful consideration of each component of the system and adjustment of tests conditions to derive representative fault scenarios. The test results were therefore able to strongly support the analytical case for sDBR-induced improvements in FRT stability.

8.2. Recommendations for Further Work

The work undertaken during the course of this PhD project and encapsulated in this Thesis provided sufficient confidence in the sDBR concept to justify commercialisation and application to certain wind farms without significant further research. This basic confidence, reinforced by site-specific simulations and scheme design, led to the brink of signing a contract for application on a 30MW wind farm project in Scotland in 2006/7. Unfortunately the opportunity was lost because of the turbine supplier's decision to withdraw from the FSWT market and its consequent reluctance to invest engineering time in innovative developments. During 2007 the other major supplier of FSWTs in Europe also withdrew from the market, leaving no European suppliers of MW-class FSWTs. This *tipping* of the European market in 2007 has shifted the direction of any future application with new large wind farms to the Asian markets such as India and China. China, in particular, has a rapidly growing wind industry with strong growth in FSWTs. The other area of possible commercialisation without significant further technical research is retrospective compliance of existing FSWT wind farms with new FRT requirements. This retrospective application is likely to be restricted to countries where there is a significant penetration of older turbines such as Denmark, Germany and Spain.

In spite of the diminishing primary market for sDBR several avenues of further research are proposed below that relate to advancing the technology and extending its application into related but distinctive markets.

8.2.1. Rearguard commercialisation

The following research and development could be carried out to investigate the market opportunities for the basic sDBR concept and develop a secure technical platform to offer the product into those markets identified:

a) Market research focusing initially on the Far-East market for new FSWTs and Grid Code requirements with prediction of likely direction over the next three years.
b) Market research focusing initially on existing FSWT wind farms in Denmark, Germany and Spain, and retrospective action to enforce compliance with current

Grid Code requirements (Energinet 2004; E.ON Nezt 2006). This would lead to transient studies assessing the potential for sDBR to contribute to compliance.

c) Further experimental work using a larger-scale test rig in the order of 15-30kW with carefully specified generator and drive characteristics that better represent the impedance and inertial parameters of a large FSWT.

d) Prototyping using an existing single FSWT turbine on a weak network. This could be a sub-MW turbine or a small wind cluster such as the experimental sites at Kirkheaton or Blyth Harbour in Northumberland, England.

8.2.2. Advanced control and optimisation

a) Investigate the benefits, issues and costs of faster switching devices, as proposed in Section 6.6.1, to improve the initial deceleration properties of sDBR. Such devices would include IGBTs, thyristors, high-speed contactors and fault-limiting circuit breakers.

b) Investigate the benefits, issues and costs of multi-stage and variable resistance sDBR, as proposed in Sections 6.6.2 and 6.6.3.

c) Investigate and optimise the integrated control of sDBR, dRPC and blade-pitch control as a means for compliance for more onerous FRT requirements, as represented by the RoI Grid Code.

8.2.3. Extended application

a) Explore the potential application of sDBR to improve the FRT stability of distribution systems with multiple embedded wind farms.

b) Explore the potential application of sDBR to improve the stability of small FSWTs in weak or isolated grids. These improvements may be driven by the customer's requirements for reliability and continuity rather than Grid or Distribution Codes.

c) Investigate application of sDBR with DFIGs. Significant potential benefits were identified by simulation during the course of the PhD but these were not pursued because of the existing Vestas patent. However, the potential benefits for control

and stability of DFIGs are significant and this option could be revisited with due regard to the existing patent.

d) Explore the application of sDBR, in conjunction with sub-millisecond switching, as a means of reducing peak fault contribution to the distribution system in cases where such contribution triggers expensive reinforcements. This is an opportunity that was investigated briefly but set aside as being outside the scope of the PhD project.

Appendices

A. Per unit system

A.1. Introduction

The per unit (pu) system is a standard method for normalising the magnitude of quantities in a system. It is used almost universally in the analysis of electrical power systems and commonly for geared mechanical drive systems. This system of units is used exclusively in this Thesis.

This Appendix has been dedicated to a "standard" system because of its importance in developing a consistent model of the representative wind farm and the discrepancies among existing texts. The per unit system used in this Thesis is contrary to most convention texts in ways that, in my opinion, improve the consistency of electrical and mechanical analogues but may cause some confusion to the reader without reference to this Appendix.

A.2. Wind Farm Drive Train

A wind farm system can be treated as an electro-mechanical drive train transferring power from its turbine blades to the electrical grid. A typical FSWT wind farm drive train is shown in Figure A-1.

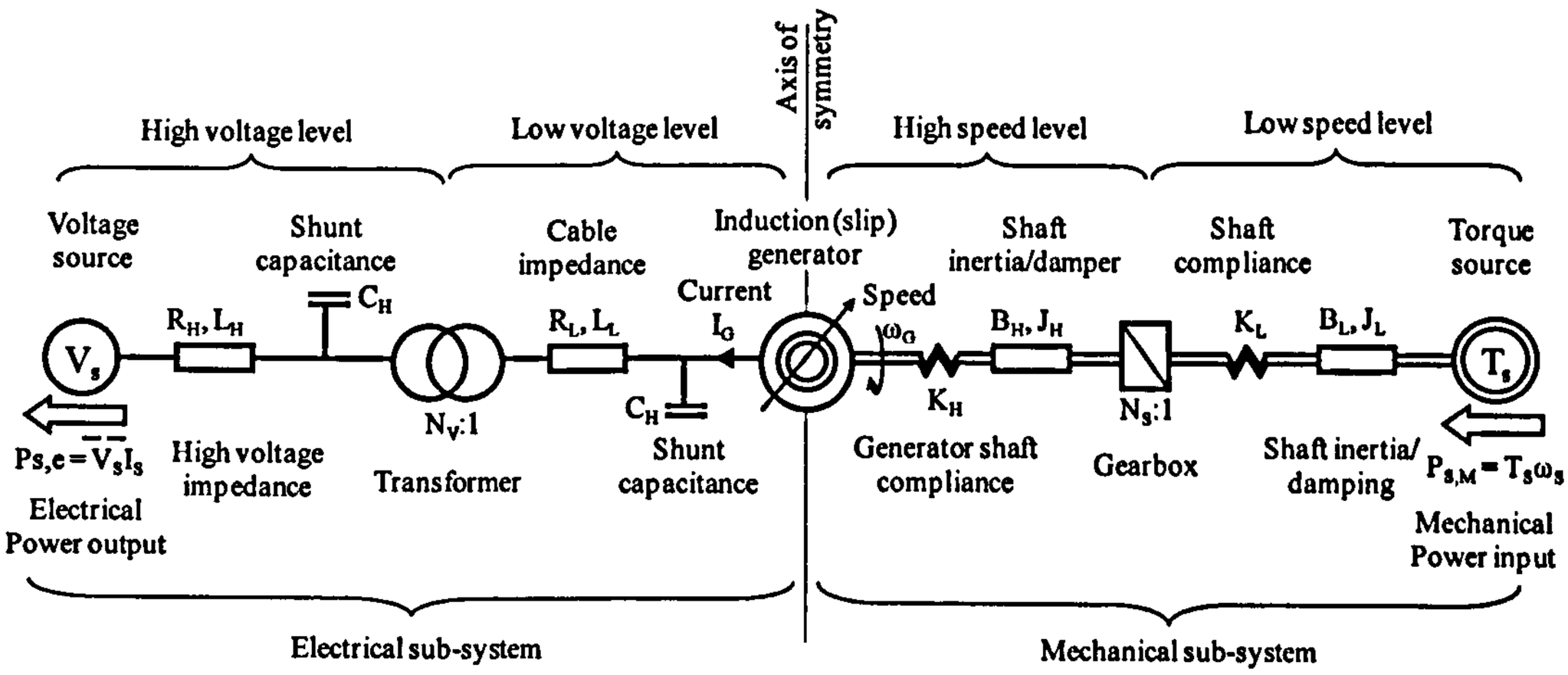

Figure A-1: Typical wind farm drive train and its components

Figure A1 highlights the analogous and near-symmetrical nature of the wind farm's electrical and mechanical sub-systems. Table A-1 catalogues the electro-mechanical analogues used in Figure A-1.

Generic term	**Electrical term**	**Mechanical term**
Power	Electrical power (P=$\bar{V}\bar{I}$)	Mechanical power (P=Tω)
Motive "force"	Voltage ($\bar{V}$)	Torque (T)
Motion	Current ($\bar{I}$)	Speed (ω)
Resistance	Resistance (R)	Damping coefficient (B)
Inertia	Inductance (L)	Moment of inertia (J)
Stiffness	Inverse capacitance (1/C)	Stiffness (K)
Transformation	Turns ratio (N:1)	Gear ratio (N:1)

Table A-1: Electrical and mechanical analogues

Table A-1 highlights two analogical discrepancies. The first apparent discrepancy is that electrical power is the scalar product of two vectors whereas mechanical power is a product of two scalars. In reality, torque and speed are given as the scalar magnitudes of co-linear vectors acting along the drive axis. The second discrepancy is that electrical sub-systems of Figure A-1 are divided by voltage (motive force) whereas the mechanical sub-systems are divided by speed (motion). The quantity used to sub-divide the systems is typically the one which remains most constant during normal operation. In the case of a wind farm, voltage and speed typically vary by less than +/-5% whereas current and torque vary from zero to rated.

A.3. Per Unit Bases

Table A-2 shows the selected per unit bases used in this Thesis.

System base values		
Quantity	*Notation*	*Value*
Active, reactive and apparent power	P_b, Q_b, S_b	$P_{WT,R}$ (W)
Time	**t_b**	**1 s**
Energy	E_b	As power
Angle, speed, acceleration	$\theta_b, \omega_b, \alpha_b$	ω_s (rads, rads s^{-1}, rads s^{-2})

Electrical base values			**Mechanical base values**		
Quantity	*Notation*	*Value*	*Quantity*	*Notation*	*Value*
Voltage	V_b	$\lvert\bar{v}\rvert_{rated}$ (volts)	Torque	T_b	$\frac{P_b}{\omega_b}$
Current	I_b	$\frac{P_b}{V_b}$	-	-	-
Resistance	R_b	$\frac{(V_b)^2}{P_b}$	Friction	B_b	$\frac{P^b}{(\omega_b)^2}$
Reactance	X_b	$\frac{(V_b)^2}{P_b}$	-	-	-
Inductance	**L_b**	$\frac{(V_b)^2}{\omega_b P_b}$	**Inertia**	**J_b**	$\frac{P_b}{(\omega_b)^2}$
Flux	λ_b	V_b	Momentum	Λ_b	$\frac{P_b}{\omega_b}$
Capacitance	C_b	$\frac{P_b}{\omega_s (V_b)^2}$	Stiffness	K_b	$\frac{P_b}{(\omega_b)^2}$

Table A-2: Base values

Table A-2 highlights in bold the important differences from conventional per-unit systems as described below:

Time base is one second rather than ω^{-1} seconds by convention. This change impacts on several other base quantities including energy, angle and acceleration.

Inductance base is a very key change from convention. Under the revised base system inductance is not equal to reactance. For a synchronous speed of 314 rad s^{-1} a reactance of 0.1pu derives from an inductance of 0.00032pu. Although inductance values under this system tend to be inconveniently small, they are consistent with their mechanical inertia analogues and therefore give a proper perspective on the huge difference in electrical and mechanical inertias in a typical power system.

Inertia base, J, is used in place of inertia constant, H. These quantities are related as

$$J = 2H.$$

A.4. Equations in Per Unit Form

Table A-3 summarises the per unit equations that describe the transient behaviour of the electrical and mechanical components of a system. In each case, the conventional form is compared with the revised form using the per unit system of Section A.3.

Quantity	Conventional	Revised
Inertial transient:		
Electrical	$\Delta\bar{v} = R\bar{i} + \frac{L'}{\omega_0}\frac{d\bar{i}}{dt}$	$\Delta\bar{v} = R\bar{i} + L\frac{d\bar{i}}{dt}$
Mechanical	$\Delta\tau = B\omega + 2H\frac{d\omega}{dt}$	$\Delta\tau = B\omega + J\frac{d\omega}{dt}$
Coupling transient:		
Electrical	$\Delta\bar{i} = \frac{1}{R}\bar{v} + \omega_b C'\frac{d\bar{v}}{dt}$	$\Delta\bar{i} = \frac{1}{R}\bar{v} + C\frac{d\bar{v}}{dt}$
Mechanical	$\Delta\omega = B\tau + \omega_b K'\frac{d\tau}{dt}$	$\Delta\omega = B\tau + K\frac{d\tau}{dt}$
Generator transient:		
Stator	$\bar{v}_s = R_s\bar{i}_s + \frac{1}{\omega_b}\frac{d\bar{\lambda}_s}{dt}$	$\bar{v}_s = R_s\bar{i}_s + \frac{d\bar{\lambda}_s}{dt}$
Rotor (short-circuited)	$R_r\bar{i}_r + \frac{1}{\omega_b}\frac{d\bar{\lambda}_r}{dt} - \omega_r M\bar{\lambda}_r = 0$	$R_r\bar{i}_r + \frac{d\bar{\lambda}_r}{dt} - \omega_r\omega_b M\bar{\lambda}_r = 0$
Electrical torque	$T_e = L_m' i_s i_s \sin\theta$	$T_e = \omega_b L_m i_s i_s \sin\theta$ (note 1)
Time constants (s)		
Electrical	$t_{dc} = \frac{L'}{\omega_b R}$	$t_{dc} = \frac{L}{R}$
Mechanical	$t_c = \frac{2H}{\omega_b B}$	$t_c = \frac{J}{B}$
Oscillation (Hz):		
Electrical	$f_{nat} = \omega_b\sqrt{\frac{1}{L'C'}}$	$f_{nat} = \sqrt{\frac{1}{LC}}$
Mechanical	$f_{nat} = \sqrt{\frac{\omega_b K'}{J}}$	$f_{nat} = \sqrt{\frac{K}{J}}$ (note 2)

Notes:

1. The inserted ω_b factor in the equation for electrical torque is derived from the partial differentiation of "coenergy" with respect to angle θ (Fitzgerald, Kingsley et al. 2002, Equations 4.64, 4.65).
2. Mechanical natural frequency, f_{nat}, is reference to a fixed point. Drive train eigen-frequencies are generally quoted for free two-mass oscillations.

Table A-3: Transient per unit equations

B. Quasi-steady-state analysis

B.1. Introduction

Steady-state stability analysis of induction generators is used to determine the stability limit for FSWT wind farms operating at reduced grid voltages (Holdsworth, Jenkins et al. 2001). The wind farm becomes unstable when the peak decelerating power is less than the maximum mechanical input power. This technique is conventionally used for considering short-term wind farm operation at reduced grid voltages. An example of such an event would be a three-minute, 15% voltage dip, as defined the NGC Grid Code and illustrated in Figure 2-14. For an event of this duration, the system would reach a new steady-state operating point, which must be stable according to the above criteria. However, in the case of the 2.5-second, 20% voltage dip of Figure 2-14, steady-state stability criteria may not apply because the system would not reach steady-state operation in this period.

A technique extending the application of steady-state analysis to dynamic stability is introduced by Akhmatov (Akhmatov, Knudsen et al. 2000; Akhmatov 2003(a)). Akhmatov uses this technique to determining the *dynamic stability limit* of FSWTs in several publications, including his recent book (Akhmatov 2005(b)). However, it is not obvious that FRT stability can be generally inferred from steady-state analysis, and my literature search revealed insufficient theoretical or empirical support. The technique is therefore assessed more comprehensively in this Appendix and designated *quasi-steady-state (QSS) analysis* throughout the Thesis. In particular, it is used extensively in Chapter 5 to infer transient FRT stability and compare the performance of sDBR and dRPC technologies under a range of fault scenarios.

B.2. Quasi-Steady-State Methodology

B.2.1. Steady state characterisation

A wind farm system can be characterised by a set of decelerating power versus speed curves distinguished by supergrid voltage. Figure B-1 characterises the wind farm system of Figure 4-12 in this manner.

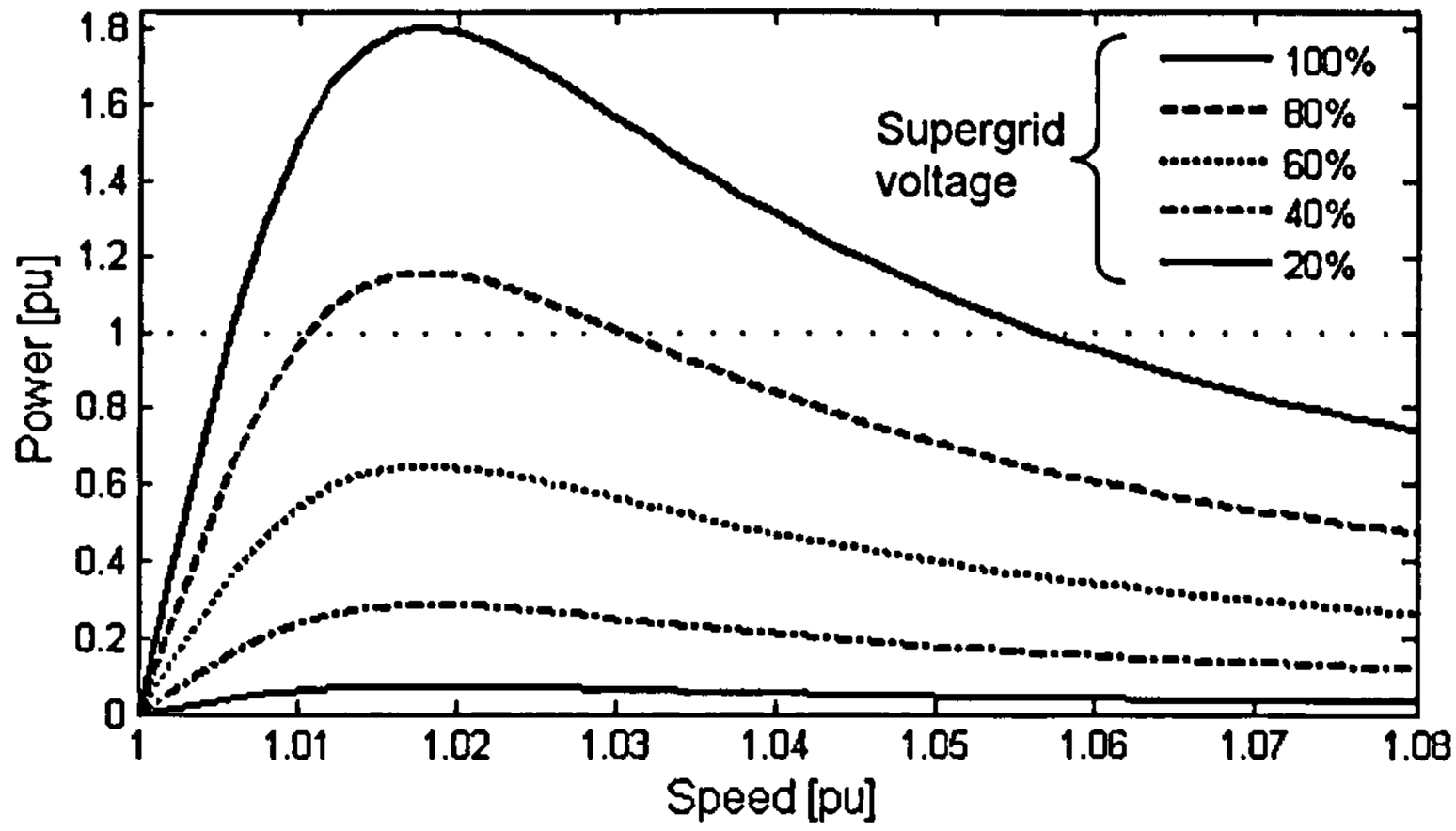

Figure B-1: Decelerating power versus speed characteristic for representative wind farm

Figure B-1 is broadly representative of the steady-state characteristic of all wind farms. Differences in wind farm parameters typically modify the magnitude and speed of the peak decelerating power and the rate of power fall-off for speeds greater than the peak. These curves are the basic reference point for QSS analysis.

B.2.2. Basic assumption

The fundamental assumption for QSS analysis is that the dynamic process can be approximated as two QSS stages, described as *fault* and *recovery*. The voltage is assumed to be constant during each stage, and the system response can therefore be characterised with reference to the relevant curves from Figure B-1.

B.2.3. Method

Assuming constant mechanical input power (justified in Section 4-2), the trajectory of the wind farm system can be represented on a power-speed graph. Figure B-2a identifies five points during fault scenario 3 that are used to trace the dynamic trajectory of the wind farm system for two inertia scenarios in Figure B-2b and c.

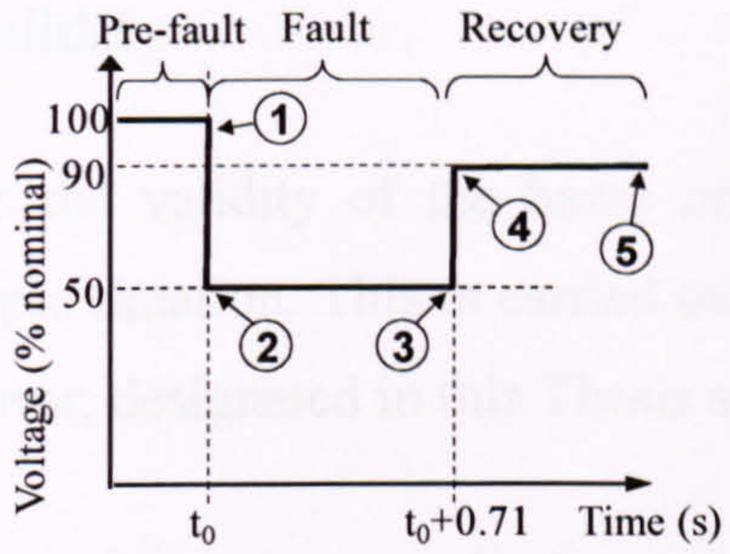

a. Fault scenario 3 profile with five reference points

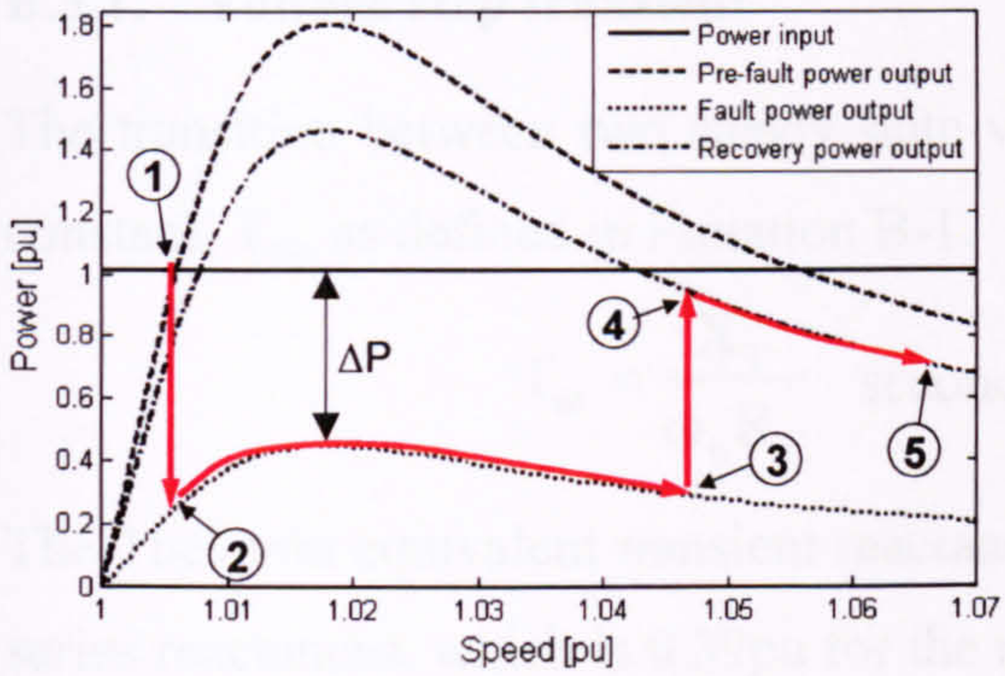

b. Power speed trajectory for unstable case

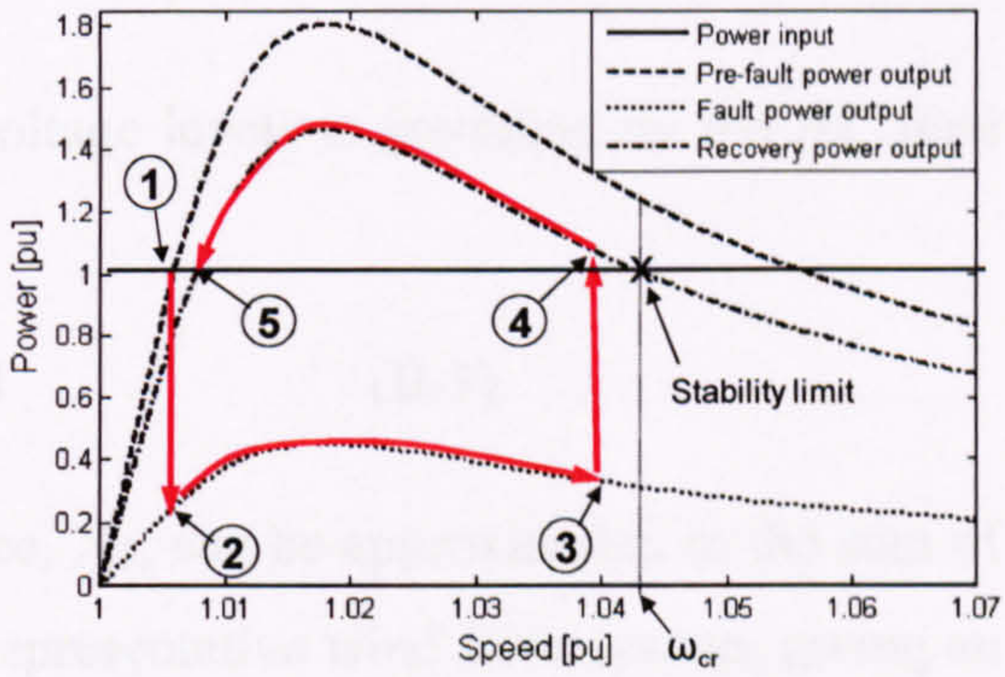

c. Power speed trajectory for stable case

Figure B-2: Dynamic trajectory of wind farm in decelerating power-speed domain

Point 1 in Figure B-2b is the steady pre-fault state, lying at the intersection of the power input and pre-fault (100% voltage) power output curves. Point 2 lies on the fault- (50% voltage) power output curve at rated speed. The dynamic trajectory then follows the fault-power output curve as speed increases due to the net accelerating power, ΔP. At fault clearance the trajectory transfers from point 3 to point 4 on the recovery- (90% voltage) power output curve. At point 4 the net accelerating power causes the drive train to accelerate towards point 5 and eventually trip.

Figure B-2c is identical to Figure B-2b except that the acceleration is reduced because of higher drive train inertia. As a result, the rotor speed at fault clearance is less and the decelerating power at point 4 is greater than the input power leading to deceleration and recovery to a new stable operating point (5) at the intersection of the power input and recovery power output curves. It can be concluded, by inspection, that the system stability limit, *critical speed*, ω_{cr} (Akhmatov 2005(b))), is at the intersection of the power input and recovery power output curves. A characteristic critical speed can be defined for any given wind farm system (including its grid connection) at specified recovery voltage and mechanical power input.

B.3. Assessment of Validity

This assessment examines the validity of the basic assumption of Section B.2.2 concerning steady-state approximation. This is carried out by isolating the two main categories of transitional error, designated in this Thesis as *voltage step transient* and *rotor dynamics.*

B.3.1. Voltage step transient

The transition between two steady-state voltage levels is governed by the AC time constant, T_{ac}, as defined in Equation B-1.

$$T_{ac} = \frac{X_T}{\omega_b R_r} \text{ second} \qquad \text{(B-1)}$$

The Thevenin equivalent transient reactance, X_T, can be approximated to the sum of series reactances, which is 0.39pu for the representative wind farm system, giving an AC time constant of about 180ms. This time constant is confirmed by the transient simulation of Figure B-3.

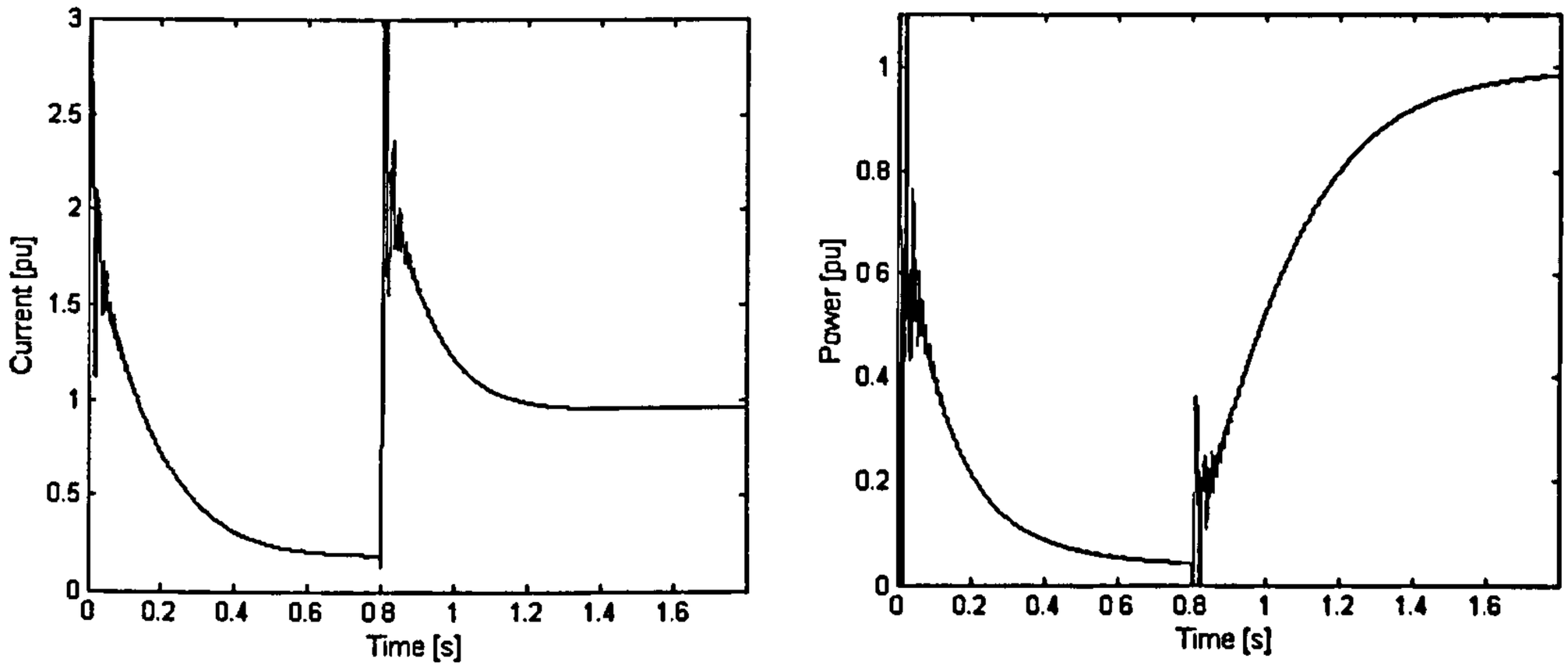

a. Current-time curve

b. Power-time curve

Figure B-3: Voltage step transient simulation results

The simulation results of Figure B-3 are derived from the transient model of the representative wind farm system of Figure 4-12 with the rotor constrained to rated speed and sDBR and dRPC set to zero. A 800ms, 80% voltage dip is applied followed by rated recovery voltage. Figure B-3a shows a current decay time constant of approximately 180ms in both cases. However, although the power decay of Figure B-3b is similar, the recovery time constant is significantly longer, governed by the longer time constants for magnetising the generator from the stator side.

For the purpose of comparing the transient performance of FRT technologies it is more important to examine whether the technologies change the base-case time constant. Figure B-4 compares the time constant of transient response for sDBR (0.1pu), dRPC (0.6pu) with the base-case.

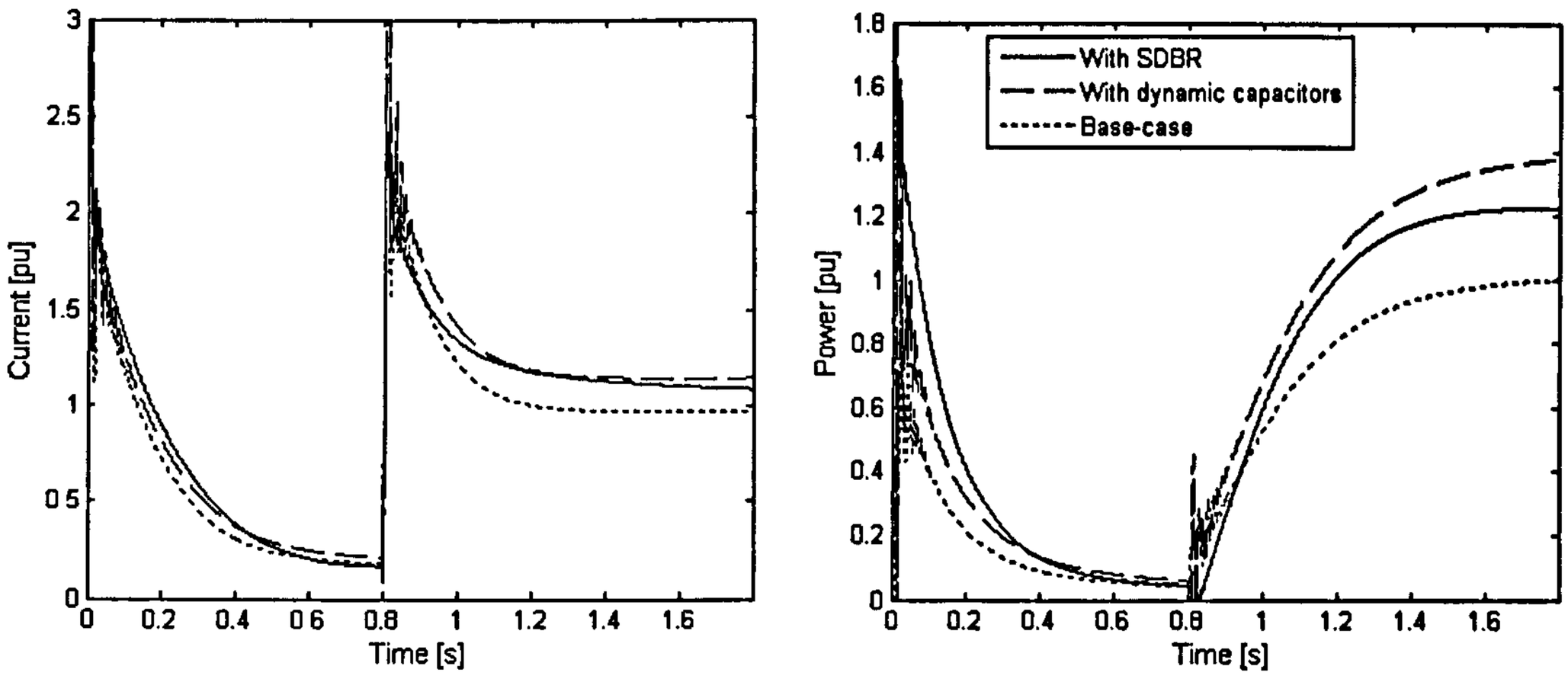

a. Current-time curve

b. Power-time curve

Figure B-4: Effect of dRPC and sDBR on transient time constants

Figure B-4a and b show that the difference in time constant is very small. As expected from Equation 7-1, sDBR makes no significant difference to the time constant whereas dRPC does marginally increase the time constant, as expected because of the increase in reactance.

It can be concluded that voltage transients introduce significant error to QSS assessment of stability for faults less than one second. However, the fact that the selected FRT technologies make little difference to the power time constants means that neglecting voltage step transients should not distort a comparative assessment.

B.3.2. Rotor dynamics

The power-speed relationship of an induction generator is dependent on rotor acceleration, as shown in Figure B-5a.

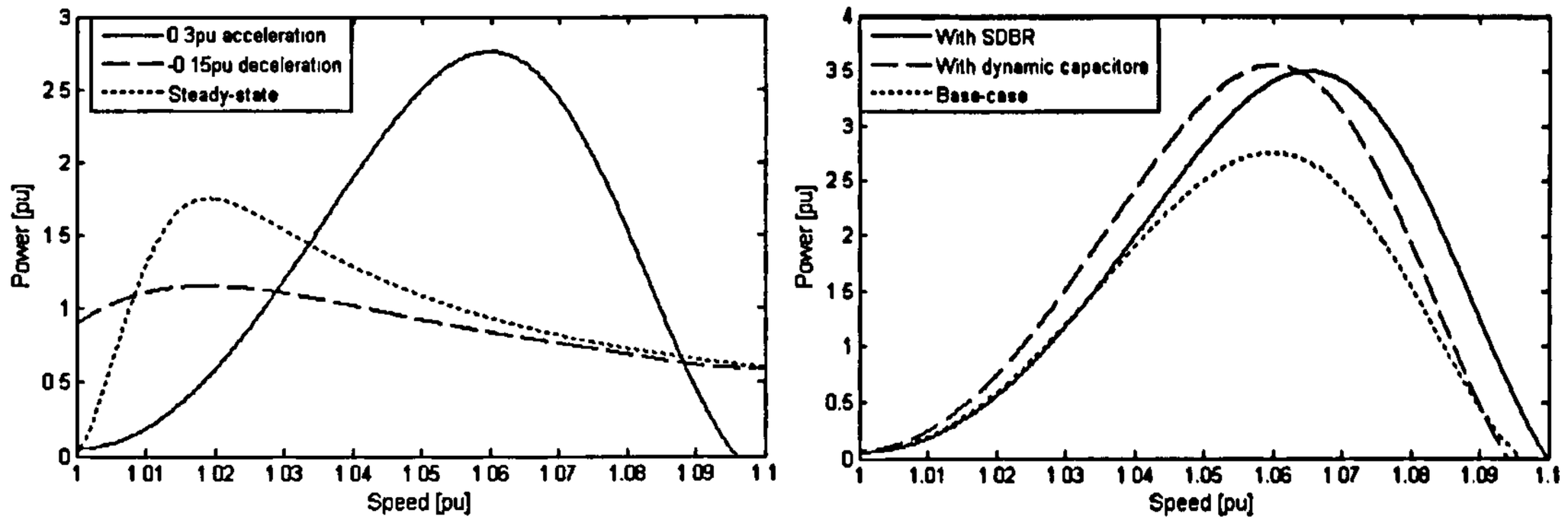

a. Effect of acceleration b. Comparison of capacitor and SDBR

Figure B-5: Dependence of power-speed characteristic on rotor acceleration

The curves of Figure B-5a and b are based on the results of simulations using the same model as Section B.3.1 but with rated supergrid voltage and constant rotor acceleration. The rotor acceleration and deceleration values are selected to represent likely worst-case magnitudes using the representative two-mass drive train model. Figure B-5a shows that acceleration "shears" the power-speed curves in the direction of higher speed and power magnitude and deceleration "shears" the power-speed curves in the direction of lower speeds and power magnitude. The overall effect of this shearing is difficult to predict because the depressed decelerating power for speeds up to 1.03pu is counteracted by boosted power at higher speeds. More importantly for comparative studies, Figure B-5b shows that acceleration has a similar shearing effect on sDBR and dRPC although the dRPC may marginally benefit from the sheared effect because of the larger decelerating power for speeds up to 1.06pu.

B.3.3. Correlation with transient simulation

Having isolated and assessed the two major discrepancies between QSS and transient analysis, the purpose of this Section is to compare the analyses for a specific study. The selected wind farm system is the one used in Sections B.3.1 and B.3.2 with 0.1pu sDBR inserted. The drive-train is modelled as a lumped equivalent inertia of 9pu and the system is subjected to fault scenario 3 of Figure 3-1. In order to apply the dynamic correction factor it is necessary to initially approximate the average acceleration and deceleration during the fault and recovery phases respectively from the results of the transient simulation, as shown in Figure B-6.

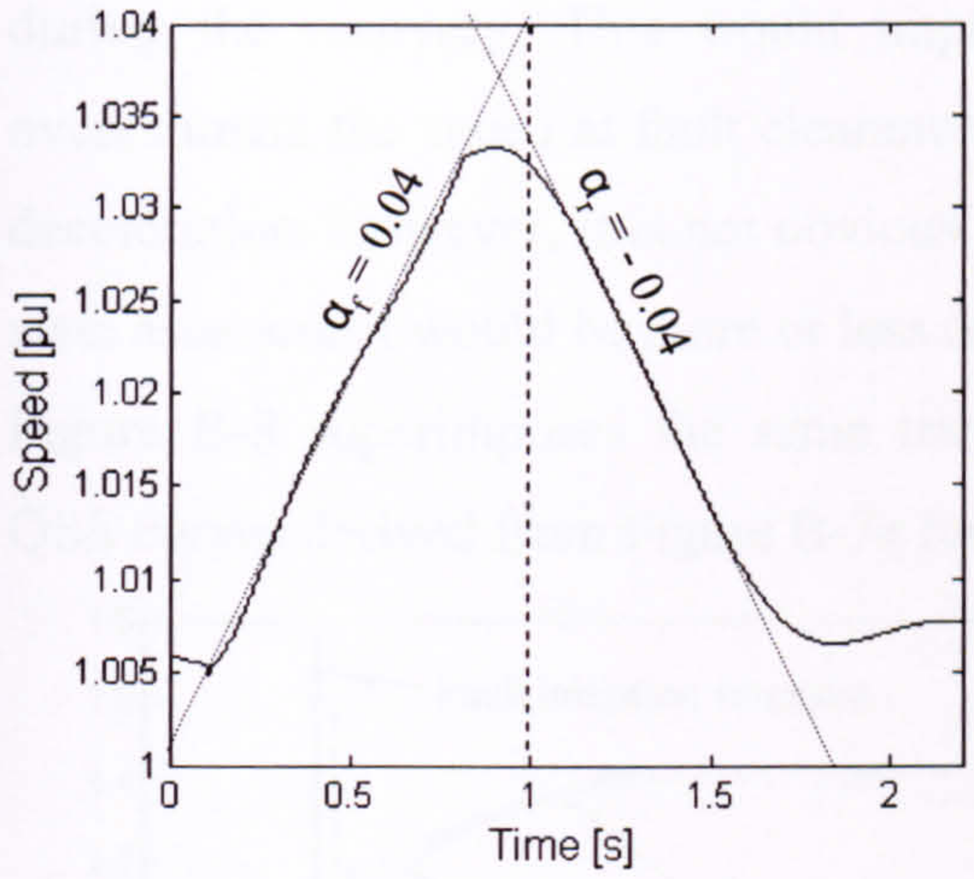

a. Speed-time response

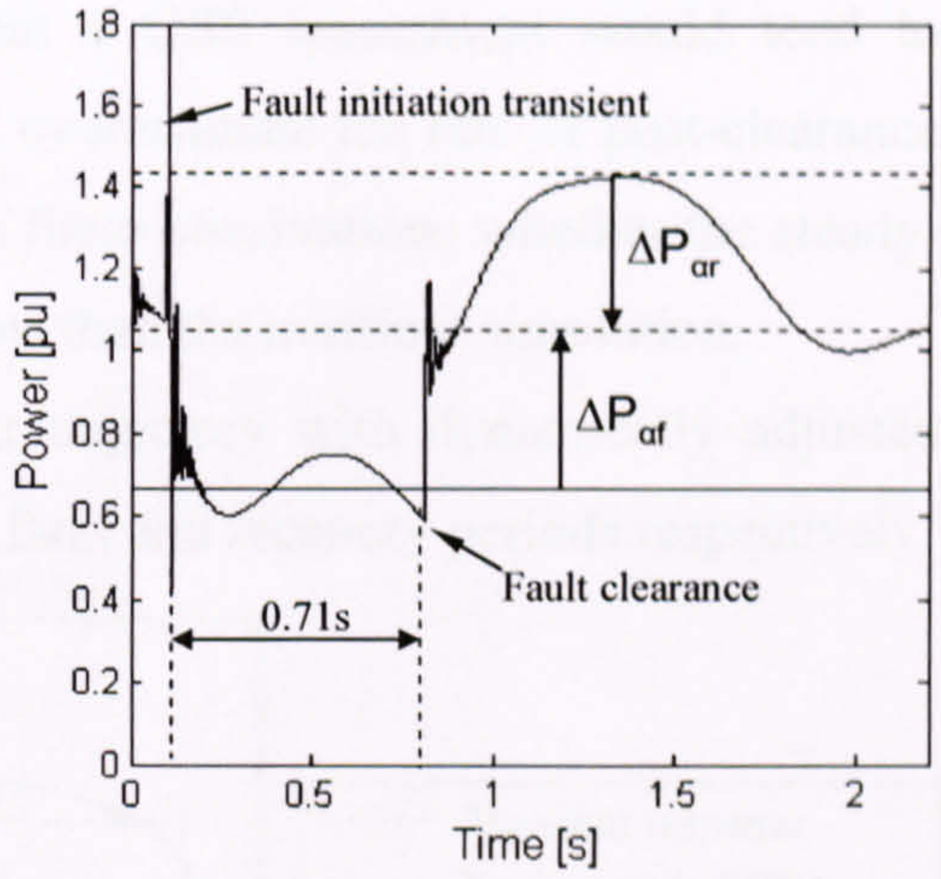

b. Power-time response

Figure B-6: Power and speed-time responses of wind farm

Figure B-6a and b show the speed- and power-time responses of the wind farm system respectively. It can be seen from Figure B-6b that the accelerating and decelerating power, $\Delta P_{\alpha f}$ and $\Delta P_{\alpha r}$, are approximately equal in magnitude (0.37pu) and opposite in sign. This is reflected in the equal and opposite acceleration rates, α_f and α_r shown in Figure B-6a. These acceleration rates are confirmed from the equation of motion, Eq. B-2.

$$\alpha = \frac{\tau}{J} = \frac{P}{\omega J} = \frac{0.37}{1.02 \times 9} = 0.040\text{pu} \qquad \text{(B-2)}$$

The transient results are superimposed on the uncorrected QSS curves in Figure B-7.

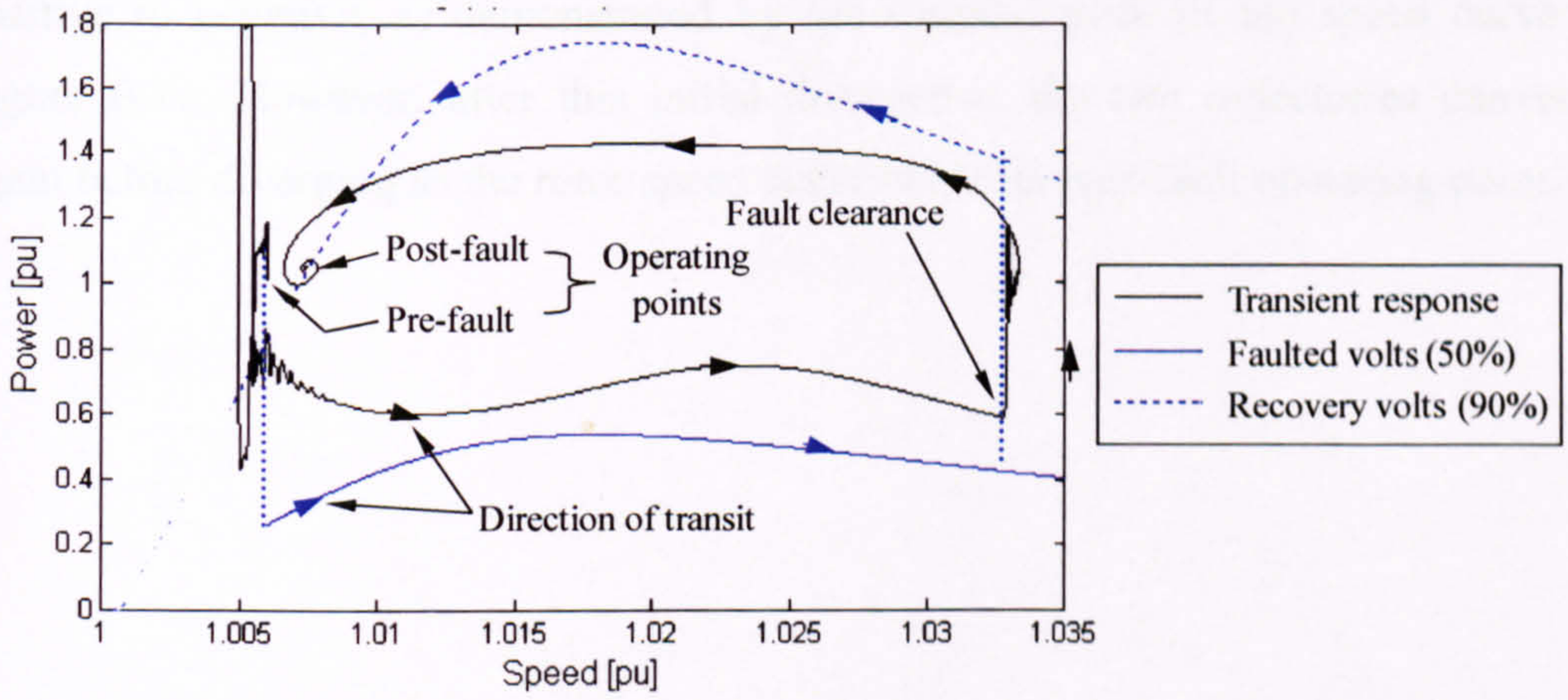

Figure B-7: Superposition of uncorrected QSS and transient power-speed trajectories

As expected, the pre- and post-fault operating points in Figure B-7 are coincident but the trajectories are otherwise quite divergent with the steady-state trajectory significantly under-estimating power during the fault and over-estimating power

during the recovery. This would imply that a QSS assessment would tend to overestimate the speed at fault clearance and overestimate the rate of post-clearance deceleration. However, it is not obvious from these observations whether the steady-state assessment would be more or less onerous than the transient simulation.

Figure B-8 superimposes the same transient trajectory with dynamically adjusted QSS curves derived from Figure B-7a for the fault and recovery periods respectively.

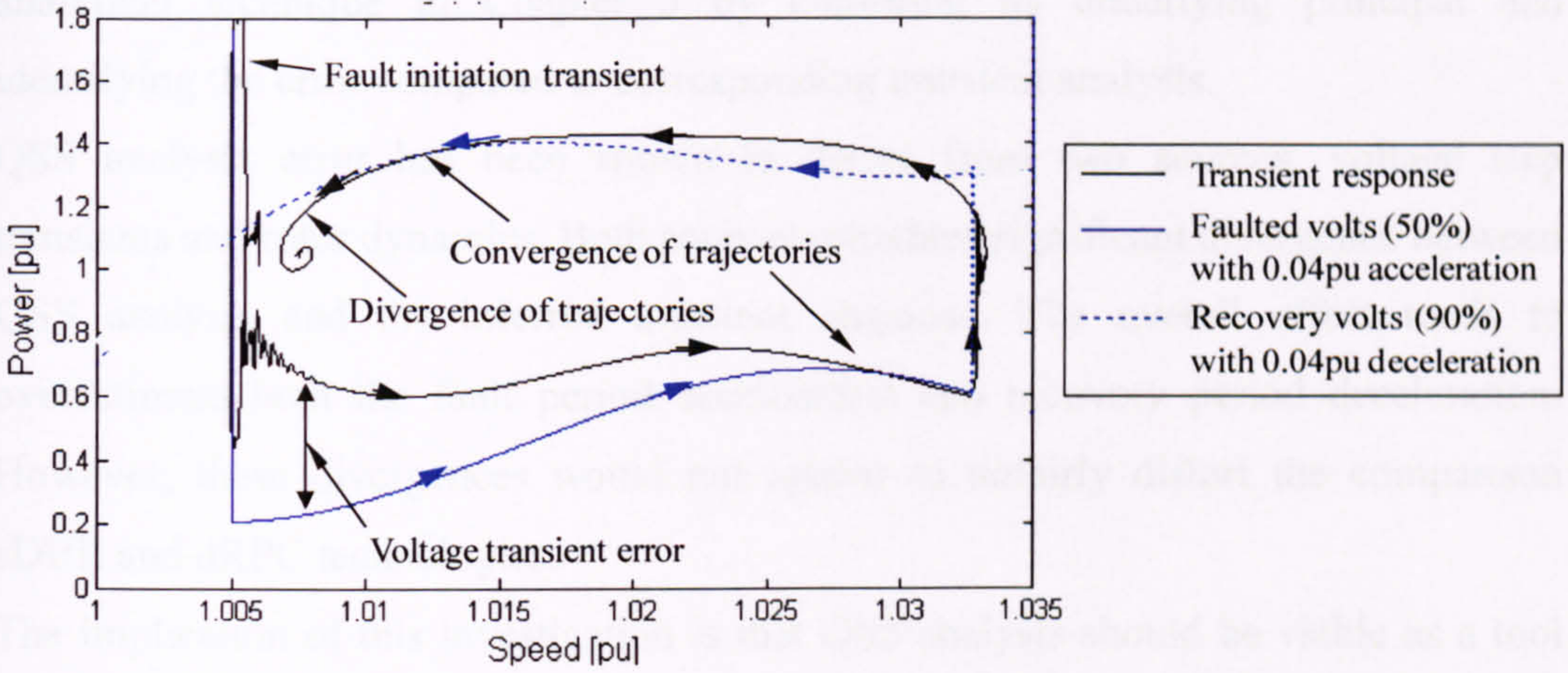

Figure B-8: Superposition of uncorrected QSS and transient power-speed trajectories

In the fault period, Figure B-8 illustrates the initial "voltage step transient" error, which subsides until the two trajectories coincide at about 1.03pu speed. In the recovery period, Figure B-8 shows an initial divergence due to a combination of the clearance "voltage step transient" error and the transition of acceleration from positive to negative, as demonstrated by the rounded peak of the speed curve in Figure B-6a. However, after this initial divergence, the two trajectories converge again before diverging as the rotor speed stabilises at its post-fault operating point.

B.4. Summary

QSS is used in published work as a tool for inferring the stability of FSWTs under short-term and faulted grid conditions. This Appendix supports the application of this analytical technique in Chapter 5 by clarifying its underlying principal and identifying the error compared to corresponding transient analysis.

QSS analysis error has been shown to derive from two sources, voltage step transients and rotor dynamics. Both sources introduce significant divergence between QSS analysis and the inferred transient response. The overall effect tends to overestimate both the fault period acceleration and recovery period deceleration. However, these divergences would not appear to unfairly distort the comparison sDBR and dRPC technologies.

The implication of this investigation is that QSS analysis should be viable as a tool for inferring the effectiveness of FRT technologies and providing an indication of the likely FRT stability of wind farm systems. There is scope for further theoretical assessment of this technique and the limits and sensitivities of its application. However, for the purpose of this Thesis the correlation of QSS analysis in Chapter 5 with transient simulations in Chapter 7 serves to demonstrate empirically the value of the technique.

C. Published IEEE Transactions Paper

The paper on the following pages is extracted directly from IEEE Transactions on Power Systems, Vol 22, No 3. August 2007.

Fault Ride-Through of Large Wind Farms Using Series Dynamic Braking Resistors (March 2007)

Andrew Causebrook, David J. Atkinson, and Alan G. Jack, *Member, IEEE*

***Abstract*—Fault ride-through (FRT) is required for large wind farms in most power systems. Fixed speed wind turbines (FSWTs) are a diminishing but significant sector in the fast-growing wind turbine (WT) market. State-of-art techniques applied to meet grid requirements for FSWT wind farms are blade pitching and dynamic reactive power compensation (RPC). Blade pitching is constrained by the onerous mechanical loads imposed on a wind turbine during rapid power restoration. Dynamic RPC is constrained by its high capital cost. These present technologies can therefore be limiting, especially when connecting to smaller power systems. A novel alternative technology is proposed that inserts series resistance into the generation circuit. The series dynamic braking resistor (SDBR) dissipates active power and boosts generator voltage, potentially displacing the need for pitch control and dynamic RPC. This paper uses a representative wind farm model to study the beneficial effect of SDBR compared to dynamic RPC. This is achieved by quasi-steady-state characterization and transient FRT stability simulations. The analysis shows that SDBR can substantially improve the FRT performance of a FSWT wind farm. It also shows that a small resistance, inserted for less than one second, can displace a substantial capacity of dynamic RPC.**

***Index Terms*—Dynamic braking resistors, fault ride-through, wind farm stability, wind turbine generators.**

I. Introduction

FAULT ride-through (FRT) is now required for connection of large wind farms in most power systems. The FRT-compliant wind farm must remain connected and actively contribute to system stability during a wide range of network fault scenarios. FRT is particularly important in securing stability in regions where wind is becoming a significant contributor to the power system's dynamic performance.

FRT performance requirements differ according to the dynamic characteristics of the power system concerned. Smaller power systems, with little or no interconnection, are more prone to frequency instability, and hence, their Codes typically emphasize the provision of active power. Ireland, with a maximum system demand of 6 GW, represents a small, near-isolated national system with a challenging requirement to restore power within one second of fault clearance [1], [2]. Great Britain, with a maximum demand of 60 GW, represents a larger near-isolated system with similar requirements [3], [4]. In contrast, frequency stability in continental European countries such as Germany is strengthened by interconnections within the Union for the Co-operation of Transmission of Electricity (UCTE). UCTE members therefore have less onerous power restoration requirements [5], [6].

Manuscript received September 6, 2006; revised March 13, 2007. This work was supported in part by the New and Renewable Energy Centre (NaREC) and in part by an EPRSC studentship. Paper no. TPWRS-00624-2006.

The authors are with the Electrical Machines and Drives Group, Newcastle University, Newcastle-upon-Tyne, U.K. (e-mail: Andrew.Causebrook@newcastle.ac.uk).

Digital Object Identifier 10.1109/TPWRS.2007.901658

TABLE I
Wind Technology Enhancements to Meet FRT Challenge

Type	FRT enhancement
A.	Dynamic reactive power compensation (RPC)
B.	As above + pitch control
C.	Rotor converter protection + pitch control
D.	Pitch control + braking resistors on dc link

The wind industry has responded to the introduction of FRT requirements in several ways according to wind turbine technology type. For the purpose of considering FRT response, it is convenient to categorize commercial wind turbines in four main types [7], [8]:

A) fixed-speed wind turbines (FSWTs) with fixed pitch;
B) FSWTs with variable pitch (active stall);
C) variable-speed wind turbines (VSWTs) with doubly-fed induction generators (DFIGs);
D) VSWTs with fully-rated converters.

Type A WTs were dominant in the 1990s but now retain less than 1% of the world market share. Type B WTs have retained a sizeable market share and have accumulated an installed world capacity of approaching 10 GW. Type C has been the dominant technology since about 2002, but type D may challenge this dominance in the future as the cost of power electronics continues to fall. Specific technical developments made in response to FRT requirements are summarized in Table I.

Pitch control is therefore a central feature of most FRT strategies for modern wind turbines. However, there are still significant response limitations when this method is applied to smaller power systems. Although the blade pitch actuators are powerful enough to fully pitch the blades within a fraction of a second, the dynamic forces resulting from restoring power at this rate are very onerous. Faster restoration times may be achieved by improved structural design, but it is likely that these dynamic forces will remain a substantial design issue where sub-second restoration times are required. As a consequence, pitch control is not the final solution for FRT compliance, and there is still an opportunity for technologies that reduce or eliminate dependence on pitch control systems or allow retrospective enhancement of existing wind farms. This paper proposes series dynamic braking resistors (SDBRs) as a promising alternative, with particular applicability to FSWTs (types A and B) and possible extension to other generation technologies. The SDBR concept was introduced by the authors in 2005-2006 [9], [10]. The purpose of this paper is to present detailed analysis and transient simulation results of its performance and assess its beneficial effects compared to state-of-art alternatives.

0885-8950/$25.00 © 2007 IEEE

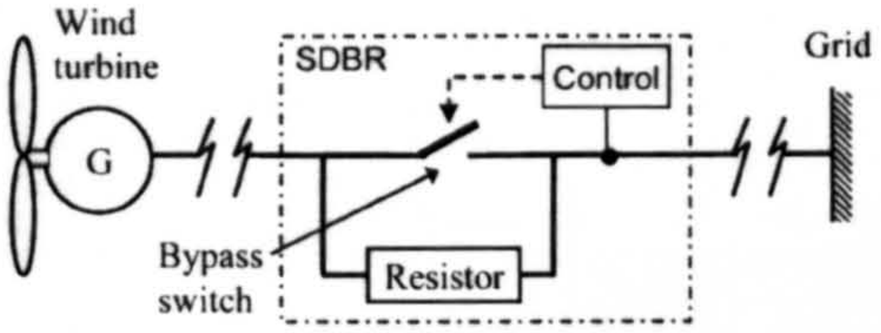

Fig. 1. SBDR schematic arrangement.

II. SDBR Concept

The SDBR concept aims to contribute directly to the balance of active power during a fault, thus displacing or eliminating the need for pitch control. It does this by dynamically inserting a resistor in the generation circuit, increasing the voltage at the terminals of the generator and thereby mitigating the destabilizing depression of electrical torque and power during the fault period.

The general schematic arrangement of SDBR is shown in Fig. 1.

SDBR is shown located between the wind turbine(s) and the grid in Fig. 1. The actual position of the device within a particular wind farm topology will depend on the space available to install it and the relative cost of switching at low, medium, and high voltage. The bypass switch could be mechanical, allowing multi-cycle response and discrete control, or static, allowing sub-cycle response and smoothly variable control. This paper focuses on single-stage mechanical switching as the lowest cost and least complex option with potential to strongly contribute to FRT compliance of FSWTs.

SDBR would operate with its switch closed under normal conditions, bypassing the braking resistor. Voltage depression below a selected set-point would lead to near-instantaneous tripping of the switch. Current would then flow through the inserted resistor for the period of the fault and the initial post-fault recovery. When voltage recovered above a minimum reference level, the switch would close and the circuit would be restored to its normal state. During the short insertion period, the energy would be dissipated in the resistor, raising its temperature. The resistor would be selected according to the limiting temperature of its resistive elements and the maximum energy dissipated during the insertion period.

Previous DBR topologies proposed by Wu [11] and Freitus [12] for wind farm stability have a shunt-connected topology, in the manner previously applied to improve transmission and synchronous generator stability [13], [14]. The distinctive advantage of series-SDBR over shunt-DBR is derived from the fact that its effect is related to *current* magnitude rather than *voltage* magnitude. SDBR is therefore most effective during the combined high generation, low residual voltage conditions that are most onerous for FRT. The effect is shown schematically in Fig. 2.

Fig. 2 shows how generated power is transferred across the wind farm system, while excess dynamic power is stored in its drive train and heat is dissipated by SDBR. The effect on stator voltage is illustrated by the phasor diagram of Fig. 3.

It can be seen from Fig. 3 that stator voltage, v_s, is increased in magnitude by the voltage, iR_{sdbr}, across SDBR. Since mechanical torque is proportional to the square of the stator voltage of an induction machine, it can be inferred that the presence of SDBR will increase the mechanical power extracted from the

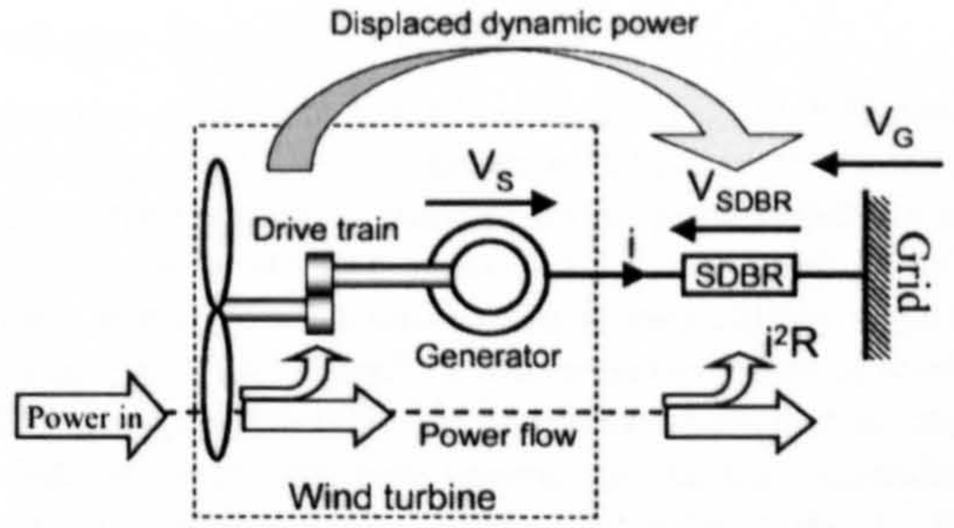

Fig. 2. Conceptual benefit of SBDR under fault conditions.

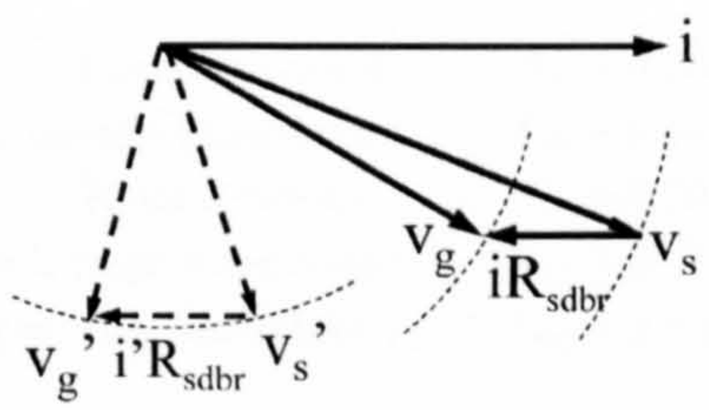

Fig. 3. Phasor diagram showing the effect of SDBR on stator voltage.

drive train and therefore reduce its speed excursion during a voltage dip. This effect would improve the post-fault recovery of a wind farm system. Fig. 3 also shows the limiting beneficial case (dotted phasors) at very low power factor when SDBR has no effect on stator voltage magnitude.

III. Methodology

Section II has introduced the SDBR concept and provided a theoretical basis for its application to FRT. Simulation and analysis are required to support this theoretical assertion and establish the magnitude and the extent of its beneficial effect compared to state-of-art dynamic RPC. This section previews the methodology used in this paper to achieve this objective.

The first step in Section IV is to establish a reduced FSWT (type A or B) system that is representative of a large modern wind farm. This representative wind farm system is then characterized by steady-state analysis in Section V to illustrate the effect of SDBR over a range of super-synchronous rotor speeds. The validity and limitation of using steady-state analysis to infer FRT performance benefits is examined. A transient model of the representative wind farm system is then presented in Section VI and used to simulate selected fault scenarios in order to verify the effect of SDBR. The dynamic response of a *one-mass* system is used to study underlying FRT characteristics and check the validity of inferring transient behavior from steady-state characteristics. The dynamic response of a *two-mass* system is then used to compare the performance of SDBR with dynamic RPC. Finally, the same transient model is used to check the effectiveness of SDBR and dynamic RPC during a prolonged phase-to-phase grid fault.

Simulation results are used to draw conclusions regarding the strength and extent of the potential FRT application of SDBR with FSWT-wind farms.

IV. Representative Wind Farm System

There is a broad range of practical wind turbine and wind farm configurations. The purpose of this section is to define a

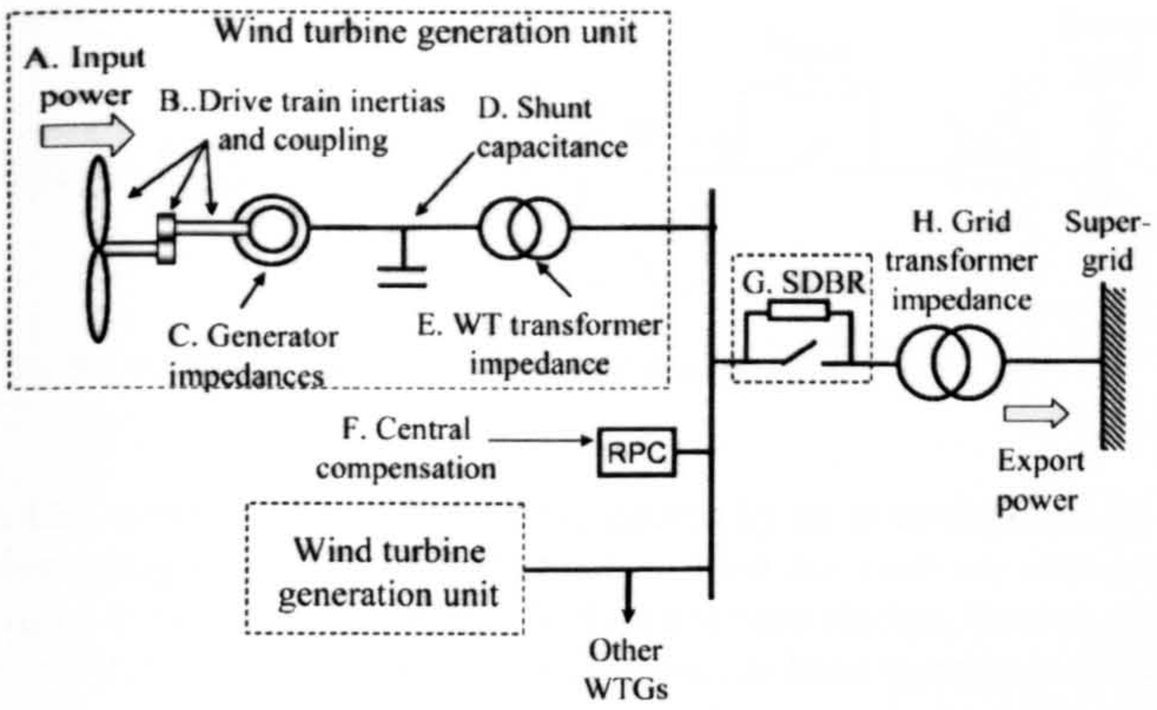

Fig. 4. Typical large wind farm single line diagram.

single representative wind farm system for all for the steady-state and transient analyses presented in this paper.

A typical large wind farm comprising multi-megawatt FSWTs and incorporating SDBR is represented by the single line diagram of Fig. 4.

Fig. 4 annotates the key parameters that influence stability of the system associated with a supergrid fault. These parameters are quantified and discussed below. All quantities are given in per unit form using wind turbine or wind farm active power rating as the power base.

A. Mechanical Power Input

Wind turbine input power is highly variable and unsteady, resulting in large and rapid variations in power transfer [15, pp. 135–136]. For the purpose of studying worst-case FRT performance, these variations detract from observation of the fundamental system dynamics. Furthermore, they are smoothed over a wind farm with a large number of WTs because of their non-coherence. An equivalent constant power input has therefore been used in this paper [16, p. 532]. Since maximum generation conditions are worst-case for FRT assessment, an *input power of 1.05 p.u.* has been chosen to account for a realistic one-second overpower condition for a large wind farm.

B. Drive Train Inertia and Coupling

Drive train inertia is highly influential in the dynamic performance of a wind farm system. Lumped inertia constants (H) for WTs are typically in the range 2.4–6.8 s [16, p. 545]. Data from commercial 1.3-MW WTs suggest that 4.5 s is a representative value for this study.

Drive train coupling is highly significant. It is now generally accepted that two-mass representation of a WT drive train is a necessary feature for dynamic analysis [17]. Data from a selection of multi-megawatt WTs suggest that a low speed to high speed inertia ratio of six to eight and an eigenfrequency of 2 Hz are broadly representative values. Mechanical friction and damping have little effect on system stability and are neglected. In summary, the following drive train parameters are used in this paper:

$$\begin{aligned} \text{Low speed inertia constant}: &\quad H_{\text{ls}} = 4\ \text{s} \\ \text{High speed inertia constant}: &\quad H_{\text{hs}} = 0.5\ \text{s} \\ \text{Eigenfrequency (free-free)}: &\quad f_{\text{eig}} = 2\ \text{Hz}. \end{aligned}$$

C. Induction Generator Impedances

Induction generator impedances are highly influential on the wind farm's FRT performance. Efficient multi-megawatt machines must have low rotor resistance and therefore a steep torque-slip curve at rated power and a low "pull-away" slip. The FRT response of a wind farm is particularly sensitive to rotor resistance, and therefore, the selected value of *0.007 p.u.* on WT rating is carefully chosen with reference to real WT data. Saturation effects, core losses, and the slip-dependence of impedance magnitudes are not accounted for in this study.

The following generator impedances have been used for all studies in this paper:

$$\begin{aligned} \text{Stator resistance}: &\quad R_s = 0.006\ \text{p.u.} \\ \text{Stator leakage inductance}: &\quad L_{\text{sl}} = 0.14\ \text{p.u.} \\ \text{Rotor resistance}: &\quad R_r = 0.007\ \text{p.u.} \\ \text{Rotor leakage inductance}: &\quad L_{\text{rl}} = 0.05\ \text{p.u.} \\ \text{Magnetizing inductance}: &\quad L_m = 3.0\ \text{p.u.} \end{aligned}$$

D. Shunt Capacitance (Local to WT)

WT shunt capacitance traditionally comprises fixed no-load and switched load compensation banks. Grid codes now impose steady-state reactive power *export* requirements and transient voltage control requirements that demand further provision met locally or centrally (see Subsection F). The base-case for the studies in this paper is *reactive power compensation* (RPC) *of 1.0 p.u. using shunt capacitors*, capable of meeting typical steady-state grid requirements. These capacitors are assumed to be connected throughout the FRT simulations. Additional dynamic RPC is used only for comparison with SDBR.

E. WT Transformer Impedance

Wind farms have dedicated step-up WT transformers. Typically multi-megawatt WT transformers have lumped series reactance of 0.06 p.u. and resistance of 0.01 p.u. The transformers are modeled as series impedance in steady state and transient analysis in this paper.

F. Central Reactive Power

Central RPC can be provided by switched capacitors, SVC [18] or STATCOM [19]. Central RPC has a marginally different effect on FRT performance than local RPC due to the interposing turbine transformers and cabling. However, for the purpose of these generic studies, central RPC has been omitted in order to allow the lumping of wind farm and grid impedance (see Subsection I).

G. SDBR

SDBR can be located centrally or distributed at each turbine transformer. Central location is advantageous where there are large numbers of WTs because a single device can be installed at the site substation, avoiding the space and/or planning constraints at the turbine tower. Although there is some difference in the FRT performance of these two options, the distributed SDBR option has been used in these studies to reduce the complexity of the wind farm equivalent (see Subsection I) and the transient model. The distributed SDBR is switched by

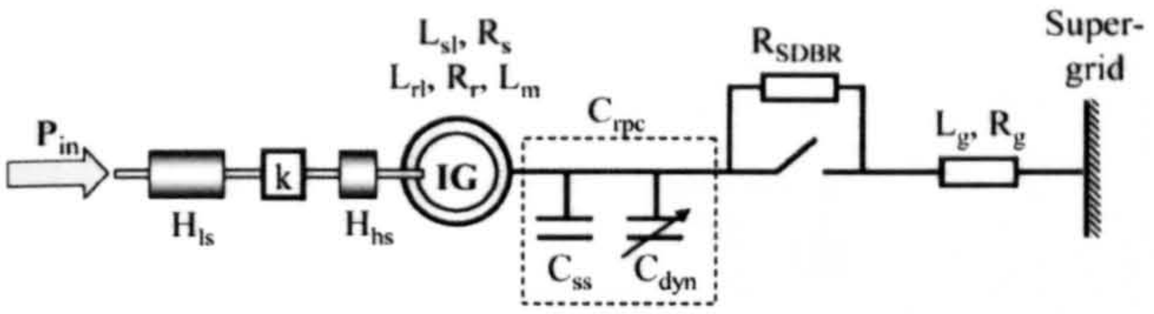

Fig. 5. Reduced schematic of representative wind farm.

a fast-acting bypass contactor triggered by an instantaneous undervoltage relay. The total insertion time for such an arrangement would be about 40 ms. In the base case studies, the resistor is switched out after one second in order to limit thermal loading on the resistor and avoid unnecessary dissipation of power after recovery.

H. Grid Transformer Impedance

The grid transformer is an important component of a large wind farm system because of its substantial impedance. A dedicated step-up transformer with a lumped series reactance of 0.10 p.u. and resistance of 0.05 p.u. is selected as representative for a large wind farm.

I. Equivalent Representation

Having defined parameters for each major component of a representative wind farm system, a reduced equivalent can be derived for the purpose of steady-state and transient analysis. The first reduction is the lumping of multiple WT units into a single equivalent with rating equal to the sum of the individual units and per unit values equal to those of the individual units. This is justified by the fact that identical power inputs and system parameters have been used for each WT unit. The second reduction is the lumping of WT and grid transformers and miscellaneous grid impedance as a single series impedance neglecting shunt capacitance and transformer magnetizsing reactance. Omission of transformer inrush is not highly significant for the comparative assessment of this paper. The following lumped values are therefore proposed for this study:

$$\text{Grid resistance :} \qquad R_g = 0.04 \text{ p.u.}$$
$$\text{Grid inductance :} \qquad L_g = 0.20 \text{ p.u.}$$

In summary, the reduced, representative model carried forward for analysis in the following sections is shown in Fig. 5.

V. Steady-State Characterization

A. Introduction

The purpose of this section is to characterize the influence of SDBR on steady-state wind farm power flows and thereby infer potential FRT enhancements of the representative wind farm system of Fig. 5. Two enhancement technologies are compared: state-of-art dynamic RPC and SDBR. However, before proceeding with this analysis, it is important to relate the time frames of fault events and system time constants. The range of applicable grid faults is defined by the voltage-duration profile of Fig. 6(a) and illustrated by the selected fault scenarios of Fig. 6(b).

Fig. 6(a) is taken from the GB Grid Code [CC.A.4.3, 4] but is of a form typical of the requirements of many modern grid codes. The profile does not describe a single fault event but the envelope of rectangular voltage notches associated with worst-case grid faults. The ac time constant, T_{ac}, for system transients is derived from the following equation:

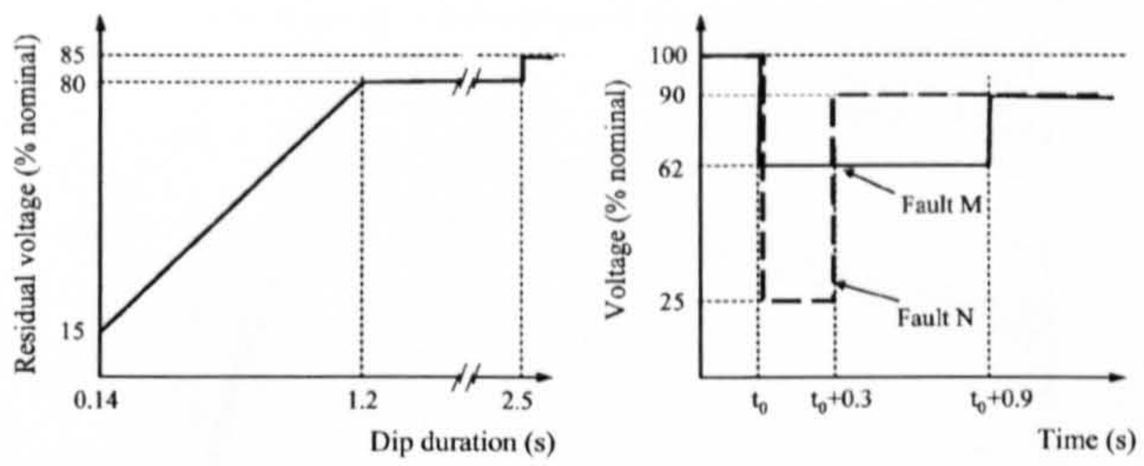

Fig. 6. Voltage-duration profiles for grid voltage dips. (a) Grid voltage-duration profile. (b) Selected grid fault scenarios.

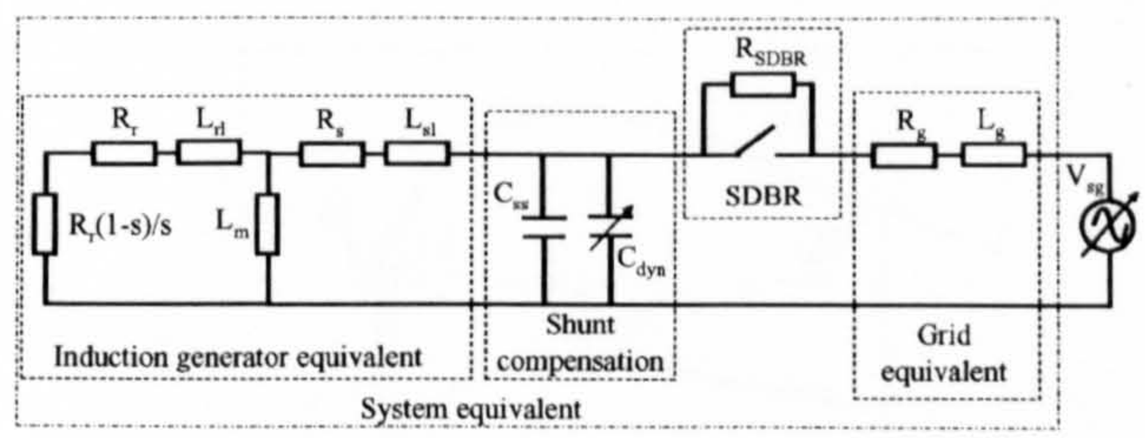

Fig. 7. Equivalent circuit and power curve for representative wind farm. (a) Equivalent circuit. (b) Decelerating power versus speed characteristic (rated grid voltage).

$$T_{ac} = \frac{X_T}{\omega R_r} \tag{1}$$

where

X_T = system Thevenin equivalent reactance(Ω);
ω = system angular frequency($\text{rad}s^{-1}$).

The time constant is calculated to be 180 ms for the system equivalent of Fig. 7 and noted to be independent of stator resistance. The two voltage-time traces shown in Fig. 6(b) are used to represent faults with long and short time durations relative to this time constant. The long duration fault, M, can be approximated as three steady-state conditions. The short duration fault, N, will be heavily influenced by the system transient response, and steady-state characteristics are less directly indicative of stability in this case (see Section V-F2).

B. Steady-State Power Characterization

The single-phase, positive sequence circuit equivalent for the representative wind farm of Fig. 5 is shown in Fig. 7(a) with per unit slip, s.

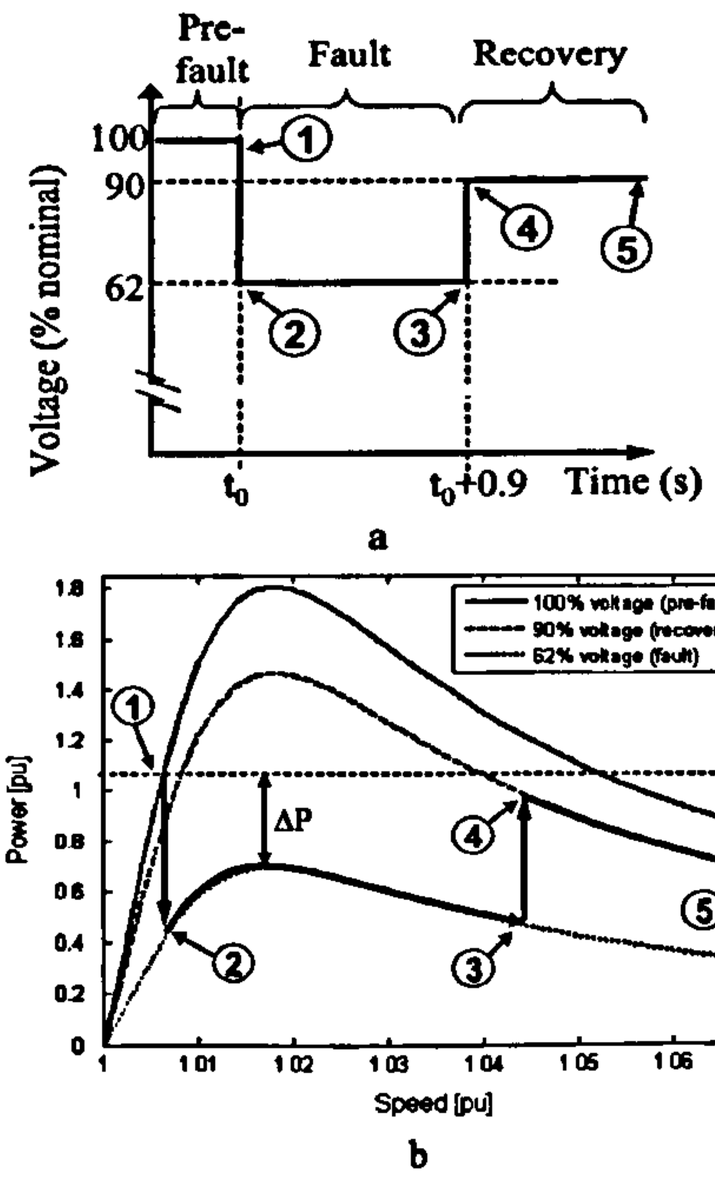

Fig. 8. Real-time power-speed trajectory. (a) Annotated fault scenario. (b) Power-speed trajectory.

The steady-state power transfer capability of an FSWT wind farm is characterized by the power-speed curves derived from the equivalent circuit of Fig. 7(a). There are two power characteristics of interest in FRT assessment: the decelerating power extracted from the mechanical system (determining the dynamic stability of the wind farm system) and the power exported to the grid (supporting the dynamic stability of the overall power system). This paper is concerned primarily with wind farm stability and therefore focuses on decelerating power characteristics, as shown in Fig. 7(b).

C. Quasi-Steady-State Assessment

Having introduced the steady-state power-speed characteristics of the wind farm system, the next step is to consider drive train dynamics within each period of the fault and plot the resulting real-time trajectory onto quasi-steady-state characteristics. In order to emphasize the effect of FRT enhancement techniques, a low lumped inertia constant of 2.5 s has been used for the following assessment. Furthermore, the effects of electrical system transients have been neglected at this stage. The resulting quasi-steady-state analysis is illustrated by Fig. 8 for the base-case wind farm system.

Fig. 8(a) shows the voltage-time characteristic of fault M. Fig. 8(b) shows the dynamic trajectory of the system superimposed onto the steady-state power-speed curves for each of the voltage levels associated with the fault. The key determinant of stability is acceleration during the fault period (driven by the net accelerating power, ΔP) and the power balance at fault clearance. In Fig. 8(b), the input power is greater than the decelerating power at this time, and therefore, the system is unstable. The primary objective of FRT enhancing technologies is therefore to improve the balance of power at this crucial point.

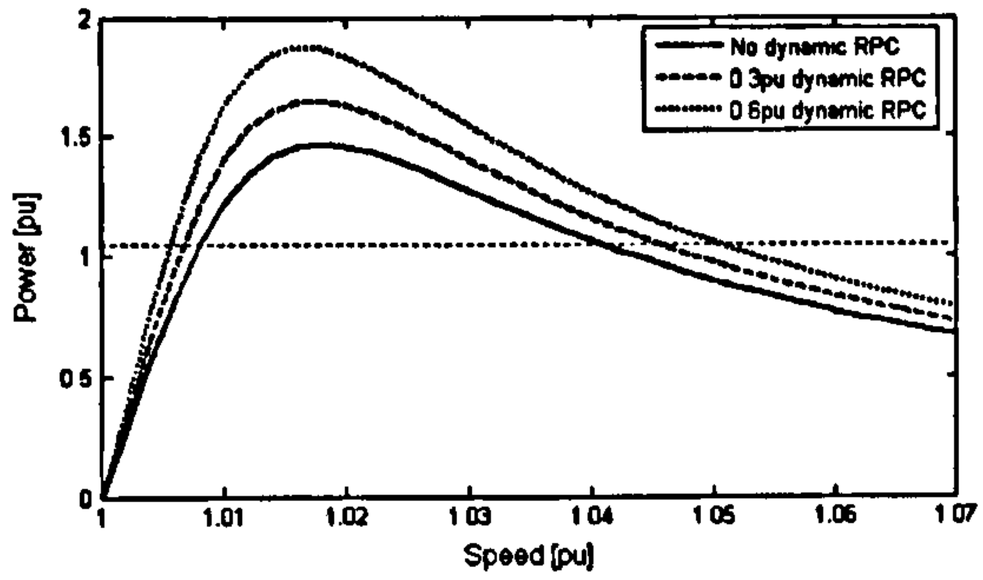

Fig. 9. Effect of dynamic RPC on steady-state characteristics.

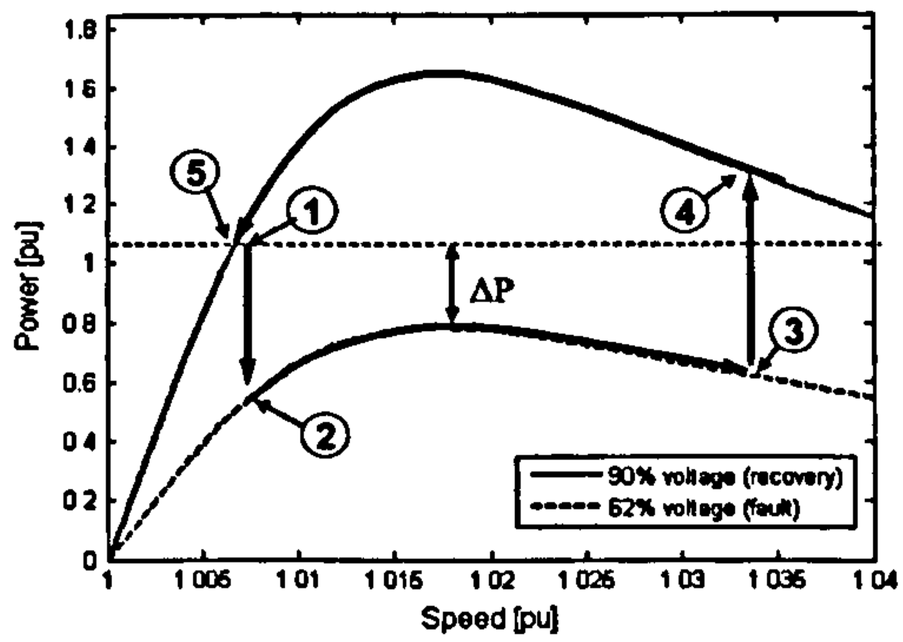

Fig. 10. Enhanced FRT response with dynamic RPC.

D. Improving Stability Using Dynamic RPC

The state-of-art method for enhancing FRT performance of wind farms comprising FSWTs is to insert dynamic RPC, using thyristor-switched capacitors, SVC or STATCOM. The effect of thyristor-switched capacitors on the steady-state system power characteristics is shown in Fig. 9.

Fig. 9 shows the effect of 0.3- and 0.6-p.u. dynamic RPC on the steady-state power characteristics with 90% grid recovery voltage. It can be observed that the dynamic RPC lifts the power characteristic throughout the speed range by about 15% for each 0.3-p.u. RPC increment.

The effect of 0.3-p.u. dynamic RPC on the quasi-steady-state response of the wind farm to fault M is shown in Fig. 10.

It can be observed that the net accelerating power, ΔP, is less than the base-case study in Fig. 8(b), resulting in reduced speed excursion at fault clearance (3). Furthermore, the recovery characteristic is greater in magnitude, resulting in a significant net decelerating power in the recovery phase. The combination of these factors means that the enhanced system has a good margin of stability.

E. Improving Stability Using SDBR

The effect of SDBR on the steady-state system power characteristics is shown in Fig. 11.

Fig. 11 shows the effect of 0.05- and 0.1-p.u. SDBR on the steady-state power characteristics with 90% grid recovery voltage. It can be observed that the peak power is increased substantially (about 40% for 0.1-p.u. SDBR), but the improvement in the power characteristic diminishes substantially with increasing speed. This qualitative effect was predicted from the phasor diagram of Fig. 3.

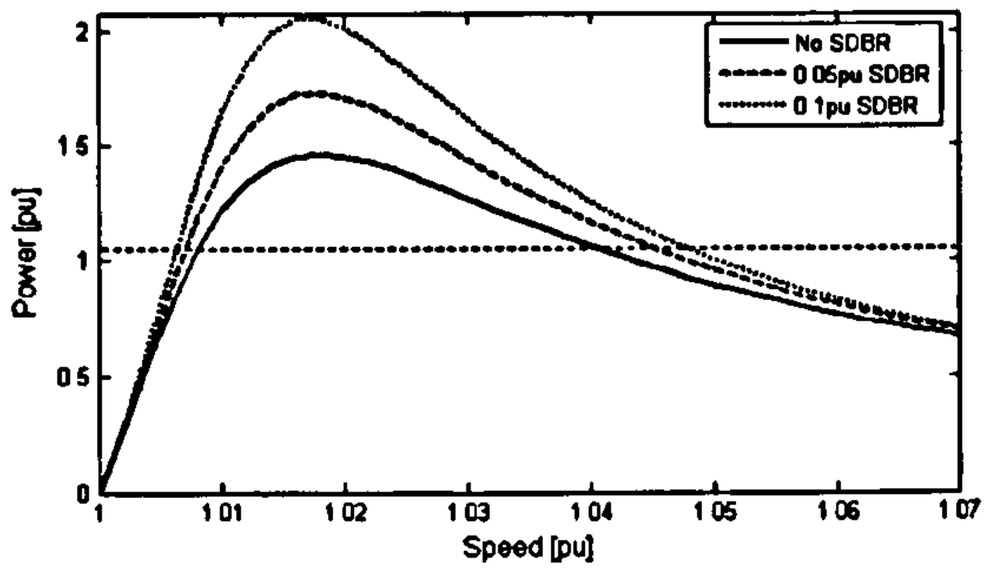

Fig. 11. Effect of dynamic SDBR on steady-state characteristics.

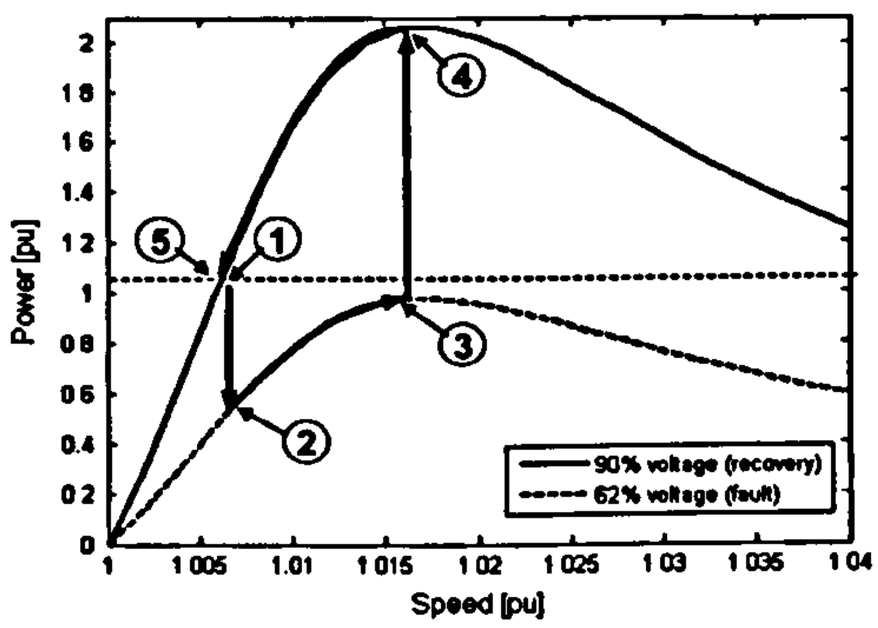

Fig. 12. Enhanced FRT response with SDBR.

The effect of 0.1-p.u. SDBR on the quasi-steady-state response of the wind farm to fault M is shown in Fig. 12.

It can be observed that the net accelerating power, ΔP, tends to zero during the fault period so that a quasi-stable position is reached at the residual voltage level. When the fault is cleared, a large decelerating power is applied (point 4), rapidly restoring the system to near-nominal speed. The enhanced system therefore has a very large margin of stability.

F. Effect of System Transients

The influence of system transients on quasi-steady-state assessment becomes progressively more significant for faults of shorter duration. These influences are conveniently categorized as *dynamical*, arising from generator rotor acceleration or deceleration, and *transient*, arising from electrical voltage steps. The following analysis seeks to examine each influence in isolation using the full transient model described in Section VI.

1) Dynamical Influence: Acceleration (α) scenarios of 0.3 p.u. and -0.15 p.u. have been selected to represent the higher end of likely acceleration magnitudes arising from two-mass simulations (i.e., Fig. 18). The acceleration and deceleration simulations, with and without SDBR, were initialized at 1.0-p.u. and 1.1-p.u. speeds, respectively. Fig. 13 shows the results of these simulations.

Fig. 13 shows that acceleration "shears" the power-speed curves in the direction of higher speed and power magnitude, and deceleration "shears" the power-speed curves in the direction of lower speeds and power magnitude. The key observation for the purpose of this qualitative assessment is that the beneficial effect of SDBR is sustained in each case.

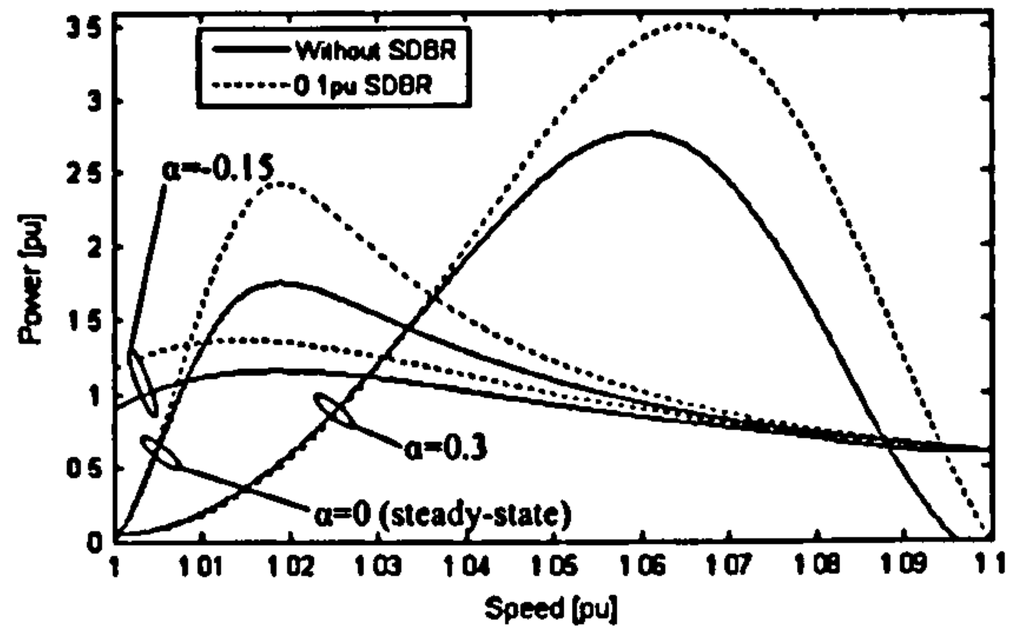

Fig. 13. Effect of acceleration on steady-state wind farm power characteristic.

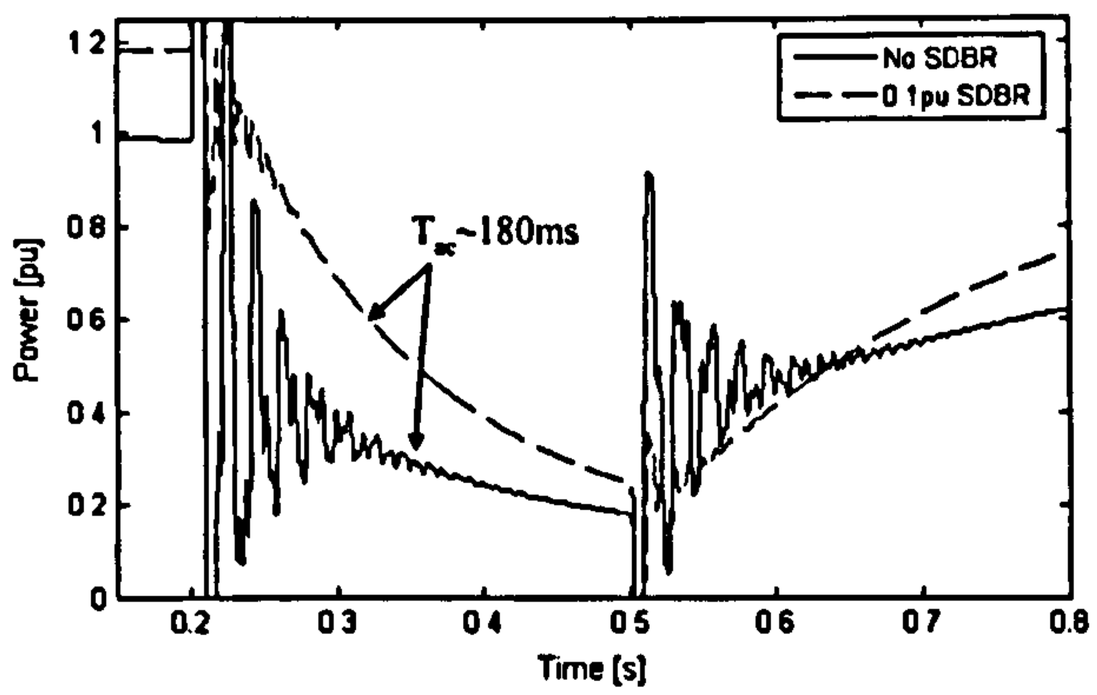

Fig. 14. Transition of mechanical power during fault N.

2) Transient Influence: Fig. 14 shows the transition of mechanical power associated with the voltage steps of fault N in Fig. 6 with speed constrained to nominal.

It can be observed that SDBR does not change the voltage decay time constant [~180 ms, as derived from (1)]. but it does substantially increase the initial mechanical power exported into the electrical system during the fault. It is also evident that SDBR strongly damps the dc-induced 50-Hz oscillating component of power in the period after each voltage transition.

After fault clearance, the power export with SDBR is initially depressed but rises quickly to exceed the base-case.

VI. Transient Simulation of Wind Farm System

A. Introduction

The benefits of SDBR and dynamic RPC have been inferred from steady-state analysis in Section V. This section introduces a transient model of the wind farm system and applies it in Matlab-Simulink to confirm these inferred benefits in comparison to dynamic RPC for balanced and unbalanced FRT simulations. The transient model is shown in the schematic diagram of Fig. 15.

Fig. 15 corresponds directly to the single line diagram in Fig. 5 with each transfer function, G(s), relating to a system component. G(s) has the general form of

$$G(s) = \frac{b(s)}{a(s)} = \frac{1}{Xs + Y} \tag{2}$$

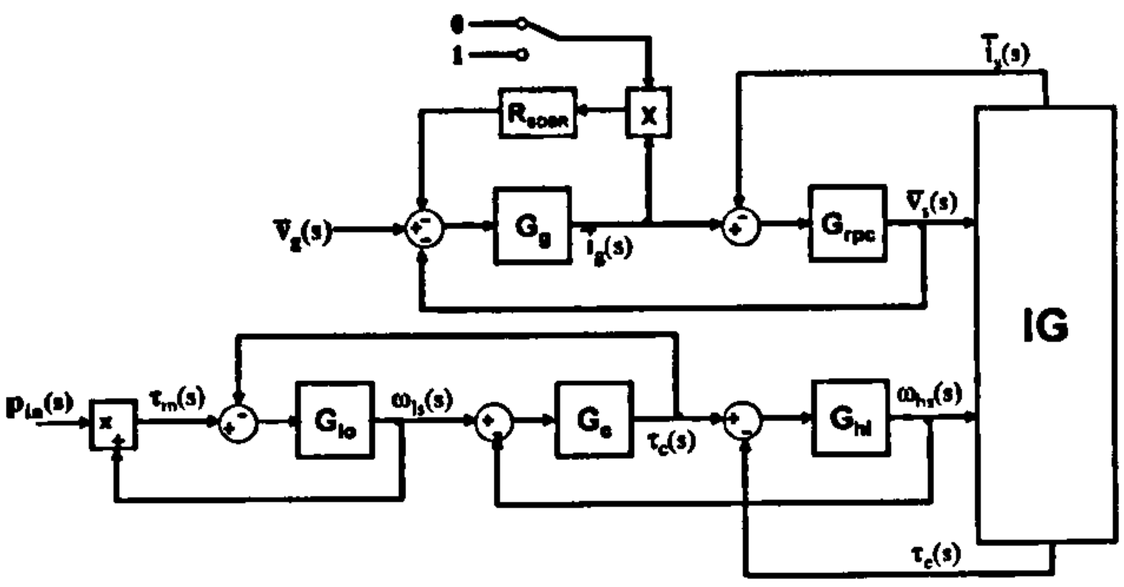

Fig. 15. Schematic diagram of transient model with single mass.

TABLE II
SYSTEM PARAMETERS

Component	Function	X	Y
Mechanical system:			
Low-speed inertia	$G_{ls}(s)$	$2H_{ls}$	0
Shaft coupling	$G_c(s)$	K_c	10^3
High-speed inertia	$G_{hs}(s)$	$2H_{hs}$	0
Electrical system:			
Grid impedance	$G_g(s)$	L/ω_0	R_g
Reactive power comp.	$G_{rpc}(s)$	C_{rpc}/ω_0	10^3
Notes: B_c & R_{rpc} *are inserted for numerical stability only* $C_{rpc}=C_{ss}+kC_{dyn}$ *where k is 1 during the fault and ramps to zero during the recovery period (no proportional control)*			

where

$a(s)$ and $b(s)$ are input and output functions, respectively :

scalar functions for mechanical system

space vector functions for electrical system

X and Y are inertia (inductance) and damping (resistance).

X and Y are referenced to physical parameters in Table II.

Typical values from Section IV are assigned to each parameter in the transient studies presented in this section. The induction generator block, IG, represents a transfer function derived from

$$\bar{v}_s = R_s\bar{i}_s + \frac{1}{\omega_0}\frac{d\bar{\lambda}_s}{dt} \tag{3}$$

$$\bar{v}_r = R_r\bar{i}_r + \frac{1}{\omega_0}\frac{d\bar{\lambda}_r}{dt} - \omega_r M\bar{\lambda}_r = 0 \tag{4}$$

where

M is $\pi/2$ rotation operator

$\bar{v}_s$ and $\bar{v}_r$ are p.u. stator and rotor space vector voltages

$\bar{i}_s$ and $\bar{i}_r$ are p.u. stator and rotor space vector currents

ω_0 and ω_r are base speed (rad/s) and p.u. rotor speed

$\bar{\lambda}_s = L_m\bar{i}_r + L_{sl}\bar{i}_s$ is p.u. stator space vector flux linkage

$\bar{\lambda}_r = L_m\bar{i}_s + L_{rl}\bar{i}_r$ is p.u. rotor space vector flux linkage.

B. Balanced Lumped Mass Simulation

The purpose of this lumped mass simulation is to establish the underlying transient effect of SDBR with minimum complexity.

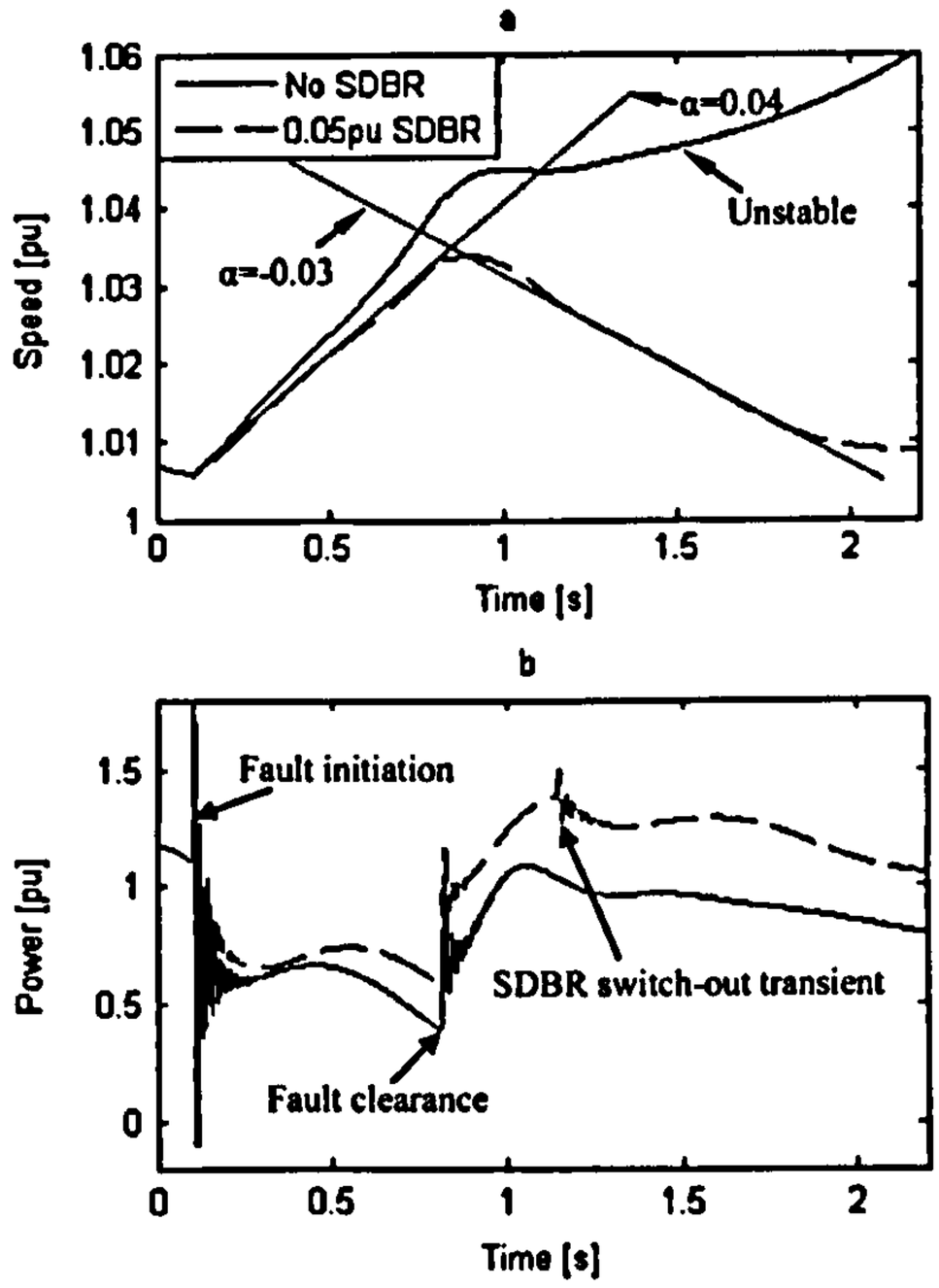

Fig. 16. Effect of SDBR on wind farm FRT performance.

The model of Fig. 15 is reduced by lumping high and low speed inertias to form a single drive train inertia constant, H, of 4.5 s.

The fault scenario selected for this example is 710 ms at 50% residual voltage, and 0.05 pu SDBR was selected as the minimum value that safely allowed recovery of the system for all fault scenarios derived from the voltage-duration profile of Fig. 6. The results of this scenario, simulated using the model of Fig. 15, are shown in Fig. 16.

Fig. 16(a) shows that SDBR transforms an unstable condition into a comfortably stable one. The reason for this improvement is illustrated by Fig. 16(b), which shows the increase in mechanical power extracted from the drive train both during and after the fault. This beneficial effect is repeated for the full range of faults described by the voltage duration profile of Fig. 6 and makes the difference between stability and instability in the fault duration range of 500–800 ms. Fig. 17 shows the correlation between the transient simulation results and those predicted from quasi-steady-state analysis with reference to the plot of rotor's power-speed FRT trajectory.

The FRT trajectory of the rotor in Fig. 17 starts at the system's pre-fault operating point (1.006, 1.05), accelerates up to the instant of fault clearance (1.033, 0.6), and then decelerates to its post-fault operating point (1.007, 1.05). The dynamically-adjusted steady-state characteristics associated with the fault (α = 0.04 p.u.) and recovery ($\alpha = -0.03$ p.u.) are superimposed onto the power-speed plot. It can be observed that the FRT trajectory converges with these characteristics in both cases following an initial voltage transient error, as predicted in Section V-F.

C. Balanced Two-Mass Simulation

Having established the reduced wind farm's underlying FRT response and correlated it with quasi-steady-state analysis, this section compares the performance and sensitivities of SDBR

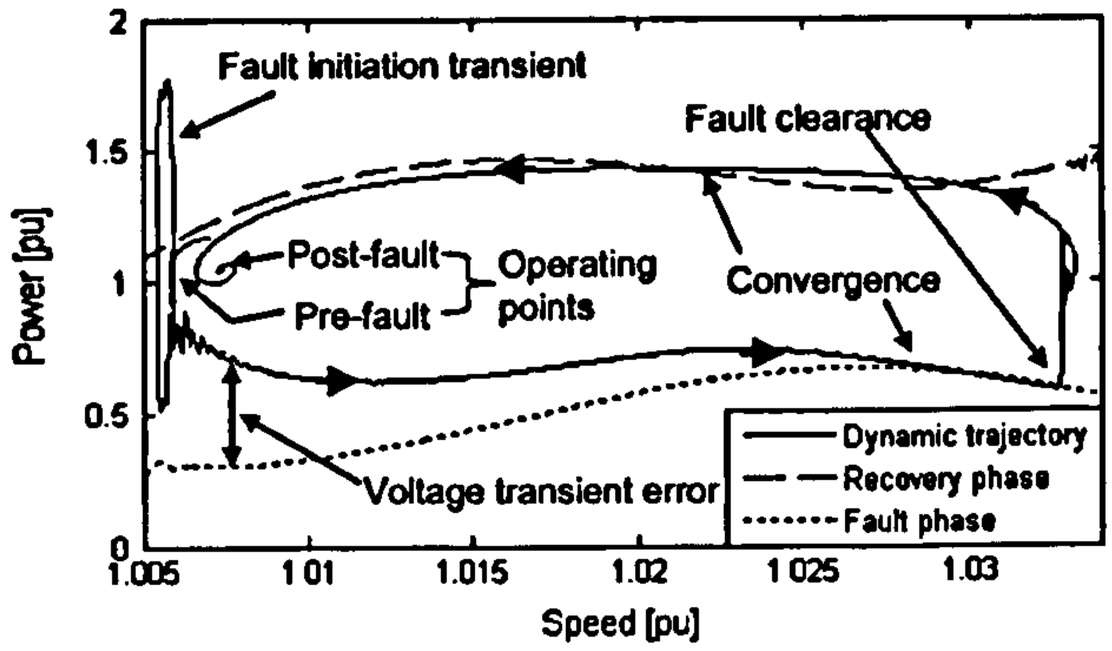

Fig. 17. Correlation of dynamic simulation with quasi-steady-state.

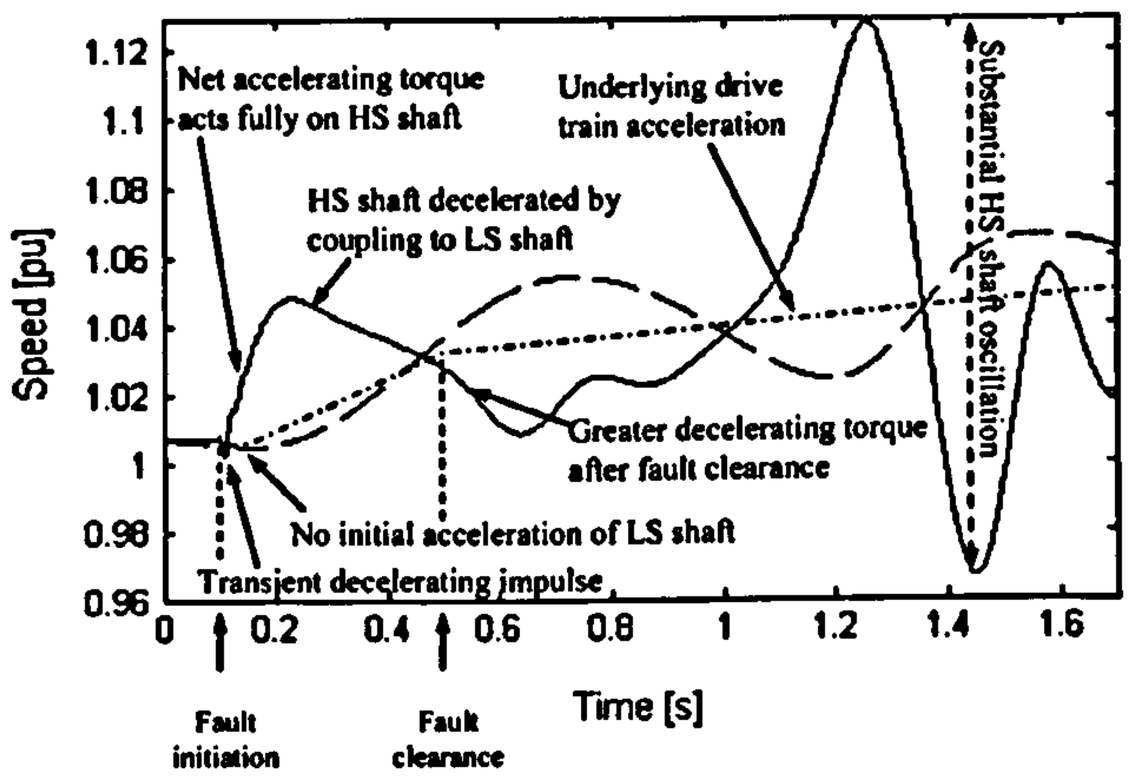

Fig. 18. Speed-time response of wind farm drive train.

and dynamic RPC technologies using a two-mass wind farm model.

The model of Fig. 15 is run with a fault scenario of 384 ms at 30% residual voltage selected from the fault duration profile of Fig. 6. A shorter, deeper voltage dip was selected because this type of fault is typically more severe for two-mass drive trains. This is because destabilizing oscillations are excited in the two-mass system by the large voltage steps associated with the shorter faults. These oscillations are shown in the results of Fig. 18.

Fig. 18 shows the base-case system's dynamic response to the 384-ms fault scenario. After an initial transient decelerating impulse at fault initiation, the step reduction in electrical decelerating torque results in large acceleration of the high-speed (generator rotor) shaft. The relatively low inertia of this shaft means that its acceleration is much larger than observed for a corresponding single mass simulation. The step torque excites two-mass oscillations superimposed on underlying drive train acceleration. Fault clearance imposes a second torque step that excites further oscillation but reduces the underlying acceleration. However, the average decelerating torque during the recovery phase is not sufficient to allow recovery of the system, and the WT would probably trip on overspeed protection during the first positive swing after fault clearance.

Having discussed the fundamental dynamic response of the base-case system, Fig. 19 compares the system response with SDBR and dynamic RPC inserted. The values of SDBR resistance and dynamic RPC capacitance used in the study were

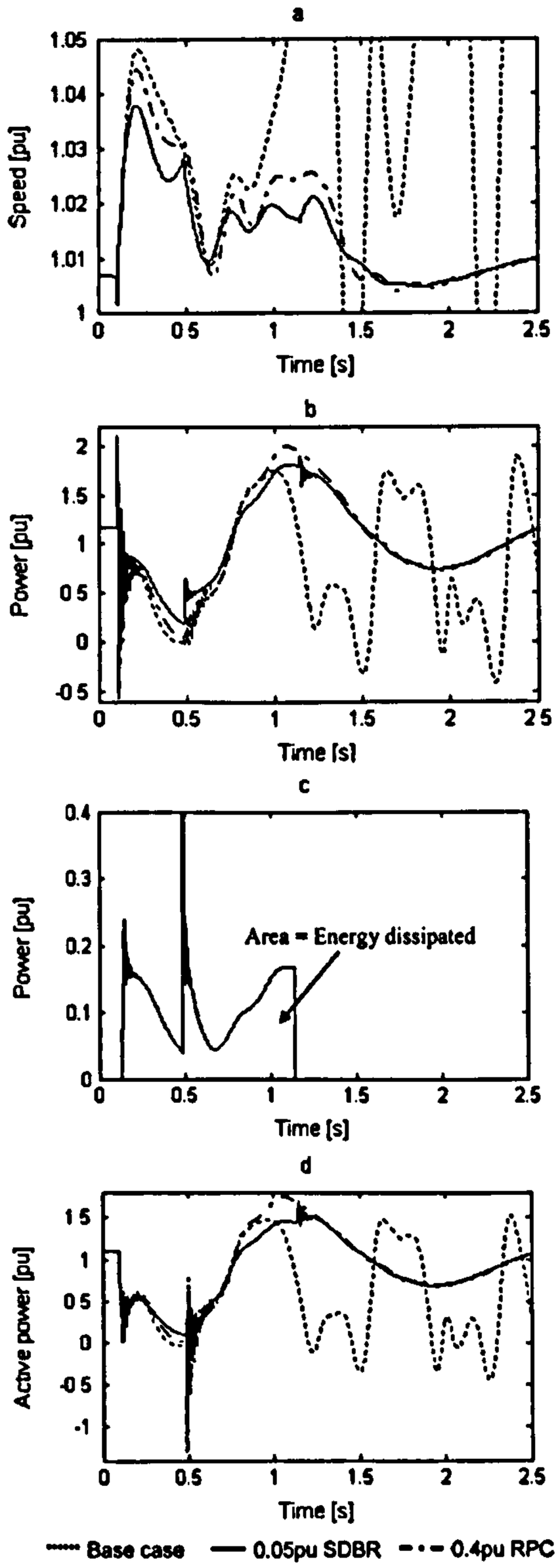

Fig. 19. Effect of SDBR and dynamic RPC on FRT performance. (a) Speed-time curves. (b) Mechanical power-time curves. (c) SDBR power-time curves. (d) Export power-time curves.

selected as the minimum necessary to secure comparable and sufficient stability over the full range of faults defined by the voltage duration profile of Fig. 6.

During the fault, SDBR mitigates acceleration more strongly than dynamic RPC [see Fig. 19(a)]. This effect is a result of the additional power extracted from the mechanical system [see Fig. 19(b)] of which some is exported into the grid [see Fig. 19(d)] and the remainder is dissipated in the SDBR resistor [see Fig. 19(c)].

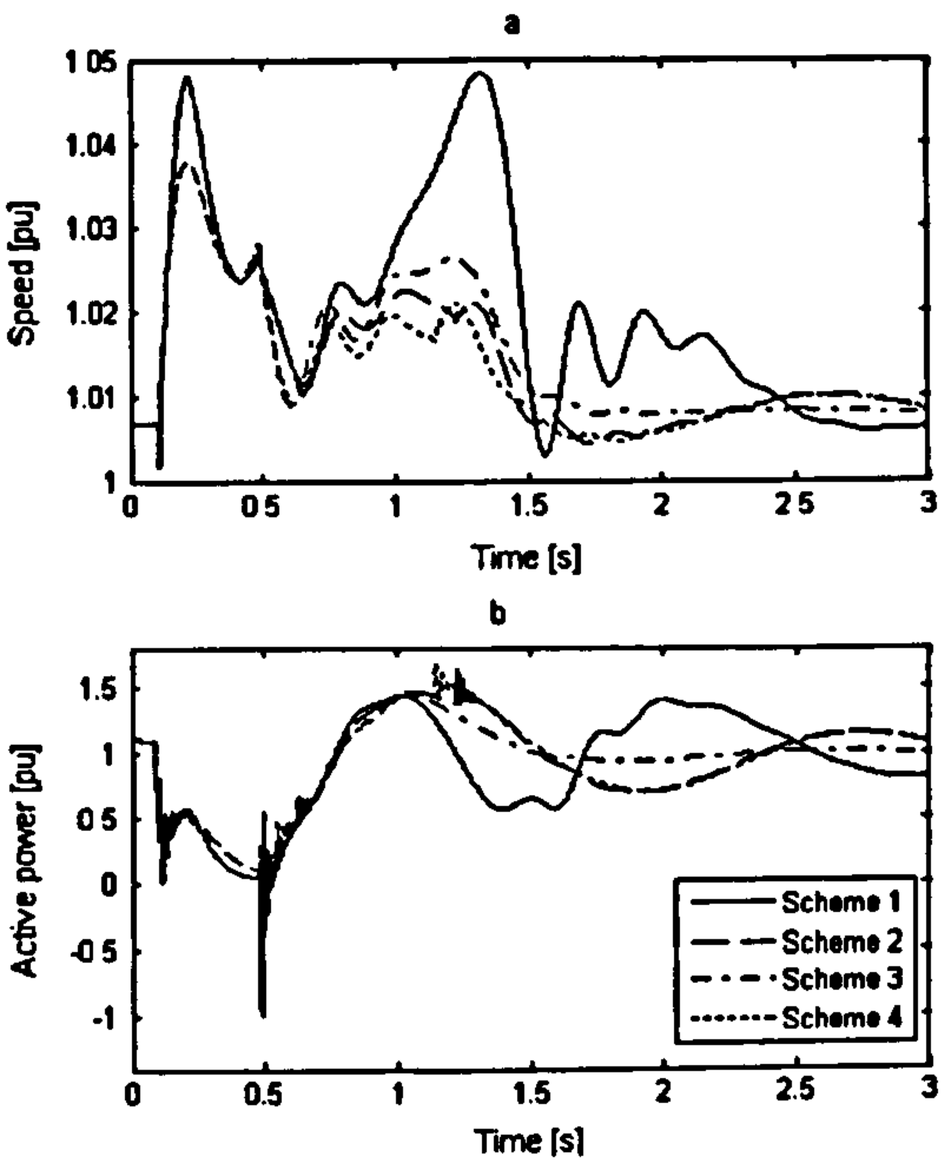

Fig. 20. Sensitivity of SDBR switching times on FRT performance. (a) Speed-time curves. (b) Export power-time curves.

TABLE III
SDBR SWITCHING SCHEMES

Scheme no.	Switch-in (s)	Switch-out (s)
1	0.12	0.52
2	0.12	1.12
3	0.04	0.44
4	0.04	1.04
Note: Time is given w.r.t. fault initiation		

During the recovery, both technologies act similarly to limit post-fault oscillations and give rise to stable operation in about 2.5 ss. In both cases, power export to the grid is restored above 0.9 p.u. within 0.5 s of fault clearance [see Fig. 19(d)], although subsequent oscillations do cause some further reduction below this level.

The energy dissipated by SDBR [see Fig. 19(c)] determines its size and cost. This energy can be optimized by changing the switch-out time. The switch-in time, on the other hand, should always be as short as possible to maximize its speed limitation effect. In this study, SDBR is modeled on the LV system, and therefore, 40 ms has been used as the likely time from fault detection to contactor interruption. In the case of central SDBR, MV switching would give rise to slower insertion times in the order of 120 ms. Fig. 20 compares the four SDBR switching schemes defined in Table III.

It can be observed that scheme 3 has the most stable response and will clearly dissipate significantly less energy in the resistor than scheme 4. The marginal stability of scheme 1 highlights the importance of rapid insertion with centralized SDBR. The energy dissipated in the resistor using the optimum scheme 2 is calculated as 0.05 p.u. This implies that a 2-MW WT would require a resistor thermally rated at 100 kJ for a distributed SDBR scheme. Alternatively, a 40-MW wind farm would require a central resistor thermally rated at 2 MJ.

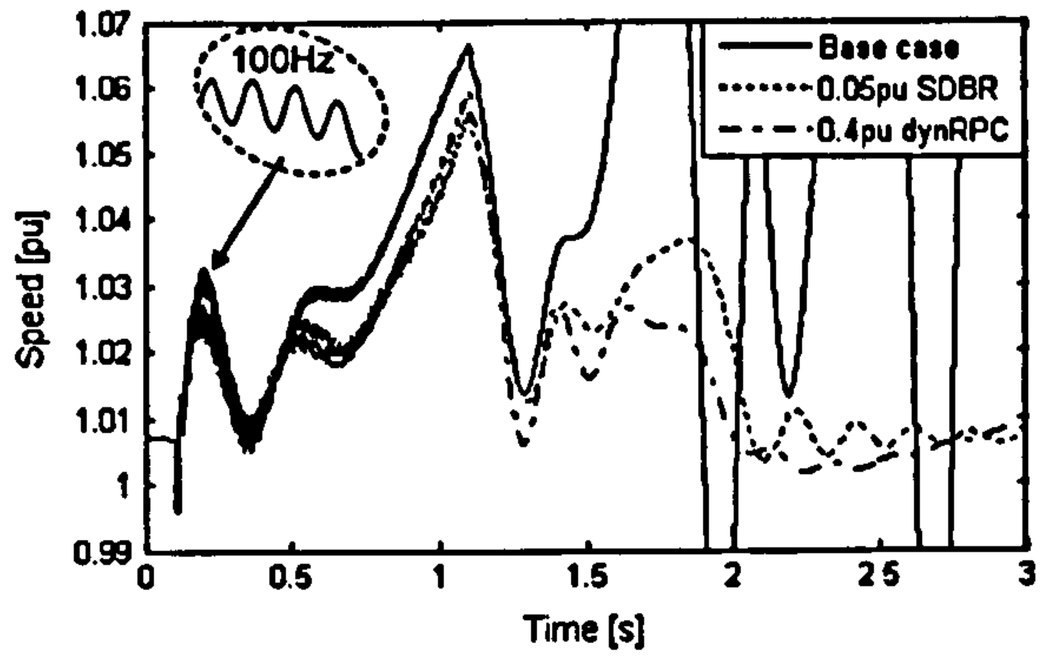

Fig. 21. Effect of SDBR and Dynamic RPC on FRT performance.

D. Unbalanced Simulation

Although the majority of grid faults are unbalanced, grid codes tend to focus on FRT requirements for balanced fault conditions. The assumption is that balanced faults are more onerous for generator stability than unbalanced ones. Although this is generally the case, it is instructive to observe the response of the representative wind farm for a shorted phase-to-phase fault cleared by slow-acting backup protection after one second. The recovery is assumed to be at rated grid voltage.

Fig. 21 shows that this is a very onerous fault that results in instability for the base-case example and marginal stability with each of the FRT technologies. The dynamic RPC actually recovers more rapidly because of the fact that SDBR is switched out only 40 ms after fault clearance (total insertion time of one second). The importance of this scenario is the fact that the energy dissipated in SDBR is higher than the balanced case (0.15 p.u. in the above example). This could therefore become the limiting factor for SDBR thermal design.

VII. Conclusion

SDBR has been shown by transient simulation to significantly improve the FRT performance of a representative large wind farm comprising FSWTs. Centralized or distributed SDBR is shown to be capable of transforming an unstable wind farm response into a comfortably stable one without the need for pitch control or dynamic RPC. This improvement is achieved over an extensive range of balanced and unbalanced faults as typically specified by grid codes. Direct comparison of SDBR and dynamic RPC for the representative wind farm concludes that a 0.05-p.u. dynamic resistor is equivalent to 0.4 p.u. of dynamic RPC. As well as a substantial capital cost advantage, SDBR has the potential for higher reliability and lower maintenance.

Quasi-steady-state analysis has been demonstrated in theory and applied as a useful tool for characterizing SDBR performance and predicting transient stability. This method illustrates the extent and limitation of the beneficial effects of SDBR and allows generic comparison with alternatives technologies such as dynamic RPC. It is shown to be particularly useful for assessment of longer faults whether the transient influences are less significant. Quasi-steady-state analysis therefore underpins the results of specific transient studies.

An important design factor for SDBR is its switching regime. A study of the sensitivity of SDBR performance to insertion delay and duration concludes that an optimum scheme would typically achieve rapid insertion and early switching out of the dynamic resistor. Such a scheme can result in rapid stabilization of export power combined with low thermal loading of the resistor.

ACKNOWLEDGMENT

The first author would like to thank A. Wilson of NaREC for his encouragement and support in the course of this project.

REFERENCES

[1] ESB National Grid, *The Grid Code: Version 1.2,* 2005.
[2] E. Fagan, S. Grimes, J. McArdle, P. Smith, and M. Stronge, "Grid code provisions for wind generators in Ireland," in *Proc. IEEE Power Eng. Soc. General Meeting*, 2005, pp. 3073–3079.
[3] A. Johnson and N. Tleis, "The development of grid code requirements for new and renewable forms of generation in Great Britain," presented at the 5th Int. Workshop Large Scale Integration of Wind Power and Transmission Networks for Offshore Wind Farms, Glasgow, U.K., 2005, unpublished.
[4] National Grid Electricity Transmission plc, *The Grid Code*, Revision 17, Issue 3, 2006.
[5] I. Erlich and U. Bachmann, "Grid code requirements concerning connection and operation of wind turbines in Germany," presented at the IEEE Power Eng. Soc. General Meeting, 2005, unpublished.
[6] E. O. Nezt, "Grid code," *High and Extra High Voltage*, 2006.
[7] L. Hansen, *Conceptual Survey of Generators and Power Electronics for Wind Turbines*. Roskilde, Denmark: Risø National Lab., 2001.
[8] A. D. Hansen, , T. Ackermann, Ed., "Generators and power electronics for wind turbines," in *Wind Power in Power Systems*. Chichester, U.K.: Wiley, 2005.
[9] A. Causebrook, "Dynamic Braking of Electric Generators for Fault Ride-through Control," U.K. Patent Application no. GB0526133.4, 2004, Newcastle Univ.
[10] A. Causebrook, D. Atkinson, and A. Jack, "Fault ride-through: shifting the balance of power from blade pitch to electrical resistance," presented at the Eur. Wind Energy Conf., Athens, Greece, 2006, unpublished.
[11] X. Wu, A. Arulampalam, C. Zhan, and N. Jenkins, "Application of a static reactive power compensator (STATCOM) and a dynamic braking resistor (DBR) for the stability enhancement of a large wind farm," *Wind Eng. J.*, vol. 27, pp. 93–106, 2003.
[12] W. Freitas, A. Morelato, and W. Xu, "Improvement of induction generator stability using braking resistors," *IEEE Trans. Power Syst.*, vol. 19, no. 2, pp. 1247–1249, May 2004.
[13] D. F. Peelo, D. W. Hein, and F. Peretti, "Application of a 138 kV 200 MW braking resistor," *Power Eng. J. [See Also Power Engineer]*, vol. 8, pp. 188–192, 1994.
[14] R. Patel, T. S. Bhatti, and D. P. Kothari, "Improvement of power system transient stability by coordinated operation of fast valving and braking resistor," *Proc. Inst. Elect. Eng., Gen., Transm., Distrib.*, vol. 150, no. 3, pp. 311–316, May 2003.
[15] J. Manwell, J. McGowan, and A. Rogers, *Wind Energy Explained*. New York: Wiley, 2002.
[16] H. Knudsen and J. N. Nielsen, , T. Ackermann, Ed., "Introduction to the modeling of wind turbines," in *Wind Power in Power Systems*. Chichester, U.K.: Wiley, 2005.
[17] V. Akhmatov, , T. Ackermann, Ed., "Full-scale verification of dynamic wind turbine models," in *Wind Power in Power Systems*. Chichester, U.K.: Wiley, 2005.
[18] V. Akhmatov and K. Søbrink, "A static VAR compensator model for improved ride-through capability of wind farms," *Wind Eng.*, vol. 28, pp. 715–728, 2004.
[19] V. Akhmatov and K. Søbrink, "Static synchronous compensator (statcom) for dynamic reactive-compensation of wind turbines," *Wind Eng.*, vol. 30, pp. 43–54, 2006.

Andrew Causebrook received the B.Sc. degree in electrical engineering from Imperial College, London, U.K., in 1986 and the M.Sc. degree in renewable energy technology from Loughborough University, Loughborough, U.K., in 1998. He is pursuing the Ph.D. degree on the fault ride-through of wind farms at Newcastle University, Newcastle upon Tyne, U.K.

He has been Principal Engineer with Econnect Ltd., U.K., since 1999, advising clients on the grid integration of wind farms. He was a member of the Scottish Grid Code Review Sub-panel in 2001–2002 that developed early requirements for the connection of wind farms. He formed AC Renewables Limited in 2007, specializing in the grid integration of renewable energy.

Mr. Causebrook is a member of the IET.

David J. Atkinson received the Ph.D. degree from The University of Newcastle upon Tyne, Newcastle upon Tyne, U.K., for research into the use of Kalman filter-based estimation on induction motor vector controlled drives.

He is currently a Senior Lecturer in the Drives and Machines Group at the University of Newcastle. His research interests include electrical drive systems, real-time estimation and control, power electronics, and wind power generation. Current research project involvement includes sensorless vector drives, fault-tolerant drives, and cascade induction generators. Prior to his university appointment in 1987, he had spent 17 years in industry.

Dr. Atkinson is a member of the IET.

Alan G. Jack (M'00) received the Ph.D. degree in 1975 from Southampton University, Southampton, U.K., for work on numerical analysis of electromagnetic fields in turbogenerators.

He is currently with Newcastle University, Newcastle upon Tyne, U.K, where he is the Chair of the Department of Electrical, Electronic, and Computer Engineering, a past head of the department, and leader of the Newcastle Electric Drives and Machines Group. He is the author of over 80 papers in the area of electrical machines and drives. He has been with the university for over 20 years, joining them from NEI Parsons, who he was with for 13 years, with roles from Craft Apprentice to Principal Design Engineer.

References

Akhmatov, V. (2003(a)). Analysis of Dynamic Behaviour of Electric Power Systems with Large Amount of Wind Power. Electric Power Engineering, Orsted-DTU, Technical University of Denmark.

Akhmatov, V. (2003(b)). "Mechanical Excitation of Electricity-Producing Wind Turbines at Grid Faults." Wind Engineering **27**(4): 257-272.

Akhmatov, V. (2005(b)). Induction Generators for Wind Power, Multi-Science Publishing Company.

Akhmatov, V., H. Knudsen, et al. (2000). "A dynamic stability limit of grid connected induction generators. Paper 319-087." Proceedings of International IASTED Conference on Power and Energy systems, Marbella, Spain, Sept: 19–22.

American_Superconductor. (2006). "Optimizing Reactive Compensation for Wind Farms: Meeting Today's Utility and Regulatory Requirements." from http://www.amsuper.com/products/applications/windEnergy/documents/WF_WP_0306_rev.pdf.

Barthold, L. O. (1988). Technical limits to transmission system operation: Final report**:** Pages: 218.

Bousseau, P., F. Fesquet, et al. (2004). "Solutions for the grid integration of wind farms-a survey." European Wind Energy Conference, London, November.

Causebrook, A. (2005). Dynamic Braking of Electric Generators for Fault Ride-through Control. UK, patent application no. GB0526133.4, Newcastle University.

Causebrook, A., D. Atkinson, et al. (2006). Fault ride-through: Shifting the balance of power from blade pitch to electrical resistance. European Wind Energy Conference, Athens.

Causebrook, A., D. J. Atkinson, et al. (2007). "Fault ride-through of large wind farms using series dynamic braking resistors." IEEE Transactions on Power Systems **22**(3): 966-975.

Doherty, R. and M. O'Malley (2005). "A New Approach to Quantify Reserve Demand in Systems With Significant Installed Wind Capacity." IEEE TRANSACTIONS ON POWER SYSTEMS **20**(2): 587.

E.ON Nezt (2006). Grid Code, High and Extra High Voltage.

Eirgrid (2004). Discussion Document for the Review of Requirements for Wind Turbine Generators under System Fault Conditions, commonly referred to as Fault Ride Through.,

http://www.eirgrid.com/EirgridPortal/DesktopDefault.aspx?tabid=Wind.

EirGrid (2007). The Grid Code, Version 2.0.

ENA (1991). "ER G59/1: Recommendations for the connection of embedded generating plant to the Public Electricity Suppliers distribution systems."

ENA (1995). "ETR 113: Notes of guidance for the protection of embedded generating plant up to 5MW for operation in parallel with Public Electricity Suppliers Distribution Systems (Revision 1)."

Energinet (2004). Wind turbines connected to grids with voltages above 100 kV. Energinet. dk, web page: www. energinet. dk. **Regulation TF 3.2. 5:** 25.

EPRI (1991). Dynamic braking resistor system (Patent no. 5198745). USA.

Erlich, I. and U. Bachmann (2005). Grid code requirements concerning connection and operation of wind turbines in Germany. Power Engineering Society General Meeting, 2005. IEEE.

ESB National Grid (2005). The Grid Code, Version 1.2.

Fagan, E., S. Grimes, et al. (2005). "Grid code provisions for wind generators in Ireland." Power Engineering Society General Meeting, 2005. IEEE: 3073-3079.

Fedderson, L. (2006). Circuit arrangements and methods for use in a wind energy installation, Vestas Wind Systems A/S.

Fitzgerald, A., C. Kingsley, et al. (2002). Electric Machinery, McGraw-Hill Science/Engineering/Math.

Freitas, W., A. Morelato, et al. (2004). "Improvement of induction Generator stability using braking resistors." Power Systems, IEEE Transactions on **19**(2): 1247-1249.

Freris, L. (1990). Wind energy conversion systems, Prentice Hall New York.

Gertmar, L., H. Christensen, C., et al. (2005). New method and hardware for grid connection of wind turbines and parks. Copenhagen Offshore Wind Conference and Exhibition, Copenhagen.

Gertmar, L., H. Christensen, C., et al. (2006). New method and hardware for grid connection of wind turbines and parks. Nordic Wind Power Conference, Espoo, Finland.

Hansen, A. D. (2005). Generators and Power Electronics for Wind Turbines. Wind Power in Power Systems. T. Ackermann. Chichester, Wiley.

Hansen, A. D. and L. H. Hansen (2007). "Market penetration of wind turbine concepts over the years." Risoe website.

Hansen, A. D. and L. H. Hansen (2007). "Wind Turbine Concept Market Penetration over 10 Years (1995–2004)." WIND ENERGY-CHICHESTER- **10**(1): 81.

Hansen, L. (2001). Conceptual survey of generators and power electronics for wind turbines. Roskilde, Risø National Laboratory.

Heier, S. (2006). Grid Integration of Wind Energy Conversion Systems, John Wiley & Sons.

Hinrichsen, E. and P. Nolan (1982). "Dynamics and Stability of Wind Turbine Generators." IEEE Transactions on Power Apparatus and Systems: 2640-2648.

Holdsworth, L., N. Jenkins, et al. (2001). "Electrical stability of large, offshore wind farms." AC-DC Power Transmission, 2001. Seventh International Conference on (Conf. Publ. No. 485): 156-161.

Horne, J., D. Flynn, et al. (2004). "Frequency stability issues for islanded power systems." Power Systems Conference and Exposition, 2004. IEEE PES: 299-306.

IEC (2001). "61400-21: Measurement and assessment of power quality characteristics of grid connected wind turbines."

Iov, F., A. D. Hansen, et al. (2007). Mapping of grid faults and grid codes. Risø-R-1617, Riso. **33**.

Jenkins, N., R. Allan, et al. (2000). Embedded Generation. London, IET.

Johnson, A. and N. Tleis (2005). The development of Grid Code requirements for New and Renewable forms of Generation in Great Britain. 5th International

Workshop on Large Scale Integration of Wind Power and Transmission Networks for Offshore Wind Farms, Glasgow.

Knudsen, H. and J. N. Nielsen (2005). Introduction to the modeling of wind turbines. Wind Power in Power Systems. T. Ackermann. Chichester, Wiley.

Kundur, P. (1993). Power System Stability and Control. New York, McGraw-Hill.

Kundur, P., J. Paserba, et al. (2004). "Definition and classification of power system stability IEEE/CIGRE joint task force on stability terms and definitions." Power Systems, IEEE Transactions on **19**(3): 1387-1401.

Machowski, J., J. Bialek, et al. (1997). Power System Dynamics and Stability. Chichester, Wiley.

Manwell, J., J. McGowan, et al. (2002). Wind energy explained, Wiley.

Morren, J., S. de Haan, et al. (2006). "Wind Turbines Emulating Inertia and Supporting Primary Frequency Control." Power Systems, IEEE Transactions on **21**(1): 433-434.

NGET (2004). "GB Security and Quality of Supply Standard (SQSS)." (v1).

NGET (2007). The Grid Code, Revision 19, Issue 3.

Peelo, D. F., D. W. Hein, et al. (1994). "Application of a 138 kV 200 MW braking resistor." Power Engineering Journal [see also Power Engineer] **8**(4): 188-192.

Ramtharan, G., O. Anaya-Lara, et al. (2006). Influence of structural dynamic representations of FSIG wind turbines on electrical transients. European Wind Energy Conference, Athens, EWEA.

Snel, H. and J. Schepers (1995). Joint Investigation of Dynamic Inflow Effects and Implementation of an Engineering Method, Netherlands Energy Research Foundation ECN.

Sorensen, P., A. D. Hansen, et al. (2003). Simulation and verification of transient events in large wind power installations. Roskilde, Denmark, Riso National Laboratory: 80.

UCTE (2006). Final Report: System Disturbance on 4 November 2006.

Wu, X., A. Arulampalam, et al. (2003). "Application of a Static Reactive Power Compensator (STATCOM) and a Dynamic Braking Resistor (DBR) for the Stability Enhancement of a Large Wind Farm." Wind Engineering Journal **27**(2): 93-106.

Wu, X., L. Holdsworth, et al. (2003). Integrating Renewables and CHP into the UK Electricity System: Investigation of the impact of network faults on the stability of large offshore wind farms, Tyndall Centre for Climate Change Research.